

HYBRID LASER-ARC WELDING OF GALVANIZED HIGH-
STRENGTH STEELS IN A GAP-FREE LAP JOINT
CONFIGURATION

Approved by:

Dr. Radovan Kovacevic

Dr. Syed Hamid

Dr. Behrouz Peikari

Dr. Wei Tong

Dr. David A. Willis

HYBRID LASER-ARC WELDING OF GALVANIZED HIGH-
STRENGTH STEELS IN A GAP-FREE LAP-JOINT
CONFIGURATION

A Dissertation Presented to the Graduate Faculty of the
School of Engineering
Southern Methodist University

in

Partial Fulfillment of the Requirements

for the degree of

Doctor of Philosophy

with a

Major in Mechanical Engineering

by

Shanglu Yang

(B.S., Henan University of Science and Technology, Luoyang, China, 2000)
(M.S., Huazhong University of Science and Technology, Wuhan, China, 2004)

May 16, 2009

UMI Number: 3359843

Copyright 2009 by
Yang, Shanglu

All rights reserved

INFORMATION TO USERS

The quality of this reproduction is dependent upon the quality of the copy submitted. Broken or indistinct print, colored or poor quality illustrations and photographs, print bleed-through, substandard margins, and improper alignment can adversely affect reproduction.

In the unlikely event that the author did not send a complete manuscript and there are missing pages, these will be noted. Also, if unauthorized copyright material had to be removed, a note will indicate the deletion.

UMI[®]

UMI Microform 3359843
Copyright 2009 by ProQuest LLC
All rights reserved. This microform edition is protected against
unauthorized copying under Title 17, United States Code.

ProQuest LLC
789 East Eisenhower Parkway
P.O. Box 1346
Ann Arbor, MI 48106-1346

Copyright (2009)

Shanglu Yang

All Rights Reserved

Shanglu, Yang

B.S., Henan University of Science and Technology, 2000
M.S., Huazhong University of Science and Technology, 2004

Hybrid Laser-Arc Welding of Galvanized,
High Strength Steels in a Gap-free
Lap Joint Configuration

Advisor: Professor Radovan Kovacevic

Doctor of Philosophy conferred May 16, 2009

Dissertation completed April 30, 2009

In order to meet the industry demands for increased fuel efficiency and enhanced mechanical and structural performance of vehicles as well as provided excellent corrosion resistance, more and more galvanized advanced high-strength steels (AHSS) have been used to fabricate automobile parts such as panels, bumpers, and front rails.

The automotive industry has shown tremendous interest in using laser welding to join galvanized dual phase steels because of lower heat input and higher welding speed. However, the laser welding process tends to become dramatically unstable in the presence of highly pressurized zinc vapor because of the low boiling point of zinc, around 906°C, compared to higher melting point of steel, over 1500°C. A large number of spatters are produced by expelling the liquid metal from the molten pool by the pressurized zinc vapor. Different weld defects such as blowholes and porosities appear in the welds. So far, limited information has been reported on welding of galvanized high strength dual-phase steels in a gap-free lap joint configuration. There is no open literature on the successful attainment of defect-free welds from the laser or hybrid welding of galvanized high-strength steels.

To address the significant industry demand, in this study, different welding techniques and monitoring methods are used to study the features of the welding process of galvanized DP steels in a gap-free lap joint configuration. The current research covers: i) a feasibility study on the welding of galvanized DP 980 steels in a lap joint configuration using gas tungsten arc welding (GTAW), laser welding, hybrid laser/arc welding with the common molten pool, laser welding with the assistance of GTAW preheating source and hybrid laser-variable polarity gas tungsten arc welding (Laser-VPGTAW) techniques (Chapter 2-4) ; ii) a welding process monitoring of the welding techniques including the use of machine vision and acoustic emission technique (Chapter 5); iii) Modeling of hybrid laser-GTAW as a preheating source welding process of galvanized steels in a gap-free lap joint configuration (Chapter 6).

Experimental results demonstrated that completely defect-free lap joints in galvanized high strength steels can be obtained in a gap-free configuration by using the laser welding process with the GTAW torch preheating and hybrid laser-VPGTAW welding technique. Effects of the welding parameters on the weld quality are discussed. The mechanical properties of the welded joints are studied. A machine vision system and an acoustic emission (AE) signal acquisition system are employed to acquire the images of the molten pool and the emitted AE signals on-line. Furthermore, image processing and Short Time Fourier Transform (STFT) techniques are employed to analyze the acquired images of the molten pool and the collected AE signals. The acquisition attempts are composed of 1) monitoring the weld defects by machine vision; 2) monitoring the formation of spatters from the AE signals; 3) detecting the weld modes by

the induced plume; and 4) monitoring the instability of the welding process by machine vision. In addition, the numerical results have been validated by the experimental data.

TABLE OF CONTENTS

LIST OF FIGURES	xv
LIST OF TABLES	xxii
NOMENCLATURE	xxiii
ACKNOWLEDGEMENT.....	xxvii
Chapter	
1. INTRODUCTION	1
1.1 Advanced High-strength Steels for Automotive Industry.....	1
1.1.1 Dual-Phase (DP) Steels.....	2
1.1.2 Transformation-Induced Plasticity (TRIP) Steels	5
1.1.3 High Hole Expansion (HHE) Steels.....	7
1.1.4 Complex-Phase (CP) Steels.....	7
1.1.5 Martensite Steels	8
1.2 Welding Issues of Galvanized Advanced High-strength Steels (GAHSS) in a Lap Joint Configuration.....	8
1.2.1 Welding Challenges of Advanced High-strength Steels.....	8
1.2.2 Techniques to Mitigate the Presence of Highly-pressurized Zinc Vapor.....	13
1.2.2.1 Removing the Zinc Coating at the Interface of Steel Sheets Prior to Welding.....	13
1.2.2.2 Setting the Spacers at the Interface of Metal Steels.....	13
1.2.2.3 Redesigning the Setting of the Top Sheet.....	14
1.2.2.4 Using the Alloying Agent to Alloy Zinc.....	14

1.2.2.5	Using the Pulsed Laser.....	15
1.2.2.6	Using Dual Laser Beam or Two Lasers.....	16
1.2.2.7	Hybrid Laser-arc Welding.....	17
1.3	Scope of Research	19
2.	FEASIBILITY STUDY ON WELDING OF GALVANIZED DUAL-PHASE DP980 STEELS IN A LAP JOINT CONFIGURATION.....	22
2.1	Introduction.....	22
2.2	Investigation of Gap-free Lap Welding of Galvanized Dual-phase Steels by Using GTAW.....	23
2.3	Investigation on Using Laser Welding with Gap-free Lap Welding of Galvanized Dual-phase Steels	28
2.3.1	Laser Welding of Galvanized DP Steels without Zinc Coating at the Interface.....	29
2.3.2	Effect of Laser Welding Speed on the Weld Quality	31
2.3.3	Effect of Laser Power on the Weld Quality	33
2.3.4	Effect of Spacer's Presence on the Weld Quality.....	34
2.3.5	Mechanisms of Spatters and Blowholes Formation.....	36
2.4	Feasibility Study of Hybrid Laser-arc Welding for Welding of Galvanized Dual-phase Steels in a Gap-free Lap Joint Configuration	38
2.4.1	Introduction of Hybrid Laser-arc Welding and Experimental Setup.....	38
2.4.2	Effect of Arc Current on the Quality of Hybrid Laser-arc Welds.....	40
2.4.3	Effect of Laser Power on the Quality of Hybrid Laser-arc Welds.....	45

2.4.4	Effect of Distance between the GTAW Electrode Torch and Laser Beam on the Quality of Hybrid Laser-arc Welds..	46
2.4.5	Effect of Distance between the GTAW Electrode Torch and Laser Beam on the Quality of Hybrid Laser-arc Welds..	47
2.5	Unstable Interaction between the Laser-Induced Plasma and the Arc Plasma.....	48
2.6	Conclusions.....	53
3.	LASER WELDING OF GALVNAIZED DP980 STEELS PREHEATED BY GTAW IN GAP-FREE LAP JOINT CONFIGURATION.....	56
3.1	Introduction.....	56
3.2	Experimental Setup	57
3.3	Results and Discussions.....	58
3.3.1	Advantages and Principle of Laser Welding of Galvanized Steels with the Assistance of GTAW as the Preheating Source.....	58
3.3.2	The Influence of the Preheating Arc Current on the Weld Quality by laser.....	70
3.3.3	Study on the Dynamic Behaviors of the Molten Pool by Machine Vision.....	74
3.3.4	Temperature Measurement along the Interface of Two Galvanized Metal Sheets during GTAW Preheating Process	78
3.3.5	Analysis of the Effect of the Welding Speed on the Quality of the Laser/GTAW Preheated Weld.....	80
3.4	Testing the Mechanical Properties of the Weld	81
3.4.1	Measurement of Microhardness of the Welds Obtained by Laser Welding of DP 980 Steel Treated by GTAW Heat.....	81
3.4.2	Tensile Shear Testing of the Weld.....	82
3.5	Conclusions.....	85

4.	FEASIBILITY STUDY OF HYBRID LASER-VARIABLE GAS TUNGSTEN ARC WELDING OF GALVANIZED STEELS IN A GAP- FREE LAP JOINT CONFIGURATION.....	87
4.1	Introduction.....	87
4.2	Experimental Procedure.....	88
4.3	Advantages of Hybrid L-VPGATW Welding of Galvanized Steels in a Gap-Free Lap Joint Configuration with the Separate Molten pool..	89
4.3.1	Fast removal of the Zinc Coating on the Top Surface of Metal Sheets.....	90
4.3.2	Oxidizing the Metal Sheets along the Weld Line.....	93
4.3.3	Controllable Heat Input into the Welded Material.....	94
4.4	Results and Discussions.....	95
4.4.1	The Hybrid L-VPGTAW Lap Joint.....	95
4.4.2	Surface Analysis of the VPGTAW Preheating Welds by XPS and EDS.....	97
4.4.3	Influences of VPGTAW Preheating Parameters	99
4.4.4	Studying of the Effects of Laser Welding Parameters.....	100
4.4.5	Mechanical Properties of the Welds.....	101
4.5	Conclusions.....	104
5.	MONITORING OF THE WELDING PROCESS.....	106
5.1	Introduction.....	106
5.2	State-of-the-art Monitoring of the Welding Process by Machine Vision And the AE Technique.....	107
5.2.1	State-of-the-art Monitoring of the Welding Process by Machine Vision.....	107

5.2.2	State-of-the-art Monitoring of the Welding Process by AE Technique.....	109
5.3	Monitoring the Transition of the Welding Modes and Stability of the Welding Process by Machine Vision.....	111
5.3.1	Experimental Setup.....	111
5.3.2	Image Processing Algorithms for the Captured Images of the Molten pool.....	113
5.3.2.1	Analysis of the Captured Images of the Molten Pool.....	113
5.3.2.2	Determination of the Threshold Value of Grey Level.....	118
5.3.2.3	Binarizing the Image of the Molten Pool.....	119
5.3.2.4	Calculation of the Major Axis Length of the Molten Pool	121
5.3.3	Monitoring of the Stability of Laser Welding Process of Galvanized Steels in a gap-free lap joint configuration.....	122
5.3.4	Monitoring of the Stability of Laser Welding Process of Galvanized Steels with the Presence of Gap at the Interface of Two Sheet Metals	127
5.3.5	Monitoring of the Stability of Hybrid Laser-Arc Welding Process of Galvanized Steels with the Common Molten pool	131
5.3.6	Monitoring of the Stability of Laser Welding Process of Galvanized Steels with the Assistance of GTAW Torch Preheating.....	134
5.3.7	Effect of Zinc Coating at the Top Surface of the First Metal Sheet on the Dynamic Behaviors of the Bright Spot.....	141
5.4	Detection of the Spatter Formation by the Measurement of the Acoustic Emission.....	144
5.4.1	Experimental Setup.....	144
5.4.2	Short Time Fourier Transform (STFT)	145

5.4.3	As-Acquired AE Signals and Welded Joints.....	146
5.4.4	The Processed AE Signals Using the Short Time Fourier Transform.....	148
5.5	Monitoring the Transition of the Welding Modes and Stability of the Welding Process by Machine Vision.....	150
5.5.1	Illumination of the Molten Pool.....	150
5.5.2	Detection of the Transition of Welding Modes by the Shape of Laser-induced Plume	152
5.5.3	On-line Monitoring of the Stability of the Laser/GTAW Preheating Welding Process.....	156
5.6	Conclusions.....	159
6.	NUMERICAL SIMULATION OF THE TEMPERATURE FIELD FOR HYBRID LASER-ARC WELDING OF GALVANIZED STEELS.....	163
6.1	Introduction.....	163
6.2	Material and Experimental Procedure.....	167
6.3	Numerical Model.....	168
6.3.1	FE Model and the Build of Hybrid Heat Source Model.....	168
6.3.2	Assumptions.....	170
6.3.3	Governing Equation, Initial and Boundary Conditions.....	171
6.3.4	Determination of the Thermophysical Properties of DP 980 for the Thermal Analysis.....	173
6.4	Results and Discussions.....	177
6.4.1	Selection of the Characteristic Parameters of the Heat Source ..	177
6.4.2	Effects of the Hybrid Laser-Arc Welding Parameters on the Temperature Distribution Profiles.....	191

6.4.2.1	Effect of Distance between Laser Beam and GTAW Preheating Torch.....	192
6.4.2.2	Effect off GTAW Arc Current.....	194
6.4.2.3	Effect off Welding Speed on the Temperature Distribution Profiles.....	196
6.5	Conclusions.....	198
7.	CONCLUSIOSNS AND FUTURE WORK.....	200
7.1	Summary and Conclusions – Feasibility Study of the Lap Joint of the Galvanized DP 980 Steel.....	200
7.1.1	The Lap Joint of Galvanized DP 980 Steel Using the GTAW.....	200
7.1.2	The Lap Joint of Galvanized DP 980 Steel Using Laser Welding.....	200
7.1.3	The Lap Joint of Galvanized DP 980 Steel Using Hybrid Laser/GTAW Welding.....	201
7.1.4	The Lap Joint of Galvanized DP 980 Steel Using Hybrid Laser/GTAW Welding Where GTAW is Used as a Preheating Source.....	202
7.1.5	The Lap Joint of Galvanized DP 980 Steel Using Hybrid Laser/VPGTAW Welding Where VPGTAW is Used as a Preheating Source.....	203
7.2	Conclusions – Monitoring of Welding Process.....	204
7.2.1	Monitoring the Formation of Weld Defects by Machine Vision	204
7.2.2	Monitoring the Formation of Weld Defects by AE Technique	204
7.2.3	Monitoring the Weld Modes and Stability of the Welding Process.....	205
7.3	Conclusions-Numerical Simulation of the Temperature Field for Hybrid Laser-Arc Welding of Galvanized Steels.....	193
7.3	Future Studies.....	194

7.3.1	Monitoring the Dynamic Behaviors of the Zinc Coating by the Optical Sensor.....	194
7.3.2	Investigate the Relationship between the Pressure Level of Zinc Vapor and Temperature by Using the Infrared Pyrometer and Microphone.....	195
	REFERENCES.....	209

LIST OF FIGURES

1.1	Classification of AHSS steels with respect to tensile strength and elongation.....	3
1.2	Schematic presentation of microstructure of DP Steel.....	3
1.3	Materials selected for ULSAB-AVC (a) ULSAB-AVC body structure steel (b) ULSAB-AVC C-Class materials.....	5
1.4	Schematic presentation of microstructure of DP steel.....	6
1.5	Stress-strain curves of HSLA,DP and TRIP steels.....	7
1.6	The samples of car components joined by the laser welding: the space frame in the Audi A2.....	11
1.7	Schematic presentation of a groove for zinc excavation	14
1.8	Advantages of hybrid laser-arc welding over laser welding and GMAW alone.....	18
2.1	Effect of welding speed on the weldability of galvanized DP steels by using GTAW (a) 6 mm/s (b)8mm/s (c) 10 mm/s (d) 12 mm/s (e) 15mm/s (f) 18 mm/s (g) 20 mm/s.....	26
2.2	Effect of arc current on the weldability of galvanized DP steels by using GTAW (a) 100A (b)120A (c) 140A (d) 160A (e) 180A (f) 200 A (g) 220A (h) 240 A (i) 260 A (j) 280 A (k) 300 A.....	27
2.3	Top view and cross-sectional views of humping (a) the top view of Humping (b) the cross-sectional view of the parallel humping (c) the cross-sectional view of the bead-like humping.....	25
2.4	Cross-sections of GTAW welds at different arc current (a) 260 A (b) 280 A (c) 300 A.....	28

2.5	Sample of laser-welded joint with the laser power of 4KW and various welding speed.....	31
2.6	The effect of the zinc vapor plume on the depth of the weld penetration.....	31
2.7	Sample of laser welds obtained by fiber laser welding at the welding speed of b) 12 mm/s (d) 15 mm/s (f) 18 mm/s (h) 20 mm/s.....	33
2.8	Top view of laser welded joints with respect to a welding speed of 18 mm/s And various laser power.....	34
2.9	Schematic experimental setups for the lap joint of galvanized steel sheets with spacers.....	35
2.10	Top view of laser welded joint with the assistance of spacers in various welding speed and laser power.....	36
2.11	Types of blowholes (a) shallow blowhole (b) burn-through blowhole.....	37
2.12	Experimental setup of a hybrid laser-GTAW welding system.....	40
2.13	Effect of arc current on the quality of hybrid laser-arc welds.....	42
2.14	Porosity present in the hybrid welds (a) at the top surface (b) in the welds.....	42
2.15	Shape of the arc plasma and the size vapor plume at different time	45
2.16	Effect of laser power on the quality of hybrid laser-arc welds.....	46
2.17	Effect of the distance between the electrode of GTAW torch and laser beam on the quality of hybrid laser-arc welds.....	47
2.18	Effect of the welding speed on the quality of hybrid laser-arc welds.....	48
2.19	Images of the single arc, single laser, laser-compressed arc, and laser-expanded arc.....	50
3.1	Experimental setup of laser/GTAW system.....	58
3.2	Top view of hybrid laser/GTAW weld	60
3.3	Relationship between the zinc pressure and temperature.....	62

3.4	Effect of the distance between the torch electrode and laser beam on the the quality of hybrid laser-arc welds.....	63
3.5	Top and back side views off preheated and welded metal sheets in a gap-free lap joint configuration.....	66
3.6	XPS analysis results of the heated surface of DP 980 galvanized steel by GTAW torch	69
3.7	Shape of the molten pool for an instable welding process.....	70
3.8	Effect of arc current on the chemical composition of the top surface of the preheating samples.....	72
3.9	Back side of the preheating samples.....	73
3.10	Effect of the preheating arc current on the weld quality obtained by laser.....	74
3.11	Images of the molten pool taken from the laser welding process of galvanized steels in a gap-free lap joint configuration.....	76
3.12	Images of the molten pool during the hybrid laser-GTAW welding process	77
3.13	Temperature measurement along the interface of two galvanized metal sheets.....	79
3.14	Effect of arc current on the maximum temperature at the interface of two galvanized metal sheets.....	79
3.15	Effect of the welding speed on the weld quality.....	81
3.16	Vickers micro-hardness profile of a laser/GTAW preheated weld.....	82
3.17	Schematics of tensile shear test coupon.....	83
3.18	Tensile shear test experimental setup.....	83
3.19	Relationship between the average tensile shear strength and the welding speed.....	84
4.1	Schematic presentation of hybrid L-VPGTAW experimental setup	89

4.2	Comparison of the treated surface for GTAW and VPGTAW as a preheating sources.....	91
4.3	Comparison of the removal rate for GTAW and VPGTAW as a preheating sources.....	93
4.4	Schematic presentation of the typical variable polarity current wave form...	95
4.5	Top views of welds obtained by (a)only laser (b) hybrid laser-GTAW welded lap joint with DCEN (c) hybrid laser-GTAW welded lap joint with DCEP.....	97
4.6	XPS spectra of the metal oxides formed on the VPGTAW preheated surface.....	98
4.7	EDS analysis result of the top surface of the VPGTAW preheated surface..	99
4.8	Tensile shear test	103
4.9	The hardness distribution profiles of hybrid L-VPGTAW lap joint along the weld zone and heat affected zone.....	104
5.1	Experimental setup and lap joint configuration.....	105
5.2	Schematic setup for acquiring the molten pool and the example of the captured image of the molten pool.....	116
5.3	Six consecutive images of the molten pool obtained in the instable welding process.....	117
5.4	Six consecutive images of the molten pool captured in the stable welding process.....	117
5.5	Infrared image of the bright spot acquired.....	118
5.6	Image processing of the bright spot.....	121
5.7	Schematic representation of the molten pool.....	122
5.8	Monitoring the instability of laser welding process of galvanized steels in a gap-free lap joint configuration.....	123
5.9	Transition from the stable keyhole status to the collapsed keyhole status.....	117

5.10	Monitoring the stability of laser welding process of galvanized steels in a gap-free lap joint configuration.....	127
5.11	Laser welded lap joint obtained in the stable welding process.....	129
5.12	Influence of the weld gap at the interface of two metal sheets on the major axis length of the molten pool.....	130
5.13	Relationship between the average length of the major axis of the bright spot and the thickness of gap.....	131
5.14	Schematic representation of experimental setup for hybrid laser-GTAW welding with the common molten pool and the top view of lap joint obtained by the hybrid laser-GTAW welding with the common molten pool.....	133
5.15	Six consecutive images of bright spot obtained in the hybrid laser-GTAW welding process.....	133
5.16	Schematic representation of the experimental setup of the hybrid laser-GTAW welding in the separate molten pool and the image of the molten pool obtained by the ordinary CCD camera.....	135
5.17	Six consecutive images of the bright spot obtained by the infrared CCD Camera during the hybrid laser-GTAW welding process with the separate molten pool	136
5.18	Length of the molten pool major axis with the GTAW preheating	137
5.19	Length of the molten pool major axis with the GTAW preheating (zinc coating at the interface is removed)	139
5.20	Length of the molten pool major axis without the GTAW preheating.....	140
5.21	Relationship between the average length of the bright spot and depth of penetration and different welding conditions.....	141
5.22	Effect of the zinc coating on the major axis length of molten pool.....	143
5.23	Laser-induced zinc plume and metal vapor.....	144
5.24	The captured images of he molten pool.....	144
5.25	Experimental setup or the acquisition of the AE signals.....	145

5.26	AE signals acquired in the welding process.....	148
5.27	A typical as-welded lap joint by laser welding.....	148
5.28	STFT processed AE signals.....	150
5.29	Experimental setup of illumination.....	151
5.30	Plasma images (a) in conduction mode (b) the keyhole mode.....	153
5.31	Six successive images of the plume when the weld pool is under the stable conduction mode.....	154
5.32	Schematic presentation of the shielding gas for blowing out the plasma plume.....	155
5.33	Effect of the shielding gas on the shape of the plasma plume and the weld penetration.....	155
5.34	Schematic of the keyhole and the molten pool.....	157
5.35	Images of the keyhole in the stable welding process.....	158
5.36	Images of the keyhole in the instable welding process.....	159
6.1	Experimental setup.....	168
6.2	3D FE model.....	169
6.3	Double ellipsoidal heat source configuration.....	170
6.4	Temperature-dependent specific heat.....	175
6.5	Temperature distribution profiles obtained by the numerical results.....	179
6.6	Experimental results obtained during the hybrid laser-arc welding process...	180
6.7	Schematic presentation of the conduction and keyhole welding modes.....	180
6.8	Effect of the correct coefficient L on the power density distribution along the weld penetration direction.....	185
6.9	Temperature distribution profiles with the laser power of 6000 W.....	185

6.10	Effect of L on the power density distribution on the ZOX plates with different Y values.....	187
6.11	Temperature distribution profiles obtained by the numerical results (L=0.2)	189
6.12	Isotherm temperature distribution profiles.....	190
6.13	The temperature history at the centre point.....	190
6.14	Comparison of the numerical and experimental temperature histories measured at the specific point.....	191
6.15	Effect of the distance between laser beam and GTAW torch preheating	193
6.16	Relationship between the peak temperature and the distance between laser beam and GTAW torch on the top surface at the time of 0.6s.....	193
6.17	Temperature distributions with various preheating arc current.....	195
6.18	Relationship between the peak temperature and the GTAW preheating arc current on the top surface at the time of 0.6s.....	195
6.19	Temperature distribution profiles in the cross-sectional view with the different arc current.....	196
6.20	Effect off welding speed on the temperature distribution profiles.....	197
6.21	The relationship between the peak temperature and the welding speed on the top surface at the time of 0.6s.....	197

LIST OF TABLES

2.1	Welding conditions used in the GTAW of galvanized DP 980 steels.....	23
3.1	Welding conditions used in Kim et al. report.....	59
3.2	Tensile shear test results for the different welding speed.....	84
6.1	Chemical composition of the DP 980 steel.....	167

NOMENCLATURE

a_f	Length of the front of the molten pool along the z axis
a_r	Length of the rear part of the molten pool along the z axis
b	Half width of the molten pool along the x axis
c	Weld depth
A_L	Molten pool area chosen
C	Velocity of light in a vacuum
C_p	Specific heat
C_{pi}^T	Heat capability of i at the temperature T ($i = \text{Fe, Cr, Si, Al, Mo, and C}$)
e	Electronic charge
f_f	Fraction of the heat deposited in the front of the joint
f_i	Weight percentage of the i ($i = \text{Fe, Cr, Si, Al, Mo, and C}$)
f_r	Fraction of the heat deposited in the rear of the joint
$f(x, y)$	Captured image
$\bar{f}(x, y)$	Filtered image
$f'(x, y)$	Binarized image
h	Planck constant

h_{con}	Heat coefficient for convection
h_{plasma}	The plasma length
I	Laser beam intensity absorbed by the welded material
I_0	Incident laser beam intensity
k_B	Boltzmann constant
k_n	Thermal conductivity normal to S_A
K	Thermal conductivity
K^T	Thermal conductivity at the temperature T
K_i^T	Thermal conductivity of the i at the temperature T ($i = \text{Fe, Cr, Si, Al, Mo, and C}$)
L	Correct coefficient
L_m	Heat of fusion
L_{major}	Length of the major axis of the molten pool
m	Discrete-time index
m_e	Electron mass
n	Refractive index of the plasma
n_e	Number of atoms
n_i	Number of ions
N	Width of the discrete time window function
q	Heat input normal to the regions S_A
$q(x, y, z, t)$	Power density distribution
$q(x, z, t)$	Heat intensity

Q_{arc}	Heat input of arc
Q_L	Energy input rate of the laser power
Q_v	Volumetric heat source
U	Arc voltage
r_b	Arc distribution radius
S_A	Regions under the heat flux
ΔT	Difference between the liquidus and solidus temperature
T	Grey level
T_0	Ambient temperature
T_e	Electronic charge
T_l	Liquidus temperature
T_s	Solidus temperature
V	Welding speed
ν	Frequency of the used laser beam
x_c	Coordinate value of the molten pool's center point at x axis
x_{max}	Maximum coordinate of the molten pool at x axis
x_{min}	Minimum coordinate of the molten pool at x axis
$x(n)$	Discrete-time acoustic emission signal
$X(m, \omega)$	STFT representation of the discrete time signal
y_c	Coordinate value of the molten pool's center point at y axis

y_{\max}	Maximum coordinate of the molten pool at y axis
y_{\min}	Minimum coordinate of the molten pool at y axis
Z	Charge number of the atom

Greek letters

ε	Emissivity
ε_p	Permittivity of free space
η_{arc}	Efficiency of arc
η_{laser}	Efficiency of laser
μ	Plasma absorption coefficient
ρ	Density
σ	Stefan-Boltzmann
ω	Discrete value for frequency
$\omega(n)$	Window function
λ	Wavelength of the used laser beam

ACKNOWLEDGEMENTS

I am most grateful to my academic advisor Dr. Radovan Kovacevic who not only provided his continuous inspiration, motivation, and support in helping me to successfully finish my research work but also showed me how to be a competitive engineer and a researcher through involvement in several intricate industrial projects and research studies. I also appreciate his continuous efforts in providing the first-class research facilities without which this work would have been impossible to accomplish. His continuous helps shed light on the most difficult time in my life.

Great thanks should also be given to Dr. Syed Hamid, Dr. Behrouz Peikari, Dr. Wei Tong, and Dr. David Willis for their service as my supervisory committee members and for their time and patience taken to review this research work and provide valuable suggestions.

Thanks should be given to Mr. Rouzbeh Sarrafi, Mr. Fanrong Kong, Mr. Wei Huang, and Mr. Eshan Foroozmehr. Without their helps, this research work could not be completed. Thanks should also be extent to Mr. Hang Yao and Miss Yue Xuan, at SMU for their help with the optical microscope and providing great discussion. I also want to say thanks to Dr. Dechao Lin, Mr. Andrew Sochaz, Dr. Hosein Artharifar, and Dr. Chunming Wang for their help in the execution of my

experiments. In addition, I want to thank the friendship from my colleagues at RCAM and CLAM at SMU. Mrs. Lorrie Carter was tremendously helpful in promoting my academic writing and in the proofreading of this work.

Financial support from the General Motors Corp., National Science Foundation, U.S. Department of Education and the Research Center for Advanced Manufacturing (RCAM) and NSF I/UCRC Center for Laser-aided Manufacturing (NSF I/UCRC CLAM) in the School of Engineering at Southern Methodist University are gratefully acknowledged.

Special thanks should go to my best friends: Dr. Ruiwen Wang, Dr. Vivian Zhao, Mr. Weixin Shu, Mr. Jingtian Li, Dr. Weisheng Xia, Dr. Lihui Liu, Dr. Coco Wang, Dr. Ke Xu, Ms. Qiuping Chen, Mr. Lechun Jin, Ms. Yan Bai, Dr. Hosein Artharifar, Mr. Rouzbeh Sarrafi, Mr. Mohammad Hendijanifard, Dr. Yu Shu, Dr. Kun Lv, and Ms. Di Yu. The eternal love and friendship delivered from their hearts to me free my soul and help me face any of challenges from the life and get through the darkest time in my life.

Finally, and most importantly, I would like to thank to my parents, my brother and sisters for their not only giving the eternal and unconditional love to me but also teaching me to spread my love to the people around me. This let me touch the beauty of life.

DEDICATION

This thesis is dedicated to my parents, my brother, my sisters, my advisors (Dr. Radovan Kovacevic and Dr. Xianghuai Dong) and the people who shed light on the journey of my life.

Chapter 1

INTRODUCTION

The increased need to reduce the weight of the vehicles and improve fuel efficiency and safety has prompted the increased use of advanced high strength steels (AHSS) in the automotive industry. These new steel grades include dual-phase (DP) steels, transformation-induced plasticity (TRIP) steels, high hole expansion (HHE) steels, complex-phase (CP) steels, martensitic steels (MS), and twinning induced plasticity (TWIP) steels [1]. In addition, these steels are usually required to be galvanized in order to improve the surface corrosion resistance before they are used for auto parts. Welding of galvanized steels in a gap-free lap joint configuration causes the generation of high-pressurized zinc vapor. This zinc vapor causes a big challenge to successfully obtaining sound lap joints. In this chapter, these new high-strength steels used in automotive industry are introduced. Challenges from the lap joint welding of galvanized steels are met by using different welding process. The description of the welding are followed. In the last section, different techniques to mitigate the presence of zinc vapor are reviewed.

1.1 Advanced High-Strength Steels for Automotive Industry

The steels with minimum yield strength of up to 210 MPa, are usually defined as low strength steels. The steels with minimum yield strengths between 210 and

550 MPa, are called high strength steels, and the steels having minimum yield strength more than 550 MPa are called ultra high-strength steels or super alloys [1]. DP steels, TRIP steels, HHE steels, CP steels and MS steels are generally called advanced high-strength steels [2]. The metallurgical characteristics and their applications of these steels are briefly introduced as follows.

1.1.1 Dual-phase (DP) Steels

Among these high strength steels, dual phase (DP) steels have become the most promising materials for the future generation of vehicle because they can be “tuned” for different strength levels and processing methods and are less expensive than other advanced high-strength steels [3]. The family of DP steels has a microstructure of mainly soft ferrite with islands of the hard martensite phase dispersed throughout. The hard martensite phase can provide substantial strength while the ferrite matrix contributes to good ductility [4]. The strength level of DP steels depends on the volume fraction of hard martensite in the microstructure that ranges from 500~1200 MPa. Figure 1.1 shows the selection of AHSS steels with respect to low-strength steels and traditional HSS, and Figure 1.2 shows the schematic presentation of the microstructure of DP steels.

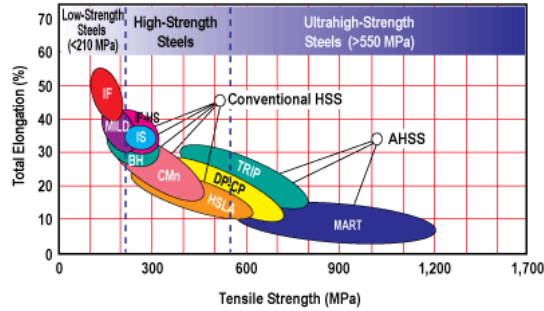


Figure 1.1 Classification of AHSS steels with respect to tensile strength and elongation [5]

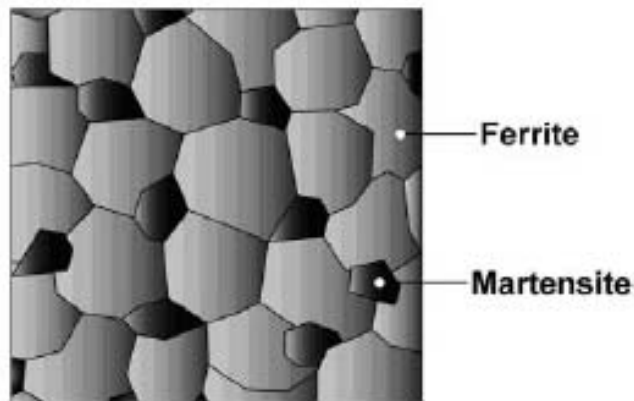
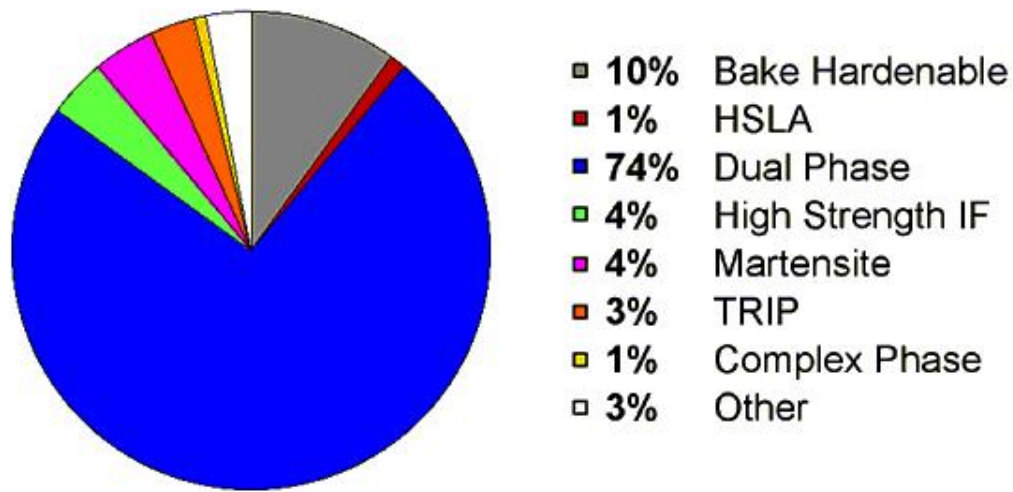


Figure 1.2 Schematic presentation of microstructure of DP steel [5]

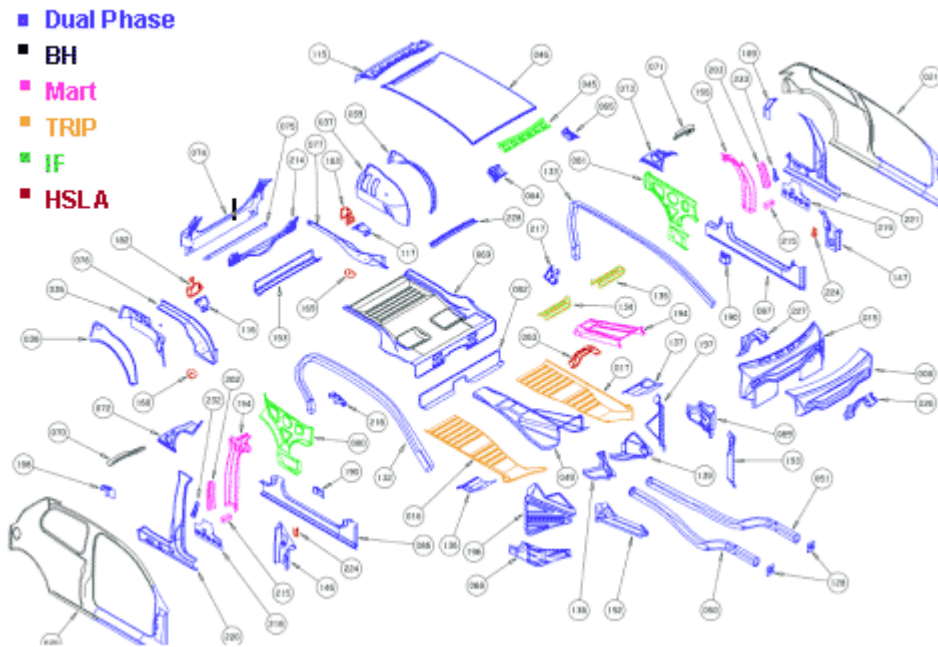
As shown in Figure 1.2, the soft ferrite phase is generally continuous, giving DP steels excellent ductility. When these steels are deformed, strain is concentrated in the lower strength ferrite phase, creating the unique high work hardening rate exhibited by these steels [5]. Furthermore, the yield strength of DP is much lower than its tensile strength. With respect to a given tensile strength, the lower yield strength will translate to higher elongation values and better formability. In addition, “enhanced energy absorption is another DP steel characteristic” [2].

With the low yield ratio, high work hardening ratio, and high bake hardening (BH) value, DP steels have been widely used in auto components that demand high

strength and good “crashworthiness and formability” such as “wheel, bumper and other reinforcements” [6]. In the UltraLight Steel Auto Body (ULSAB) program, 90 percent of the ULSAB body structure is constructed of high-strength steels (HSS) whereas in the UltraLight Steel Auto Body (ULSAB)-Advanced Vehicle Concepts (ULSAB-AVC) program, 100 percent of the ULSAB-AVC body structure is made of high strength steel (HSS), with over 80 percent being AHSS steels [7]. Figure 1.3 shows the ULSAB-AVC body structure steel types and the ULSAB-AVC C-Class materials. As shown in Figure 1.3, DP steel is the most promising material for the future generation of vehicles.



(a)



(b)

Figure 1.3 Materials selected for ULSAB-AVC (a) ULSAB-AVC body structure steel (b) ULSAB-AVC C-Class materials [7]

1.1.2 Transformation-Induced Plasticity (TRIP) Steels

Like DP steels, soft ferrite comprises mainly the microstructure of TRIP steels. While DP steels have only the martensite phase, the phases in TRIP steels include martensite, bainite, and retained austenite, which offer their unique balance of properties. Figure 1.4 shows the microstructure schematic of TRIP steels. As shown in the Figure 1.4, the retained austenite is embedded in a primary matrix of ferrite. Furthermore, a minimum of 5 percent volume of retained austenite is required. However, the percent volume of hard phases such as the martensite and bainite are present in varying amounts [5].

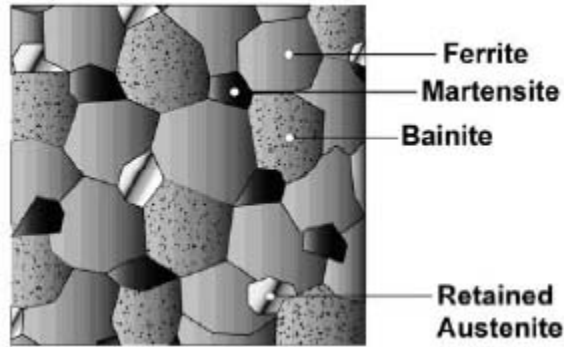


Figure 1.4 Schematic presentation of microstructure of TRIP steel [5]

When strain increases, the retained austenite in the TRIP steels is progressively transformed to martensite; thus, increasing the work hardening rate. Therefore, the high work-hardening rate can persist at higher strains in TRIP steels, while this phenomenon does not happen in DP steels. Therefore, TRIP steels provide excellent crash energy absorption during crash deformation. The stress-strain behaviors of high strength low alloyed steels (HSLA) compared to the behavior of DP and TRIP steels of approximately similar yield strengths, are demonstrated in Figure 1.5. The difference in the microstructure between DP steels and TRIP steels provides the enhanced formability of TRIP steels over DP steels.

In order to stabilize the retained austenite phase below ambient temperature, a higher percentage of carbon is presented in the TRIP steels than in the DP steels. The application of higher contents of silicon and aluminum in the TRIP steels accelerate the formation of ferrite and bainite. Furthermore, silicon and aluminum suppress the formation of carbide precipitation in the bainite region [12].

The strain level at which retained austenite begins to transform to martensite depends on the carbon content in TRIP steels. The higher the carbon levels, the

more stable the retained austenite phase. When the carbon content is higher, the transformation of retained austenite to martensite only begins at strain levels beyond those produced during forming [5].

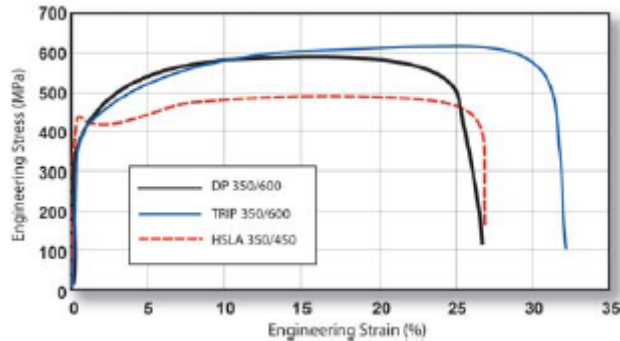


Figure 1.5 Stress-strain curves of HSLA, DP and TRIP steels [4]

1.1.3 High Hole Expansion (HHE) Steels

The microstructure of the HHE steels consists primarily of ferrite and bainite with some retained austenite. High strength, high formability, and high sheared-edge extension (hole flanging) capability are exhibited in these steels. The ferrite-bainite microstructure is associated with high hole-expansion values [2].

1.1.4 Complex-Phase (CP) Steels

CP steels are characterized by a very fine microstructure of ferrite and a higher volume fraction of hard phases (martensite and bainite), strengthened further by fine carbon or nitrogen precipitates of niobium, titanium, or vanadium [5]. The series of these steels have been utilized for parts that require high energy-absorption capacity, such as bumpers and B-pillar reinforcements [10].

1.1.5 Martensitic Steels

As its name shows, its microstructure consists of 100 percent martensite. The range of the minimum tensile strength of this family of steels is typically between 900 and 1,500 MPa. To increase hardening, manganese, silicon, chromium, molybdenum, boron, vanadium and nickel are used in various combinations. Typical applications for martensitic steels are usually those that require high strength and good fatigue resistance such as belt-line reinforcement, side-sill reinforcement, and bumper reinforcement [11].

1.2 Welding Issues of Galvanized Advanced High Strength Steels (GAHSS) in Lap Joint Configuration

1.2.1 Welding Challenges of Advanced High Strength Steels

Different welding techniques such as resistance spot welding (RSW) [8-16], arc welding [17,18], laser welding [19,20], dual-beam laser welding[21,23], hybrid welding [24,25],friction stir welding (FSW) and friction stir spot welding [26-28] have been applied to join galvanized steels in a lap joint configuration. Khan [26] used the FSW and resistance spot welding (RSW) techniques to weld high strength low alloy (HSLA), DP 600, DP 780, and TRIP 780 steels. In his study, the mechanical properties and microstructure of the RSW welded steel alloys were detailed and the relationship between chemical composition and hardness was developed. Furthermore, the relationship between the joint microstructure and impact performance of the spot welded AHSS steels was also developed. In a comparative study of RSW and the friction stir spot welding (FSSW) of DP 600, it was found that the failure modes were different; for the FSSW welds, fracture

initiated between the two sheets and propagated through the interface of the material. For the FSSW welds, fracture is initiated at the unbounded region and is propagated through the upper sheet just under the shoulder. Nevertheless, it has been found that when using the RSW to join galvanized steels, a large number of weld defects such as solidification-related weld cracks are produced [29,30]. Another major issue is the shortened electrode life because of the chemical reaction between the Zn coating, the copper electrode, and the high welding force [31].

Feng et al. [31,32] conducted a feasibility study on the FSSW of uncoated DP 600 with a nominal strength of 600 MPa. To evaluate the mechanical properties of the obtained welds, the hardness in the weld nugget was measured, and tensile-shear and cross-tension mechanical testing was performed for the welds obtained under selected welding conditions. It was found that the microstructure and hardness in the joint region remained similar to the base metal for the studied DP 600 steel. Mile [33] also used the FSSW technology to weld DP steels. In his study, the hardness measurement in the weld nugget and the tension and formability testing of the welded coupons were carried out. In comparison to the results obtained from laser welding of the same grade of DP steels, it was found that a lower hardness in the weld nugget was obtained during FSSW of DP steels, which resulted in better formability. However, FSSW requires a large amount of mechanical loading in order to generate higher temperature needed for successful tool plunging and material stirring. Thus, the FSSW of the weld high-strength steels requires a tool material that is heat resistant and wear resistant. This requirement limits the wide application of using FSW to join high strength steels in the

automotive industry. As mentioned above, different arc welding techniques are also used to weld AHSS steels for auto parts. Ford Motor Co. and Lincoln Electric Co. used Gas Metal Arc Welding (GMAW) to weld AHSS steels. It is found that AHSS steels are sensitive to heat input and the range of their welding parameters is very narrow [34]. Besides, Yan's study revealed that joint efficiency, which is the ratio of the strength of the joint to the strength of the base metal, decreases with the increase of a fractional increase of martensite. Furthermore, martensitic steels exhibit reduced weld strength from the softening of the heat affected zone (HAZ) when GMAW is used to weld DP and MS steels [35].

With respect to high speed, high productivity, the narrow heat-affected zone, and low heat input in comparison to conventional welding, laser welding has been widely used in the automotive industry. Laser welding provides the high aspect (weld depth-to-width ratio), which results in a deep penetration and narrow weld with good appearance [19,20,36]. In addition, laser welding can be integrated with the robotic arm. Therefore, it is possible to achieve automation of the welding process. Laser welding has been used to weld different materials such as steel, aluminum and magnesium that have been used widely in vehicles [37-38]. "The car body parts such as body panels, door inners, and the complete side frames are usually accomplished by the laser welding "[39]. As shown in the Figure 1.6, the space frame in the Audi A2 is produced by laser welding.

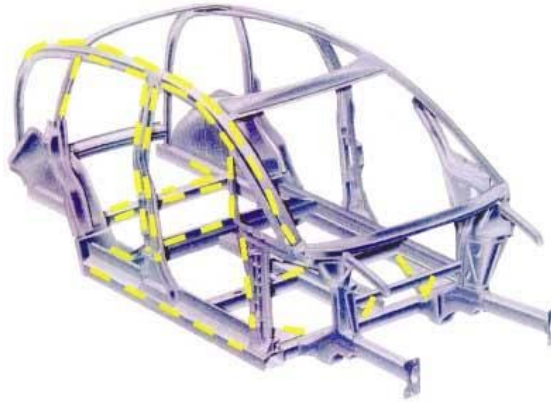


Figure 1.6 The samples of car components joined by the laser welding: the space frame in the Audi A2 [39]

Many efforts have been made on using laser welding or hybrid welding techniques to join AHSS steels. Kang et al. [40] used Nd: YAG laser to weld DP 600 steel. In his study, the hardness, microstructure, mechanical properties and formability were investigated. The results showed that the maximum hardness was obtained at HAZ near the fusion zone (FZ), and the microstructure of FZ was mainly composed of acicular ferrite. However, the HAZ near the FZ contained bainite and ferrite at a low welding speed. A diode laser was also employed to join the DP tailored blanks in Bocos's study et al. [41]. The metallorgraphic characteristics of weld beads and the mechanical behavior of the obtained welds were examined. Tests on microhardness, drawing, tension and fatigue were also carried out in his study. Gallagher et al. [42] used a 4.5 kW Nd:YAG laser for the lap weld of four types of high strength steels: HSLA 350, DP 600, M 900 and M 1310. This study has demonstrated that the weld tensile strength is dependent on various steel gauge/grade combinations and the weld width. Moreover, the weld

fatigue strength appeared to be independent of the steel grade and microstructure but depended on the gauge thickness. Similarly, the bead-on-plate welding of 800 MPa class TRIP steels was carried out by Han's et al. [43] using a CO₂ laser to study the weld defects, microstructure, mechanical properties and formability. Furthermore, in the Auto/Steel Partnership's project the application of the various hybrid welding techniques (laser + plasma and laser + GMAW) were studied by welding a sequence of grades of high strength DP steels, such as galvanized DP600, DP780 and DP 980 steels [44]. The cross-sections of the weld beads, the shear strength, the microhardness, and the impact strength were also investigated in this study.

Considering various advantages of laser welding, the automotive industry has shown tremendous interest in applying the laser beam to weld galvanized AHSS steels for auto parts. However, it is still extremely difficult to weld galvanized high strength steels in gap-free lap joint configuration [45]. One of the restraints is the lower boiling temperature of zinc (906° C) compared to the melting temperature of steel (1530° C). When joining galvanized AHSS in a gap-free lap joint configuration, the pressurized zinc vapor between the metal sheets tends to explode from the molten pool and form spatters and blowholes. These weld defects will greatly decrease the mechanical properties of laser welded joints. Additional procedures will be needed to repair the blowholes or clean the weld surface; thus, greatly increasing the cost.

1.2.2 Techniques to Mitigate the Presence of Highly-Pressurized Zinc Vapor

To eliminate the effects caused by the high-pressurized zinc vapor, a number of techniques have been tested for the past several decades. Some of the most common techniques will be discussed as follows.

1.2.2.1 Removing the Zinc Coating at the Interface of Steel Sheets Prior to Welding

The simplest approach to mitigate the effect of the Zn-coating is to remove the zinc coating completely by mechanical means prior to welding [46], which has been recommended by the American Welding Society standards [47]. By using this method, a sound weld can be achieved. However, it is costly to remove a specific amount of zinc coating precisely, and it is difficult to apply to a large-volume production line.

1.2.2.2 Setting the Spacers at the Interface of Metal Sheets

Another technique that has been proven effective is to intentionally form a small gap between the two metal sheets [48]. The technique is based on placing two small strips in between two metal sheets a few millimeters away from the welding line to make a space for zinc vapor to be evacuated instead of entering into the molten pool. The recommended gap is 0.1-0.2 mm [48]. However, to place spacers precisely along the welding line prior to welding is time-consuming and costly. In addition, this gap will produce new problems related to corrosion because the welding process will damage the zinc coating along the welding line. The

corrosion process could start from the area in which the zinc has been damaged or burned [49].

1.2.2.3 Redesigning the Setting of the Top Sheet

One of the techniques developed to mitigate the effect of the zinc vapor is redesigning the lap joint [48-51], shown in Figure 1.7. Zinc vapor can be evacuated before the molten pool reaches the interface. However, filling in the groove at the top sheet metal to make the paint job smooth is difficult. Again, the problems related to corrosion and to the increased cost caused by design are of concern.

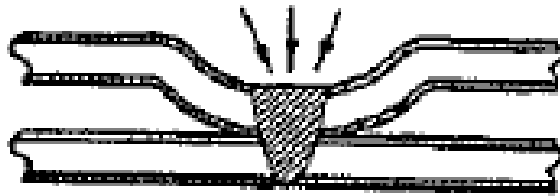


Figure 1.7 Schematic presentation of a groove for zinc excavation [48]

1.2.2.4 Using Alloying Agent to Alloy Zinc

Mazumder et al [52] patented and described in the papers [53,54] a technique that places a thin copper sheet between two steel sheets along the welding line. The copper has a melting temperature of 1083°C (between the melting temperature of steel and the boiling temperature of zinc) and can be alloyed with the zinc before the steel is melted. However, the presence of copper in the steel could generate new problems, such as hot cracking and corrosion concerns [55]. Recently, Li et al. [56] patented and described in the paper [57] a technique that sets the aluminum foil layer in the weld zone at the interface of two galvanized steel sheets to form the Al-

Zn alloy; thus, lowering the effect of the zinc vapor pressure. In order to use this method to weld galvanized steels in a lap joint configuration, there is a requirement of tightly clamping the two metal sheets. If there is the existence of gap at the interface of two metal sheets, the weld defects will be formed [57]. Furthermore, the dissolution of aluminum-steel alloy into the weld, which makes the weld brittle, has the potential to deteriorate the weld quality.

1.2.2.5 Using the Pulsed Laser

Instead of making components suitable for laser welding, a gap-free lap joint is the best choice in laser welding. There have been attempts to accommodate the welding parameters that contribute to the mitigation of the effect of Zn-vapor. One of the approaches is to use a pulsed laser instead of a continuous mode laser. Sound welds can be achieved through the controlled shape and appropriate peak power of the laser. In this approach each pulse will melt a part of the previously solidified bead in order to help the entrapped zinc vapor to escape from the weld zone [58-60]. However, Tzeng's articles [58-60] made some controversial reports. One paper published in 1999 [58], shows that a good quality weld can be obtained by using a CO₂ laser with the proper pulse parameters. It was also shown in this article that the weld quality was very sensitive to some welding parameters. For example, the excessive average peak power density resulted in cutting, while insufficient peak power density caused incomplete penetration. However, Tzeng's published article in 2006 showed the porosity was still formed while the welds were visually sound [60]. The conclusion of the recent report is based on the longitudinal-section of the

sample rather than on the cross-sectional view reported in the 1999 article. Therefore, the porosities caused by zinc can not be eliminated completely by using pulsed laser. Baardsen et al. [61] deposited a thin layer of a flux material such as iron oxide adjacent to the fusion zone at the interface of the metal sheets. The flux material combines with the zinc and produces a compound by the heat of the laser beam. This compound has the same or lower boiling point than steel, so the expulsion of the liquid melt from the molten pool by the high-pressured zinc vapor is prevented. Consequently the porosity in the welds was eliminated [61]. Recently, Chen et al [62] combined the CO₂ laser with a pulsed Nd: YAG laser to conduct the gap-free lap joint of the galvanized steel sheets with the thickness of 0.68 mm. In their study, the pulsed Nd: YAG laser was firstly used to pre-drill the vent holes along the weld line. After the completion of the vent holes, the laser beam is then applied to seam weld the galvanized steel sheets in a gap-free lap joint configuration. They claimed that the pre-drilled vent holes could provide the place to vent out the highly-pressurized zinc vapor developed at the interface of two metal sheets during the followed laser welding process and the weld defects such as porosity, spatter, and loss of penetration could be avoided, thus achieving the sound lap joint welds.

1.2.2.6 Using Dual Laser Beam or Two Lasers

Splitting a laser beam into two laser beams [63-67] or simply using two laser beams [68] are promising methods for welding of galvanized steels. Forrest et al. [63-65] has reported a good weld quality in lap welds by using dual beam laser

welding. The enhancement of the weld quality in this case “have been attributed to a more stable fluid flow, a wider keyhole [59], less frequency of keyhole collapse, and a reduced cooling rate “[58]. A specific laser-head has been designed for this application [69]. However, splitting precisely one laser beam into two laser beams with different power distributions and focuses is difficult to achieve when using one laser system and it is expensive to use two laser systems for welding.

1.2.2.7 Hybrid Laser-Arc Welding

Recent research on hybrid laser welding with the integration of a laser system and GMAW, shown in Figure 1.8, shows that GMAW can produce a larger molten pool allowing the laser beam to easily make a deep penetration in order to evacuate the Zn-vapor and reduce defects in the weld [70-76]. This hybrid laser-GMAW technique has produced visibly sound joints for welding galvanized steels in a lap joint configuration with a specific gap setting at the interface of the two metal sheets [76]. The molten metal blown off by the zinc vapor in laser welding is supplemented by melting the feeding wire, so the gap tolerance can be equal to the thickness of the metal sheets [76]. The downfall of this technique is that GMAW generates bumps on the top of the workpiece, which may be difficult to remove in order to get a smooth surface for body painting, and again the gap between the two sheets causes concern for corrosion because laser-GMAW damages and burns more of zinc coating.

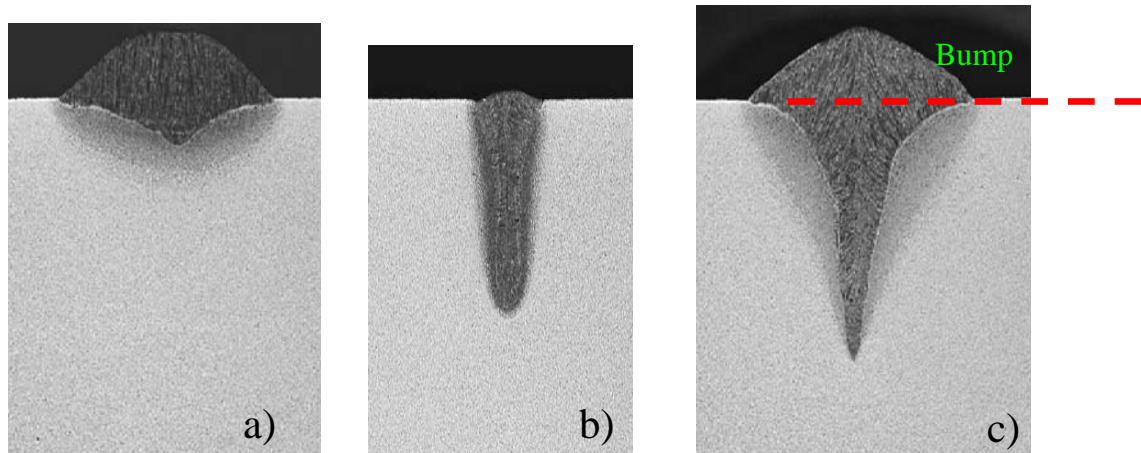


Figure 1.8 Advantages of hybrid laser-arc welding over laser welding and GMAW alone [75]

- (a) GMAW weld bead with shallow penetration and concave bead**
- (b) Laser weld bead with deep penetration**
- (c) Hybrid laser-arc weld bead with combined advantages**

Recently, Kusch, and Thurner used the plasma-GMAW technology to braze electrogalvanized and hot-dip-galvanized steel sheets [77]. The influence of the plasma arc current, the welding travel speed and the filler materials on the quality of welds obtained by the plasma-GMAW process was investigated. It was found that the plasma arc plays a decisive role in the plasma-GMAW process and the heat from the plasma arc can improve the wetting capability of the brazing materials. A visually sound weld without spatters is obtained. Kim et al. [78] used the hybrid laser/gas tungsten arc welding (GTAW) welding to join the SGCD1 galvanized steel plates in a gap-free lap joint configuration. It was demonstrated in their study that welding this type of galvanized steel was enhanced by the increase of arc current in the GTAW as well as by increasing the distance between the laser beam and the arc. However, the experimental results have revealed that it is still extremely difficult to join the ultra-high strength galvanized steels in a gap-free lap

joint configuration by hybrid laser/arc welding. Porosity and blowholes are also found at the welds. Additionally, welding the galvanized steels was affected by the chemical composition and thickness of the steel sheets. Therefore, it is necessary and important to develop a more robust welding technology to join the galvanized steels in a gap-free lap joint configuration to obtain the defect-free welds with the high strength.

1.3 Scope of Research

Although many efforts have been put on the welding of galvanized steels in a gap-free lap joint configuration over the past decades, until now there is no reported cost-effective, robust and easy-to-use welding technique in the open literature. To meet the automotive industry demand, it is important to develop a new welding procedure for the gap-free lap joint of galvanized steels. The provided chapters in this study are divided into three distinct parts. The first part (part I) mainly focuses on the feasibility of welding of galvanized steels in a gap-free lap joint configuration, which is consisted of Chapter 2, Chapter 3, and Chapter 4. In the second part, a machine vision system and a non-destructive test (NDT) based on the acoustic emission sensor are used to real-time monitor the welding process of galvanized steels, which lies in Chapter 5. In the third parts, numerical model is developed in Chapter 6 to simulate the temperature distribution during the welding process of hybrid laser-GTAW welding of galvanized DP 980 steels with the separated molten pool.

In Chapter 2, laser welding, gas tungsten arc welding (GTAW), and hybrid laser-GTAW welding (L-GTAW) with the common molten pool are employed to lap join the galvanized high strength dual phase (DP) steels in a gap-free configuration. Effects of the laser power, traverse welding speed as well as the arc current are investigated. In Chapter 3, laser welding process is separated from the GTAW preheating torch to lap join the galvanized steels in a gap-free configuration. Different surface analysis methods such as the x-ray photoelectron spectroscopy (XPS) and energy-dispersive x-ray spectroscopy (EDS) are used to detect the chemical composition of the preheating surface. Additionally, the tensile shear test is performed to evaluate the strength of the lap joint welds and the features of the hardness distribution of lap joint welds are also studied. The microstructure feature in different zones of welds is investigated by the scanning electron microscope (SEM). In Chapter 4, hybrid laser-variable polarity gas tungsten arc welding (L-VPGTAW) is introduced to carry out the gap-free lap joint of the galvanized DP 980 steels. Initially in this chapter, the mechanisms of hybrid L-VPGTAW of galvanized steels are analyzed. Then, effects of key welding parameters as the preheating arc current and traverse welding speed on the weld quality are investigated. Furthermore, XPS is implemented to analyze the chemical composition on the preheated surfaces.

Chapter 5 focuses on using the machine vision and acoustic emission technique to monitor the stability of welding process, different welding modes, and effects of gap and zinc coating on the molten pool behavior and better understand the formation mechanisms of weld defects such as blowholes and spatters. The Chapter

6 is dealing with the development of a finite element model to simulate the temperature distribution during the hybrid laser-GTAW welding process with the separated molten pool. Influences of distance between laser beam and GTAW preheating torch and GTAW preheating arc current on the temperature distribution during hybrid laser-GTAW preheating welding of galvanized with the separated molten pool are investigated by the developed numerical model. Furthermore, in order to verify the developed model the temperature distributions are experimentally measured with the thermocouples in different locations of the welded specimens. It is shown that there is a good agreement between modeled and measured results.

Finally, Chapter 7 begins with the summary and conclusions of this study. Then, future works are followed to extend the current researches.

Chapter 2

FEASIBILITY STUDY ON WELDING OF GALVANIZED DUAL-PHASE DP 980 STEEL IN LAP JOINT CONFIGURATION

2.1 Introduction

Among advanced high strength steels (AHSS), dual-phase (DP) steels become the most promising candidates to replace traditional materials for car parts such as aluminum and magnesium because of their adjustable levels of strength achieved from processing methods as well as their affordable cost [79-80]. Up to now, most efforts are placed on using resistance spot welding (RSW) to weld DP steels [81-88]. There are a limited number of publications on welding galvanized dual-phase steels by using arc, laser or hybrid laser-arc welding techniques [89-91]. In this chapter, the welding techniques such as gas tungsten arc welding (GTAW), laser and hybrid laser-arc welding for welding galvanized DP steels in a gap-free lap joint configuration are studied. The major features of the welds obtained by each of these welding techniques are discussed in the following sections starting with the GTAW, then laser welding, followed by laser-arc hybrid welding. The material used in this study is DP 980 steel with thickness of 1.2mm and 1.5 mm. A 1.2-mm thick sheet is selected as the top of two metal sheets during the lap joint welding process.

2.2 Investigation of Gap-free Lap Welding of Galvanized Dual-Phase Steels by Using GTAW

The primary welding parameters of GTAW arc current and welding speed are varied in order to study the weldability of galvanized DP steels in gap-free lap joint configuration. The effects of GTAW welding parameters on weldability were experimentally determined. During the welding process, the shield gas flow rate is kept at 30 SCFH (standard cubic feet per hour). Table 2-1 shows the two groups of different welding conditions.

Table 2-1 Welding conditions used in the GTAW of galvanized DP 980 steels

Welding conditions	Arc current (A)	Welding speed (mm/s)
Group 1	280	4/6/8/10/12/15/18/20/30
Group 2	180/200/220/240/260/280/300	10

In Group 1, the arc current is kept at the 280 A while varying the welding speed from 4 mm/s to 30 mm/s. For Group 2, the welding speed is kept at 10 mm/s and the arc current was gradually increased from 180 A to 300 A with an interval of 20 A. The experimental results corresponding to the welding conditions shown in Table 2-1 are presented in Figure 2.1 and Figure 2.2. For the welding conditions in Group 1, the GTAW welds are characterized by different weld defects such as humping, burn-through holes, porosity and spatters, as shown in Figure 2.1. For the welding conditions in Group 2, the zinc coating at the top surface of the specimen is removed by the arc, and only a shallow molten pool is produced during the GTAW process. The experimental results indicate that the two metal sheets are not jointed together, and only partial penetration is achieved in the GTAW welds when the arc current is below or equal to 240 A, as shown in Figure 2.2. However, when the arc

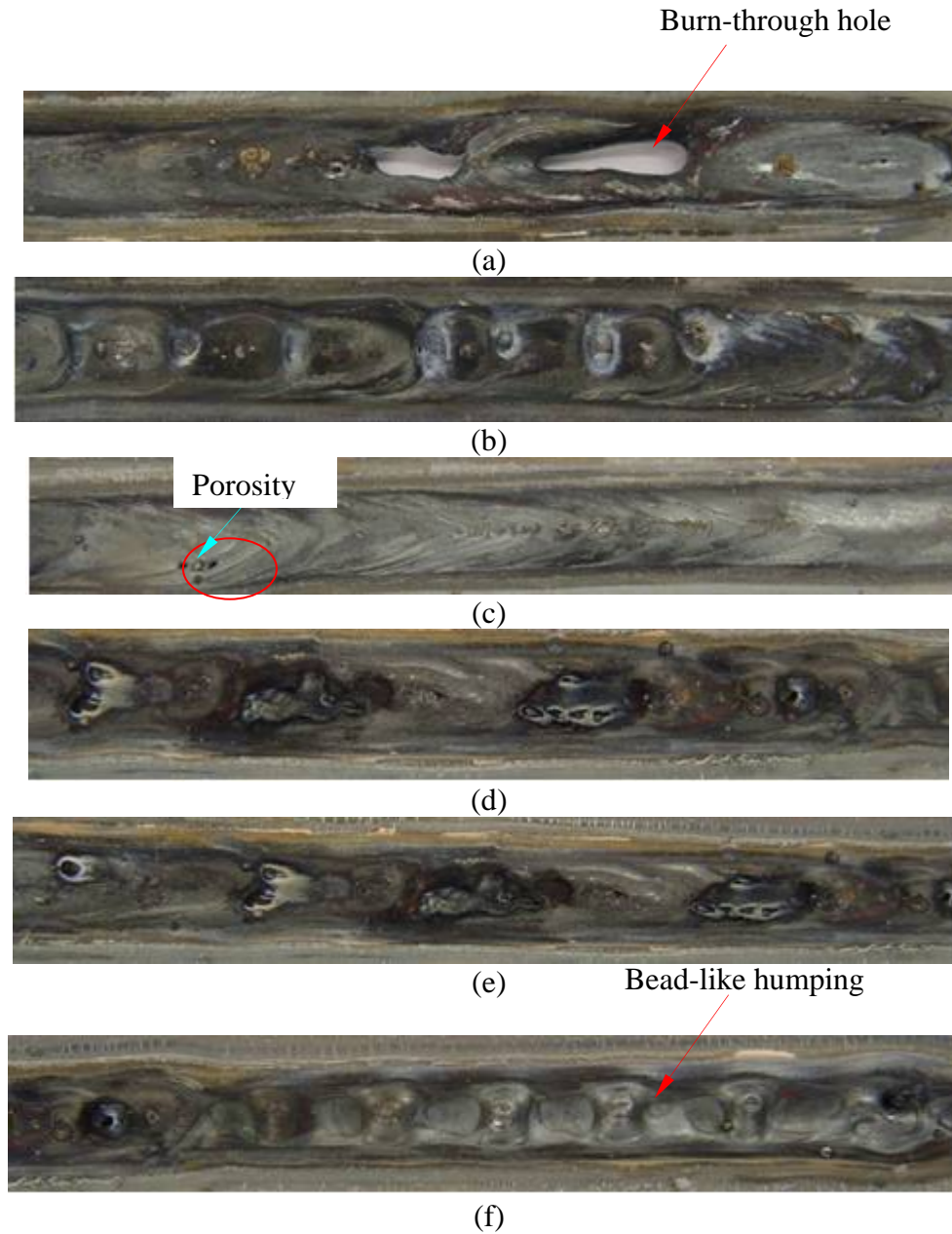
current is 260 A, a sound weld is obtained, as shown in Figure 2.2 (i). When the arc current is more than 260 A, the porosity, humping and burn-through holes appear in the welds.

Figure 2.3 shows the top and cross-section views of two types of humping: the bead-like humping and parallel humping. At the same time, Figure 2.4 shows the cross-sectional view for the welds at arc current of 260 A, 280 A, and 300 A, and a welding speed of 10 mm/s, respectively. Only partial penetration is achieved from the welds obtained at an arc current from 100 A to 240 A.

Comparing Figure 2.1(g) to Figure 2.2 (i), it is found that with an increase in the welding speed, humping is produced. Humping is also generated by an increase in the arc current while keeping the welding speed constant. The reasons for the formation of humping are “the action of the arc on the liquid weld pool or by the capillary instability of a liquid cylinder” [92]. As illustrated in Figure 2.1 (a), the formation of a burn-through hole arises from too much heat input into the specimens. In addition, if the argon shield gas is trapped in the molten pool, porosities are susceptible of being formed. It is also found that when the arc current is high, like 280 A, and the welding speed is lower than 6 mm/s, lots of spatters are generated during the welding process. These spatters contaminate the tungsten electrode. This contamination will require the frequent stopping of the welding process in order to reshape the electrode.

From the above discussion, different weld defects such as humping, porosity and burn-through holes are readily produced in the GTAW welds of galvanized DP steels in the lap joint configuration. Sound welds can be only obtained in a narrow

range of the welding parameters. Moreover, the low welding speed in the GTAW welding process does not meet the requirement of the automotive industry for high productivity. Therefore, the GTAW technique is not an effective method to join galvanized DP steels.





(g)

Figure 2.1 Effect of welding speed on the weldability of galvanized DP steels by using GTAW (a) 6mm/s (b) 8 mm/s (c) 10 mm/s (d) 12 mm/s (e) 15 mm/s (f) 18 mm/s (g) 20 mm/s



(a)



(b)



(c)



(d)



(e)



(f)



(g)



(h)



(i)



(j)



(k)

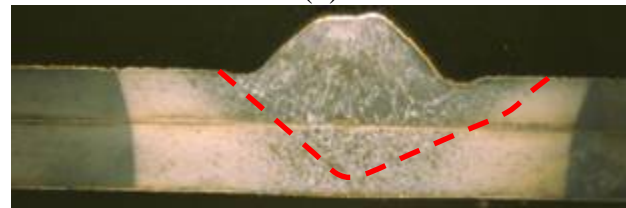
Figure 2.2 Effect of arc current on the weldability of galvanized DP steels by using GTAW (a) 100A (b) 120A (c) 140A (d) 160A (e) 180A (f) 200A (g) 220A (h) 240A (i) 260A (j) 280A (k) 300A



(a)

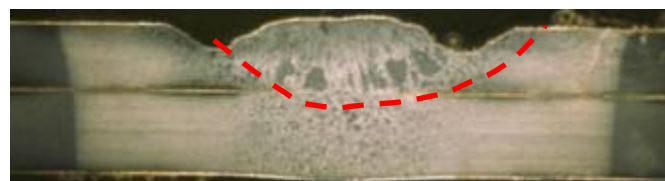


(b)

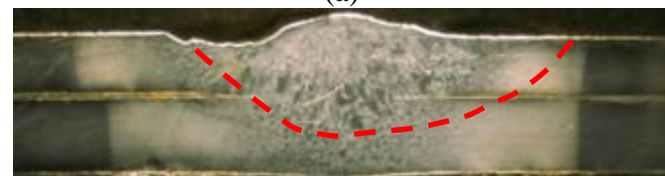


(c)

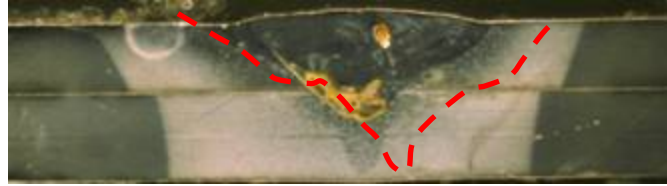
Figure 2.3 Top and cross-sectional views of humping (a) the top view of humping (b) the cross-sectional view of the parallel humping (c) the cross-sectional view of the bead-like humping (welded at a welding speed 30 mm/s and an arc current of 260 A)



(a)



(b)



(c)

Figure 2.4 Cross-sections of GTAW welds at different arc current (a) 260 A (b) 280 A (c) 300 A

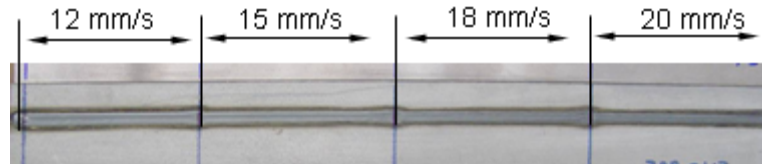
2.3 Investigation on Using Laser Welding with Gap-free Lap Welding of Galvanized Dual-phase Steels

In the last decade, the laser welding technique has been widely used to weld auto parts in the automotive industry. Considering several advantages of laser welding over traditional welding, an application of laser welding to form the lap joint of galvanized DP steel sheets is of considerable interest to the automotive industry. In this work, experiments are performed to study the weldability of galvanized DP steel in a gap-free lap joint configuration by using only a laser beam. A fiber laser with 4 kW power is selected as the heat source during the welding process. Pure argon gas is chosen as the protection gas. In order to characterize the weld defects from the laser welding of galvanized DP steels in lap joint configuration, two kinds of experiments are carried out: laser welding of non-galvanized DP sheets and laser welding of galvanized DP sheets. Furthermore, the effects of laser power, the welding speed and the assistance of spacers between steel sheets on the features of the laser-welded joints are investigated in detail.

2.3.1 Laser Welding of Galvanized DP Steels without Zinc Coating at the Interface

As discussed in Chapter 1, the main problem of welding galvanized steels in gap-free lap joint configuration stems from the development of the high-pressurized zinc vapor at the interface. In order to confirm this fact, the zinc coating at the interface is removed from the metal sheets before they are joined together by the laser beam. Figure 2.5 shows this type of as-welded lap joint obtained by the fiber laser of 4 kW power and welding speeds of 12, 15, 18, and 20 mm/s respectively. In order to eliminate the effect of back scattering from the laser beam to the fiber cable, the laser head is tilted 6 degrees with respect to the orthogonal to the welding samples. As shown in Figure 2.5, defect-free sound joints are achieved. At the same time, the welding process is very stable. Meanwhile, it is found that the plume produced by the zinc coating on the top surface of the specimen fluctuates dramatically, which affects the coupling of the laser beam with the specimen. This fluctuation has an influence on the depth of penetration of the welds as shown in Figure 2.5 (c), (e) and (g). Comparing the results in Figure 2.5 (b) and (d) with those in Figure 2.5 (f) and (h), it is found that with an increase in the welding speed, deeper weld penetration is achieved. This phenomenon can be explained by the fact that when the welding speed is lower, more zinc coating is removed by the laser beam and the size of the induced plume is larger, which defocuses and scatters more of the laser energy. Therefore, for practical applications, it is also important to select the optimal welding speed to ensure the weld penetration that is wanted. In order to verify this phenomena, the other experiment for the gap-free lap joint laser welding of 1.5 mm-to-1.5 mm metal sheet without zinc coating at the interface is

carried out under the following welding conditions: a laser power of 3000 w and a welding speed of 30 mm/s. Figure 2.6 shows the top and longitudinal cross-sectional view and the penetration depth of the laser welded joint. As shown in the Figure 2.6, the depth of the laser weld penetration is a function of the distance away from the beginning of the weld.



(a) Overview of the laser welds at the welding speeds of 12 mm/s, 15 mm/s, 18 mm/s and 20 mm/s



(b) Top view of the laser weld at the welding speed of 12 mm/s



(c) Backside view of the laser weld at the welding speed of 12 mm/s



(d) Top view of the laser weld at the welding speed of 15 mm/s



(e) Backside view of the laser weld at the welding speed of 15 mm/s



(f) Top view of the laser weld at the welding speed of 18 mm/s



(g) Backside view of the laser weld at the welding speed of 18 mm/s

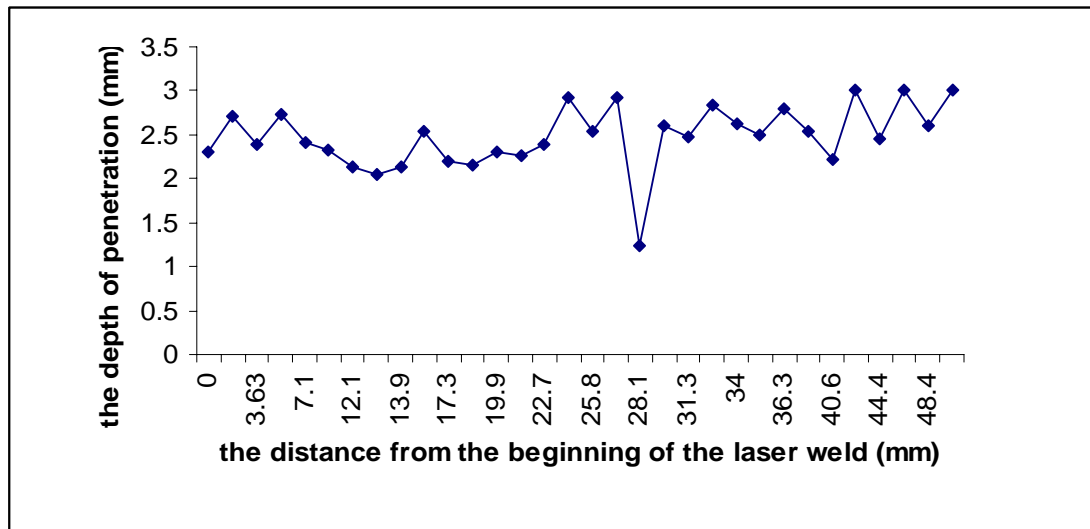
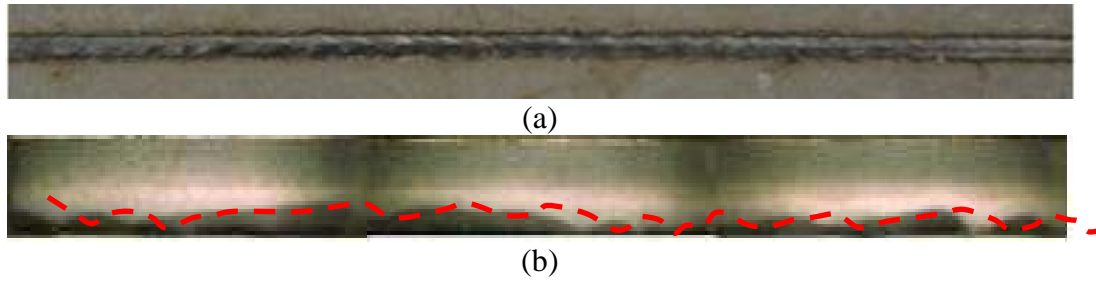


(h) Top view of the laser weld at the welding speed of 20 mm/s



(i) Backside view of the laser weld at the welding speed of 20 mm/s

Figure 2.5 Sample of laser-welded joint with the laser power of 4 kW and a welding speed of 12 mm/s, 15 mm/s, 18 mm/s and 20 mm/s without zinc coating at the interface



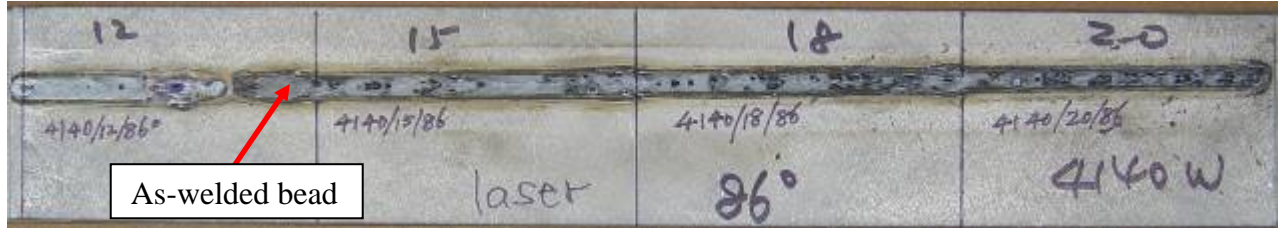
(c)

Figure 2.6 Effect of the zinc vapor plume on the depth of the weld penetration (a) the top view of the laser welded lap joint (b) the longitudinal cross-sectional view of the laser welded lap joint (c) the depth of the laser weld penetration over the distance

2.3.2 Effect of Laser Welding Speed on the Weld Quality

Using the same parameters as in the previous case, the laser welding of galvanized DP sheets in a gap-free configuration proceeded. As shown in Figure 2.7, a large amount of blowholes and spatters are produced in the laser welds, which

leads to the discontinuity of welds and a decrease in the weld mechanical properties. Figure 2.7 (b) - (i) shows higher magnification photos of the laser welded joints for each welding speed. The spatters generated in the welding process present a potential source of damage to the laser protection optics.



(a) Overview of the specimen



(b) Top view of laser weld at welding speed of 12 mm/s



(c) Backside view of laser weld at welding speed of 12 mm/s



(d) Top view of laser weld at welding speed of 15 mm/s



(e) Backside view of laser weld at welding speed of 15 mm/s



(f) Top view of laser weld at welding speed of 18 mm/s



(g) Backside view of laser weld at welding speed of 18 mm/s



(h) Top view of laser weld at welding speed of 20 mm/s



(i) Backside view of laser weld at welding speed of 20 mm/s

Figure 2.7 Sample of laser welds obtained by fiber laser welding at the welding speed of 12 mm/s (b,c), 15 mm/s (d,e), 18 mm/s (f,g) and 20 mm/s (h,i)

As shown in Figure 2.7, more spatters are produced at the higher welding speed. This phenomenon can be explained by the fact that a smaller molten pool is produced at higher speed compared to the molten pool produced at the lower welding speed. The higher speed provides a small spacer for the high-pressurized zinc-vapor to escape from the interface. However, the pressure of the zinc vapor at the interface of two metal sheets is more developed in the higher welding speed than the pressure developed in the lower speed at the same laser power.

2.3.3 Effect of Laser Power on the Weld Quality

Four experiments are conducted to study the effect of laser power on the quality of laser welds. In these experiments, the welding speed is kept constant, 18 mm/s. However, the laser power is varied at four levels: 2500 W, 3000 W, 3500 W and 4000 W. Figure 2.8 shows the experimental results. As shown in Figure 2.8, it is obvious that the change of laser power does not have a significant impact on the weld quality. All the welds obtained in these experiments are characterized by a large amount of spatter deposited on the weld zone or around the weld zone. In addition, some blowholes are produced in the weld zone. The weld quality is slightly improved by a decrease in the laser power. This phenomenon can be

explained by the fact that the lower power reduces the development of high-pressurized zinc vapor at the interface.

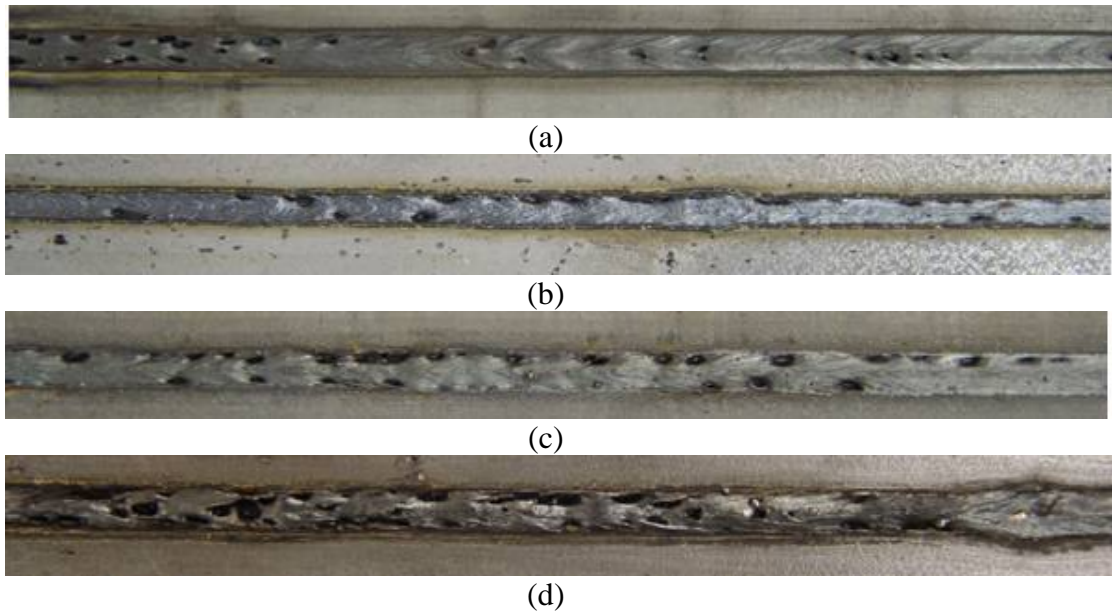


Figure 2.8 Top view of laser welded joints with respect to a welding speed of 18 mm/s and various laser powers (a) laser power of 2500 W (b) laser power of 3000 W (c) laser power of 3500 W (d) laser power of 4000 W

2.3.4 Effect of Spacers Presence on the Weld Quality

As mentioned in the Chapter 1, the use of spacers between two metal sheets can help to vent out the highly-pressurized zinc vapor from the interface. To study the feasibility of achieving sound welds with the assistance of spacers, stainless steel foil of various thicknesses was placed at locations about 10 mm away on both sides of the weld center line. The thicknesses of the spacers used in these experiments were chosen as 0.1 mm, 0.2mm and 0.4 mm. The experimental setup is schematically shown in the Figure 2.9.

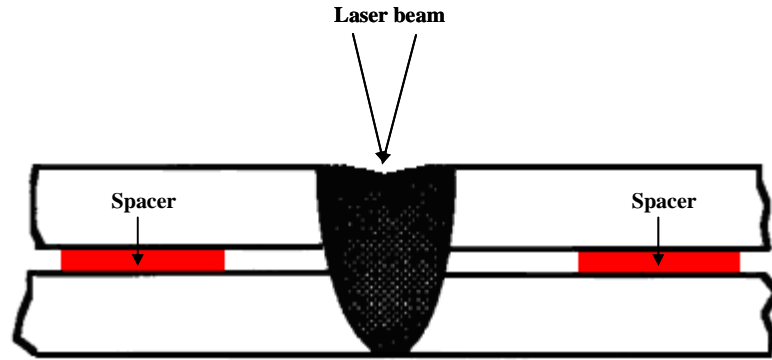


Figure 2.9 Schematic experimental setups for the lap welding of galvanized steel sheets with spacers

Figure 2.10 shows the experimental results with the assistance of spacers of different thicknesses. The results clearly demonstrate that a sound lap joint of galvanized DP steels can not be achieved by using laser welding with the assistance of spacers. In the same fashion as in the laser welding without the spacer, the blowholes and spatters are not eliminated by the help of the spacers. However, the number of blowholes and spatters is reduced. With an increase in the spacer thickness, the welding process became more stable because the highly-pressurized zinc vapor had more space to be vented through.

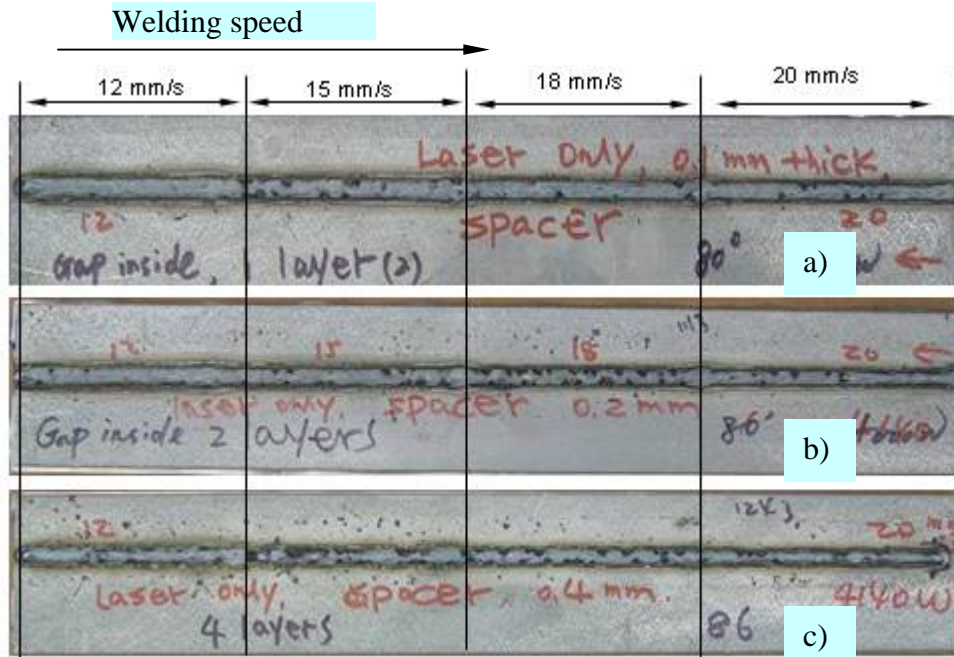


Figure 2.10 Top view of laser welded joint with the assistance of spacers in various welding speed and laser power a) $t=0.1\text{mm}$ b) $t=0.2\text{mm}$ c) $t=0.4\text{ mm}$ (welded at the laser power of 4000 W and the welding speed of 12 mm/s, 15 mm/s, 18 mm/s and 20 mm/s)

2.3.5 Mechanisms of Spatters and Blowholes Formation

The main reason for the occurrence of the spatters and blowholes is the presence of the highly-pressurized zinc vapor at the interface of the two metal sheets during the gap-free lap welding of galvanized DP steel 980. Because the boiling point of Zinc (around 906°C) is lower than the melting point of steel (over 1400°C), the high-pressurized zinc vapor is readily developed at the interface of two metal sheets. If the highly-pressured zinc vapor at the interface can not completely be vented out, it violently expands, expels from the molten pool and removes the liquid metal out of the molten pool [93]. The removed liquid metal out of the molten pool is

condensed in the air and produces spatters of the different sizes that scatter in all directions and deposit around the weld zone.

Moreover, “the explosion may lead to a cavity in the weld zone. If the cavity can not be refilled by the sufficient liquid metal, then a shallow blowhole is produced,” as illustrated in Fig 2.11 (a) [94]. There are two ways for the highly-pressurized zinc vapor to escape from the zero-gap interface: through the keyhole or through the molten pool. Another reason for the blowhole formation is that too much heat is input into the specimen that directly creates a burn-through hole in the weld, as shown in Figure 2.11 (b).

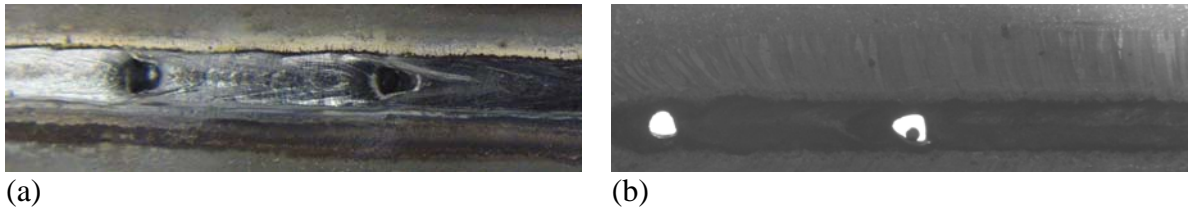


Figure 2.11 Types of blowholes (a) shallow blowhole (b) burn-through blowhole

The blowhole formation is also associated with the collapse of the keyhole that is created by the metal vapor recoil force and “maintained by the equilibrium between the hot metal gas pressure in the keyhole, the hydrostatic pressure and the hydrodynamic pressure exerted by the surrounding liquid metal” [95]. Previous investigations have demonstrated that if the mass flow of the molten metal is irregular, then the keyhole is readily collapsed [95-98]. During the welding process of the lap joint of the galvanized steels, the irregular motion of the highly-pressurized zinc vapor from the interface of two sheets causes an irregular motion of the molten metal flow that leads subsequently to the collapse of the keyhole.

When the keyhole is collapsed, a portion of the highly-pressurized zinc vapor is trapped in the molten pool. The trapped, highly-pressurized zinc vapor explodes from the molten pool and extracts the considerable liquid metal out of the molten pool, causing the blowhole occurrence.

2.4 Feasibility Study of Hybrid Laser-Arc Welding for Welding of Galvanized Dual-phase Steels in Gap-free Lap Joint Configuration

2.4.1 Introduction of Hybrid Laser/Arc Welding and Experimental Setup

Hybrid laser-arc welding combines laser welding and a conventional arc welding such as gas tungsten arc welding (GTAW), gas metal arc welding (GMAW), or plasma welding and has exhibited significant advantages over a single laser welding process or an arc welding process, providing an improved robustness, efficiency, and quality of the welding process. Unlike a sequential configuration where two separate weld processes act in succession, hybrid welding may be viewed as a combination of both welding processes. Depending on the process parameters, the processes influence each other to a different extent and in different ways. The laser/GTAW process is the most commonly used to weld thin and light metal sheets [99]. The combination of the MIG/MAG process with focused radiation of the laser beam is applied to join thick metal plates. In this process, the MIG/MAG process provides the appropriate amount of molten filler material to fill the gap or the groove, while the laser beam penetrates deeper through the already established molten pool [100]. There is increasing interest in applying the hybrid welding technique to join galvanized steels. It has been reported that the enlarged

molten pool provided by the arc in hybrid laser/GTAW welding can reduce the formation of spatters [101].

In this work, the feasibility of using the hybrid laser/GTAW for welding galvanized DP 980 steel in a gap-free lap joint configuration is performed. In addition, it is shown that the total heat efficiency of the laser-arc process, defined as the ratio of the thermal power consumed from weld metal melting to the total power of the laser radiation and the arc discharge, was higher in the case when the arc torch was located ahead of the laser beam in the welding direction [102]. The GTAW is chosen to lead the laser beam during the hybrid laser/GTAW welding process. A series of experiments are carried out to study the effects of arc current, laser power and the distance between the GTAW electrode and laser beam on the weld quality.

The laser/GTAW hybrid welding experiments are performed by using the fiber laser with the power of 4 kW and the GTAW-Dynasty 300 DX AC/DC inverter argon arc welder manufactured by Miller company. A GTAW electrode 3 mm in diameter is used in the hybrid welding process. A charge-coupled device (CCD) video camera is used to monitor the welding process. The video frame rate is set at 30 interlaced frames per second. Pure argon shielding gas is selected as the protecting gas. The experimental setup is shown in Figure 2.12. In this work, the effects of the arc current, laser power and the distance between the GTAW electrode and laser beam on the quality of the hybrid laser-arc welds are investigated in detail. For all experiments of hybrid laser-arc welding, the height of the electrode tip with respect to the top surface of metal sheets is fixed at 3 mm and

the angle of the electrode tip is kept constant in order to keep all experiments in the same welding conditions except the laser power, arc current and the distance between the electrode and laser beam [103]. In addition, the flow rate of argon gas is kept at 30 standard cubic feet per hour (SCFH). An extensive study was performed to determine the angular arrangement between the GTAW torch and the laser welding head. It was found that the vertical position of the GTAW torch with respect to the weldment provides the best results. The laser welding head was inclined with respect to the GTAW torch for an angle of 16 degrees.

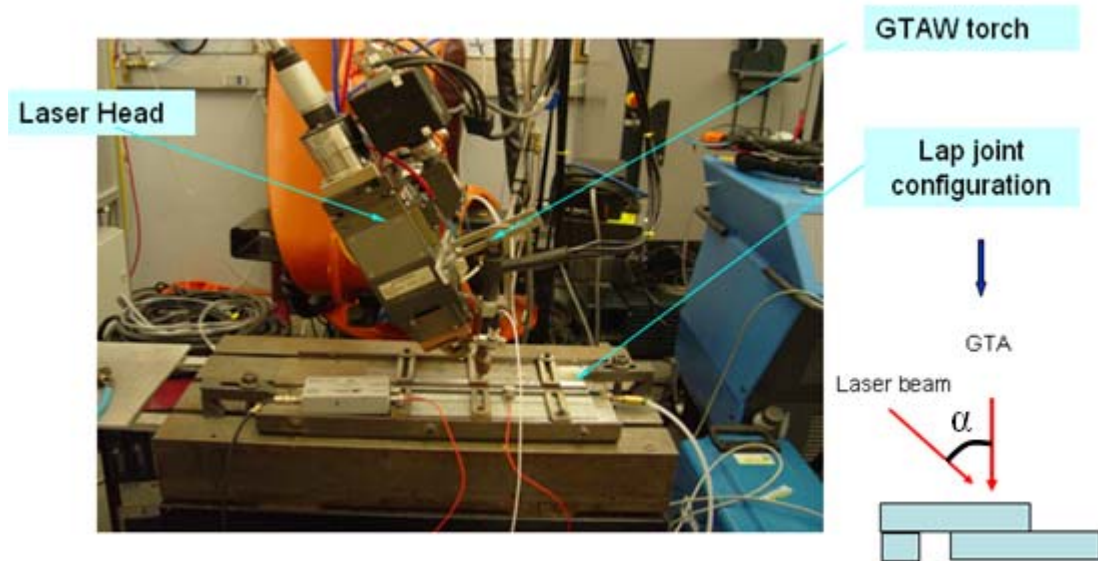


Figure 2.12 Experimental setup of a hybrid laser-GTAW welding system

2.4.2 Effect of Arc Current on the Quality of Hybrid Laser-arc Welds

Figure 2.13 shows the top surface of hybrid welded joints obtained under the arc currents of 120 A, 160 A, 200 A and 240 A. In these 4 experiments, the laser power, the welding speed and the distance between the electrode torch and laser beam are kept at 3000 W, 30 mm/s and 3 mm, respectively. The experimental

results show that the hybrid laser/GTAW welding process is still very instable. The welds shown in Figure 2.13 indicate that spatters and blowholes are reduced and the weld quality is improved with an increase of arc current. However, despite the fact that the enlarged molten pool created by the arc suppresses the effect of the high-pressurized zinc vapor on the formation of weld defects to some extent, the spatters, blowholes, porosities and humping are still present in the welds in the same manner as in the laser welding process, as shown in Figure 2.13. When the arc current is increased to 240 A, the weld quality is degraded dramatically. The degradation of the weld quality is due to the high arc current that results in the formation of humping. Furthermore, the increase of arc current leads to the significant absorption and defocusing of the laser beam energy by the arc plasma. Therefore, a critical level of arc current from this effect exists based on the other selected welding conditions. It is found that with the increase in laser power, the threshold of arc current is increased [105].



(a)



(b)



(c)



(d)

Figure 2.13 The effect of arc current on the quality of hybrid laser-arc welds at (a) an arc current of 120 A (b) an arc current of 160 A (c) an arc current of 200 A (d) an arc current of 240 A

Another problem that is present in the hybrid laser-arc welding process is the formation of porosity at the weld surfaces or internally in the weld, as shown in Figure 2.14. The formation of porosity is associated with the entrapment of the shielding gas or air in the molten pool. If the weld shield gas or air is entrapped in the weld pool and does not have enough time to escape from the molten pool during the hybrid laser-arc welding, porosity is formed.

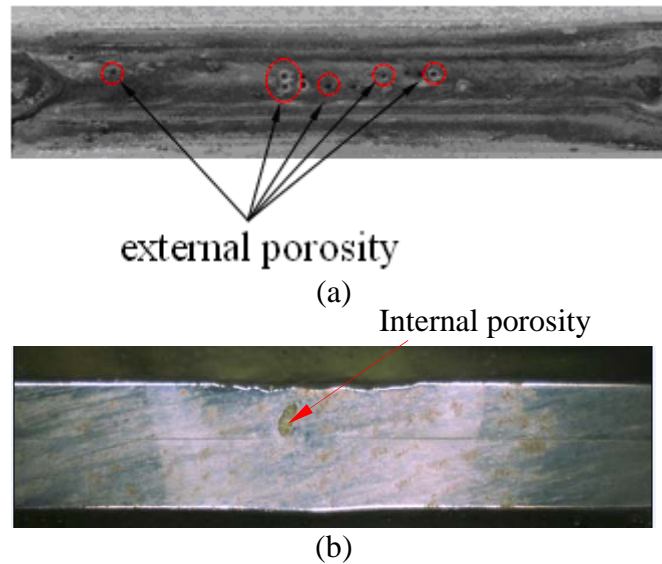


Figure 2.14 Porosity present in the hybrid welds (a) the porosity present at the top surface (b) the porosity present in the welds

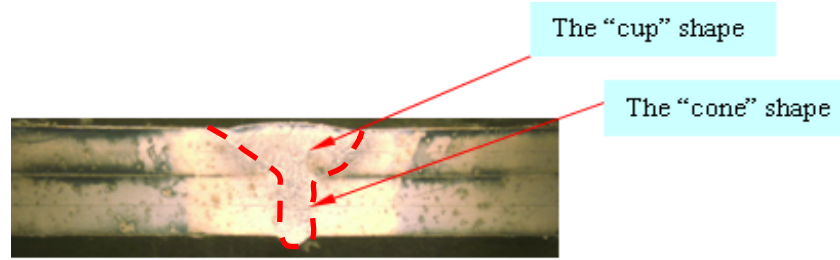
In addition, the collapse of the keyhole is another primary reason for the formation of porosity in the hybrid welding. When the laser beam moves forward along the welding direction, the recoil pressure on the keyhole wall disappears quickly. Because the zinc vapor plume inside the keyhole no longer receives intense irradiation from the laser beam intensity, and the heat capacity of plasma is small, the temperature of the keyhole wall drops dramatically. The heat is transferred from the keyhole wall to the surrounding liquid metal quickly because of the high temperature gradient. Under the function of surface tension, hydrostatic pressure, and heat loss, the solidification process begins, and the keyhole starts to contract. The bottom of the keyhole solidifies first, and the liquid metal begins to fill back the keyhole. However, because of the slow motion of the irregular metal flow, the liquid metal does not immediately fill back to the keyhole along the keyhole wall but moves along an irregular path [106]. At the same time, the top of the keyhole also begins to solidify. If some of the zinc vapor plume can not completely escape from the keyhole, porosity is produced in the internal welds. Porosity is generally formed at the bottom of the collapsed keyhole. The location of porosity depends on the depth of the keyhole, the solidification speed of the keyhole, and the melt flow states [106].

Similar to the laser welding process, the zinc vapor plume is induced by the zinc coating. During the hybrid laser/ arc welding process, the shape and size of the arc plasma and plume significantly fluctuate. As shown in the Figure 2.15, the plasma shape is irregular and the shape and size of the zinc vapor plume also change over time. For this reason, the coupling of laser beam energy into the

specimen is dramatically different during the hybrid welding process than from coupling in a pure laser welding process. The instability of the arc plasma and the zinc vapor plume will result in the frequent collapse of the keyhole. Consequently, the welding mode is transferred from the keyhole mode to the heat conduction mode. As a result, the depth of weld penetration switches between partial and full penetration, as shown in the Figure 2.16. Furthermore, the completely open keyhole allows the highly-pressurized zinc vapor to escape from the interface. The collapse of the keyhole results in the failure of the zinc vapor at the interface to be vented out. When the keyhole is open, the plume above the specimen can be clearly observed. If the keyhole is closed, the plume disappears and the melted liquid is ejected from the molten pool; thus, a large amount of spatters are produced. In addition, the remaining zinc vapor in the molten pool leads to the internal porosity of the weld. In general, the weld bead shape at the top of the hybrid weld is in the form of a “cup” shape like the shape of the GTAW weld; but, the weld bead shape at the bottom of the hybrid weld is of a “cone” shape like the shape of the laser weld, as shown in Figure 2.15 (b).



(a)



(b)

Figure 2.15 Effect of the arc plasma and the zinc vapor on the weld penetration (a) partial penetration of hybrid laser-arc weld (b) full penetration of hybrid laser-arc weld

2.4.3 Effect of Laser Power on the Quality of Hybrid Laser-arc Welds

For the study on the effect of laser power on the hybrid weld quality, four experiments are carried out with respect to laser power at 2000 W, 2500 W, 3000 W and 3500 W. The welding speed, arc current and shielding gas flow rate are kept at 30 mm/s, 200 A and 30 SCFH, respectively. Figure 2.16 shows the produced welds. Spatters, blowholes and humping are found in these welds. It can be seen that the welds obtained at a laser power of 2000 W and 2500 W are of better quality than those welds produced at a higher laser power of 3000 W and 3500 W. These phenomena can be explained by the fact that the higher pressure of zinc vapor at the interface of two metal sheets is formed by the larger laser power. The porosity increases at a higher laser power.



(a)

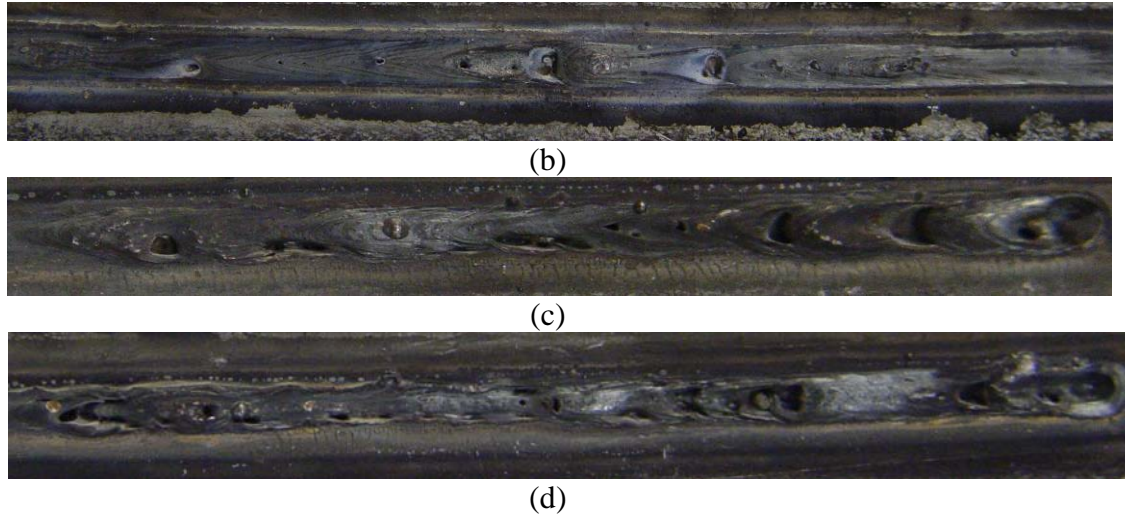


Figure 2.16 Effect of laser power on the quality of hybrid laser-arc welds at a laser power of (a) 2000 W (b) 2500 W (c) 3000 W (d) 3500 W

2.4.4 Effect of Distance between the Electrode of GTAW Torch and Laser Beam on the Quality of Hybrid Laser-arc Welds

Due to the interaction of laser beam and arc, the distance between the electrode of the GTAW torch and the laser beam is one of the critical welding parameters for hybrid laser /arc welding. In order to investigate this effect, the distance between the electrode of the GTAW torch and the laser beam on the weld quality is varied: 2 mm, 6 mm, 10 mm, 30 mm and 60 mm. During the hybrid welding process, the laser power, the welding speed and the shielding gas flow rate were kept at 3000 W, 30 mm/s and 30 SCFH, respectively. The experimental results show that the farther the distance is, the less spatters are produced. As can be seen in Figure 2.17, the weld quality is dramatically improved by the increase in the distance. When the trailing laser beam is separated from the leading arc, the welding process is not affected by the plume induced by the zinc coating on the top surface of the

specimen because the arc removes the zinc coating layer before the laser beam is irradiated on the specimen.

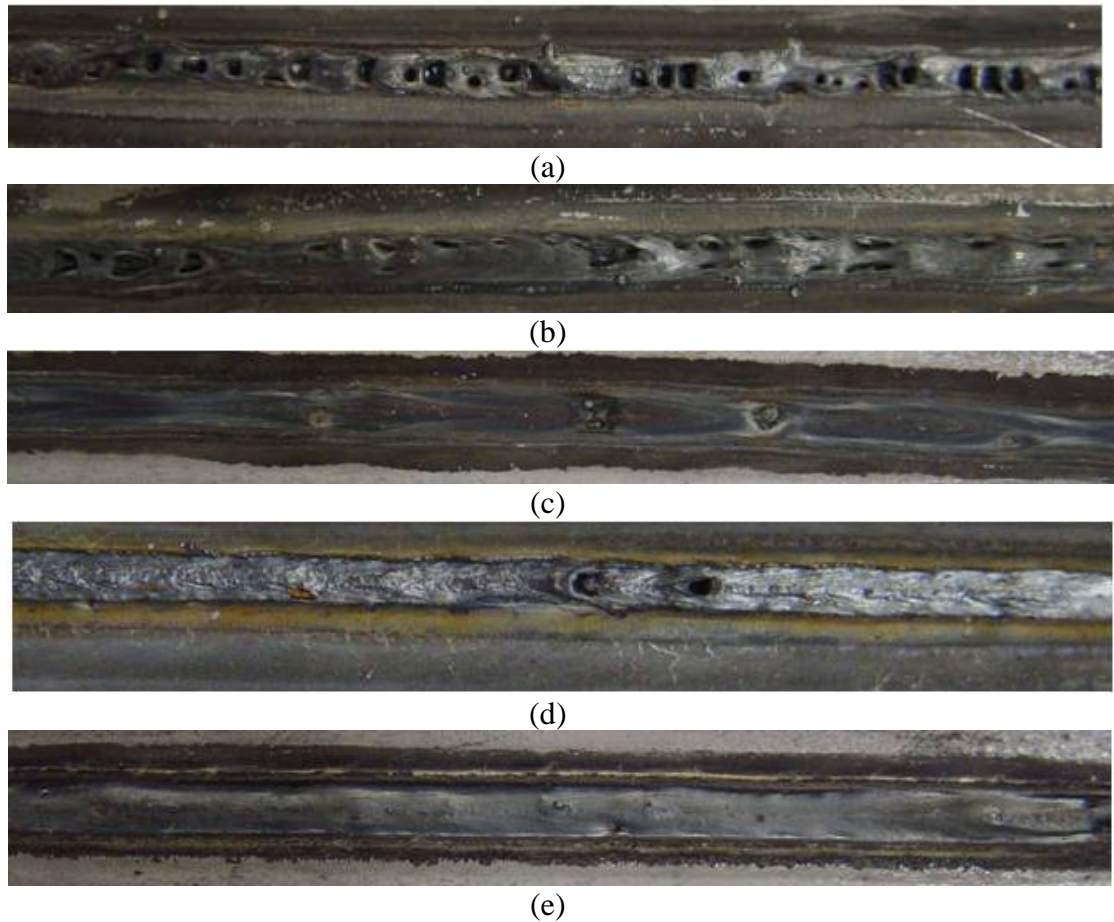


Figure 2.17 Effect of the distance between the electrode of GTAW torch and laser beam on the quality of hybrid laser-arc welds (a) at the distance of 2 mm (b) at the distance of 6 mm (c) at the distance of 10 mm (d) at the distance of 30 mm (e) at the distance of 60 mm

2.4.5 Effect of Welding Speed on the Weld Quality of Hybrid Laser/arc Weld

Figure 2.18 indicates the effect of the welding speed on the weld quality of hybrid welds. The welding parameters used in this experiment are: laser power of 3000 W, an arc current of 200 A, a distance of 10 mm between the electrode of the

GTAW torch and the laser beam, a shielding gas flow rate of 30 SCFH and welding speeds of 30 mm/s, 35 mm/s and 40 mm/s. It can be seen that an increase in the welding speed decreases the weld quality. One of reasons for this outcome is due to the collapse of the keyhole, because the high welding speed tends to cause the collapse of the keyhole [106]. Also increasing the welding speed decreases the time for the zinc vapor at the interface to escape from the molten pool. If the zinc vapor at the interface does not have enough time to completely be vented out, some of it will be trapped in the molten metal and explodes from the molten pool when the laser beam moves away from the liquid molten pool and the molten metal begins to solidify.

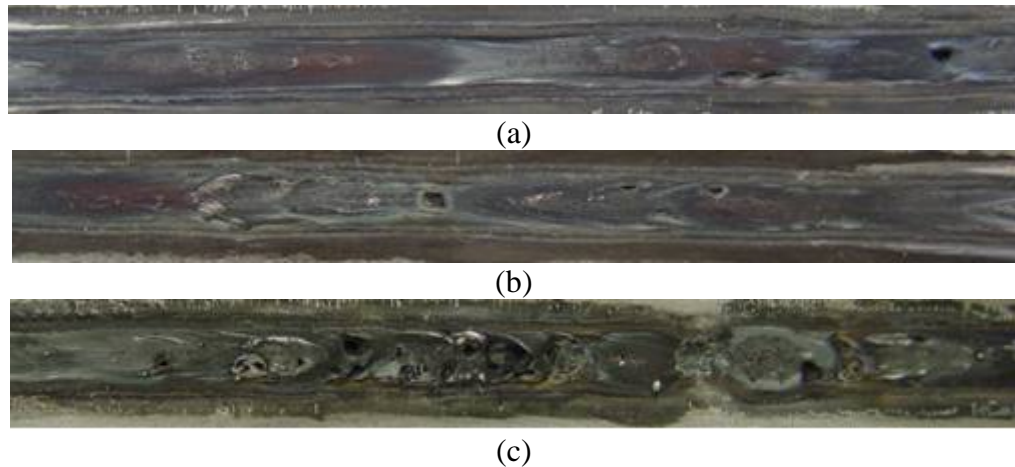
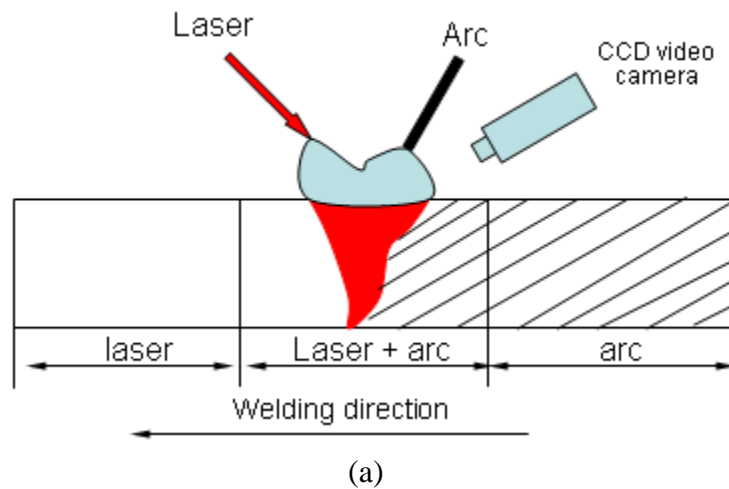


Figure 2.18 Effect of the welding speed on the quality of hybrid laser-arc welds (a) at the welding speed of 30 mm/s (b) at the welding speed of 35 mm/s (c) at the welding speed of 40 mm/s

2.5 Instable Interaction between the Laser-Induced Plasma and the Arc Plasma

The interaction between laser-induced plasma and arc plasma is significantly instable when laser beam shares the common molten pool with the arc. Figure 2.19

demonstrates the images of the different shapes of the plasma taken by the CCD video camera in a single welding process where firstly runs arc welding, then runs the laser-arc hybrid laser welding and last only runs the laser welding of galvanized steels. As mentioned previously, the zinc plasma is readily formed due to its very low first ionization potential. Compared the plasma shape in Figure 2.19 (b) to that in Figure 2.19 (c), it can be seen that the stationary arc plasma is expanded by the addition of the zinc plasma during the arc welding of galvanized steels. Furthermore, the hybrid laser-arc induced plasma is significantly erratic, as shown in Figure 2.19 (d) - (f). In comparison with the arc plasma in Figure 2.19 (c) with those in the Figure 2.19 (d) – (f), it can be clearly seen that the arc plasma produced in the single arc welding is remarkably compressed during the hybrid laser-arc welding process. In addition, the left side of the arc root near the laser beam is consistent to be attracted inversely toward the laser beam along its axis.



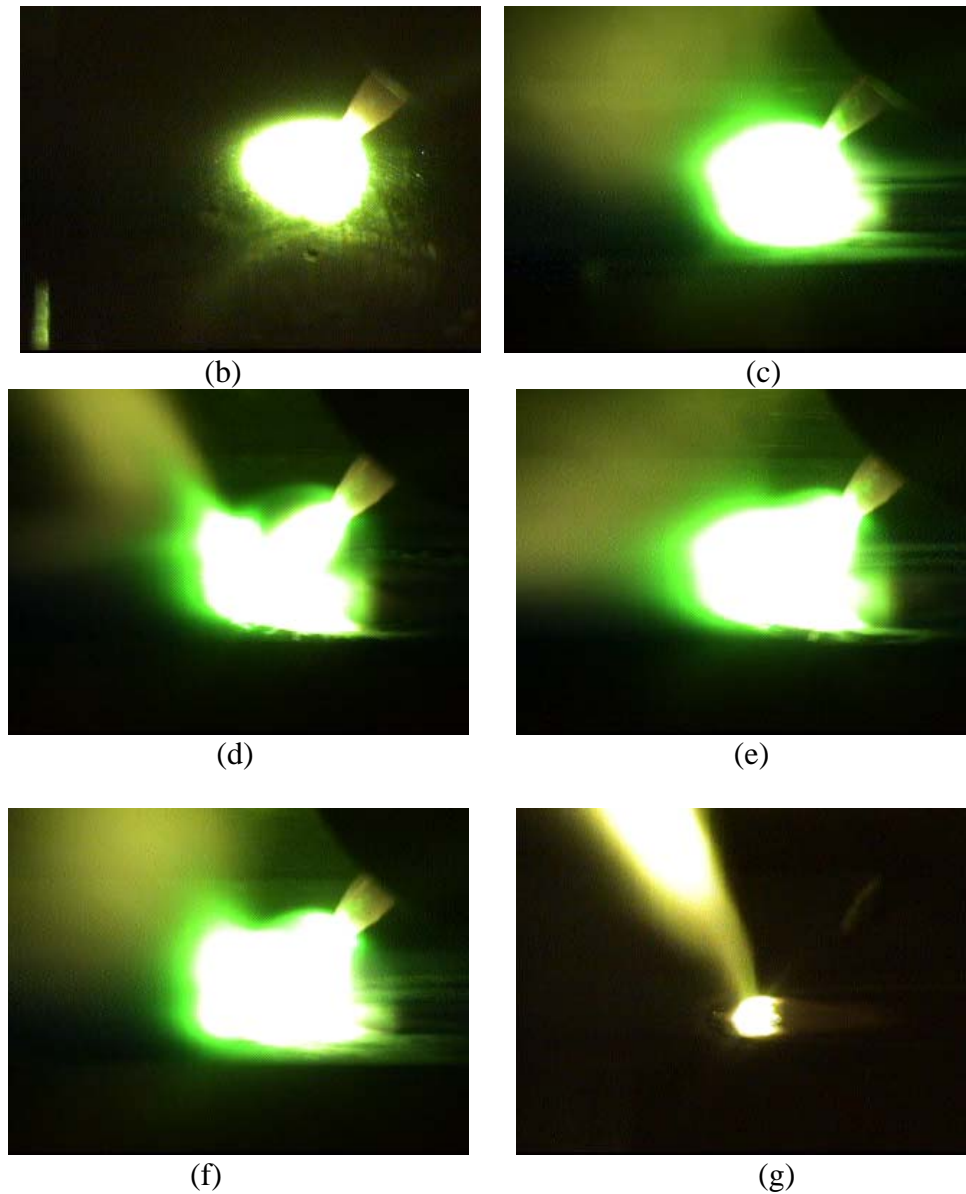


Figure 2.19 Images of the single arc, single laser, laser-compressed arc, and laser-expanded arc (a) the schematic presentation of single arc welding, hybrid laser-arc welding and laser welding of galvanized steels (b) $t=0$ s (stationary arc) (c) $t= 14.33$ s (single arc welding process) ; (d) $t= 18$ s (hybrid laser-arc welding); (e) $t = 18.033$ s (hybrid laser-arc welding);(f) $t= 18.070$ s (hybrid laser-arc welding)(g) $t=28.750$ s (single laser welding) (Arc current: 260 A; laser power: 3000 W; welding speed: 30 mm/s)

The unstable and strong interaction between the laser-induced plasma and the arc plasma during the hybrid laser-arc welding of galvanized steels mainly comes

from their different characteristics and the unstable zinc plasma. Laser-induced plasma has a higher temperature and particle density in comparison with the arc plasma [108]. During the hybrid laser-arc welding process in a common molten pool, a large amount of laser-induced zinc and iron plasma are preferably formed in the metal vapor-argon gas mixture since the iron and zinc plasma have the lower first ionization potential (9.3941 eV for zinc and 7.9024 eV for iron) than that of the argon (15.7 eV). There is a channel built between the laser-induced plasma and the arc plasma, through which the charged ionized particles of laser-induced metal plasma, is passed to the arc plasma [108]. Due to the significant increase of the charged zinc and iron ionized particle in the arc plasma, the resistance of arc will be reduced, the arc current conductivity will be improved and the ionizability of the arc is increased [109]. As a result, the arc will be compressed due to the increased current in terms of the minimum voltage principle [108]. Since the zinc plasma is significantly instable when hybrid laser-arc welding of galvanized steels in a gap-free lap joint configuration, the transition between the laser-induced plasma and the arc plasma is also instable. Consequently, the shape of the hybrid laser-arc induced plasma is fluctuated over the time. In addition, the arc root is generally focused on the laser spot and the stability of the arc is improved by the reduced resistance of arc. Since the arc volume is reduced and the ionizability in the arc is increased, the arc energy will be more concentrated and the stability of the arc ignition is also improved [108]. However, there is a balance between the increased coupling efficiency by the energy concentration by the compression of arc by laser beam and the defocused and absorbed effect of arc plasma on the laser beam energy during

hybrid laser-arc welding process [110]. It has been found that for a specific laser power there exists a critical arc current, beyond which the effect of the compression of the arc plasma by the laser beam on the coupling efficiency is weakened and contrarily the arc plasma will be dramatically expanded due to the dramatic absorbed energy from the laser beam [110]. There is a relationship between the plasma height and the laser energy absorbed by the welded materials, which is given by the following equations [111-112]:

$$I = I_0 e^{-\mu h_{plasma}} \quad (2.1)$$

where I is the laser beam intensity absorbed by the welded material, I_0 is the incident laser beam intensity, μ is the plasma absorption coefficient, and h_{plasma} is the plasma length. Here, the inverse bremsstrahlung (IB) absorption coefficient μ is expressed as [111,113]:

$$\mu = n_i n_e Z^2 e^6 \ln(2.25 k_B T_e / h \nu) \lambda^2 / [24 \pi^3 \varepsilon_p^3 c^3 m_e n k_B T_e (2 \pi m_e k_B T_e)^{1/2}] \quad (2.2)$$

where h is the Planck constant, k_B is the Boltzmann constant, n_i is the number of ions, Z is the charge number of the atom, n_e is the number of atoms, e is the electronic charge, c is the velocity of light in a vacuum, T_e is the electronic charge, ε_p is the permittivity of free space, m_e is the electron mass and n is the refractive index of the plasma, ν and λ are the frequency and wavelength of the used laser beam, respectively. Equation (2) indicates that the absorption coefficient of the plasma is linearly proportional to the square of the laser beam wavelength. For the fiber laser with the wavelength of $1.07 \mu m$, the value of μ is very small. From the above discussion, the absorbed laser beam energy is mainly dependent on the length

of the plasma. The variation of the plasma length will dramatically change the coupling of laser beam energy into the welded material. When using hybrid laser-arc welding method to gap-free lap joint configuration of galvanized steels in the common molten pool, the shape of the plasma formed is dramatically fluctuated over the time by the highly-pressurized zinc vapor. Therefore, the keyhole becomes very instable and tends to be closed due to the instable coupling of the laser beam energy into the welded material. Consequently, a large number of weld defects such as the spatters and blowholes are generated in the welds during the instable welding process.

2.6 Conclusions

The weldability of galvanized DP 980 steel in a gap-free lap joint configuration is evaluated by using GTAW, laser welding and hybrid laser-arc welding. The main problem in welding of this type of steel is linked to the low boiling point of zinc. The instable highly-pressurized zinc vapor at the interface between two metal sheets leads to the ejection of the liquid metal from the molten pool that results in different weld defects such as spatters, blowholes, and porosity. The GTAW welds are characterized by different weld defects such as humping, spatters and blowholes. Only in a very narrow range of welding conditions can sound welds be achieved. Similarly, a large amount of spatter and blowholes are produced around the weld zone in the laser welding process. The optics of the laser welding head and the protective glass are easily damaged by the spatters. The experimental results have shown that it is not possible to join galvanized DP steels by using laser welding

alone. Furthermore, the zinc vapor induced by the laser beam significantly affects the coupling of the laser beam energy into the specimen and determines the depth of the weld penetration.

The experimental results have demonstrated that the introduction of the arc in the hybrid laser-arc welding process can suppress the formation of spatters and blowholes to some extent. However, it is still very difficult to obtain sound welds. Similarly, the shape and size of the arc plasma and the intensity of the zinc vapor plume are changed over time, like in the laser welding process. These changes result in the instability of the welding process that dramatically influences the level of coupling of the laser beam energy with the specimen. Furthermore, the experimental results suggest that the weld quality is improved by an increase of the arc current. However, there exists a threshold level of arc current. If the arc current is more than the threshold value, the weld quality declines. The coupling of laser beam energy with the specimen is not affected by the zinc vapor plume if the distance between the electrode of GTAW torch and the laser beam is increased. The leading arc removes the zinc coating before the laser beam irradiates the specimen. The experimental results have shown that the weld quality is enhanced by increasing the distance between the electrode of GTAW torch and laser beam. The hybrid weld performance is also affected by the welding speed. The high welding speed will result in the collapse of the keyhole and leads to the instability of the welding process. During the hybrid welding process, the keyhole easily collapses if the arc plasma and the zinc vapor plume are unstable. This collapse results in the

formation of porosity. The porosity is observed at the surface of the weld as well as internally in the weld.

Chapter 3

LASER WELDING OF GALVANIZED DP 980 STEEL PREHEATED BY VPGTAW IN A GAP-FREE LAP JOINT CONFIGURATION

3.1 Introduction

As with discussion in Chapter 2, weld quality and performance are largely dependent on the stability of the welding process. For the successful welding of galvanized DP steels in gap-free lap joint configuration, the high-pressurized zinc vapor should be fast vented out from the interface between the two metal sheets in order to prevent the explosion of the metal from the molten pool. Considering the effect of the interaction of the laser beam and arc plasma on the coupling of laser beam energy into the specimen, the electrode of gas tungsten arc welding (GTAW) torch is separated from the laser beam and the GTAW is only used as a preheating source in this study. During the laser welding process, the surface along the weld line is preheated from the heat generated by the GTAW torch. As a preparation for welding, the heating of the GTAW torch changes the chemistry of the top surface and contributes to a much better coupling of the laser beam energy to the material. The outcome of this preparation is manifested in a high quality laser welded galvanized DP 980 steel in a gap-free lap-joint configuration. A number of experiments are performed to study the effect of the heating parameters such as the arc current, the scanning speed, and the distance between the GTAW torch

electrode as well as the laser beam on the laser weld quality. The major characteristics and advantages of the laser/GTAW preheating method for the welding of galvanized DP steels in a gap-free lap joint configuration is discussed. The chemical analysis of the top surface of the galvanized metal sheet that is preheated by the GTAW torch is performed using the X-ray photoelectron spectroscopy (XPS) method. The effect of the laser welding parameters on the weld quality is investigated. In addition, the microhardness measurement, tensile and shear test of the laser/GTAW preheated welds are carried out. The temperature of the zinc coating at the interface between two metal sheets is also measured to study the behavior of the zinc coating when preheated by the GTAW torch.

3.2 Experimental Setup

The material used in this study is galvanized DP 980 steel with thickness of 1.2 mm and 1.5 mm. The dimensions of the metal sheets used in this work are 200 mm X 85 mm X 1.2 mm and 200mm X 85 mm X 1.5mm. The gap between the two metal sheets is kept tight during welding, assuming that the gap is equal to zero. The laser/GTAW hybrid welding experiments are performed by using the fiber laser with the 4 kW in power and the GTAW welding machine, Dynasty 300 DX AC/DC inverter argon arc welder made by Miller. The pure argon gas with a flow rate of 30 standard cubic feet per hour (SCFH) is used as the shielding gas. A GTAW electrode of 3 mm in diameter is used. A high speed charged coupled device (CCD) video camera is used to monitor the welding process. The video frame rate is set at 30 interlaced frames per second. The experimental setup is shown in Figure 3.1.

During the welding process, the GTAW is used as the preheating heat source and the trailing laser beam is applied to provide the welding.

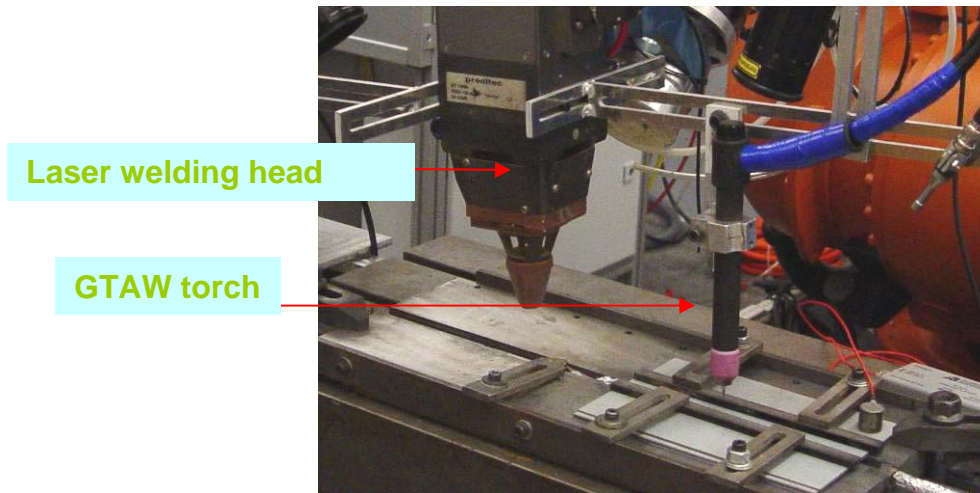


Figure 3.1 Experimental setup of laser/ GTAW system

3.3 Results and Discussions

3.3.1 Advantages and Principles of Laser Welding of Galvanized DP Steels with the Assistance of GTAW as the Preheating Source

Recently, Kim et al. [114] used a CO₂ laser with the tungsten inert gas (TIG) to weld the galvanized low strength SGCD 1 steel plates with the yield strength of 147 MPa in a gap-free lap joint configuration. The welding conditions used in their report are shown in Table 3.1.

Table 3.1 Welding Conditions Used in Kim's Report

Specimen	SGCD 1 (300 mm x 100 mm x 1 mm)
Laser power	4000 W
Shielding gas	He 100% (15L/min)
Electrode diameter	1.6 mm
Torch angle	45 deg.
Welding current	80A,100A,120 A
The distance between the laser beam and electrode torch	5 mm, 7 mm, 9 mm
The distance between the electrode tip and the top surface of specimens	0.4 mm, 1.0 mm, 2.0 mm

It was claimed [114] that with a higher melting point than steel the generated gap and oxidized zinc along the interface of the two metal sheets postpone the formation of the high-pressurized zinc vapor. The outcome of this experiment is much better weld quality. Contradictorily, in the later section of their report they said the electrode tip is significantly damaged by the spatters produced in the welding conditions, under which the sound weld is achieved. In order to further verify this, the same welding conditions used in their study are used to weld galvanized DP 980 steels in a gap-free lap joint configuration with respect to laser power at 4000 W, an arc current of 100 A, a distance of 7 mm between the laser beam and the electrode torch and a distance of 1 mm between the electrode tip and the top surface of the metal sheets. Figure 3.2 shows the experimental results. As shown in the Figure 3.2 (a), the spatters are still produced. In addition, spatters damaged the electrode tip, as illustrated in Figure 3.2 (b). During the hybrid welding process, the damaged electrode tip causes fluctuation and an erratic behavior of the arc that leads to instability of the welding process. Furthermore, the instability of the metal plume also causes the instability of the hybrid laser/TIG

welding process. Therefore, it is important and necessary to develop a more robust welding technique of galvanized steels to ensure the quality of welds.

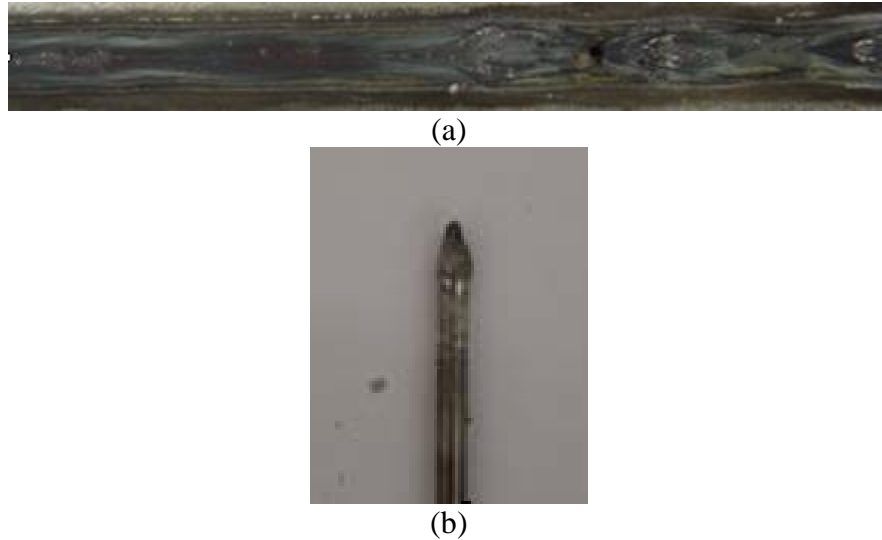


Figure 3.2 Top view of hybrid laser/GTAW weld obtained under the following welding conditions: laser power of 4000 W, arc current of 100 A and distance of 7 mm between the torch electrode and laser beam (a) the top view of the hybrid laser/GTAW weld (b) the damaged electrode tip

As discussed in Chapter 2, the quality of the weld in hybrid welding process is dramatically changed by the increase in the distance between the laser beam and the torch electrode. Moreover, it is difficult to prevent the electrode tip from damage and to control the irregular behavior of the zinc plume when a short distance between the laser beam and torch electrode is used. Also, it has been reported that during laser welding of metal sheets most of laser beam energy is reflected by the metal sheet surface and only a very small portion of laser beam energy is coupled into the specimen when the laser welding process is performed under the conductive mode [117]. However, the absorption of laser beam energy is dramatically enhanced through the multiple reflection mechanism when the laser

welding is in the keyhole mode [118]. It was also found that the coupling efficiency of laser beam energy can be significantly raised by 150-300 percentage when some of the metal oxides such as zinc, aluminum and iron and the soot of substances are formed on the surface of the metal sheets before the laser welding process is started [119]. Xie et al. [117] claimed that the reflectivity of cold-rolled thin sheet steel was found to be in the range of 65-80 percent in CO₂ laser welding. The reflectivity decreased to about 30 percent when the sheet surface was oxidized before laser welding. More importantly, it has been revealed that the pressure level of the zinc vapor is exponentially increased by the increase in the temperature, as shown in Figure 3.3 [120]. When the laser beam shares the common molten pool with the arc, the temperature at the interface of two metal sheets will be dramatically increased due to the higher heat input; thus the pressure level of zinc vapor reaches very high. This fact implies that the function of the arc-enlarged molten pool can not completely compensate for the increase of the pressure level. From the further experimental results, it was found that only in a very narrow optimized welding condition the spatters and blowholes can be dramatically decreased and sound weld can be obtained with the introduction of arc. Additionally, the zinc coating at the top surface and interface of two metal sheets is widely damaged by the arc and the weld surface is un-uniform when laser beam and GTAW torch share the common molten pool.

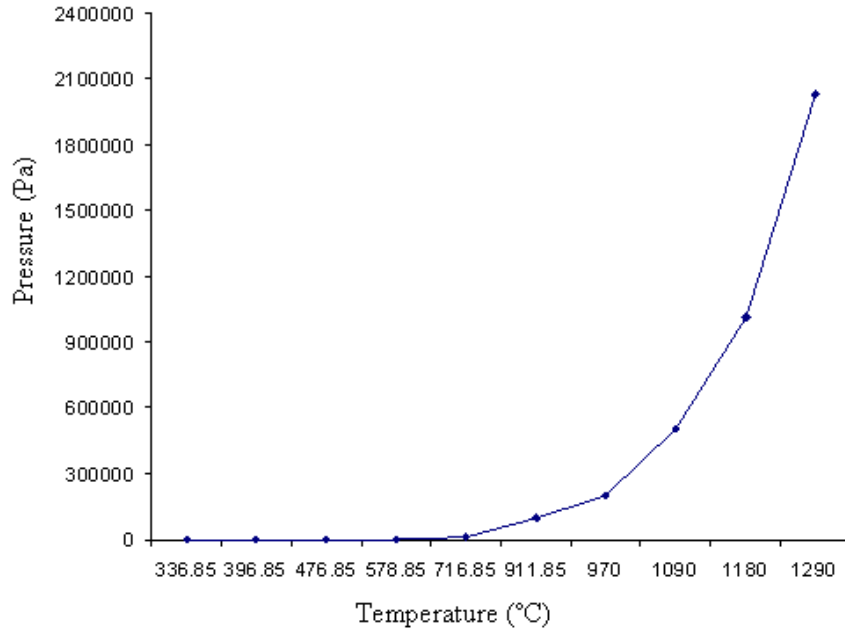


Figure 3.3 Relationship of the zinc pressure and temperature [120]

In this study the GTAW welding is kept far away from the laser beam in order to avoid the formation of a common molten pool. The GTAW torch is only used to provide the preheating of the metal sheets that are laser welded afterwards. Three tests are carried out under the following welding conditions: laser power of 3000 W, welding speed of 30 mm/s and distances of 60 mm, 120 mm and 180 mm between the torch electrode and laser beam. It was found that the longer distance between the torch electrode and laser beam, the less spatters are produced and the more stable the welding process. Figure 3.4 shows the results under the welding conditions above. Full penetration is achieved in all three welds, shown in the Figure 3.4. As shown in Fig 3.4 (c), a completely defect-free weld is achieved at a distance of 180 mm. No spatters, blowholes or porosity are presented at the surface of two welds. It was found that the longer distance between the torch electrode and

laser beam, that the less spatters are produced and that the more stable the welding process is. In all of the three welds, the full penetration is achieved. Therefore, the distance between the torch electrode and laser beam play a critical role in guarantying the achievement of the sound welds for the laser/GTAW preheated welding process. This phenomenon can be explained by the fact that when the distance between the GTAW electrode torch and laser beam is far enough, the pressure of zinc vapor is significantly decreased due to the heat lost. The decreased pressure of the zinc vapor helps to stabilize the welding process. It should be mentioned that the distance between the laser beam and the GTAW torch could be decreased by the introducing the cooling media such as cold air or copper sheet as well as optimizing the other welding parameters such as the flow rate and direction of the shielding gas.

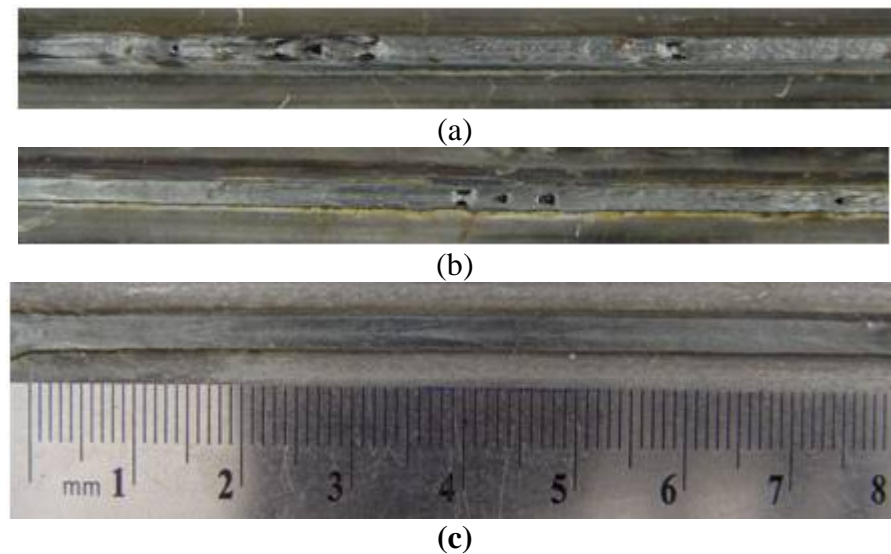


Figure 3.4 Effect of the distance between the torch electrode and laser beam on the quality of the laser/GTAW welds at various distances (a) 60 mm (b) 120 mm (c) 180 mm

In order to further verify the influence of the preheating by the GTAW torch on the weld quality, another test was carried out with an arc current of 200 A, a laser power of 3000 W, a welding speed of 40 mm/s, and a distance of 180 mm. A defect-free weld was also achieved, as shown in Figure 3.5. The cross-sectional view of the laser/GTAW weld demonstrates that there is no porosity in the weld. Therefore, the conclusion can be made that sound welds can be achieved in a gap-free lap joint configuration of galvanized steels by the laser/GTAW method under optimized welding conditions.

The success in achieving a sound weld is contributed to the dramatically increased efficiency of coupling the laser energy beam into the specimen. By using the GTAW to preheat the specimen, part of the zinc coating is removed from the top surface of the metal sheet, and the rest is transferred into zinc oxide. Zinc oxides are expected to form at both surfaces of the metal sheets along the interface. In order to confirm these hypotheses, X-ray Photoelectron Spectroscopy (XPS) tests are carried out by PHI 5000 VersaProbe scanning ESCA Microprobe equipment, which is produced by ULVAC-PHI, Inc. The analysis results further confirm the fact that zinc oxides form at the top surface and interface of the metal sheets when they are exposed to the heat generated by a GTAW torch. The analyses are done at points at the top surface and the interface of two metal sheets. As shown in Figure 3.6 (b)-(c), only zinc oxides are produced and no iron oxides are generated.

The change of chemical composition of the top surface of the specimen improves the coupling of laser beam energy to the material and keeps the welding process stable. In addition, the electrode tip is also safe from the damage of the

spatters. Once the incident laser power intensity is larger than the threshold value, the keyhole is formed. Usually, the threshold value for the keyhole formation is dependent on the material to be welded and the laser beam wavelength [119]. The oxide layer at the specimen produced by the GTAW preheating ensures the improved coupling of the laser beam energy into the specimen; thus, providing the condition for the keyhole formation during the laser welding process. The sustained presence of the keyhole allows the high-pressurized zinc vapor to escape from the interface. Furthermore, the stable keyhole “decreases the mean fluid velocity inside the melt pool” and “facilitates the achievement of better welds” [121-122]. It was found that when the keyhole is open, the welding process is very stable and no spatter is produced. However, once the keyhole is collapsed, lots of spatters are produced. Therefore, one of the most important factors in achieving a sound weld is the open keyhole during the welding process. In the instable welding process, the open keyhole alternates with the collapsed keyhole. Figure 3.8 shows the shape of the molten pool for instable welding process (the images of the molten pool are obtained by the CCD video camera, as introduced in Chapter 4). The keyhole is presented in Figure 3.8 as the black spot in the frontal side of the molten pool. In addition, another advantage of the laser/GTAW preheating is that the pressure of the zinc vapor at the interface is decreased because of the lower heat input; whereas, the optimized distance provides a longer cooling time during the hybrid laser/TIG welding process. For the welding of galvanized steel, the melt metal has a lower pressure than that of the zinc vapor at the interface. If the pressure of the zinc vapor is higher than a certain value, the zinc vapor will break the stability of the molten

pool and explode from the molten pool. When the distance between the electrode torch and laser beam is far enough, the pressure of zinc vapor will be significantly lessened due to the lower heat input, as compared to the short distance. The decreased pressure of the zinc vapor also help the stability of the welding process. Therefore, the stability of the welding process is improved compared to the hybrid laser/GTAW welding process and the laser/GTAW preheating process because of the short distance between the electrode torch and laser beam.

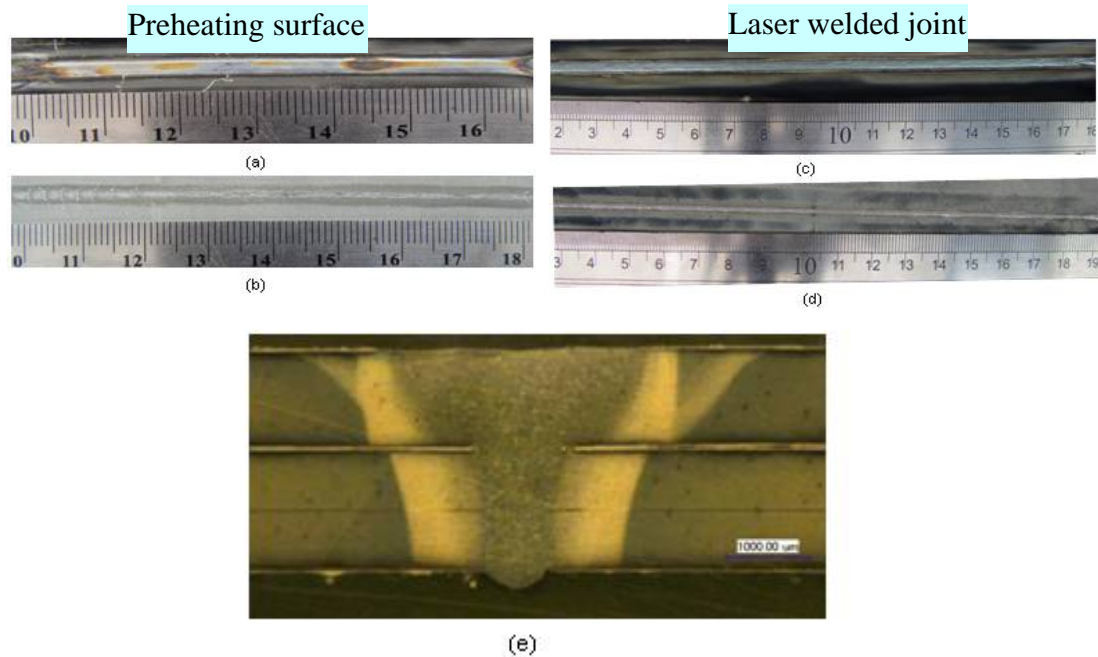
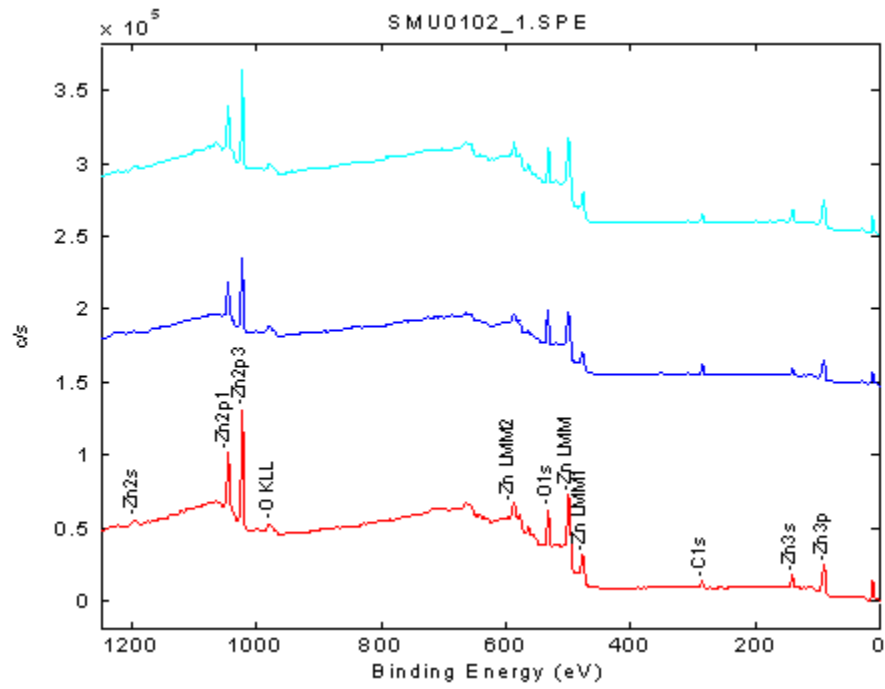
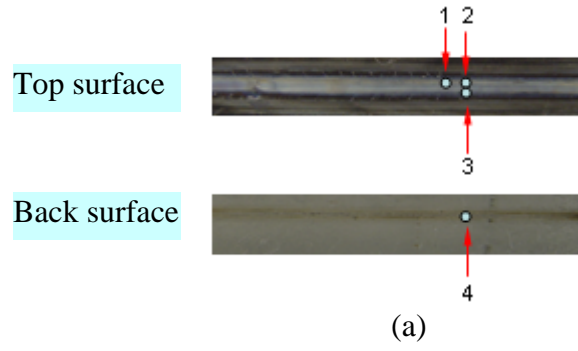
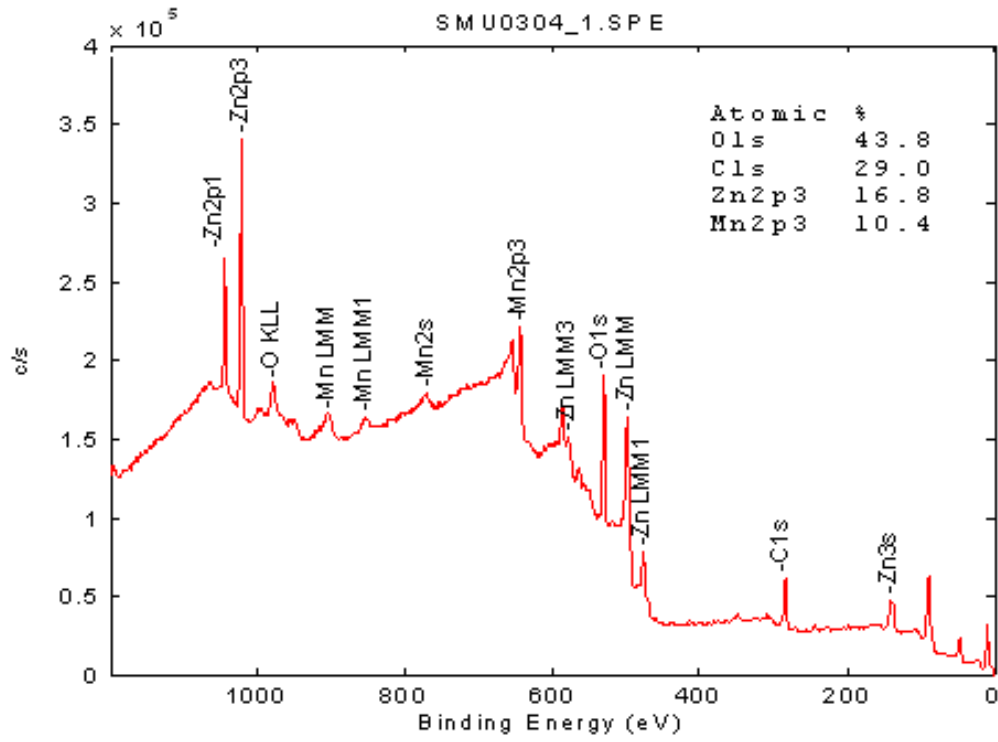


Figure 3.5 Top and back side views of preheated and welded metal sheets in gap-free lap joint configuration a) heat marks of preheated top surface b) heat marks of preheated back surface c) top view of the welded joint d) back view of the welded joint e) the cross-section view of the welded joint



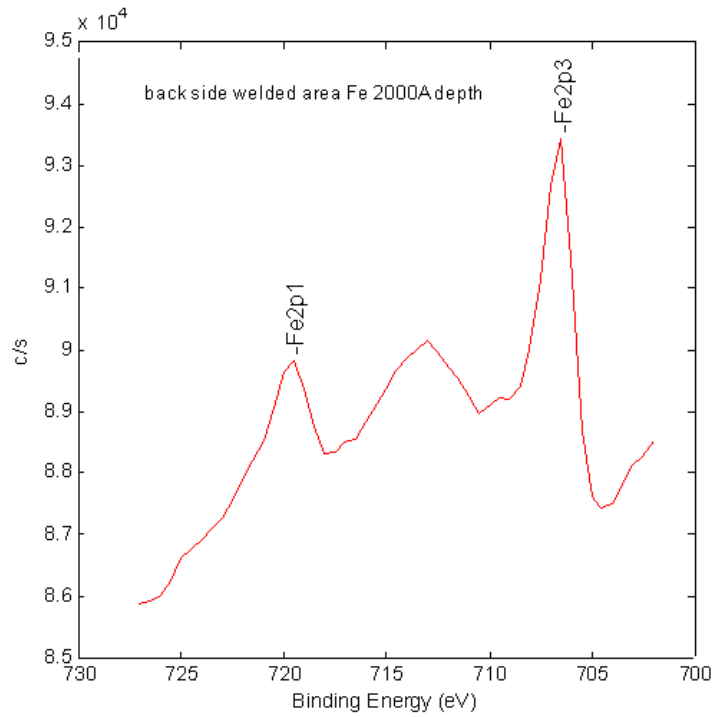
Atomic Concentration Table			
	C1s	O1s	Zn2P3
Point 1	18.98	47.67	33.35
Point 2	33.79	46.14	20.08
Point 3	19.27	50.33	30.40

(b)



Atomic Table	Concentration			
		C1s	O1s	Mn2p3
Point 4		29.02	43.75	10.39
				Zn2p3
				16.83

(c)



(d)

Figure 3.6 XPS analysis results of the heated surface of DP 980 galvanized steel by GTAW torch (a) the measured points (1-4) (b) the XPS analysis results on the top surface (c) the XPS analysis results on the interface (d) the XPS analysis of the backside area under 2000 angstrom (Preheated at the arc current of 200 A, welding speed of 30 mm/s, a thickness of 1.2 mm for the top metal sheet and a thickness of 1.5mm for the bottom metal sheet)



(a)



(b)



(c)

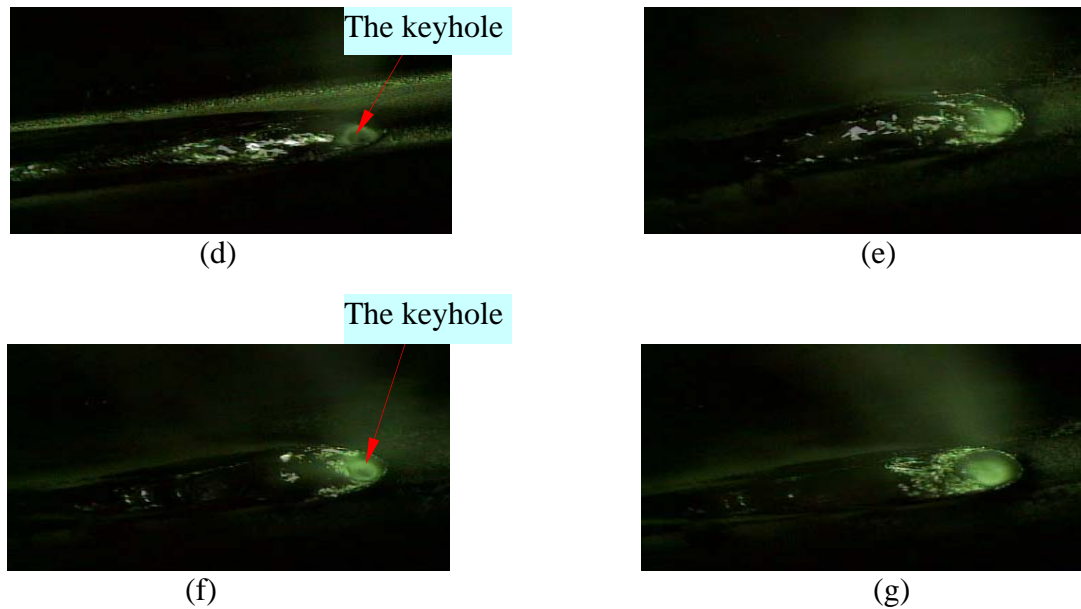


Figure 3.7 Shape of the molten pool for an instable welding process (a) the top view of the laser/GTAW weld (b) $t = 6.2$ s (collapsed) (c) $t=6.230$ s (collapsed) (d) $t= 6.270$ s (open) (e) $t=6.30$ s (collapsed) (e) $t=6.330$ s (open)(f) $t=6.370$ s (collapsed) (preheated at the arc current of 160 A, welded at the laser power of 3000 W and the preheating speed and welding speed of 30 mm/s)

3.3.2 The Influence of the Preheating Arc Current on the Weld Quality of Laser

During the GTAW preheating process, it is found that different chemical compositions are formed on the top surface of galvanized DP 980 steel. In order to investigate this phenomenon, a series of tests are carried out. The arc current is gradually increased from 100 A to 260 A with an interval of 20 A. Figure 3.8 shows the results of preheating under various arc currents with a constant traverse speed of 30 mm/s and a shielding gas flow rate of 30 SCFH. As shown in the Figure 3.9 (a)-(c), the top surface at the metal sheet is covered only by a thin layer of black soot when the arc current is below or equal to 140 A. For an arc current from 160 A to 220 A, there exist different colors of heat marks at the top surface, which indicate that various chemical compositions are produced during heating by the GTAW

torch. When the arc current is 240 A, a small hump forms at the top surface indicating that melting of top surface is occurring. When the arc current reaches 260 A, an excessive melting of the top surface is present causing the formation of humps. By directly observing the surfaces of the metal sheets along the interface, it is found that a portion of the zinc coating is melted and oxidized, as shown in Figure 3.9.

In order to study the influence of the GTAW arc currents on the weld quality, a 3000 W laser beam and a travel speed of 30 mm/s is used to weld the preheated samples in lap joint configuration. The weld quality differs among these laser welds, as shown in Figure 3.10. When the arc current is below or equal to 160 A, lots of spatters and blowholes are generated in the welds like in the laser welding process and the hybrid laser/arc welding process. Sound welds without spatters and blowholes are produced at the arc currents of 200 A, 220A, and 240A. With an arc current of 260 A, a sound weld is still obtained; however, the weld surface is not as smooth as in the welds obtained when the arc currents are 200 A, 220A and 240 A. Some of the ripples appeared in the weld zone of the non-uniform melt flow, caused by the presence of humping produced by the high arc current during preheating. The CCD video camera used to monitor the dynamics of the molten pool revealed that the keyhole was always present when the arc current was ranged from 180 A to 260A. However, the keyhole was not formed when the arc current was changed from 100 A to 160A. Based on the obtained results, it could be concluded that the presence of keyhole in laser welding of galvanized steels in a gap-free lap joint configuration will provide the conditions to achieve the weld of high quality. By

comparing the experimental results of laser welding of galvanized DP 980 steel without the zinc coating at the interface in Chapter 2, it could be concluded that the zinc oxides produced by the GTAW preheating process will significantly improve the coupling efficiency of the laser beam energy into the specimen. This will lead in turn to the sustained presence of the keyhole during laser welding.

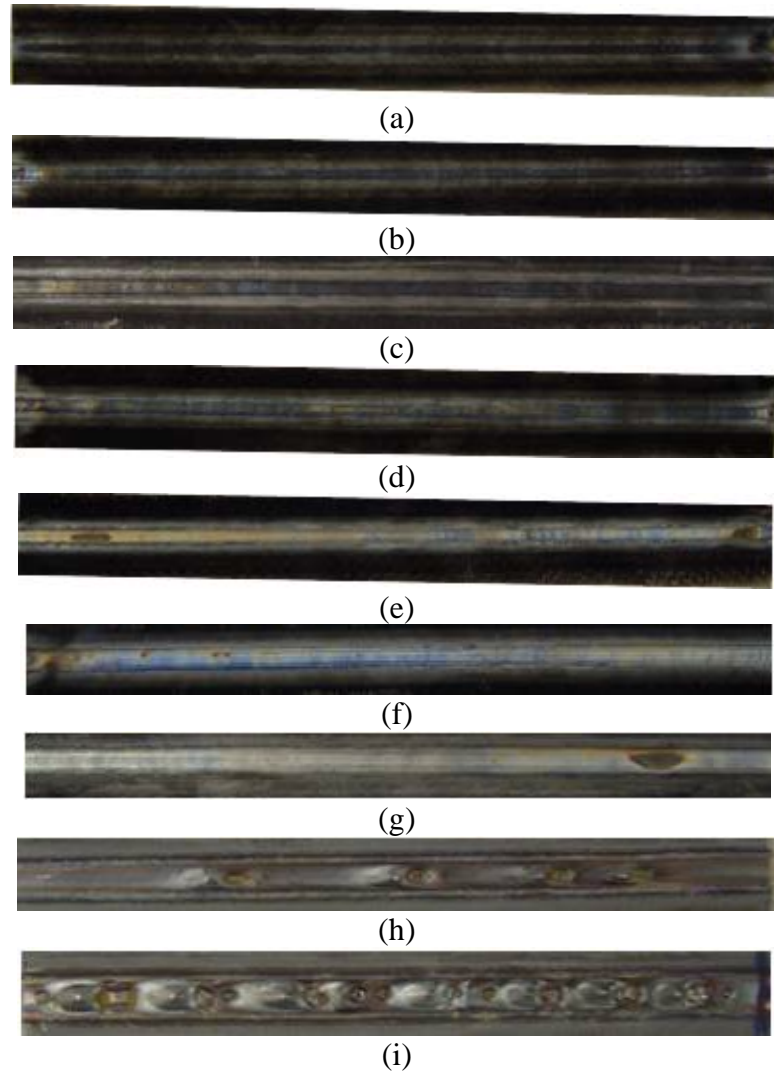
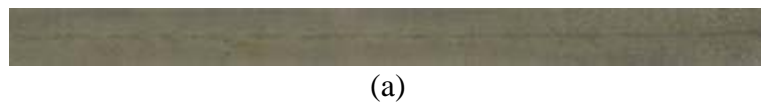


Figure 3.8 Effect of arc current on the chemical composition of the top surface of the preheating samples (a) arc current 100 A (b) arc current 120 A (c) arc current 140 A (d) arc current 160 A (e) arc current 180 A (f) arc current 200 A (g) arc current 220 A (h) arc current 240 A (i) arc current 260 A



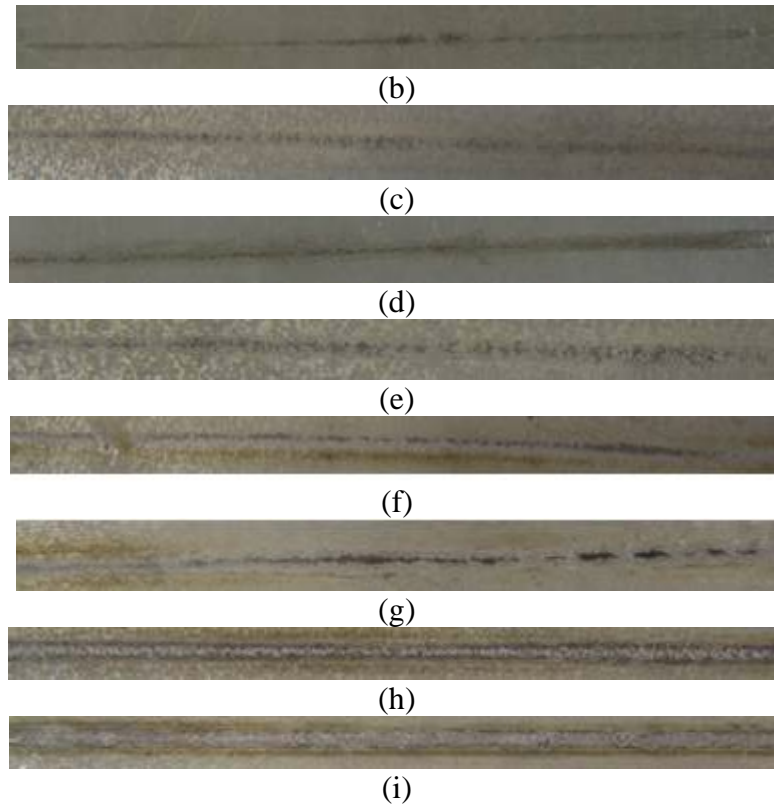
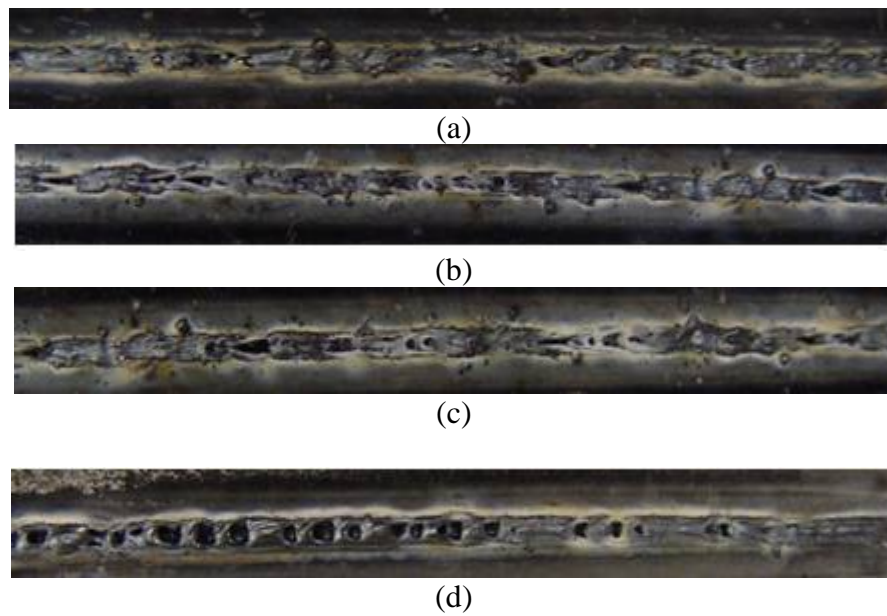


Figure 3.9 Back side of the preheating samples (a) arc current 100 A (b) arc current 120 A (c) arc current 140 A (d) arc current 160 A (e) arc current 180 A (f) arc current 200 A (g) arc current 220 A (h) arc current 240 A (i) arc current 260 A



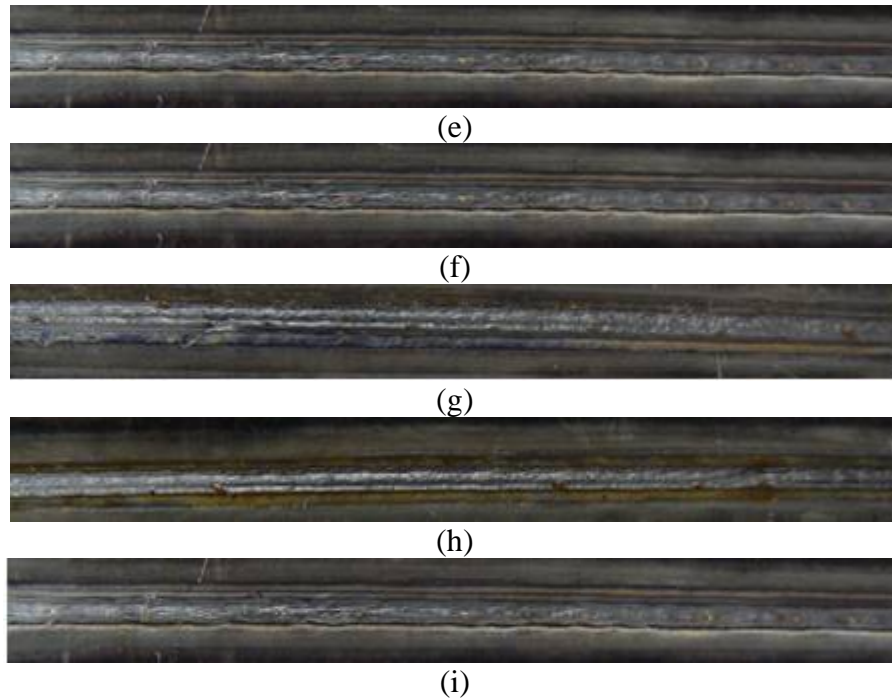


Figure 3.10 Effect of the preheating arc current on the weld quality obtained by laser (laser power of 3000 W and welding speed of 30 mm/s) (a) arc current 100 A (b) arc current 120 A (c) arc current 140 A (d) arc current 160 A (e) arc current 180 A (f) arc current 200 A (g) arc current 220 A (h) arc current 240 A (i) arc current 260 A

3.3.3 Study on the Dynamic Behaviors of the Molten Pool by Machine Vision

In order to study the mechanisms of the formation of weld defects during the laser welding and hybrid laser-GTAW welding of galvanized steels, the high speed CCD camera (4000 f/s) was applied to on-line monitor the dynamic behaviors of the molten pool. Figure 3.11 demonstrates the twelve consecutive images taken from the instable laser welding of galvanized steels in a gap-free lap joint configuration. As shown in the Figure 4.9, the fluid motion is significantly turbulent. Consequently, the shape of the molten pool is dramatically changed as a function of time. The instability of the laser welding or hybrid laser-GTAW welding of

galvanized steels in a common molten pool is mainly caused by the highly-pressurized zinc vapor developed at the interface of two metal sheets.

Usually, during laser welding process the driving forces for the liquid motion include the gravity force, the temperature-induced buoyancy force, and temperature-induced surface tension force as well as the recoil force. Among these forces, the major driving forces for the fluid flow motion are the surface tension force and the vapor-induced recoil force. For the laser keyhole welding or hybrid laser-GTAW welding of galvanized steels in a gap-free lap joint configuration, the recoil force becomes to dominate the other forces and mainly control the stability of the welding process due to the high level of the zinc vapor. Due to the instable coupling of laser beam energy into the welded material, the keyhole significantly fluctuates over time, which dramatically changes the direction of the zinc vapor and bends the keyhole. Thus, the fluid flow is swirling under the function of the tremendous recoil forces induced by the highly-pressurized zinc vapor. When the direction angle of the zinc vapor with respect to the normal of the workpiece is large, the welding process becomes very instable and the keyhole is collapsed and the highly-pressurized zinc vapor is expanded inside the molten pool. It is found that the larger the angle of the zinc vapor thrust direction with respect to the normal of workpiece, the more instable the welding process. As shown in Figure 3.11 (d)-(f), it can be seen that a large volume of the liquid metal in the rear part of the molten pool is ejected and spatially propagated by the recoil force (i.e tangential drag viscous force between the zinc vapor and the liquid metal layer around the keyhole). The liquid metal droplets are condensed in the air and deposited in or around the

weld zone by the gravity force. As a result, a large amount of spatters and blowholes are formed in the welds.

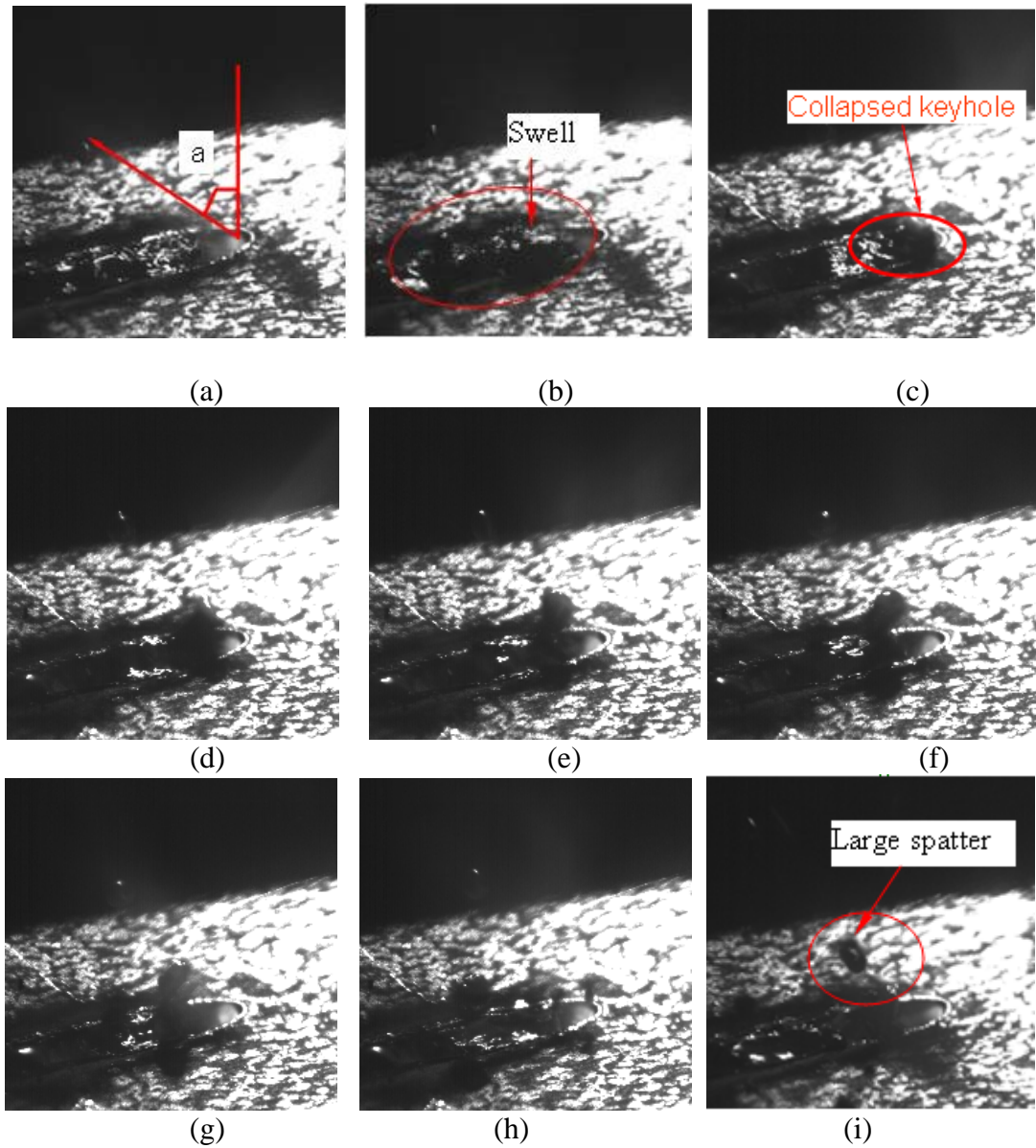


Figure 3.11 Images of the molten pool taken from the laser welding process of galvanized steels in a gap-free lap joint configuration (laser power: 3000 W; Welding speed: 50 mm/s)

Figure 3.12 shows the six consecutive images of the molten pool obtained by the CCD camera during the hybrid laser-GTAW welding of galvanized steels in a

gap-free lap joint configuration. By separating the laser beam and GTAW preheating process, the coupling of laser beam energy into the welded material is stable, which produces the stably open keyhole. Under this circumstance, the zinc vapor is stably vented out from the interface of two metal sheets; thus, the welding process is very stable and the fluid flow is stable. As shown in Figure 3.12, keyhole is kept open and the fluid flow motion is stable, which slightly vibrates along the weld penetration direction during the hybrid laser-GTAW welding process. Consequently, the sound lap joint is obtained.

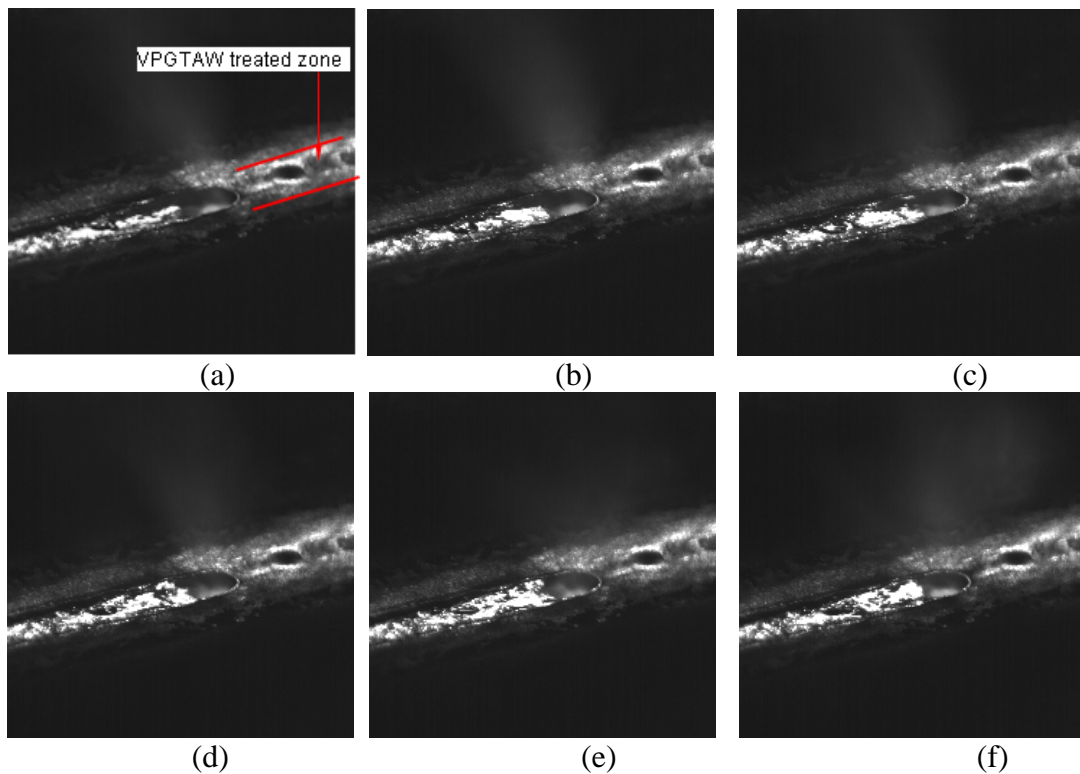
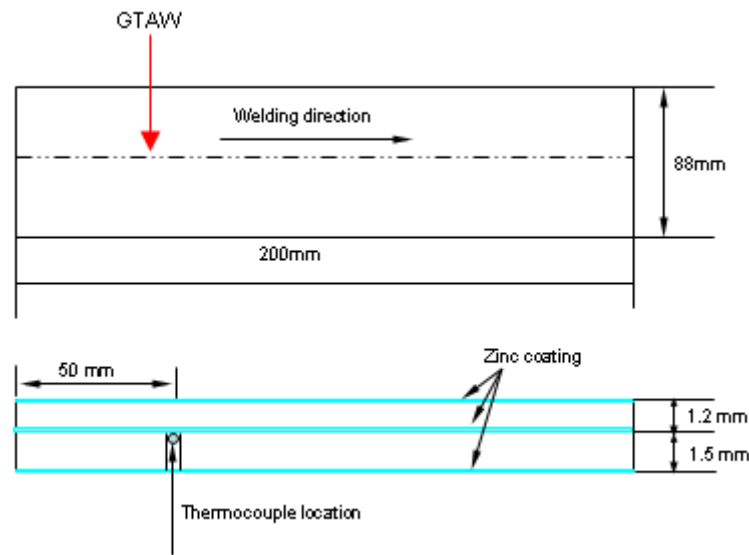


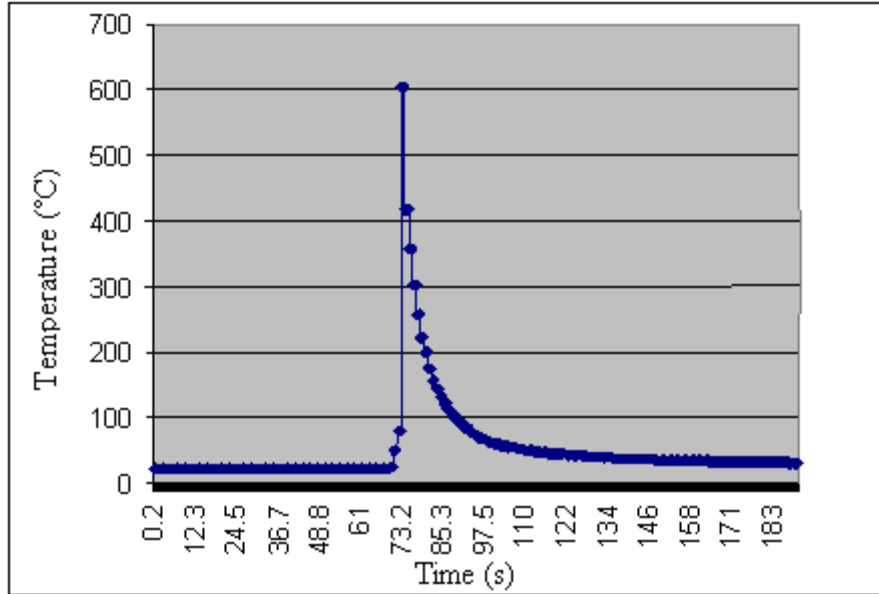
Figure 3.12 Images of the molten pool during the hybrid laser-GTAW welding process (laser power: 3000 W; the welding speed: 50 mm/s; the arc current: 300 A; the distance between laser beam and VPGTAW torch: 8 mm)

3.3.4 Temperature Measurement along the Interface of Two Galvanized Metal Sheets during GTAW Preheating Process

Figure 3.13 (a) shows the schematic of thermocouple location at the interface of two galvanized metal sheets. The temperature history at the designed point is shown in Figure 3.13 (b) with respect to arc current of 200 A and welding speed of 30 mm/s, respectively. As shown in the Figure 3.13 (b), the maximum temperature is 604°C, which is more than the melting temperature but lower than the boiling temperature of zinc. Furthermore, the arc current is varied in the range of 120 A to 260 A with the interval of 20 A. The results of measured temperature at the specified point are illustrated in the Figure 3.13. As shown in Figure 3.14, the maximum temperatures are all below the boiling temperature of zinc and they increased with the increase in arc current in this case.



(a)



(b)

Figure 3.13 (a) Temperature measurement along the interface of two galvanized metal sheets (b) Temperature history at the selected position

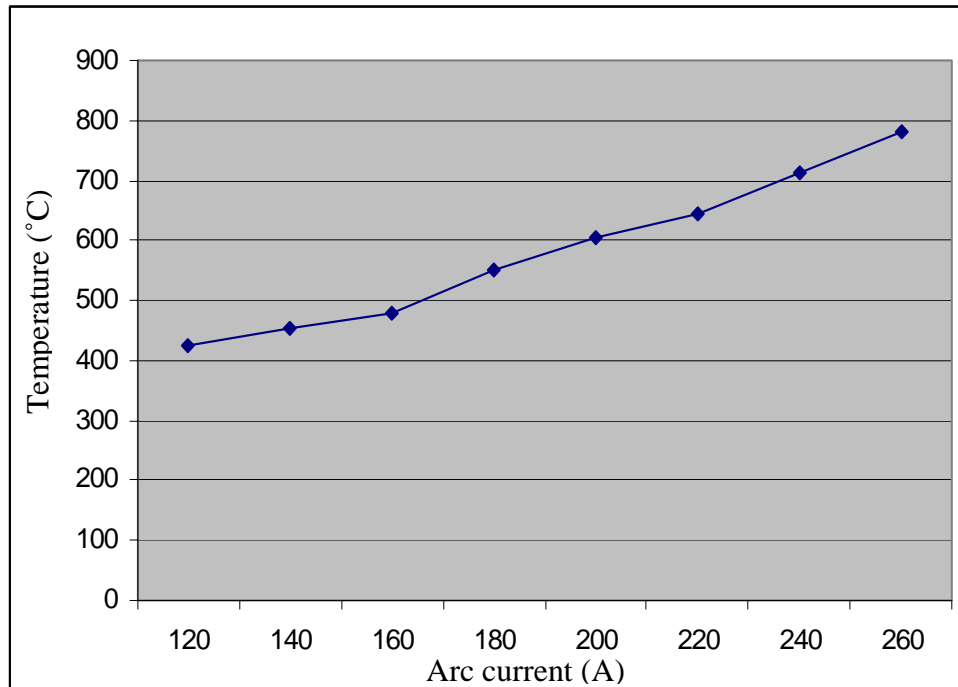


Figure 3.14 Effect of arc current on the maximum temperature at the interface of two galvanized metal sheets

3.3.5 Analyses of the Effect of the Welding Speed on the Quality of the Laser/GTAW Preheated Weld

As discussed in Chapter 2, the quality of the hybrid welded joints decreases with an increase in the welding speed. In order to investigate the influence of the welding speed on the weld quality of the laser/GTAW preheated welded joints, the welding speed is changed from 30 mm/s to 50 mm/s in increments of 5 mm/s while the laser power and the arc current are kept at 3000 W and 200 A, respectively. Figure 3.15 shows the experimental results. As shown in the Figure 3.15, the completely defect-free welds are achieved under welding speeds ranging from 30 mm/s to 50mm/s. The direct observation of the backside of the laser/GTAW preheated welds indicated that full penetration is achieved in all of these welds. Figure 3.15 (f) shows the cross-sectional view of the weld obtained at a welding speed of 50 mm/s. It looks like that the welding speeds in the range from 30 mm/s to 50 mm/s does not affect the weld quality. By comparing, the results of the laser welding process to the hybrid welding process analyzed in Chapter 2, a better weld quality is achievable under a higher welding speed if the preheating is done before the laser welding is performed.



(a)



(b)



(c)



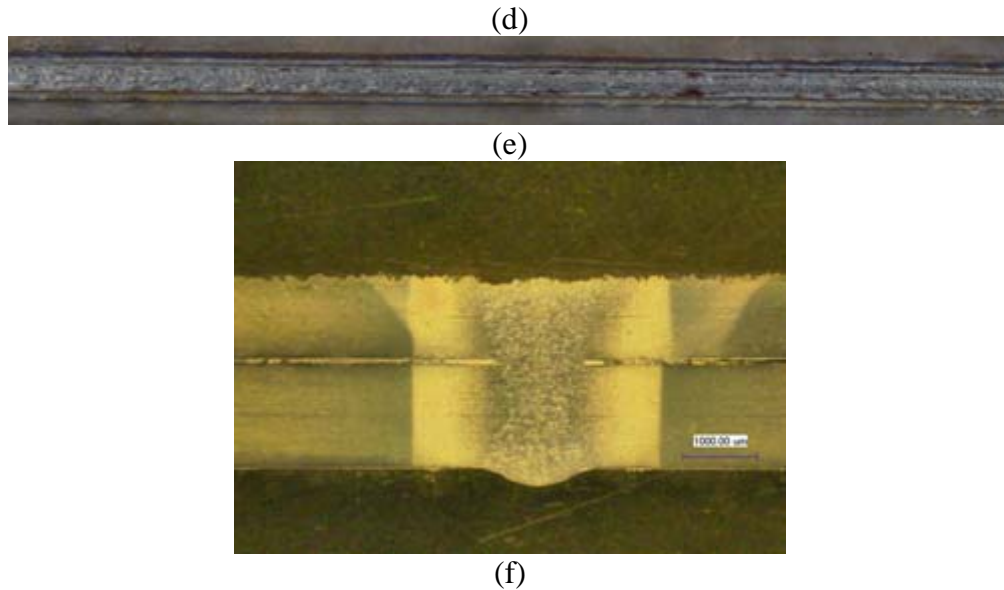


Figure 3.15 Effect of the welding speed on the weld quality (a) $v = 30$ mm/s (b) $v = 35$ mm/s (c) $v = 40$ mm/s (d) $v = 45$ mm/s (e) $v = 50$ mm/s (f) the cross-section view of the laser/GTAW preheated welds at a welding speed of 50 mm/s

3.4 Testing the Mechanical Properties of the Weld

3.4.1 Measurement of Microhardness of the Welds Obtained by Laser Welding of DP 980 Steel Treated by GTAW Heat

The microhardness distribution of the welds provides valuable information about the structural changes in the welded joint [124]. This distribution is also associated with the mechanical properties of the welded joints such as a failure location and the tensile strength. Microhardness of the weld bead is measured along the line indicated in Figure 3.15. The indenter load used in the microhardness test is 200g. The impressions are made in increments of 0.25 mm away from the interface of the two metal sheets as shown in the red line in the weld cross section. Figure 3.16 shows the micro-hardness profile across the cross-section of the weld. It can be seen that the hardness distribution is not uniform along the weld. The maximum

hardness value (426.2 HV) is located at the center of the weld. The minimum hardness value (195.1 HV) is found in the HAZ. As shown in the Figure 3.15, the HAZ has a lower hardness value than its values in the base metal and the welded zone, which indicates that the HAZ is softened. It can be seen that the hardness value in the fusion zone is relatively uniform [125].

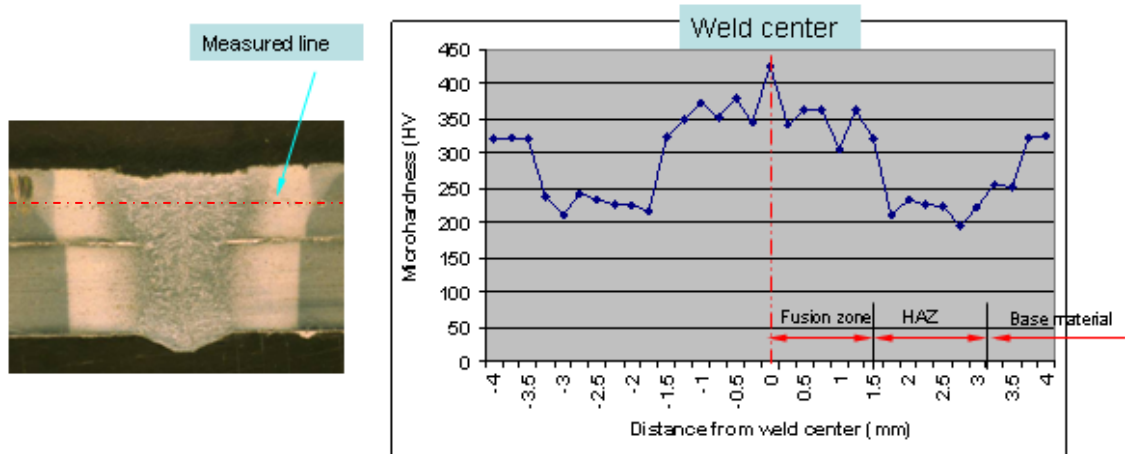


Figure 3.16 Vickers micro-hardness profile of a laser/GTAW preheated weld (the laser power of 3000 W, an arc current of 200 A and a welding speed of 30 mm/s)

3.4.2 Tensile Shear Testing of the Weld

In order to evaluate the strength of the welds and characterize the weld deformation, tensile shear tests are carried out. The specimen geometry is shown in Figure 3.17. Figure 3.18 demonstrates the experimental setup and the failure location in the weld. Table 3-2 gives the tensile shear test results for the laser/GTAW preheating welds under the welding speeds ranging from 30 mm/s to 50 mm/s. Figure 3.19 shows the relationship between the average tensile shear strength and the welding speed. It can be seen that with an increase of the welding

speed, the strength of the welds has a slight decrease then increases by a small value. However, the strength of the welds does not fluctuate in a wide range. Therefore, the welding speed does not show a significant influence on the welded joints strength.

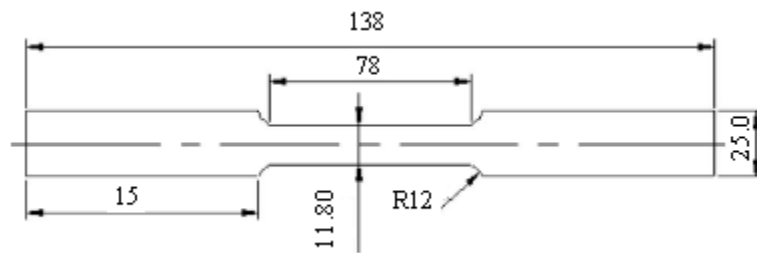


Figure3.17 Schematics of tensile shear test coupon



(a)



(b)

Figure 3.18 Tensile shear test experimental setup (a) and the test result (b)

Table 3-2 Tensile shear test results for the different welding speed

Welding speed (mm/s)	Sample No.	Width (mm)	Force (pounds)	Tensile Shear strength (N/m ²)
30	1-1	12.01	11076.08	808.98
	1-3	11.93	11120.56	817.68
	1-5	11.96	11387.45	835.20
35	2-1	11.95	11298.48	829.37
	2-3	12.01	11120.56	811.55
	2-5	11.93	11298.48	830.76
40	3-1	12.00	11209.52	819.41
	3-3	11.95	11120.56	816.31
	3-5	12.01	10497.80	766.74
45	4-1	11.99	10942.63	800.57
	4-3	11.99	10942.63	800.57
	4-5	12.00	10942.63	799.97
50	5-1	11.91	10942.63	805.94
	5-3	11.91	11298.48	832.15
	5-5	12.00	11031.59	806.40

(*The tensile strength of the base materials is 980 MPa)

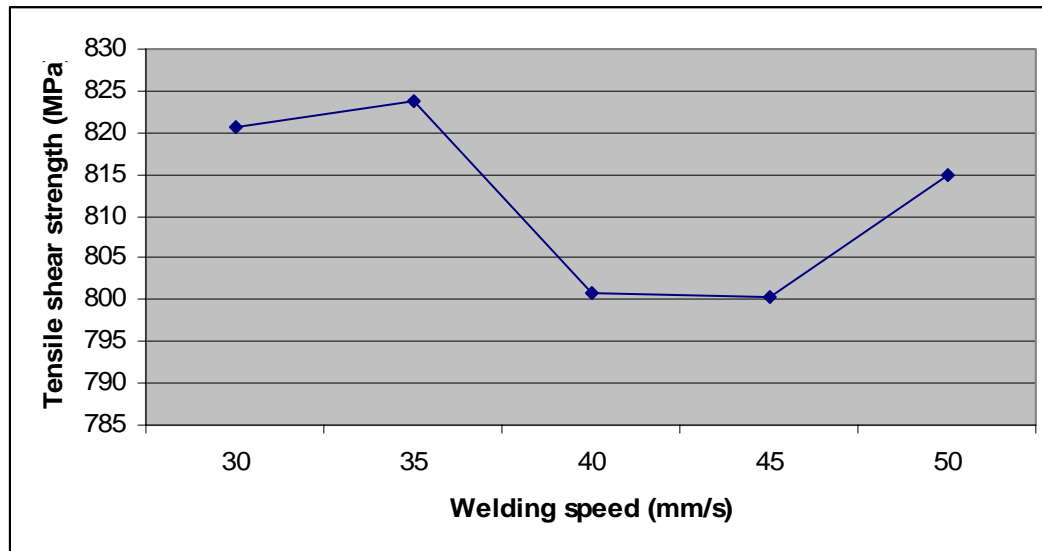


Figure 3.19 Relationship between the average tensile shear strength and the welding speed

3.5 Conclusions

By using the GTAW preheating process, a portion of the zinc coating on the top surface of the specimen is removed before the laser welding begins. This effect prevents the laser welding from the influence of the induced zinc plume in that the absorption efficiency of the laser beam energy for the material is improved. Moreover, a portion of the zinc coating at the top surface of the metal sheet is transformed into zinc oxide. This transformation significantly enhances the coupling efficiency of the laser beam energy into the specimen. Once the incident laser power intensity is beyond the threshold, the keyhole is formed. The uniform zinc oxide layer on the top surface of the specimens produced by the GTAW preheating welding process stabilizes the keyhole formation. The sustained presence of the keyhole allows the high-pressurized zinc vapor developed at the interface of the two metal sheets to escape from the molten pool. Therefore, spatters, blowholes and porosity are not produced during the welding process and sound welds are achieved. It is worth noting that the distance between the electrode torch and the laser beam has a crucial effect on the quality of the weld in laser welding. In addition, the recoil force determines the shape of the molten pool and the stability of welding process. It is found that the larger the angle of the zinc vapor thrust direct with respect to the normal of workpiece, the more instable the welding process.

Temperature measurement results confirm that the zinc coating at the interface of two metal sheets is partially melted. An extensive chemical analysis of the surface of the metal sheet was conducted. The main chemical composition produced

in the GTAW preheating process is zinc oxide. In addition, it is found that chemical compositions produced by different arc currents show the change in the coupling capacity of the laser beam energy as it enters the specimen. This difference in the chemical composition has a tremendous influence on the final weld quality. The micro-hardness profiles of the welded joints show that the HAZ is softened during the laser/GTAW preheated welding process. For the tensile shear test, the welded joints usually fail in the HAZ zone and the test results indicate that high strength is achieved in the welds. Additionally, it is shown that the welding speed has no significant effect on the weld strength.

Chapter 4

FEASIBILITY STUDY OF HYBRID LASER-VARIABLE GAS TUNGSTEN ARC WELDING OF GALVANIZED STEELS IN A GAP-FREE LAP JOINT CONFIGURATION

4.1 Introduction

In the previously studied hybrid laser-GTAW of galvanized steels in a lap joint configuration (see Chapter 3), it was found that arc current should be over 160 A for the welding speed of 30 mm/s, in order to completely burn out the zinc coating from the top surface of workpiece. The higher arc current is, the higher generated heat at the interface of the two metal sheets. The higher heat at the interface of the two metal sheets will increase the presence of the vaporized zinc. In order to decrease the presence of zinc vapor there is a need to separate the laser and GTAW torch for more than 100 mm. The larger distance between two heat sources limits the application of this hybrid welding process for automated welding of complex structures.

In order to shorten the distance between the laser beam and GTAW torch, the variable polarity gas tungsten arc welding (VPGTAW) is proposed as a preheating source combined with the laser beam to join the galvanized steels in a gap-free lap joint configuration. The VPGTAW has the capability of faster removal of the zinc coating from the top surface of workpiece with respect to the GTAW process.

Consequently, lower arc current will be required to remove the zinc coating on the top surface of workpiece. Since the heat input from the arc is reduced by the application of VPGTAW, the zinc vapor will be under less pressure and the distance between laser beam and VPGTAW torch will be shortened. Similar as in the case of using the GTAW torch as a preheating source process, the application of VPGTAW torch as a preheating source will form a thin layer of metal oxides on the top surface of the workpiece, which improves the coupling of laser beam energy into the welded material. In addition, effects of the key welding parameters on the weld quality of the lap joints are analyzed. Mechanical properties of the lap joint obtained by the hybrid L-VAPGTAW welding method are evaluated by the tensile shear test and Vicker's micro-hardness test. In this study, hybrid laser-VPGTAW where VPGTAW is used a preheating source welding is termed as hybrid L-VPGTAW welding.

4.2 Experimental Procedure

During the hybrid L-VPGTAW, the VPGTAW is used as a preheating source. The followed CW high power fiber laser (full power of 4 kW), which is delivered by an optical fiber of 400 μ m in diameter to the laser welding head, is used to join the galvanized DP 980 steel in a gap-free lap joint configuration. The focal length of the laser welding head is 200 mm. The dimensions of the top and bottom sheets are 150 mm X 60 mm X 1.2 mm and 150 mm X 60 mm X 1.5 mm, respectively. The 3.2-mm tungsten electrode is used for the VPGTAW torch. The stand-off distance of the electrode tip with respect to the top surface of the workpiece is 3mm.

The pure argon is used as the shielding gas with the flow rate of 30 SCFH. Electrode positive setting of 20% of each AC cycle is tested with a fixed frequency of 60 Hz. X-ray photoelectron spectroscopy (XPS) and energy-dispersive X-ray spectroscopy are used to analyze the chemical composition of the VPGTAW treated surface. Figure 4.1 shows the schematic setup for the hybrid L-VPGTAW welding process.

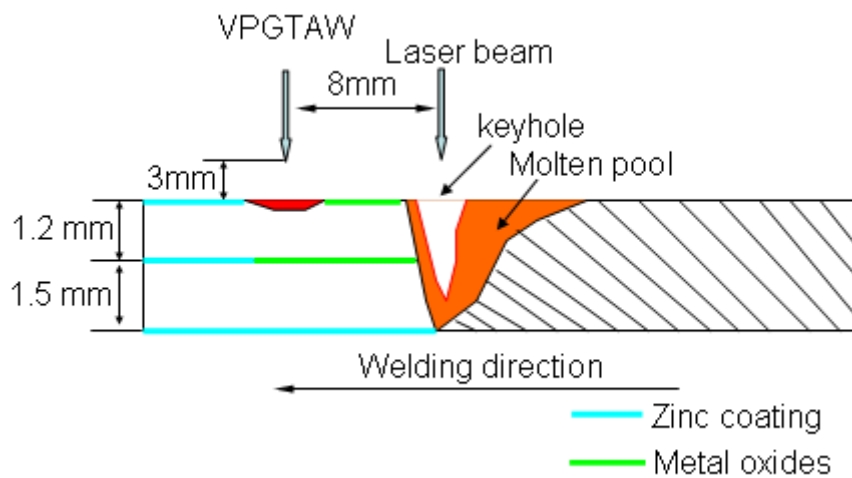


Figure 4.1 Schematic presentation of Hybrid L-VPGTAW experimental setup

4.3 Advantages of hybrid L-VPGTAW Welding of Galvanized Steels in a Gap-Free Lap Joint Configuration with the Separate Molten Pool

The main advantage of hybrid L-VPGTAW welding of galvanized steels over the hybrid Laser-GTAW where GTAW torch is used as a preheating source of galvanized steels in a gap-free lap joint configuration is the fast removal of the zinc coating at the top surface of workpiece and formation of a thin layer of metal oxides at the top surface of the workpiece under a relatively low current. In addition, the heat input into the welded material can be controlled by adjusting the VPGTAW

parameters such as the use of different amplitude and duration of arc current in direct current electrode positive (DCEP) and direct current electrode negative (DCEN) period. The heat treated top surface of the workpiece will improve the coupling of the laser beam into the welded material that will result in the formation of stable keyhole, through which the zinc vapor will be vented out.

4.3.1 Fast removal of the Zinc Coating on the Top Surface of Metal Sheets

As discussed in the Chapter 3, a large volume of zinc plume and plasma are generated directly on the top surface of the workpiece due to the very low first ionization potential and the boiling point of zinc (9.3941 eV and 906°C, respectively). If the zinc coating at the top surface of the workpiece does not be completely removed and the thin layer of metal oxides is not formed at the top surface and interface of workpiece, the good quality lap welds can not be achieved. In order to remove the zinc coating prior to the laser welding process, there is a requirement of the minimum value of the GTAW arc current corresponding to the specific welding speed during the GTAW preheating process. Furthermore, the distance between the laser beam and GTAW torch should be kept at a relatively large distance in order to provide enough time to cool down the zinc vapor at the interface of two metal sheets. In order to shorten the distance between the laser beam and GTAW torch, the heat input from the arc into the welded material should be reduced.

It is found that the zinc coating at the top surface of workpiece can be removed by using the VPGTAW as the preheating source under a relatively low arc current

with respect to the GTAW preheating process. The effect of VPGTAW as a preheating source on the removal of zinc coating at the top surface is compared with respect to that of GTAW as a preheating source under the following welding conditions: (1) GTAW arc current: 240 A; welding speed: 50 mm/s (2) VPGTAW arc current: 240 A; 20% DCEP; and welding speed: 50 mm/s. In the case of GTAW as a preheating source, the arc current of 240 A can not completely remove the zinc coating at the top surface of the workpiece and only the soot is produced at the top surface of the workpiece, as shown in Figure 4.2 (a). However, by using the VPGTAW torch as a preheating source with the same level of the arc current but with 20% DCEP the zinc coating is removed completely, as shown in Figure 4.2 (b). The complete removal of zinc coating will open up the top surface for the formation of metal oxides.

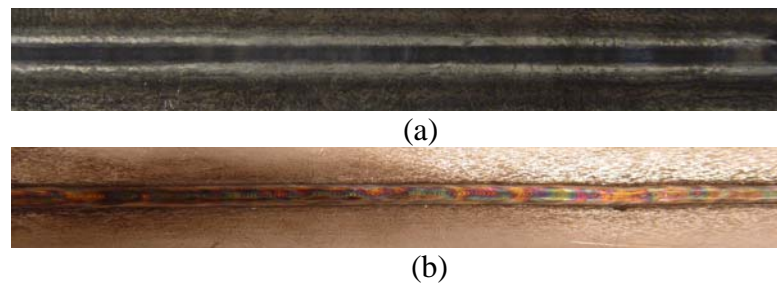


Figure 4.2 Comparison of the treated surface for GTAW and VPGTAW as a preheating sources (a) GTAW; arc current: 240 A; welding speed: 50mm/s; (b) VPGTAW; arc current: 240 A; welding speed: 50mm/s; DCEP percentage: 20%;

Figure 4.3 shows the images of the treated top surfaces of the galvanized steel by GTAW and VPGTAW as the preheating sources, which are acquired by the high speed CCD camera with the assistance of illumination by the green laser (532 nm).

As shown in Figure 4.3, it can be clearly seen that the larger area of zinc coating is removed by the VPGTAW and a shallow molten pool is formed during the VPGTAW preheating process. In contrast, the zinc coating is almost not removed by the GTAW under the same level of arc current. The reason for the fast removal of zinc coating by the VPGTAW as preheating source may be contributed by the formation of “cathode spots”. The formation of the “cathode spots” in DCEP GTAW is connected to the removal of metal oxides from the treated surface [136]. It is understood that these small spots have a very high energy flux density in a very small emission zone, which quickly and superficially heats and evaporates the zinc coating [137]. In contrast, when GTAW is used as a preheating source the arc is in the contact with the zinc coating at the top surface of the workpiece along a relatively large area that will result in the decrease of the energy flux density, as shown in Figure 4.3 (a). During the leading VPGTAW preheating process, a jet of vapor was observed to be blown away from the top surface of the workpiece while this is not observed during the GTAW as a preheating source. The cathode jets carry away the zinc vapor from the cathode layer with a high velocity. Thus, the evaporation of the zinc layer is intensive in the VPGTAW. This observation agrees with the formation of cathode spots on the zinc layer during DCEP VPGTAW as a preheating source process because high-velocity vapor jets are directly associated with the formation of cathode spots on non-thermionic materials (with velocities as high as $10^3 m/sec$) [137-138]. As shown in Figure 4.3 (b), the cathode cleaning area of the zinc coating on the top surface of metal sheets is mainly distributed

around the shallow molten pool, which is slightly wider than the fusion zone obtained by the followed laser beam.

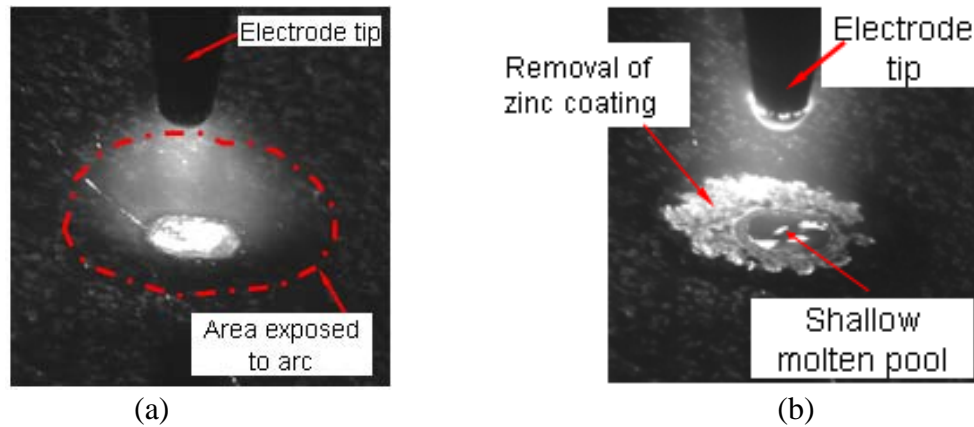


Figure 4.3 Comparison of the removal rate of zinc coating by GTAW and DCEP VPGTAW as a preheating source (a) GTAW; arc current: 240 A; (b) VPGTAW; arc current: 240 A; 20% DCEP

4.3.2 Oxidizing the Metal Sheets along the Weld Line

As mentioned previously, after the VPGTAW remove the zinc coating at the top surface of metal sheets and moves forward, the heated surface comes in the contact with the air and a thin layer of metal oxides is formed on the top surface. In addition, the surface along the weld line at the top surface of workpiece is roughened by the VPGTAW preheating. The surface roughness is directly related to the preheating current, which will proportionally decrease with the increase in the arc current density [139]. The formation of the oxides, roughening the surface of the welded material as well as the removal of the zinc coating by the VPGTAW can dramatically increase the coupling of laser beam energy into the workpiece.

4.3.3 Controllable Heat Input into the Welded Material

When using GTAW to preheat the workpiece, the large amount of high energy electrons is released toward the top surface of the workpiece [127]. This released energy from the emitted electrons will result in the transfer of more energy into the workpiece; thus generating the high temperature in the welded material. In contrast, some of heat can be deposited at the electrode tip by changing the polarity of arc current when using the VPGTAW as a preheating source. In the VPGTAW as a power source, the duration and the intensity of the DCEN and DCEP can be adjusted in order to control the heat distribution between the top surface of the workpiece and the electrode tip [140]. Through switching the arc preheating mode from the DCEN polarity to DCEP polarity of GTAW combined with the optimal setting of the other welding parameters, it is possible to dramatically reduce the heat into the welded materials. Consequently, the pressure level of zinc vapor at the interface of two metal sheets will be decreased. Figure 4.4 presents the typical variable polarity current waveform.

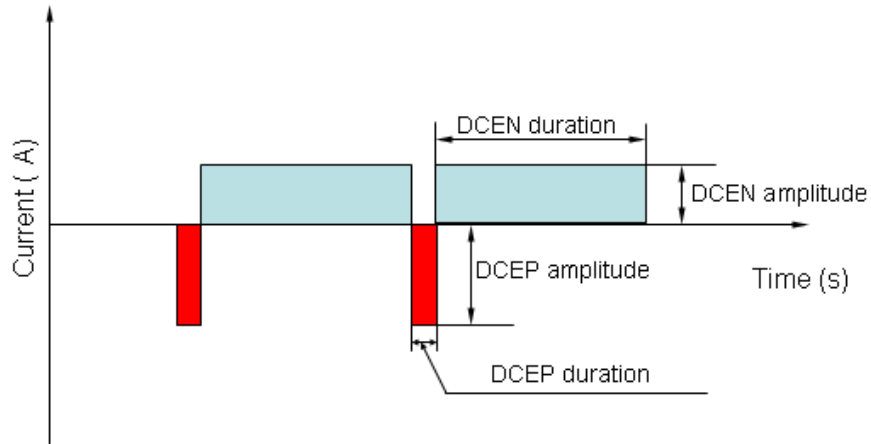


Figure 4.4 Schematic presentation of the typical variable polarity current waveform

4.4 Results and Discussions

4.4.1 The hybrid L-VPGTAW Lap Joint

Figures 4.5 (a)-(c) present the top views of welds obtained by only laser welding, hybrid laser-GTAW as a preheating source and hybrid laser-VPGTAW with 20% DCEP as a preheating source. As shown in Figure 4.5 (a), a large amount of spatters and blowholes are produced in the welds obtained only by the laser beam due to the ejection of a large amount of liquid metal from the molten pool by the highly-pressurized zinc vapor. The weld defects are dramatically suppressed by applying the hybrid laser-GTAW where GTAW torch is used as a preheating source, as shown in Figure 4.5 (b). However, several spatters and blowholes are still produced in the welds during hybrid laser-GTAW process. For the welding speed of 50 mm/s, there is a minimum requirement of arc current 300 A to remove the zinc coating at the top surface of the workpiece and the optimal distance between the laser beam and the GTAW torch is 16 mm with the cooling of the lateral shielding gas. By using the hybrid L-VPGTAW welding procedure with DCEP of 20%, the

spatters were completely eliminated and the completely defect-free weld with a full penetration was obtained under a relative low arc current, as shown in Figure 4.5 (c) and (d). The selected distance between the laser beam and the GTAW torch is only 8 mm under the same level of the arc current and the welding speed as in the case of hybrid laser-GTAW. The distance of 8 mm will separate two heat sources and avoid the instable interaction between laser beam and arc that is the cause of the poor quality weld. From one side, it is possible to shorten the distance between laser beam and GTAW preheating torch by the adjustment of the heat input from the arc source into the welded material and obtain the sound lap joint of galvanized steels. From the other side, the short distance will provide the condition of assembling the laser head with the VPGTAW torch in much more compact assembly that could be attached at the robot arm.

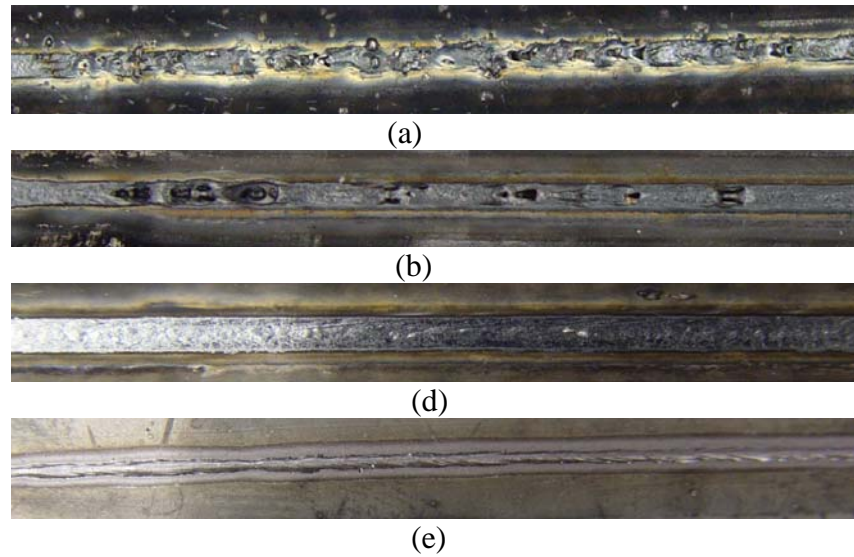
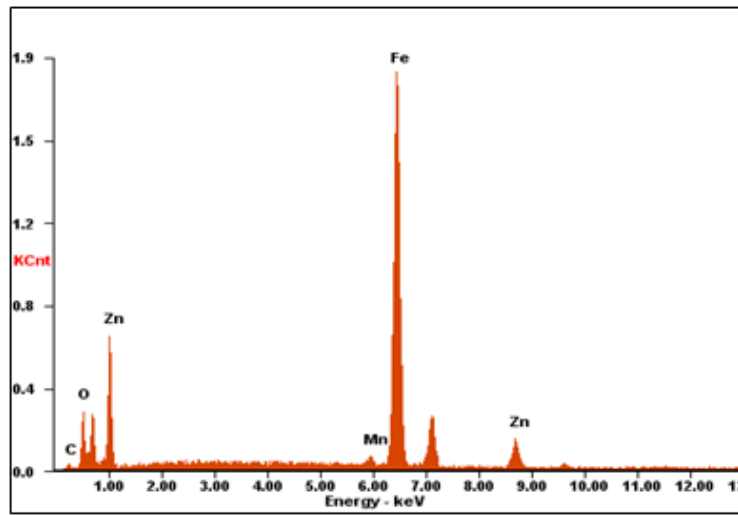


Figure 4.5 Top views of welds obtained by (a) only laser (b) hybrid laser-arc welded lap joint with DEC (c) Top view of hybrid L-VPGTAW with 20% DCEP (d) Back view of hybrid L-VPGTAW with 20% DCEP (laser power: 3000 W; the welding speed: 50 mm/s; the arc current: 240 A; the distance between laser beam and GTAW torch: 8 mm; the distance between laser beam and VPGTAW torch: 8 mm; DCEP percentage: 20%)

4.4.2 Surface Analysis of the VPGTAW Preheating Welds by XPS and EDS

XPS was used to measure the chemical composition on the top surface preheated by VPGTAW. Figure 4.6 shows the typical XPS measurement results of the top surface of the preheated top surface by the VPGTAW. In XPS, the peaks denote the core level of chemical elements where the photoelectron is excited and ejected. As shown in Figure 4.7, a strong oxygen peak (O1s: 531.0 eV) is presented, which indicates that the preheated top surface is covered by oxides. Furthermore, the binding energy of 711.2 eV for the Fe 2p₃ main peak is also observed, which is consistent with the typical values for the iron oxides revealed in the open literatures ($\alpha - Fe_2O_3$: 710.9 eV; $\gamma - Fe_2O_3$: 710.7 eV; Fe_3O_4 : 710.8 eV; FeO :) [139-133]. In addition to the O1s and Fe 2p₃, the binding energy of 1022.9



(a)

<i>Element</i>	<i>Wt%</i>	<i>At%</i>
<i>CK</i>	04.92	16.60
<i>OK</i>	08.68	21.99
<i>MnK</i>	01.65	01.22
<i>FeK</i>	72.82	52.81
<i>ZnK</i>	11.92	07.39
<i>Matrix</i>	Correction	ZAF

(b)

Figure 4.7 EDS analysis result of the top surface of the preheated top surface by VPGTAW (a) EDS spectra (b) wt% and At% of chemical elements

4.4.3 Influences of VPGTAW Preheating Parameters

The removal of the zinc coating at the top surface is influenced by the VPGTAW preheating parameters, including the level of preheating arc current, the stand-off distance between the VPGTAW torch tip and the top surface of the metal sheet, the angle of the tip, the DCEP percentage and frequency of the AC arc current as well as the welding speed. Among all these VPGTAW parameters, the VPGTAW arc current is the most critical one, which should be selected with the

respect to the welding speed (the same as the laser welding speed since the laser welding process and the VPGTAW preheating process are synchronously conducted.). The higher welding speed will required, more heat input during preheating is. If the VPGTAW arc is below a threshold, the zinc coating can not be completely removed at the top surface and the amount of metal oxides at the top surface will be drastically lowered. The surface roughness and the removal rate of the zinc coating on the top surface are influenced by the arc current density at the cathode spot [139]. In addition, the relatively low VPGTAW preheating arc current has no capability of transforming the zinc coating at the interface of two metal sheets into the zinc oxides.

4.4.4 Studying the Effects of Laser Welding Parameters

Experimental results have shown that the stable keyhole is the decisive factor to guarantee the sound lap joint of galvanized steels in a gap-free configuration. The welding process of galvanized steels in a gap-free lap joint configuration is very sensitive to the variations of the welding parameters, which is directly related to the stability of the keyhole [126]. In order to maintain the open keyhole, the welding parameters should be optimal. Among the laser welding parameters, laser power is the most important, which should be sufficient enough to generate the keyhole for venting out the highly-pressurized zinc vapor from the interface of two metal sheets as well as to provide the required depth of weld. It is worth noting that for a specific welding speed, high laser power may lead to high heat input into the welded materials, which can form the burn through holes into the welded material. The high

heat will also increase the pressure of the zinc vapor. As a consequence, a large amount of the spatters and blowholes will be produced during the hybrid laser-VPGTAW welding process. Furthermore, it should be kept in mind that there is a minimum distance between laser beam and VPGTAW torch in order to avoid formation of the common molten pool. When this distance is under the threshold value, the welding process is becoming significantly instable like in the case of a laser welding of galvanized steels in a gap-free lap joint configuration (See Chapter 2).

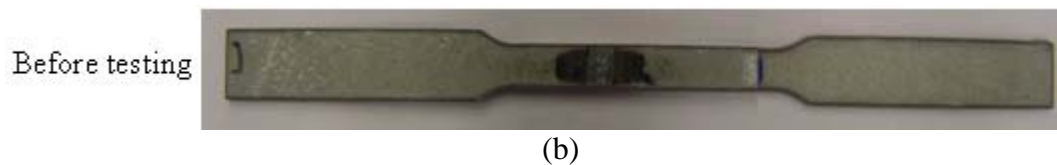
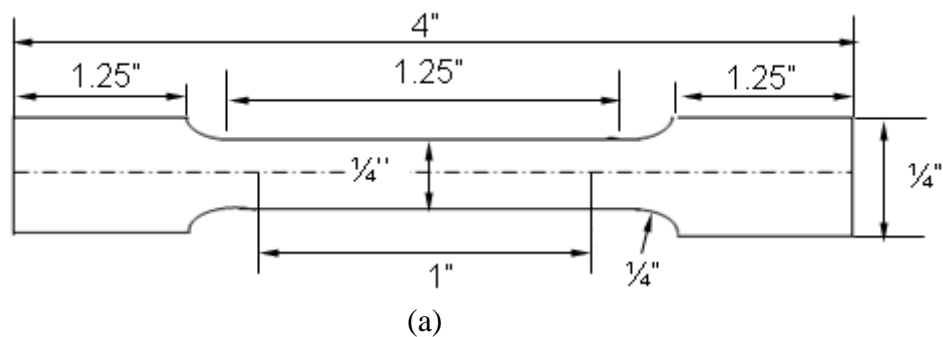
For the specific laser power, high welding speed may leads to the collapse of the keyhole, which will result in the instable process [141]. Consequently, the weld defects will be generated in the welds. In addition, the focus location of laser power and the angle of incident laser beam also determine the laser beam energy into the welded material.

4.4.5 Mechanical Properties of the Welds

The tensile shear test was carried out to evaluate the strength of the hybrid laser-VPGTAW welded lap joints. Figure 4.8 demonstrates the tensile shear test procedure recommended by ASTM standard. The experimental results have demonstrated that most of the tested coupons are broken in the HAZ instead of in the base material (the number of the tested samples: 16). Only two specimens are broken in the weld fusion zone. The welding was performed with the welding speed of 50 mm/s and laser power of 3 kW as well as the VPGTAW preheating arc current 240 A . The mean value of the tensile shear strength is around 820 MPa,

which is slightly lower than that of the base DP 980 steel (980 MPa). The tensile shear test results confirmed the fact that the HAZ is softened during the welding process.

In order to determine the hardness distribution profiles along the weld zone and heat affected zone, Vicker's micro-hardness measurement is used. The indenter load used in the microhardness test is 200 g. The impressions are made in the increment of 0.25 mm away from the interface of the two metal sheets. Figure 4.9 shows the typical cross-sectional profile of the lap joint obtained by hybrid L-VPGTAW. As can be seen in Figure 4.9 (b), the hardness distribution is not uniform along the weld. The hardness distribution is relatively uniform across the weld bead. However, the hardness value begins to gradually decrease in the HAZ. The maximum hardness value (388.9 HV) is located close to the center of the weld. The minimum hardness value (197 HV) is found in the HAZ region. The degradation of the hardness in the HAZ has the weakening effect on the mechanical properties of the obtained joint.





(c)

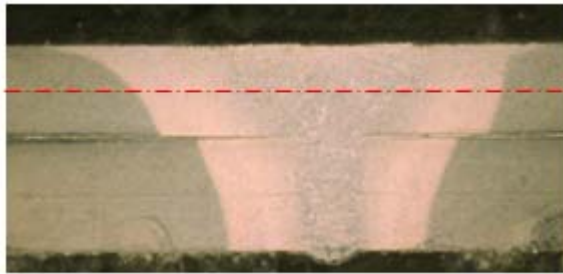
Fractured in the HAZ

After testing

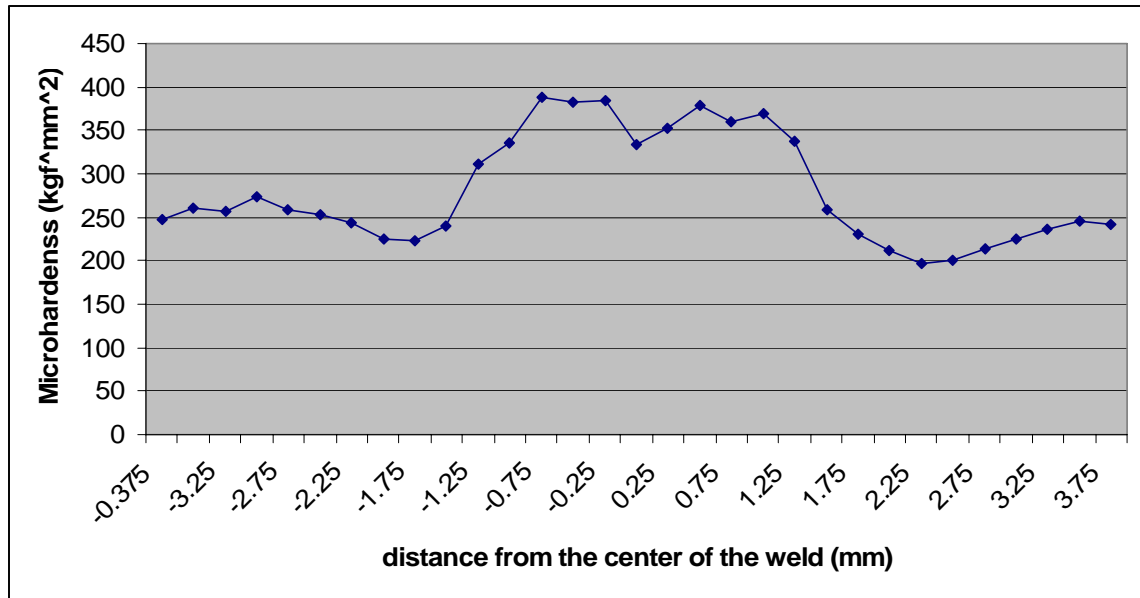


(d)

Figure 4.8 Tensile shear test (a) schematic of tensile shear test coupon (b) the shape of test coupon; (c) experimental setup; and (d) fracture location of the hybrid laser-VPGTAW welds (laser power: 3000 W;Welding speed: 50 mm/s; VPGTAW arc current: 240 A; DCEP: 20%)



(a)



(b)

Figure 4.9 the hardness distribution profiles of hybrid L-VPGTAW lap joint along the weld zone and heat affected zone

4.5 Conclusions

With the use of the proposed hybrid L-VPGTAW welding procedure, a high quality weld of galvanized steels in a gap free configuration can be achieved. Based on the experimental results, the main conclusions can be drawn as the follows:

1. The zinc coating at the top surface of the metal sheet is removed by the DCEP VPGTAW preheating process under a lower arc current with respect to the GTAW used as a preheating source. At the same time, a thin layer of metal oxides are generated on the top surface of metal sheet and the zinc coating along the weld zone.
2. The generated metal oxides and the roughened top surface of the metal sheet will contribute to the better coupling of the laser beam energy into the welded

material. Under these circumstances, the keyhole is readily formed and is maintained open. The open keyhole allows the highly-pressurized zinc vapor to be vented out. The completely defect-free lap joints have been obtained in a gap-free configuration. More importantly, the distance between laser beam and VPGTAW torch is dramatically shorten by lowering the heat input into the welded material from the VPGTAW torch. This will allow to assembly the laser welding head with the VPGTAW torch in more compact unit that will be easily attached at the robot arm for welding more complex 3D structures.

Chapter 5

MONITORING OF THE WELDING PROCESS

5.1 Introduction

In the past, most efforts were focused on finding the optimal welding procedure to weld galvanized steels in a gap-free lap joint configuration. On-line monitoring of the welding process of galvanized steels can provide a better understanding of the mechanisms that form weld defects. However, there are only a few reports published on monitoring the laser welding process of galvanized steels in gap-free lap joint configuration [190-192]. In addition, the effects of the zinc coating at the top surface of the top plate and the presence of gap on the dynamic behaviors of the molten pool during the welding process of galvanized steels are not revealed in the open literature. A direct image of the molten pool surface is a direct and powerful way to identify the dynamic behaviors of the molten pool and the primary mechanism for identifying the formation of weld defects that occur during the welding process. In this study, a machine vision system based on a high-frame rate infrared CCD camera and acoustic emission techniques is used to capture the images of the bright spot on-line at the front of the molten pool and record the AE signals from the welding process. Then, a set of image processing algorithms are used to eliminate the noises i.e laser-induced plume and spatters from the captured images. After applying the image processing algorithms to the captured images, the

background and the bright spot at the front of the molten pool area are clearly separated from each other. Furthermore, the length of the major axis of the bright spot at front of the molten pool is calculated on-line to monitor the stability of the laser welding process of galvanized steels. Three sets of tests are conducted to reveal the effects of (1) the zinc coating at the top surface, (2) GTAW torch preheating (3) the presence of gap on the dynamic behaviors of the molten pool in details.

5.2 State-of-the-art Monitoring of the Welding Process by Machine Vision and the AE Technique

5.2.1 State-of-the-Art Monitoring of the Welding Process by Machine Vision

In the past, different sensors have been used to monitor the various welding processes. Among these sensors, machine vision is considered to be the most powerful tool for real-time monitoring the welding process. It has been used in weld seam tracking [142-143], the control of weld penetration [144-147], the extraction of the weld pool characteristics [148-151], the dynamic feedback and control of the weld bead geometry [152], and gap inspection [153]. Xu et al. [142] used a circular laser scanner with an area-array charge-coupled device (CCD) camera in the welding robot system to track the weld seam. Based on the acquired front image signal of the weld pool, a real-time closed-loop feedback control system was developed to control the weld penetration in variable polarity plasma arc welding (VPPAW) of aluminum alloys [145]. Saeed et al. [151] used a CCD camera assisted by structured light to extract the molten pool surface features. Holbert et al. [147] applied a CCD camera to monitor weld penetration during the CO₂ laser welding

process. Wang et al. [150] acquired the images of the molten pool; the area of the molten pool was extracted by the designed image processing algorithm. Kovacevic et al. [152] combined a high-frame rate CCD camera with a nitrogen laser as an illumination source to acquire the images of the molten pool from the GTA welding process. Based on the proposed image processing algorithm, the pool boundary was detected and used for controlling the welding process. So far, there is still no report in the open literature on the monitoring of the weld defects formation by machine vision for the laser welding or hybrid welding process of galvanized steels in lap-joint configuration. In laser butt joint, it usually takes a long time to align the focused laser beam with the welding gap because of the very small gap size. Jeng et al [153] employed a CCD camera and several image processing techniques to track the weld seam and calculate the welding gap size. It was illustrated in his study that the gap size can be inspected and an accurate alignment between the laser beam and weld gap can be achieved based on the information obtained from the machine vision system.

Furthermore, in order to better understand the welding phenomena, some efforts have been made to investigate the underlying mechanisms of the welding process by using machine vision [154-155]. Chen et al. [154] used a video CCD camera with a maximum frame rate of 50 frames per second to record the images of arc plasma and laser induced plume to investigate the effect of the welding parameters on the weld characteristics in the hybrid laser/arc welding of 4mm thick AISI 321 stainless steel. It was found that different weld characteristics under various welding conditions are reflected by different types of arc shape. When the

welding process is under the deep penetration mechanism, the root of arc is compressed. However, the arc is expanded quickly when the welding process is switched from the deep penetration mode to the heat conduction mode because of the absorption or defocus of the laser beam by an increase in the arc current. Natio et al. [155] employed a CCD camera with the sample time of 1/30s and a high-speed camera with a maximum frame rate up to 40,500 frames per second (fs) to study the behavior of the keyhole, the molten material flow and the mechanism for porosity formation. It was found that the reduced number of porosity formations in hybrid welding is attributed to the stable molten material in comparison to the instable material to which porosity is attributed in the laser welding.

5.2.2 State-of-the-Art Monitoring of the Welding Process by the AE Technique

The AE technique, one of the most powerful monitoring techniques, can detect the presence generation of any released transient elastic stress in the material and its wave propagation by using a piezoelectric sensor that is directly mounted on the surface of the metal sample [156]. The released elastic stress produces small displacements on the surface of the metal sample that are converted by the AE sensor into the electrical signals. The signals can be collected on-line by the AE acquisition system to monitor the undergoing changes in the different manufacturing processes [157-160].

So far, AE techniques have been applied to monitor different manufacturing processes such as the machining processes, the cutting processes and the welding processes [161-163]. To monitor the crack growth in stainless steel welds, the AE

technique was used by Jolly [164] to monitor the welding process. It was found that a maximum AE rate is directly related to the number of cracks in the weld defect zone. This work is considered to be the first most significant milestone in the application of the AE technique for monitoring the welding process [165]. Bohemen et al. [166] used the AE technique to study the martensitic transformation during the gas tungsten arc (GTA) welding of 42CrMo4 steel. The analysis of obtained results demonstrated that there was a linear relationship between the root mean square (RMS) value of the measured AE and the volume rate of the martensite formation during GTA welding. Furthermore, Steen and Weerasinghe [167-168] applied the AE technique to study the keyhole formation and its failure by measuring the back reflection signals during laser welding. It was found that as the keyhole collapses, the amplitude of the AE is slightly increased. Duley et al. [169] used AE to study the laser welding process of aluminum. It was found that the formation of a keyhole originates from the AE signals in the frequency range of 3-9 kHz. Recently, Grad et al. [170] employed acoustic signals from short circuit gas metal arc welding to monitor on-line the stability of the process and detect weld defects. The main drawback of the AE technique in the industry comes primarily from the requirement of directly attaching the AE sensor to the specimen surface, which limits its wider use in industry

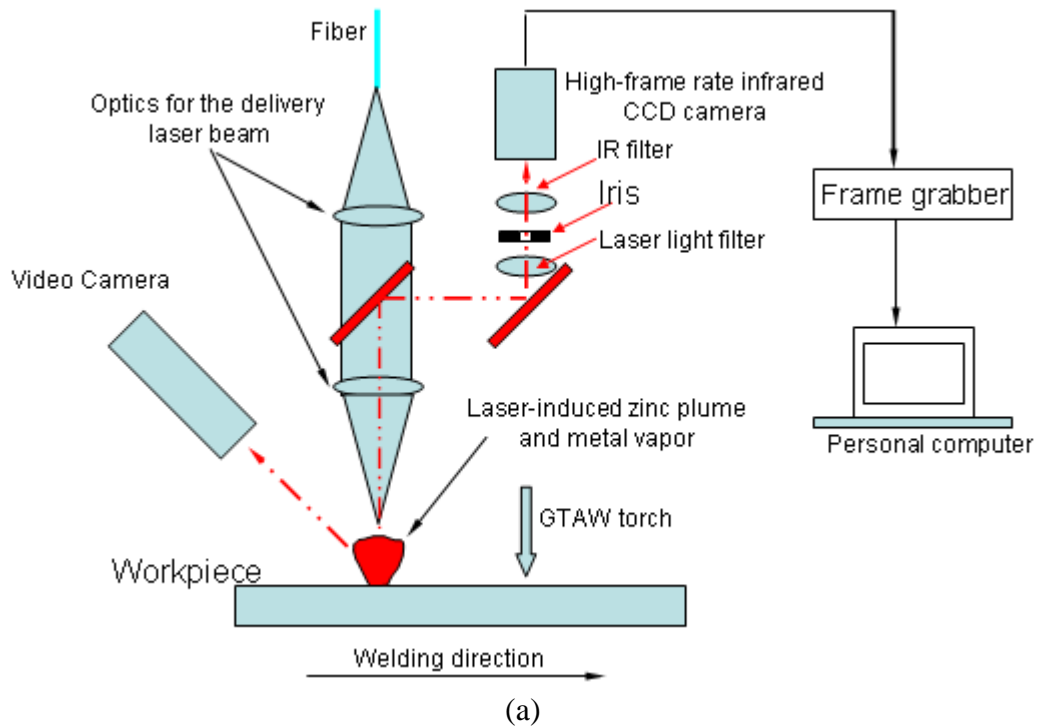
5.3 Monitoring the Transition of the Welding Modes and Stability of the Welding Process by Machine Vision

5.3.1 Experimental Setup

The material used in this study is the galvanized DP 980 steel sheet. The dimensions of the top and bottom plates are 200 mm x 85 mm x 1.2 mm and 200mm x 85 mm x 1.5mm, respectively. The coupon with a thickness of 1.2 mm is selected as the top metal sheet during the lap joint welding process. Four sets of experiments are conducted to study the welding phenomena occurring in the welding process of galvanized steels: (1) the direct laser welding of galvanized steels in a gap-free lap joint configuration without any processing; (2) the laser welding of galvanized steels in lap joint configuration with the presence of a gap of different thickness; (3) the laser welding of galvanized steels in a gap-free lap joint configuration with the assistance of GTAW torch preheating; and (4) the hybrid laser-GTAW welding of galvanized steels in a gap-free lap joint configuration sharing a common molten pool. In the case of the laser welding of galvanized steels with the presence of gap, the stainless steel foil of different thickness is intentionally inserted at the interface of two metal sheets to create the gap.

Laser welding is performed by a fiber laser of 4 kW in power and the preheating is done by the GTAW welding machine. The pure argon gas with a flow rate of 30 SCFH is used as the shielding gas. The GTAW electrode of 3 mm in diameter is used. An infrared CCD camera with a frame rate of 800 per second is used to monitor the welding process. An infrared CCD camera is equipped with an infrared filter and with a notch-filter that blocks light of $1070 \pm 5nm$ in wavelength. The images of the bright spot at the front of the molten pool are real-time recorded

by the infrared CCD camera coaxially installed in the laser head, which contains the keyhole. In addition, a color CCD video camera with the frame rate of 30 interlaced frames per second is installed at the side of the laser beam to monitor the behavior of the laser-induced zinc plume and metal vapor directly produced at the top surface of the first metal sheet. Furthermore, one ordinary CCD camera is also installed at the side of the laser head to capture the images of the entire molten pool to study the process and the formation of the weld defects. The green laser with the band pass of 532 nm at wavelength is used as the illumination source. The experimental setup is schematically shown in Figure 5.1(a) and two types of lap joint configuration are shown in Figure. 5.1 (b) and (c).



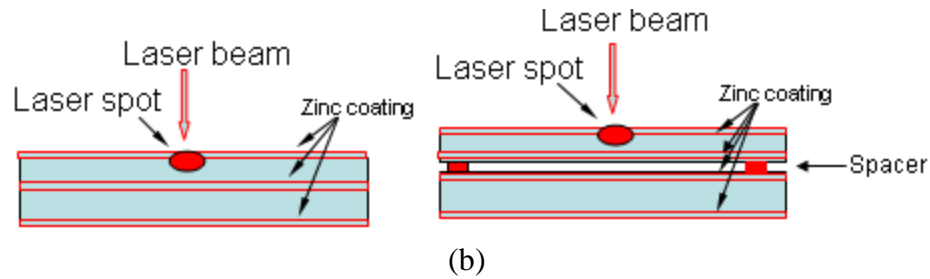


Figure 5.1 Experimental setup and lap joint configurations (a) Schematic presentation of experimental setup (b) zero gap configuration (c) non-zero configurations

5.3.2 Image Processing Algorithms for the Captured Images of the Molten Pool

5.3.2.1 Analysis of the Captured Images of the Molten Pool

Because of the strong laser light reflected from the molten pool, from the experimental results, it is very difficult to obtain a clear shape of the molten pool when the high-frame infrared CCD camera is coaxially installed. To suppress the bright light reflected from the molten pool, a set of optic filter lens should be complicatedly combined to set in the channel through which the laser light passes to the CCD camera except the use of IR filter, laser filter and the illumination of green laser of 532 nm in wavelength. Only in a very narrow window of light wavelength, can the clear images of the molten pool be obtained. This fact increases the complexity of the sensing system. Additionally, the long exposure time for the molten pool images is needed to make the liquid part in the molten pool apparent, which leads to decrease in the frame rate of the camera used.

In order to investigate the welding process, at the beginning of this study an ordinary CCD camera is installed on the side of the laser head with the assistance of the illumination of green laser light, as shown in Figure 5.2 (a). The side installation

significantly avoids the strong laser light reflected from the molten pool and a clear image of the molten pool can be obtained. Figure 5.2 (b) shows a typical example of the images of the molten pool taken by an ordinary CCD camera from the side of the laser head with the illumination of the green laser at 532 nm in wavelength. As shown in Figure 5.2 (b), the bright spot and the boundary between the liquid part of the molten pool and the background are clearly seen. However, the liquid part in the molten pool is somewhat blurred. The degradation of the image of the molten pool is caused by the noises such as spatters and laser-induced zinc plumes as well as the impurity flowing in the liquid molten pool that are produced during the laser welding process of galvanized steels. If we want to use the entire molten pool image to real-time monitor the dynamic behaviors of the molten pool, the shape or size of the molten pool should be determined first. However, it is difficult to determine the clear shape and size of the molten pool without applying some of the image filtering algorithms on the captured images of the molten pool to remove the noises mentioned above before calculating the shape and size of the molten pool, as shown in Figure 5.2 (c). In general, the use of image filtering techniques is complicated and time-consuming. Furthermore, the calculation of the shape and size of the entire molten pool is also time-consuming. These factors limit the use of this technology to be used for real-time monitoring the welding process of galvanized steels.

Further studies on the defect formation using the CCD ordinary camera revealed that when the shape and size of the bright spot at the front of the molten pool is dramatically changed, the welding process becomes instable and the shape

and size of the molten pool are always varied, as shown in Figure 5.3. During the instable welding process, a large number of weld defects such as spatters and blowholes are generated in the welds. Nevertheless, when the shape and size of the bright spot at the front of the molten pool are almost kept constant the welding process is very stable, as shown in Figure 5. 4. Therefore, the bright spot at the front of the molten pool can be used to reflect the instability of the welding process and monitor the formation of weld defects for welding of galvanized steels in a lap joint configuration. Based on the above analysis, the images of the bright spot at front of the molten pool were on-line recorded with the coaxial Infrared CCD camera to investigate the dynamic behavior of the molten pool in different welding conditions. Due to the reduction in the size of the image, the processing speed is dramatically improved. Before recording the images of the bright spot at the front of the molten pool, the iris and the exposure time should be set at the optimal value in order to adjust the light intensity to get clear images of the bright spot. At the same time, the infrared filter (> 700 nm) is selected to reduce the high intensity laser light reflected from the molten pool. Also the laser blocker (1060 nm) is used to prevent the infrared CCD from damage by the laser light.

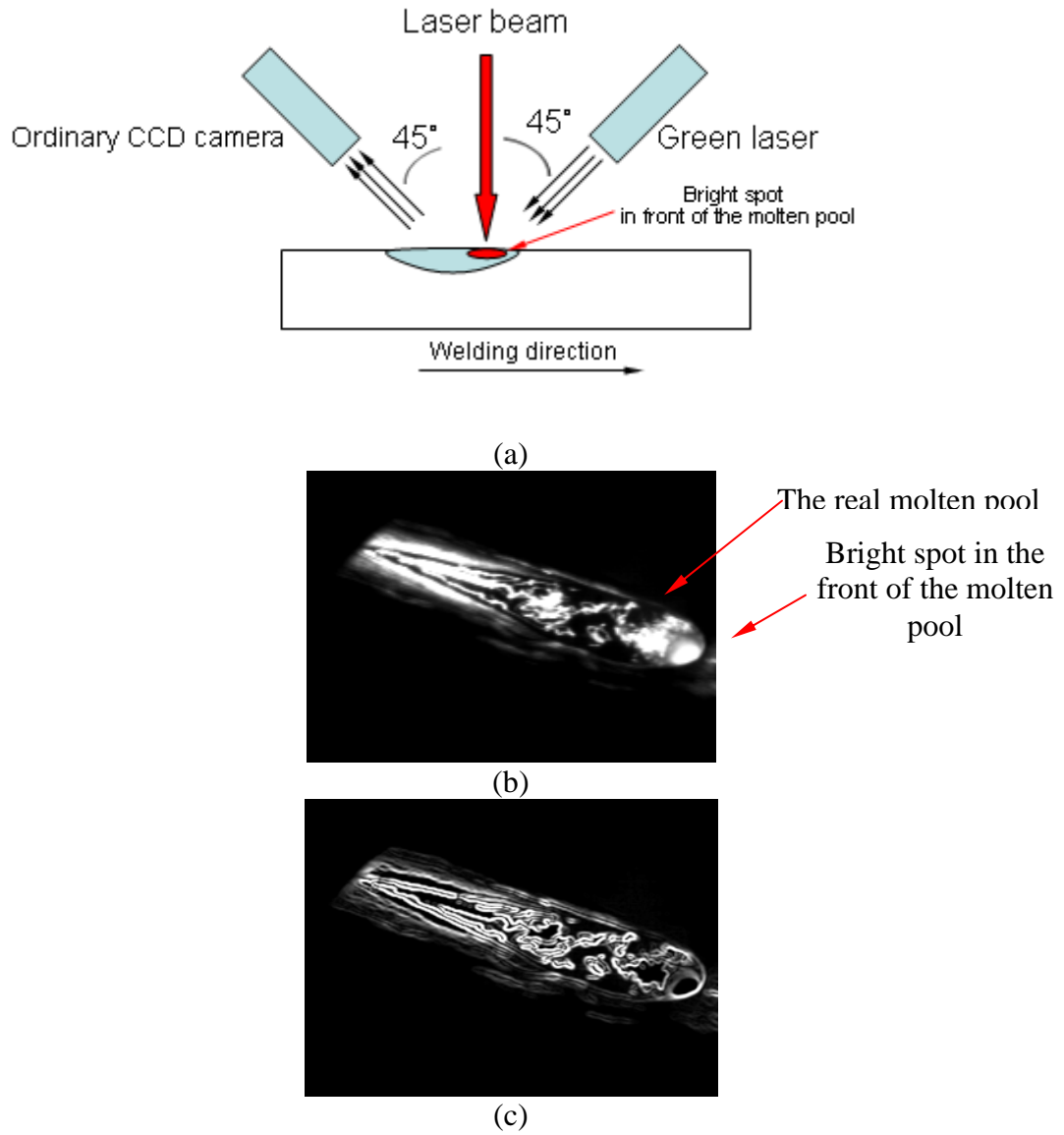


Figure 5.2 Schematic setup for acquiring the molten pool and the example of the captured image of the molten pool (a) The schematic setup for acquiring the molten pool (b) the example of the captured image of the molten pool (c) the edge detection image of the captured molten pool corresponding to (b)

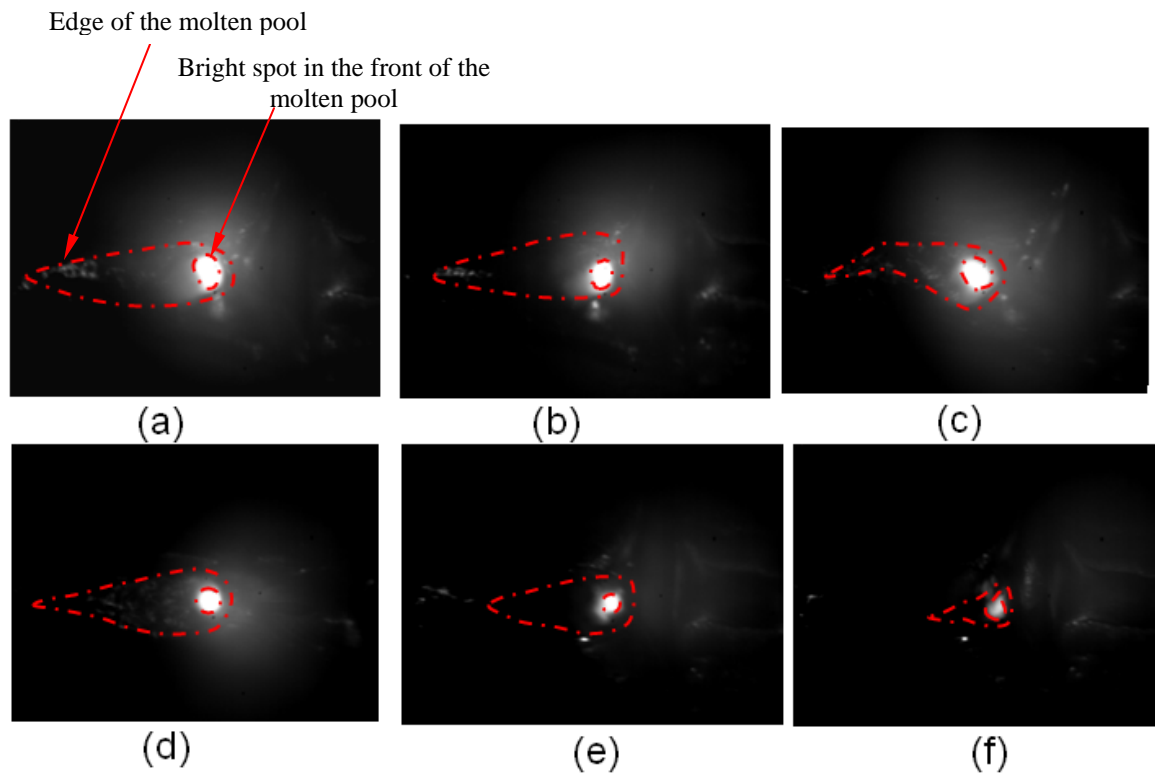


Figure 5.3 Six consecutive images of the molten pool obtained in the instable welding process

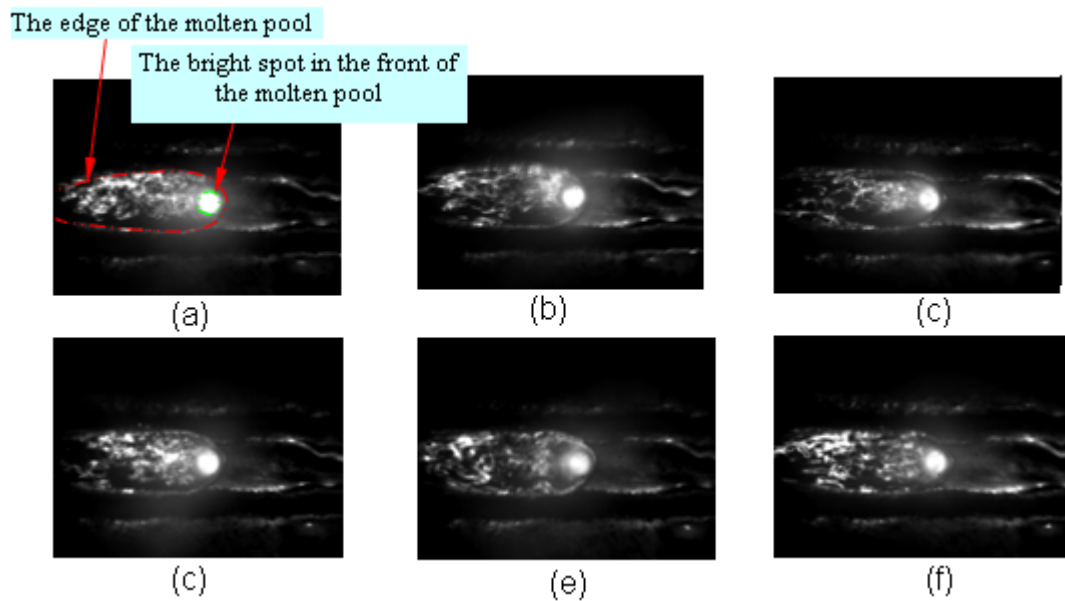


Figure 5.4 Six consecutive images of the molten pool captured in the stable welding process

5.3.2.2 Determination of the Threshold Value of the Grey Level

The temperature distribution of the molten pool is reflected in the acquired infrared image, which can be used to determine the boundary between the liquid part in the molten pool and the bright spot. Figure 5.5 show the original infrared image acquired by the coaxial infrared CCD camera and the grey level isotherm distribution of the corresponding infrared image that presents the temperature distribution in the molten and the background area. As shown in Figure 5. 5(a), the image of the bright spot can be clearly obtained by the coaxial infrared CCD camera with the help of the IR filter and the laser blocker as well as the optimal adjustment of the iris and exposure time.

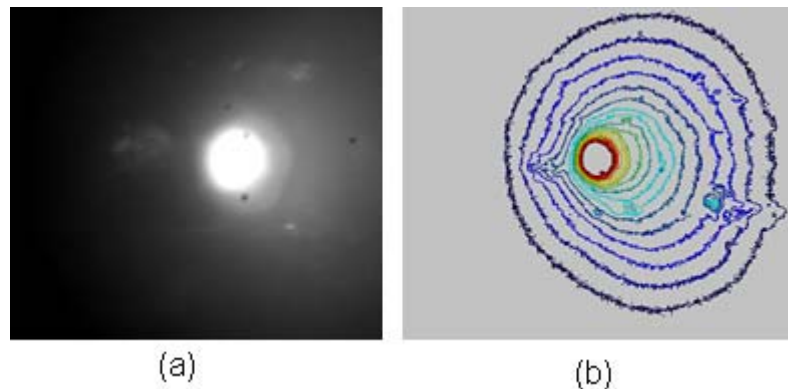


Figure 5.5 Infrared image of the bright spot acquired (a) original infrared image of the bright spot (b) grey level isotherms of the infrared image corresponding to (a)

In order to use the bright spot for monitoring the welding process, the real size of the bright spot should be computed. To this end, the mapping method is used to determine the grey level for the segmentation of the bright spot section from the liquid part in the molten pool and the background area [194]. Two CCD Cameras

are used synchronously. One is the ordinary CCD camera with high-shutter speed set up at the side of the laser head, as shown in Figure 5.2 (a), the other is the infrared CCD camera coaxially installed at the laser head, as shown in Figure 5.1 (a). Additionally, the green laser is utilized to illuminate the welding zone to suppress the intensive laser light. With the illumination of the green laser, the clear image of the bright spot is obtained from the side by an ordinary CCD camera. Then the canny edge detector is used to determine the ordinary images acquired with the high-speed shutter ordinary camera [195-196]. After the edge detection of the image of the bright spot is obtained by the ordinary CCD camera, it is mapped to the corresponding infrared image of the bright spot with a coordinate transformation [194]. The grey level value can be obtained to determine the boundary between the bright spot and the liquid part of the molten pool.

5.3.2.3 Binarizing the Image of the Molten Pool

After the determination of the grey level T , the bright spot can be separated from the liquid section in the molten pool and the background, which is treated as the completely black. The bright spot size are defined as the region which has the pixels of value equal or more than T . At the same time, the background and the liquid section in the molten pool is defined as the area which has pixels of a value less than T . This algorithm can be presented as the following formulation:

$$f'(x,y) = \begin{cases} 1, & \text{if } f(x,y) > T \\ 0, & \text{if } f(x,y) < T \end{cases} \quad (5.1)$$

Where $f(x, y)$ is the captured image and $f'(x, y)$ is the binarized image corresponding to the captured image. In this formulation, 1 represents the white and 0 denote the dark.

After binarizing the input image of the molten pool, the image is further filtered to eliminate the noises in the image of the bright spot at the front of the molten pool. In this step, the largest bright area A_L is chosen as the molten pool area and kept for the further calculation of the molten pool along the axis length. The remaining other areas are treated as background and the value of pixels in these areas is set to zero. The filtered algorithm is described as the following:

$$\bar{f}(x, y) = \begin{cases} f'(x, y), & \text{if } (x, y) \in A_L \\ 0, & \text{if } (x, y) \notin A_L \end{cases} \quad (5.2)$$

Where $\bar{f}(x, y)$ is the filtered image.

Figure 5.6 shows the original image, the binarized image and the filtered image of the bright spot, respectively. As shown in Figure 5.6 (a), the image of the original bright spot is degraded and blurred by the laser-induced plume and spatters. After the binarizing the laser-induced plume is eliminated from the originally captured image, as shown in Figure 5.6 (b). However, the small bright area caused by the spatter is still present in Figure 5.6 (b). As shown in Figure 5.6 (c), the small bright area corresponding to the spatter is completely removed with the further use of the filtering algorithm and the boundary between the molten pool and the background is clearly indicated.

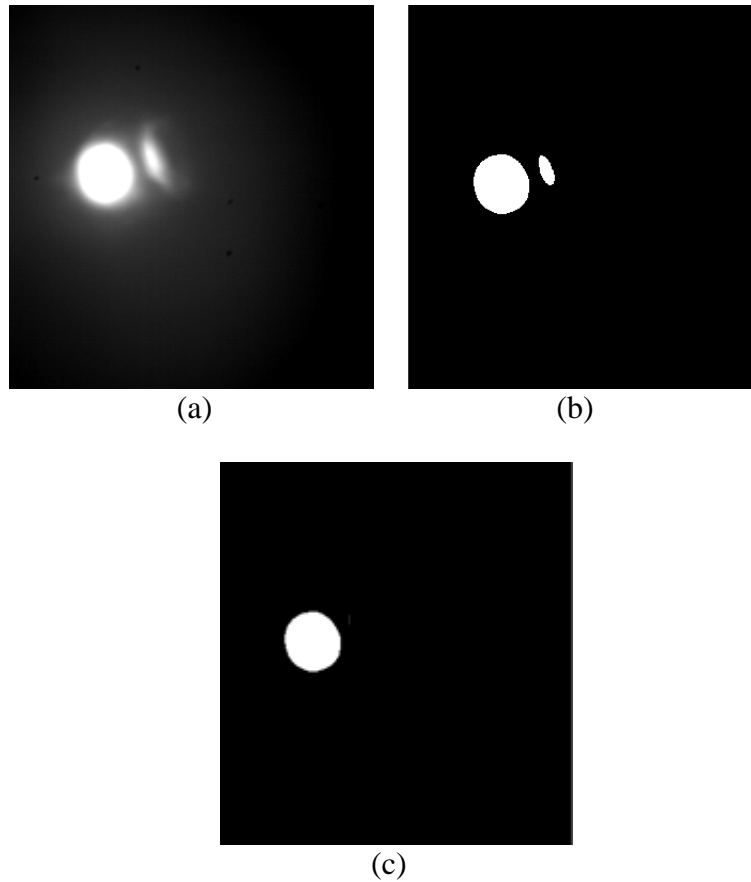


Figure 5.6 Image processing of the bright spot (a) the original infrared image (b) the binarized image (c) the filtered image

5.3.2.4 Calculation of the Major Axis Length of the Molten Pool

From the previous study, the length of the bright spot in the front of the molten pool can be used for real-time monitoring of laser welding of galvanized steels [192]. After filtering the binarized image, the length of the major axis length of the bright spot is calculated. Figure 5.7 demonstrates the schematic of the molten pool. The center coordinates and the length of the major axis of the bright spot can be determined by using Equations (6) and (7), respectively.

$$\begin{cases} x_c = \frac{x_{\max} + x_{\min}}{2} \\ y_c = \frac{y_{\max} + y_{\min}}{2} \end{cases} \quad (5.3)$$

$$L_{Major} = |x_{\max} - x_{\min}| \quad (5.4)$$

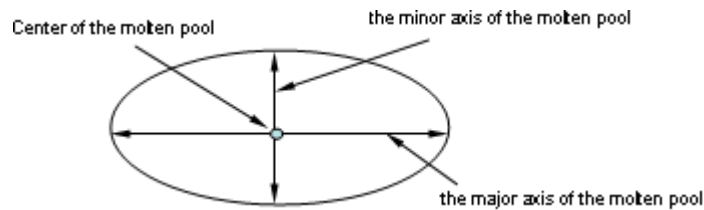
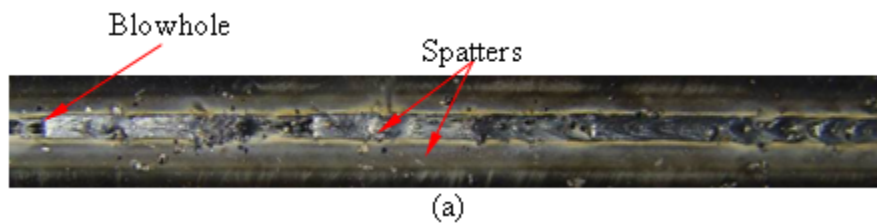


Figure 5.7 Schematic representation of the molten pool

5.3.3 Monitoring of the Stability of Laser Welding Process of Galvanized Steels in a Gap-Free Lap Joint Configuration

Laser welding of galvanized steels in a gap-free lap joint configuration is characterized by spatters and blowholes, as shown in Figure 5. 8 (a). The highly-pressurized zinc vapor that develops at the interface of two metal sheets during the laser welding process tends to bring the liquid metal out and produce the spatters and blowholes in and around the weld zone [184].



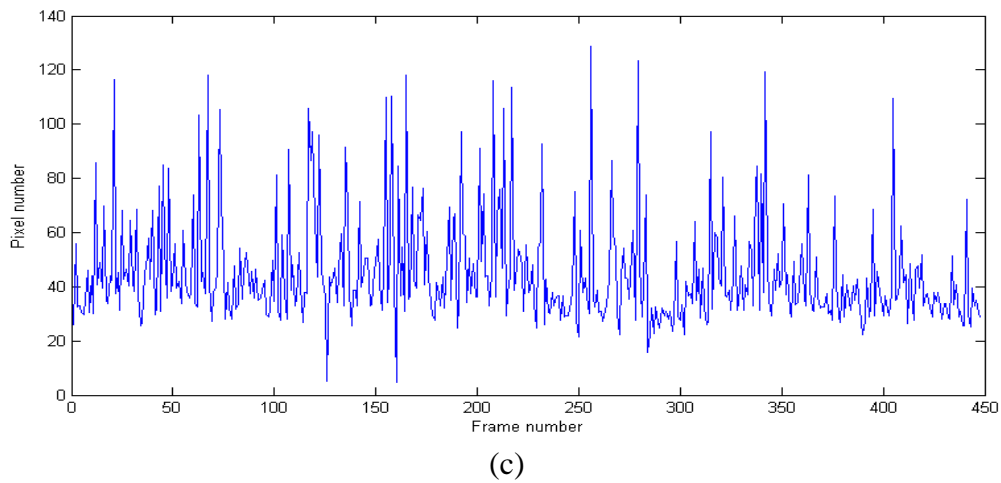
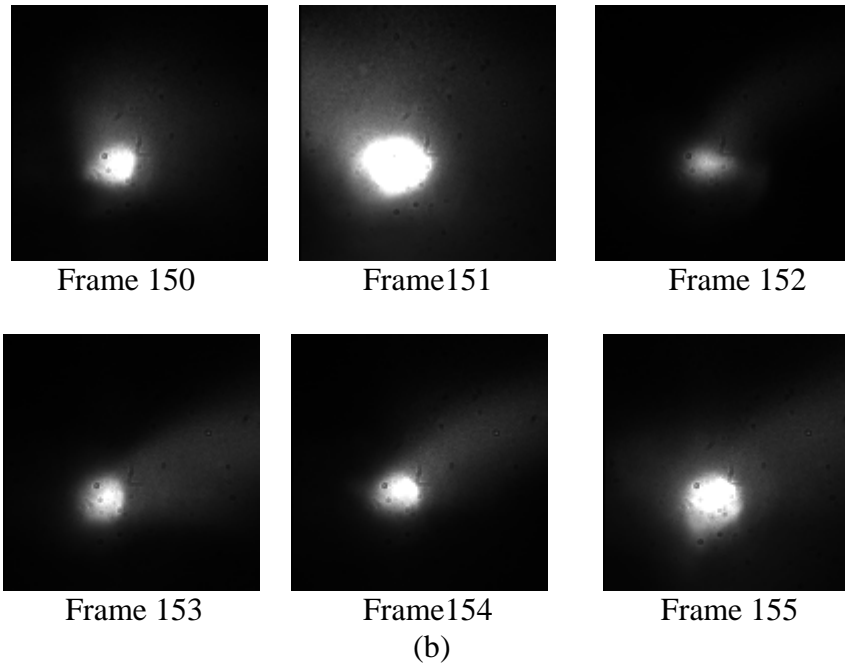


Figure 5.8 Monitoring the instability of laser welding process of galvanized steels in a gap-free lap joint configuration (a) the laser-welded lap joint obtained in the instable welding process (b) the six consecutive captured images of the molten pool (c) the major axis length as the function of frame numbers ((Laser power: 3000 W; Welding speed: 50 mm/s)

By using the image process mentioned in the above section, the length of the major axis of the bright spot at the front of the molten pool are monitored on-line to determine the stability of the welding process. When the welding process is instable, the irregular fluid flow at the rear part of the molten pool is observed and the

keyhole is opened and closed by the instable highly-pressurized zinc vapor. When the keyhole is closed, there is no channel for the evacuation of the highly-pressurized zinc vapor. Consequently, many spatters and blowholes are generated in the non-uniform weld surface appearance. The keyhole is contained in the bright spot. Figure 5.9 demonstrates the transition from the stable keyhole to the collapsed keyhole. It is found that the spatters are formed after the collapse of the keyhole, as shown in Figure 5.9 (c). When the keyhole is collapsed, there is no place for the highly-pressurized zinc vapor developed at the interface of two metals to vent out and spatters form. Consequently, the highly-pressurized zinc vapor quickly expands in the body of the molten pool and brings the liquid metal out of the molten pool. When the liquid metal is condensed in the air, the spatters form and scatter in the weld zone or the weld surface so that a post-processing is required to clean them after the laser welding process. Furthermore, the mechanical properties of the laser welds dramatically decrease by the formation of the spatters. In the infrared image of the bright spot, it is difficult to distinguish the keyhole from the surrounding area. However, the keyhole can be easily distinguished from its surrounding area in the image of the molten pool taken by the color CCD camera. As shown in the Figure 5.9 (d), the black spot in the center presents the keyhole formed. Figure 5.8 (c) shows the calculation of the major axis length values of the molten pool as a function of the number of frames. As shown in Figure 5.8 (c), the length of the major axis of the bright spot significantly fluctuates over time, indicating that the welding process is dramatically instable. It is found that spatters are produced when the length of the major axis of the bright spot suddenly changes from a small value to a large value.

As the length of the major axis of the bright spot reaches zero, blowholes are produced in the weld [192]. Figure 5.8 (b) shows the six consecutive images of the molten pool captured on-line during the laser welding process.

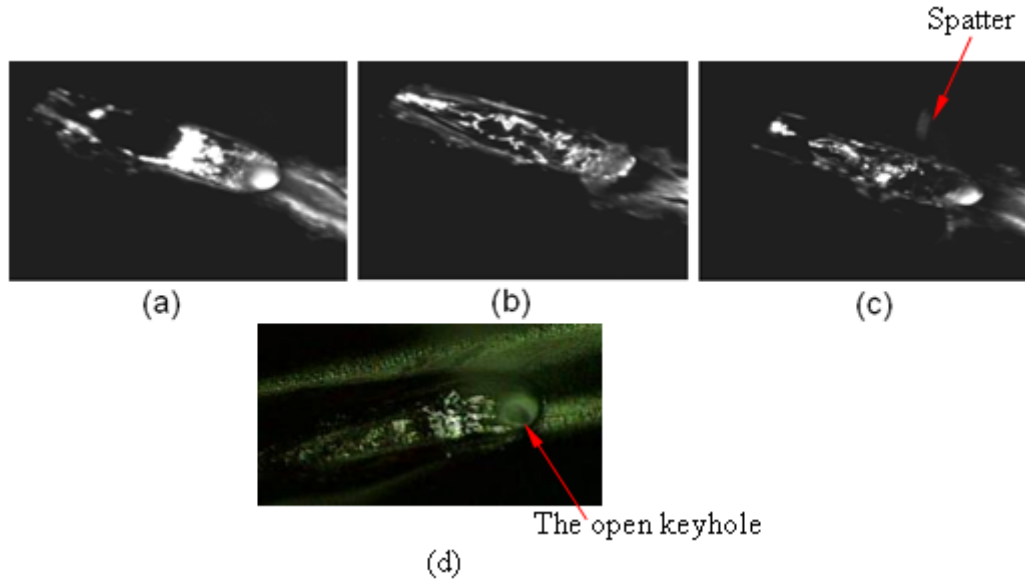


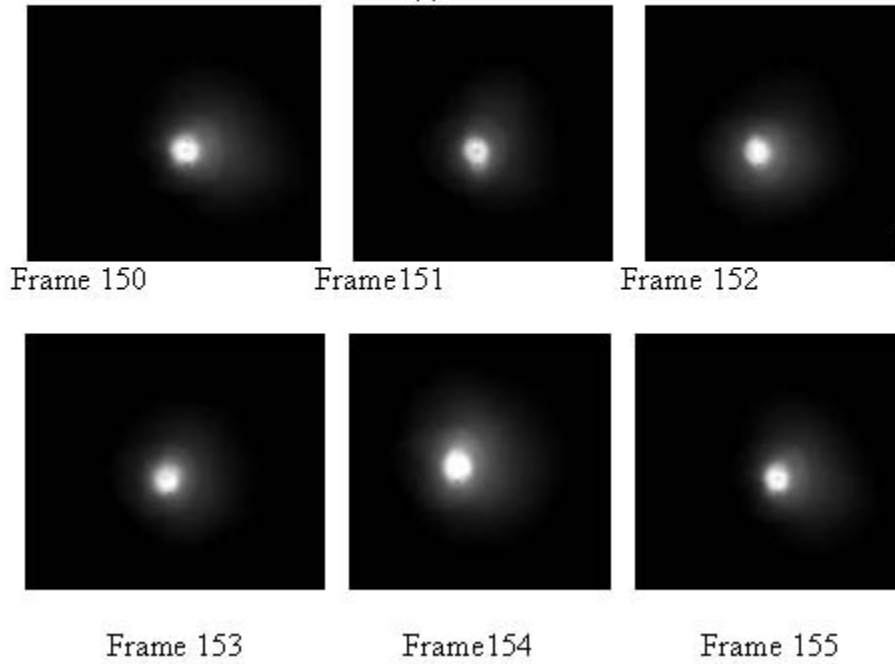
Figure 5.9 Transition from the stable keyhole status to the collapsed keyhole status (a) the stable keyhole status (c) the formation of the spatter (d) the image of the open keyhole acquired by the color CCD camera

To obtain a sound weld, the zinc coating at the interface of two metal sheets is removed prior to the laser welding process. Without the presence of the zinc coating at the interface of two metal sheets, no highly-pressurized zinc vapor is developed at the interface and the welding process is very stable from the beginning of the welding process to the end. Therefore, no spatters and blowholes are present in the weld, as shown in the Figure 5. 10 (a). Figure 5.10 (c) shows the features of the length of the major axis of the bright spot as a function of the number of the frames obtained under the above welding condition. As shown in Figure 5.6 (c), the major axis length values of the molten pool are almost kept at a constant value. In

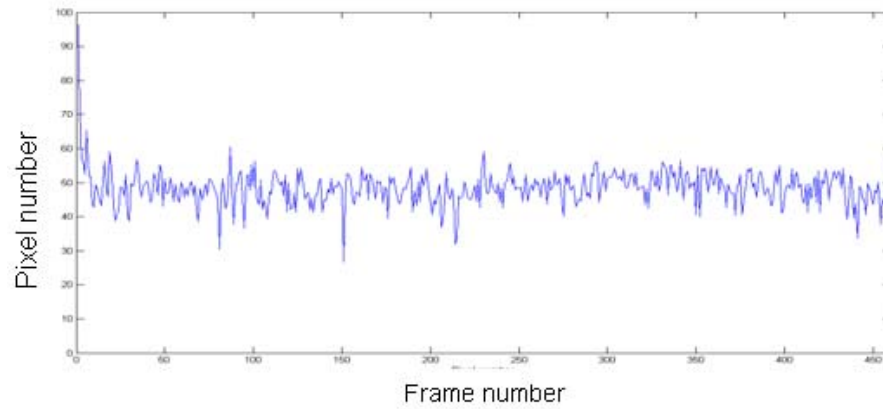
additionally, Figure 5.10 (b) shows the six consecutive images of the molten pool captured on-line during the laser welding process. It can be seen that the shape and size of the bright spot is very constant.



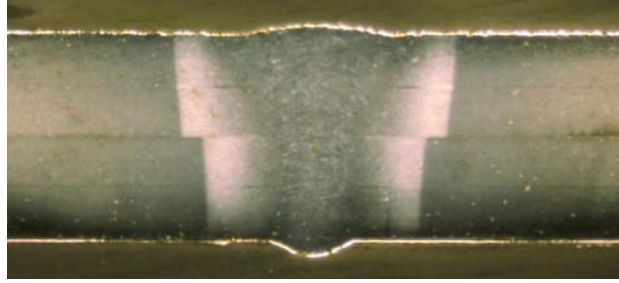
(a)



(b)



(c)



(d)

Figure 5.10 Monitoring the stability of laser welding process of galvanized steels in a gap-free lap joint configuration (a) the laser-welded lap joint (b) the six consecutive captured images of the molten pool (c) the major axis length as the function of frame numbers (d) the cross-sectional view of laser-welded lap joint (Laser power: 3000 W; Welding speed: 50 mm/s)

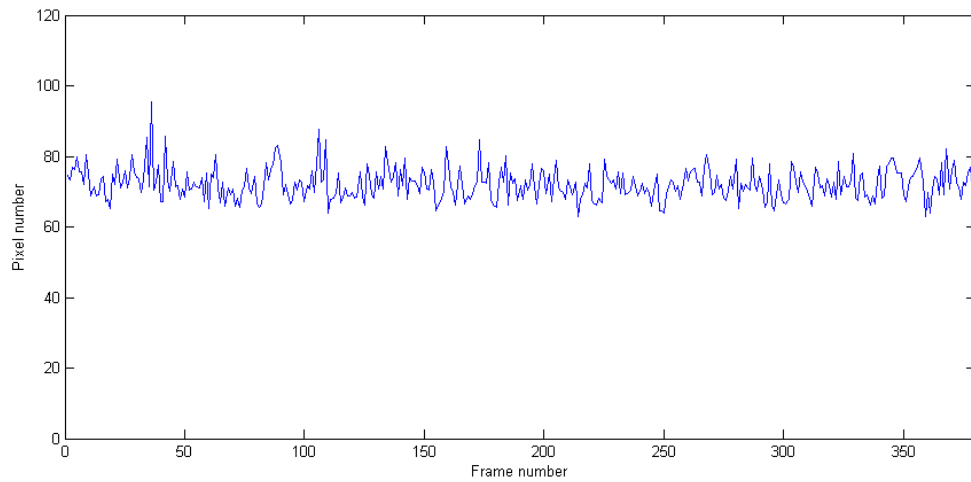
5.3.4 Monitoring of the stability of Laser Welding Process of Galvanized Steels with the Presence of Gap at the Interface of two Sheet Metals

The use of a gap at the interface of two sheet metals prior to laser welding of galvanized steels allows the highly-pressurized zinc vapor to escape from the interface so that a good weld can be obtained [197-198]. In order to study the effect of a gap at the interface of two metal sheets on the dynamic behavior of the molten pool, laser lap joints of galvanized steels are performed with three kinds of welding conditions: (1) having no gap after the removal of the zinc coating at the interface of the two metal sheets; (2) setting the stainless steel foil spacers to a thickness of 0.2mm and 0.4 mm gaps and (3) having gaps to intentionally create more gaps at the interface of the two metal sheets. For these three different kinds of welding processes, the laser power and welding speed as well as the flow rate of the shielding gas are kept at the same. Examples of the experimental results are shown in Figure 5.11 and Figure 5.12. When the laser welding process is performed without the presence of a gap and after the removal of the zinc coating at the

interface of the two metal sheets, the major axis length of the molten pool has the largest value compared to those lengths obtained under the welding conditions of 0.2- mm and 0.4- mm thick gaps at the interface of two metal sheets. Figure 5.12 shows the results with the gaps 0.2-mm and 0.4-mm gaps. As shown in Figure 5.12, the major axis length values of the molten pool are dramatically decreased with the increase of the gap thickness. Moreover, the introduction of a gap into the interface of the two metal sheets causes the undesirable deep concave underfills in the weld, as shown in the Figure 5. 12 (d) and (e). With the increase in the thickness of the gap, the depth of undercut in the welds becomes deeper. The reason for the formation of underfills is the shrinkage of the molten pool and the lack of material to be filled in the molten pool during the solidification process. Furthermore, the existence of a thin layer of air decreases the coupling of the laser beam energy into the second metal sheet, thus reducing the depth of penetration in the weld. Only partially shallow penetrations are achieved in the both cases of the gap 0.2-mm and 0.4-mm gaps. In order to achieve full penetration, the laser power should be increased or the welding speed should be decreased to some extent. Figure 5.13 demonstrates the relationship between the average length of the major axis of the bright spot and the thickness of the gap used at the interface of the two sheet metals.

As shown in Figure 5.12 (b) and (c), it is possible to obtain the acceptable weld geometries by introducing an optimal gap. However, introducing a gap at the interface of the two metal sheets is time consuming and costly and can not meet the industrial constraints. Moreover, the introduction of a gap at the interface of the two metal sheets leads to new issues such as the undesirable undercuts mentioned above.

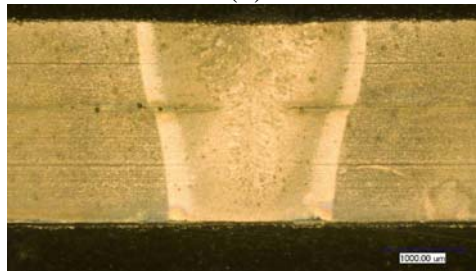
In a serious case, the gap produces unbonded welds. Additionally, the corrosion problem and the weld strength relative to the gap are also of concern. According to these results, therefore, it is possible for the proposed vision-based sensing system to determine on-line whether an excessive gap exists during the welding process by the remarkable jump in the major axis length of the molten pool in comparison with the preset value during stable and specific welding conditions.



(a)

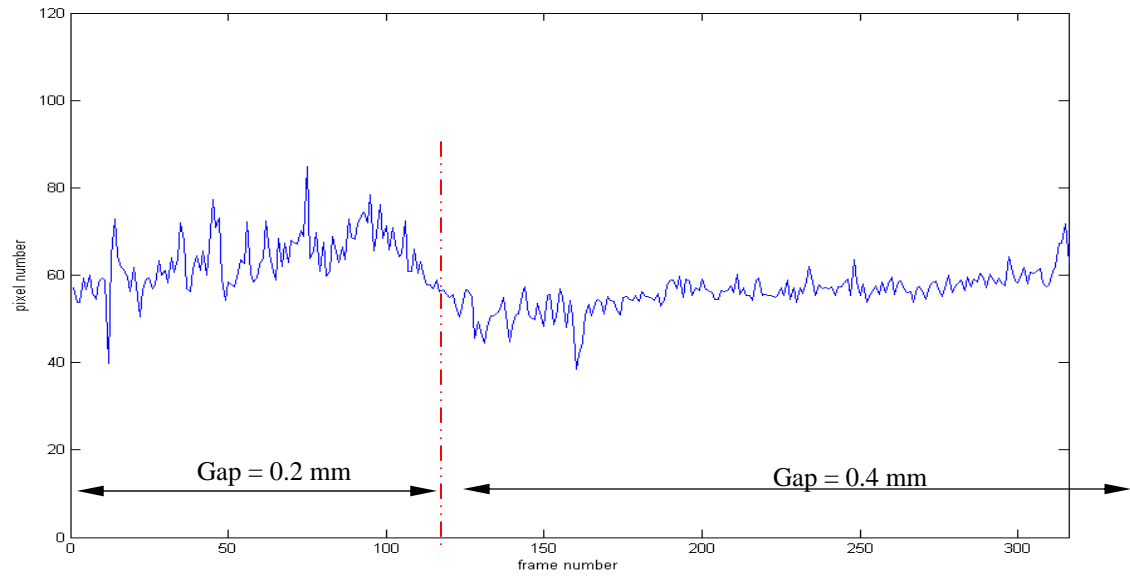


(b)



(c)

Figure 5.11 Laser welded lap joint obtain in the stable welding process (Laser power 3600 W; Welding speed 50 mm/s; no zinc coating at the interface of two metal sheets)



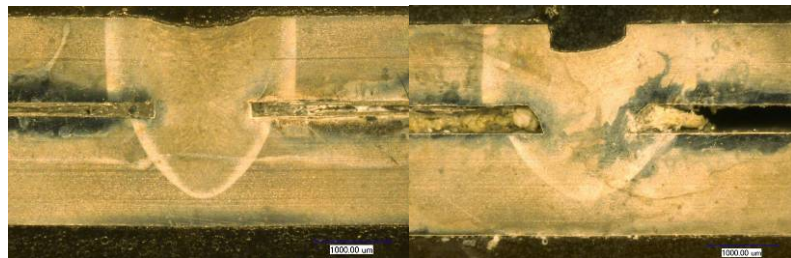
(a)



(b)



(c)



(d)

(e)

Figure 5.12 the influence of the weld gap at the interface of two metal sheets on the major axis length of the molten pool (Laser power 3600 W; welding speed 50 mm/s; Gap 0.2 and gap 0.4 mm)

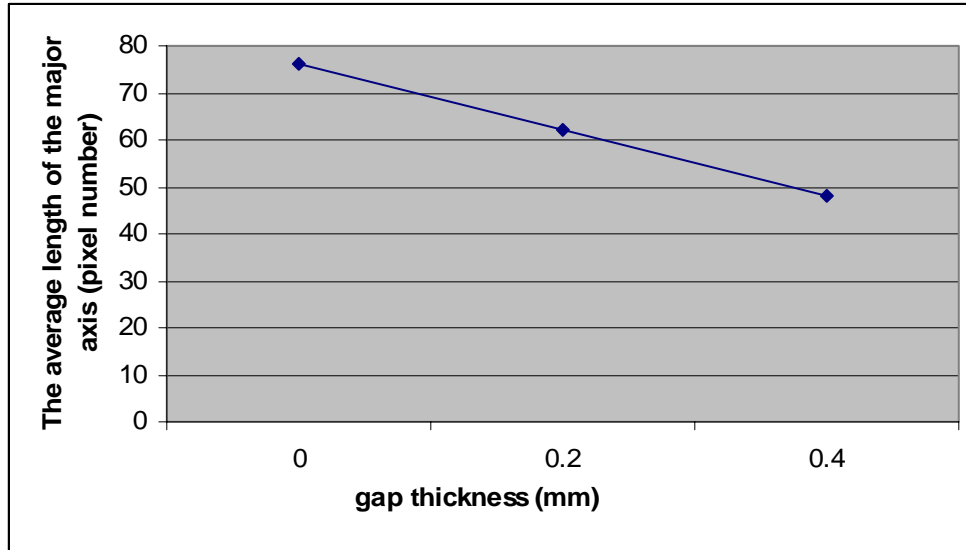


Figure 5.13 Relationship between the average length of the major axis of the bright spot and the thickness of gap

5.3.5 Monitoring the Stability of the Hybrid Laser-Arc Welding Process of Galvanized Steels with a Common Molten Pool

The lap joint welding of galvanized steels is also conducted by using the hybrid laser-GTAW welding method with a common molten pool where the GTAW torch leads the laser welding, as shown in Figure 5.14 (a). Figure 5.14 (b) shows the typical lap joint obtained by using hybrid laser-GTAW welding in the common molten pool. As shown in Figure 5.14 (b), the number of spatters and blowholes is dramatically decreased compared to the lap joint in Figure 5.8 (a) obtained by single laser welding. The enhanced stability is attributed to the function of the GTAW torch preheating. First, the leading GTAW torch plays a role in preheating the specimens. Preheating can improve the coupling of the laser beam energy into the welded materials compared to a single welding process. Second, the GTAW torch softens and partially melts the specimens. These two factors facilitate the

formation of the keyhole in the molten pool through which the highly-pressurized zinc vapor can be vented out from the interface. Although the stability of the welding process of galvanized steels is improved compared to the single laser welding of galvanized steels, the spatters and blowholes are still present in the welds. These phenomena can be explained by the fact that the instable interaction of the GTAW arc and laser beam tends to collapse the keyhole. Thus, there is no channel for the zinc vapor at the interface of two metal sheets to be vented out. Under this situation, the liquid melt metal is expelled from the molten pool, condensed in the air, and scattered in the weld zone or weld surface. Of serious concern, a blowhole is produced in the weld when there is no enough material filled back.

During the hybrid laser-GTAW welding process, the images of the bright spot were also recorded by the coaxial infrared CCD camera. It is found that the CCD camera is readily saturated by the intensive arc light and the images of the bright spot are not always clear. Figure 5.15 shows the six consecutive images of the bright spot taken during the hybrid laser-GTAW welding process within the common molten pool. As shown in Figure 5. 16, the images of the bright spot are very bright and their shapes and sizes fluctuate over time indicating the welding process is not stable.

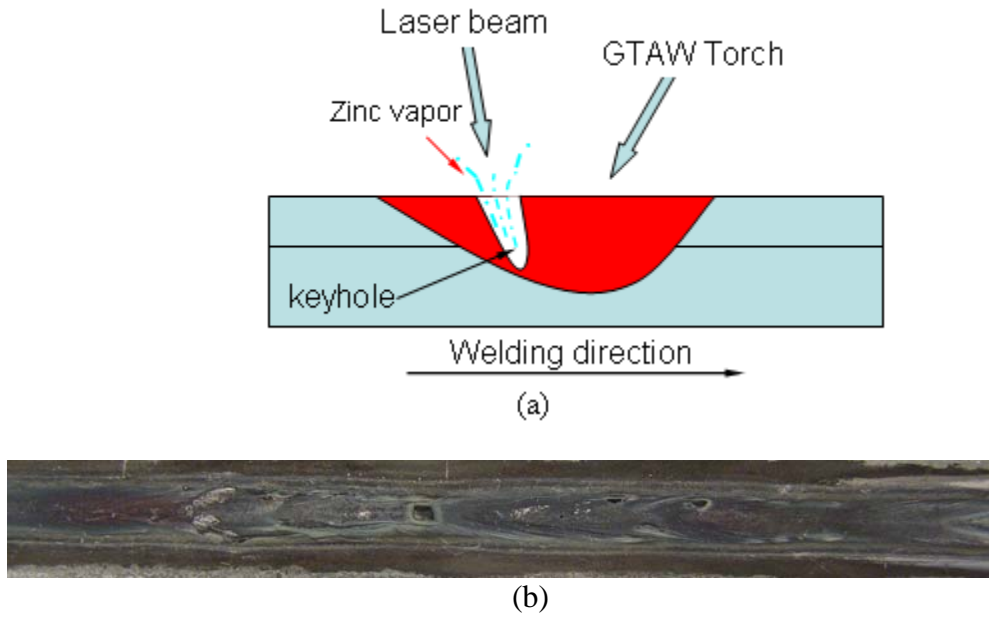


Figure 5.14 Schematic representation of experimental setup for hybrid laser-GTAW welding with the common molten pool and the top view of lap joint obtained by the hybrid laser-GTAW welding with the common molten pool (a) schematic representation of experimental setup (b) hybrid laser-GTAW welded lap joint

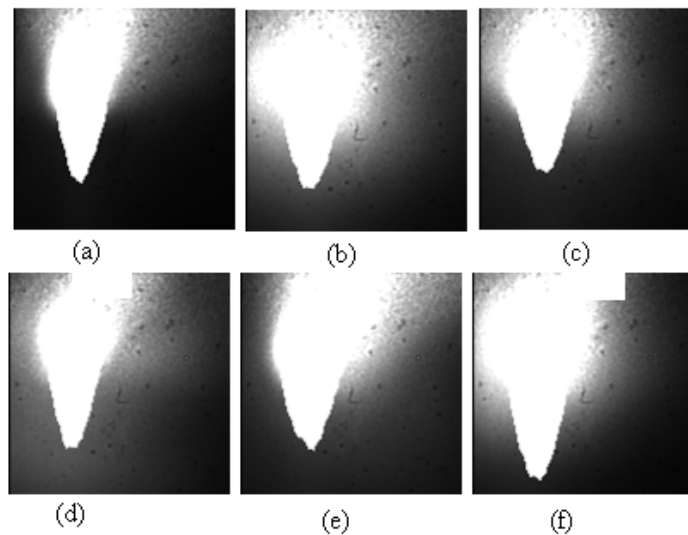


Figure 5.15 Six consecutive images of bright spot obtained in the hybrid laser-GTAW welding process

5.3.6 Monitoring of the Stability of Hybrid Laser-Arc Welding Process of Galvanized Steels with the Assistance of GTAW Torch Preheating

The completely defect-free gap-free lap joints of galvanized steels were obtained by using laser welding with the assistance of GTAW preheating in the separate molten pool [189]. Figure 5.16 shows the schematic representation of hybrid laser-GTAW preheating in the separate molten pool and the typical image of the molten pool taken by the ordinary camera installed at the side of the laser head. As shown in Figure 5.16 (a), the GTAW torch preheating process is separated from the laser welding process at a specific distance between the laser beam and GTAW torch to create two separate molten pools. Here, the GTAW torch is used only to preheat the welded material that burns the zinc coating at the top surface of the metal sheets under the controlled heat from the GTAW torch. Meanwhile, a thin layer of metal oxides is formed at the top surface and dramatically improves the coupling of laser beam energy into the welded materials [199-200]. Under these welding conditions, a stable keyhole is continuously maintained that provides a channel for the evacuation of the zinc vapor from the interface of two sheet metals. Furthermore, the zinc coating around the weld line at the interface is transformed into zinc oxides, which has the higher melting point than that of steel and further stabilizes the welding process. Consequently, the welding process avoids the formation of weld spatters and blowholes. Additionally, the weld is free from the formation of porosity in the welds because the shielding gas is not trapped in the molten pool generated by the laser beam. Thus, high quality welds are achieved.

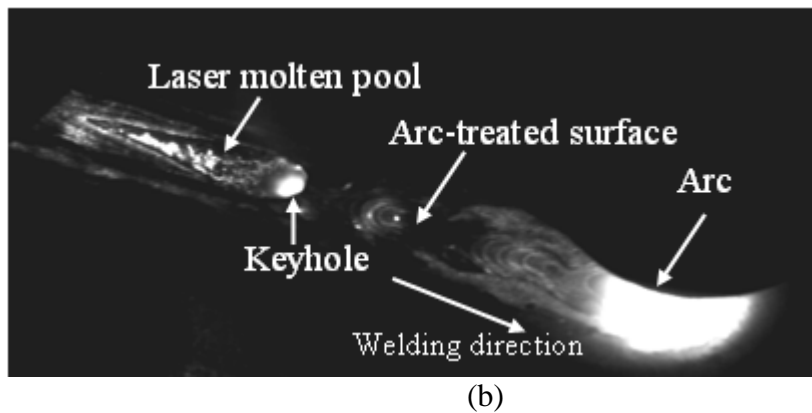
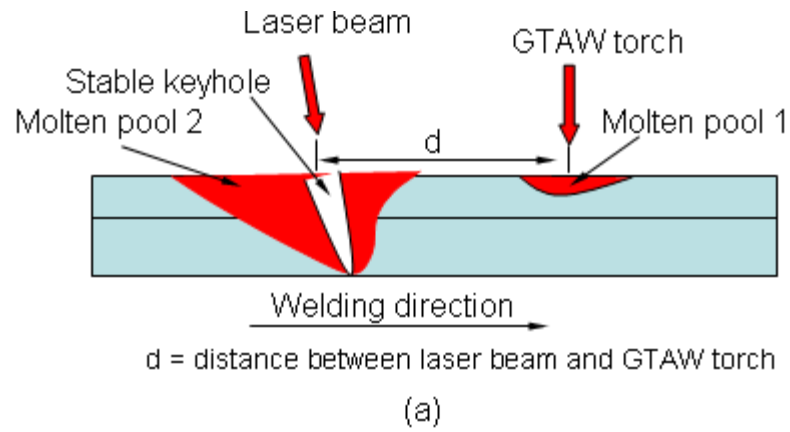


Figure 5.16 Schematic representation of the experimental setup of the hybrid laser-GTAW welding in the separate molten pool and the image of the molten pool obtained by the ordinary CCD camera (a) the schematic representation of experimental setup (b) example of the typical image taken by the ordinary CCD camera installed at the side of laser head

Figure 5.17 shows the six consecutive images of the bright spot taken by the infrared CCD camera when the leading GTAW torch and laser welding process are simultaneously conducted at a distance of 20mm between the laser beam and GTAW torch. Since the GTAW torch is far away from the view field of the infrared CCD camera, the images of the bright spot is not affected by the intense arc light and clear images are obtained. As shown in Figure 5. 17, the shape and size of the bright spot is very uniform and constant, which indicates the achievement of a

stable welding process. Figure 5.18 (a) and (b) illustrate the top view and cross-sectional view of the lap joint obtained by hybrid laser-GTAW welding with a separate molten pool. As shown in Figure 5. 18 (a) and (b), there are no spatters and wholes or porosity presented in the welds. Additionally, Figure 5.18 (c) plots the length of the major axis of the bright spot as a function of a number of frames. As shown in Figure 5. 18 (c), the length of the major axis of the bright spot varies in a very narrow arrange.

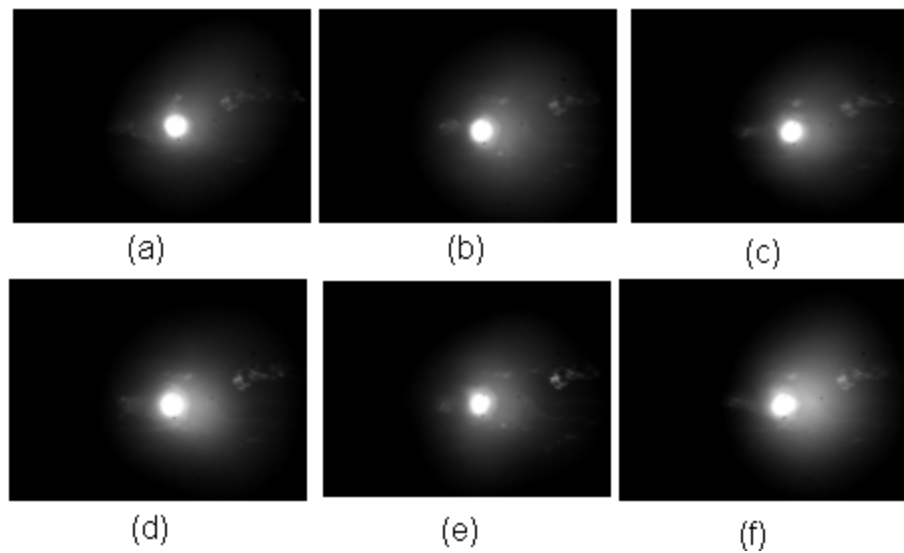
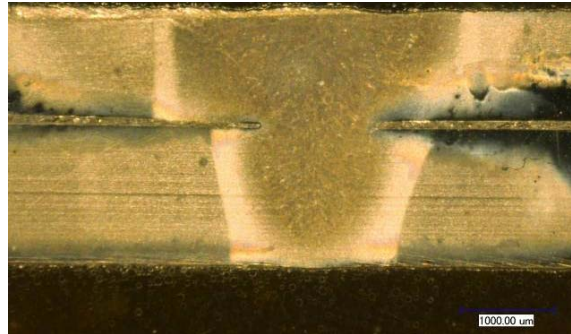


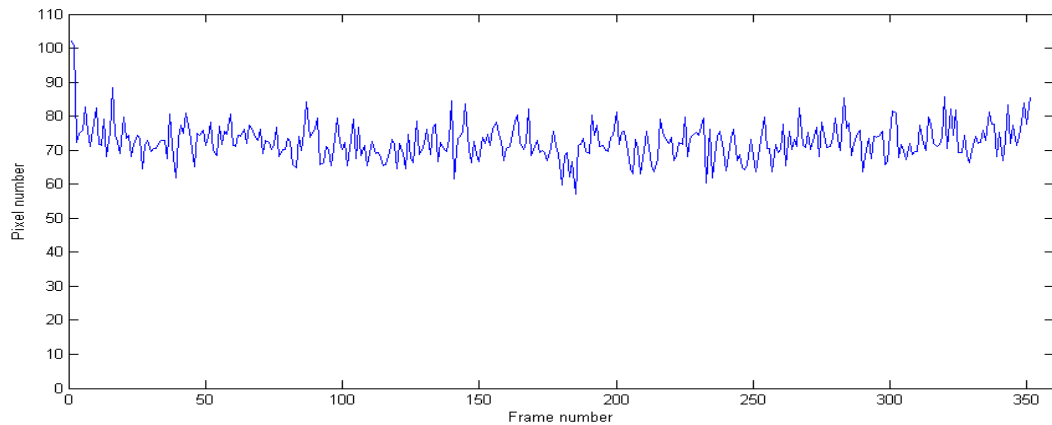
Figure 5.17 Six consecutive images of the bright spot obtained by the Infrared CCD camera during the hybrid laser-GTAW welding process with the separate molten pool



(a)



(b)



(c)

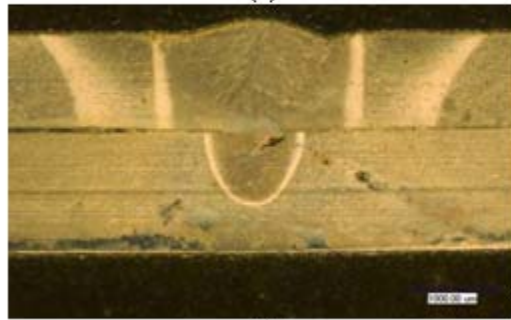
Figure 5.18 Length of the molten pool major axis with the GTAW preheating (laser power: 3200 W; preheating GTAW current: 200; Distance between laser beam and GTAW torch: 20 mm; welding speed 50 mm/s)

Figure 5.19 shows the experimental results when the GTAW preheating is completed and cooled down before the laser welding process is conducted. Figure 5.20 shows the experimental results without the GTAW preheating. The zinc coating at the top surface of the specimens is kept constant for these three experiments and corresponds to the welds in the Figure 5.18, Figure 5.19, and Figure 5.20. Comparing Figure 5.18 (a), Figure 5.19 (a) and Figure 5.20 (a), it is

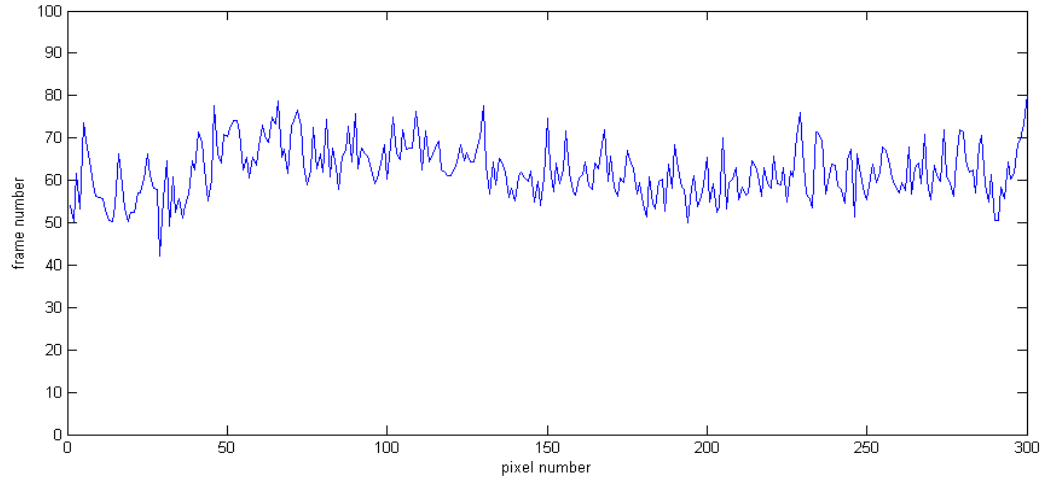
observed that the largest average major axis length of the molten pool and the deepest depth of the weld penetration are obtained in the welding process when the GTAW preheating process and laser welding process are performed simultaneously. As shown in Figure 5.18 (b), the full penetration is obtained when the leading GTAW preheating process and laser welding process are conducted simultaneously. However, only the partial penetration is obtained when the GTAW preheating process is separated from the laser welding process. This phenomenon can be explained by the fact that when the GTAW preheating process and the laser welding process simultaneously conducted, the specimens are hotter than the cool specimens with the GTAW preheating and without the GTAW preheating. The absorption efficiency of the laser beam is higher for the hotter specimens compared to that for the cold specimens.



(a)



(b)

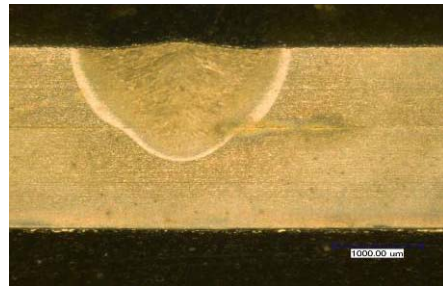


(c)

Figure 5.19 Length of the molten pool major axis with the GTAW preheating (laser power: 3200 W; Preheating GTAW current: 200 A; Welding speed 50 mm/s; Zinc coating at the interface of two metal sheets is removed)



(a)



(b)

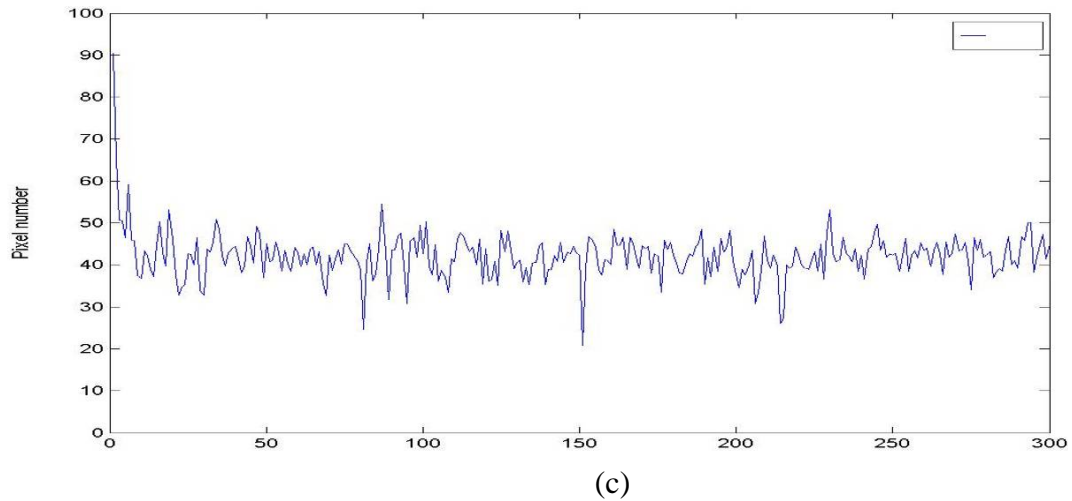


Figure 5.20 Length of the molten pool major axis without the GTAW preheating (laser power: 3200 W; Welding speed 50 mm/s; Zinc coating at the interface of two metal sheets is removed)

Figure 5.21 shows the relationship between the average length of the major axis of the bright spot and depth of the penetration under different welding conditions. As shown in Figure 5.21, the average length of the major axis length of the bright spot that corresponds to the weld in Figure 5. 19 (a) has a larger value than the value obtained in the weld without the GTAW preheating corresponding to the weld as shown in Figure 5.20 (a). This phenomenon can be explained by the fact that with the GTAW preheating a thin layer of metal oxides is formed that can dramatically improve the coupling efficiency of laser beam energy into the specimens. The higher the coupling efficiency of laser beam energy into the specimens, the larger the molten pool and the deeper the depth penetration. Additionally, the laser-induced plume defocuses and blocks a portion of the laser beam energy into the welded material during the laser welding process that corresponds to Figure 5.20 (a). However, the laser welding process corresponding

to the weld shown in Figure 5.19 (a) is free from the influence of the laser-induced plume due to the removal of the zinc coating with the GTAW torch preheating prior to the laser welding process. Therefore, more laser beam energy is coupled into the welded materials during the laser welding process, as shown in Figure 5.19 (a).

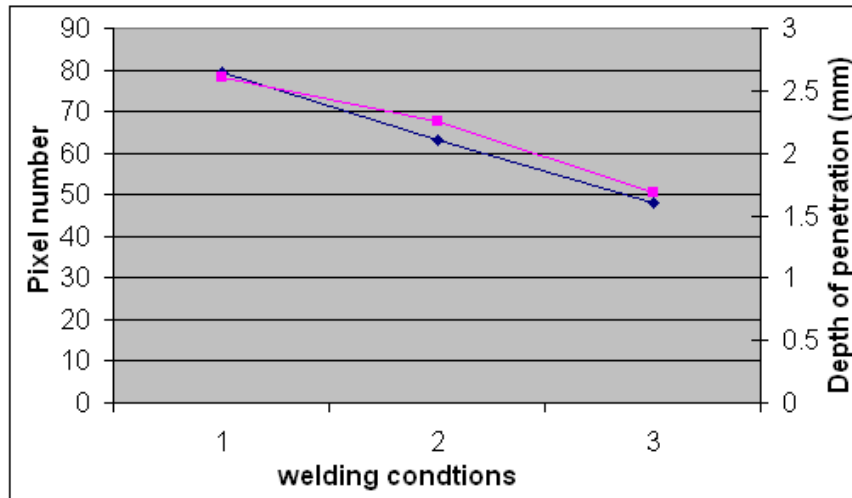
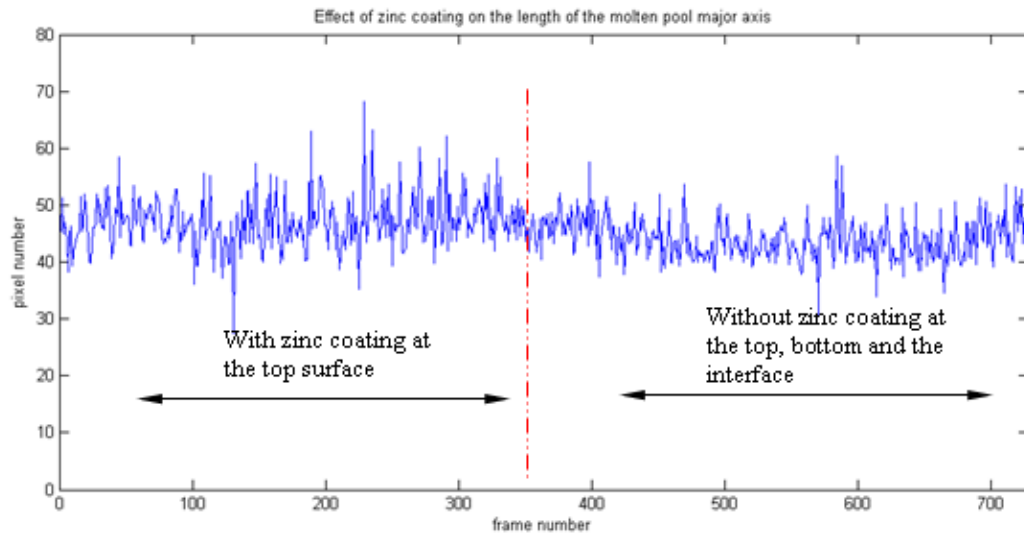


Figure 5.21 Relationship between the average length of the bright spot and depth of penetration and different welding conditions (1: GTAW torch preheating and laser welding is synchronously performed; 2 GTAW torch preheating the welded materials)

5.3.7 Effect of Zinc Coating at the Top Surface of the First Metal Sheet on the Dynamic Behaviors of the Bright Spot

To investigate the effect of the zinc coating at the top surface on the dynamic behaviors of the bright spot, the zinc coating at the interface of the two metal sheets is removed before the welding process is conducted. Figure 5.22 shows the experimental results. As shown in Figure 5. 22 (a), the length of the major axis of the bright spot that corresponds to the weld obtained with the zinc coating at the top surface of the specimens is slightly larger than the length obtained without the zinc

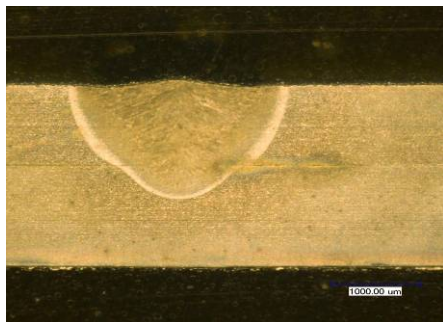
coating at the top surface of the specimens. Additionally, it is observed that when the zinc coating exists at the top surface, the weld surface is smooth, uniform, and free from the formation of reinforcement or underfills. When the zinc coating at the top surface is removed, however, a small reinforcement and small underfills are presented in the center and both sides of the welds respectively, as shown in the Figure 5. 22 (d). Additionally, it is observed that the depth of weld penetration in the welds with the zinc coating at the top surface is reduced compared to that obtained without the zinc coating at the top surface, as shown in Figure 5.22 (c) and (d). This phenomenon can be explained by the fact that when the zinc coating exists at the top surface, a large volume of laser-induced zinc plume and metal vapor is formed directly on the top surface of the specimens due to the low boiling point of zinc and the use of high power, as illustrated in Figure 5.23. The laser-induced plume defocuses, blocks and absorbs a portion of the laser beam energy [193]. The defocused laser beam is reradiated to the workpiece, which enlarges the molten pool area. However, the reduced coupling efficiency of the laser beam energy into the specimens produces a shallower depth of penetration than that obtained without a zinc coating at the top surface of metal sheet. Figure 5.24 shows the six successive images of the bright spot when the laser beam passes away from the transition line between the zinc coating surface and no zinc surface.



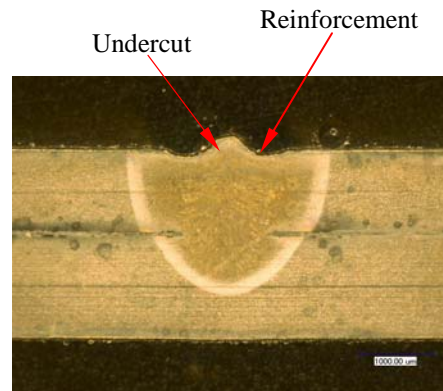
(a)



(b)



(c)



(d)

Figure 5.22 Effect of the zinc coating on the major axis length of molten pool (Laser power: 3000 W; welding speed: 50 mm/s; no zinc coating at the interface of two metal sheets)

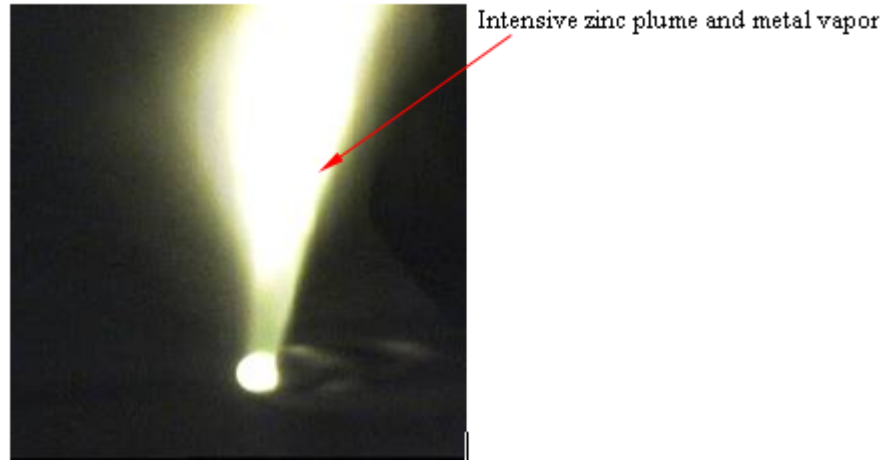


Figure 5.23 Laser-induced zinc plume and metal vapor

Transition line between the zinc coating surface and no zinc coating surface

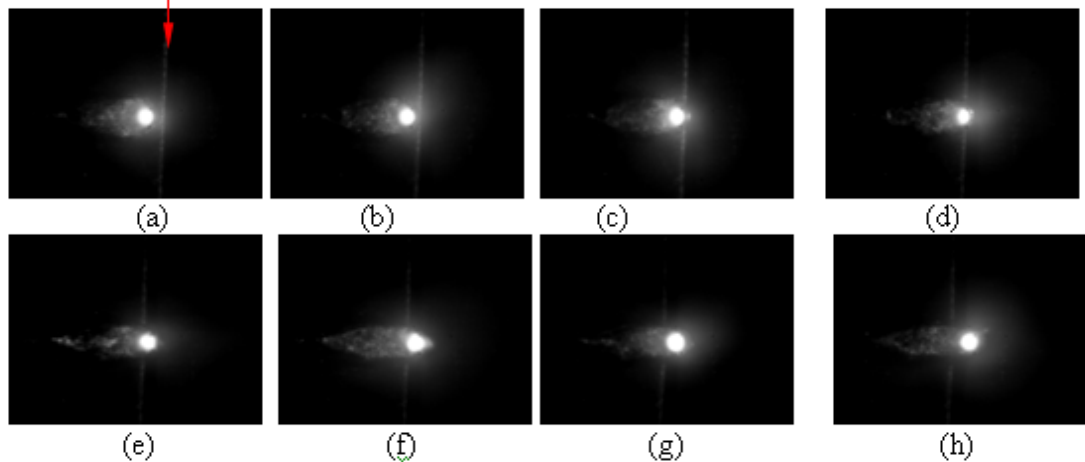


Figure 5.24 Captured images of the molten pool (laser power:3000 W; Welding speed:50mm/s)

5.4 Detection of the Spatter Formation by the Measurement of the Acoustic Emission

5.4.1 Experimental Setup

The gap-free lap joint weld of two galvanized steel sheets with a thickness of 1.2 mm and 1.5 mm is carried out using a continuous wave fiber laser of 4 kW in power. A 6-axis high precision robot is programmed to control the welding process.

The experimental setup is shown in Figure 5.25. Pure argon gas is used as the shielding protection of the molten pool. A strong air-knife blowing system is installed in the laser head to protect the laser optics from the damage by any spatters. An AE measurement system is developed to monitor the welding process on-line. The system consists of an AE sensor (Physical Acoustic PAC R30), a preamplifier, a digital (A/D) converter and AEWn AE data acquisition software that run in a continuous-sampling mode with a sampling rate of 2.56×10^6 . The developed AE acquisition system is schematically shown in Figure 4.8. The welding parameters used in this experiment are the laser power of 4 kW with a welding speed of 30 mm/s and an argon air flow rate of 30 CFH.

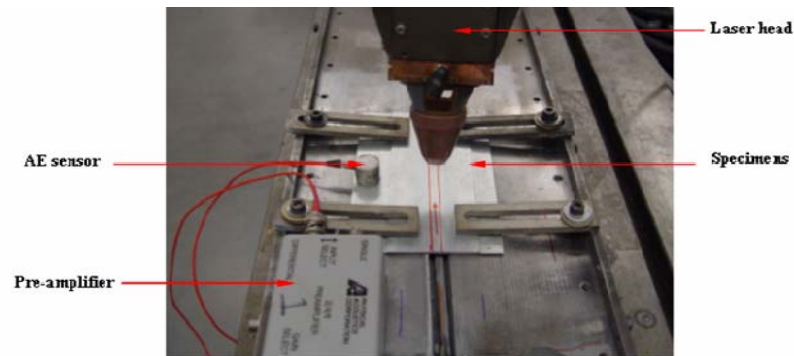


Figure 5.25 Experimental setup for the acquisition of the AE signals

5.4.2 Short Time Fourier Transform (STFT)

In general, a Short-Time Fourier Transform (STFT) is selected to determine the phase and frequency content of a signal that changes over time. Before applying the STFT method to determine the changes of a signal in the local section, a window function is needed to define a non-zero short period of time. Then, the value is multiplied by the function that needs to be transformed. The resulting signal further

takes the Fourier Transformation, which is selected as the second window. By sliding the second window along the time axis, the time-frequency representation of the AE signal is achieved. The resolution for time and frequency is adjustable.

Mathematically, if $x(n)$ represents the AE discrete-time signal to be transformed, the STFT can be written as [204-205]:

$$X(m, \omega) = \sum_{n=-\infty}^{\infty} x(n)w(n-m)e^{-j\omega n} \quad (5.5)$$

where $X(m, \omega)$ is the STFT representation of the discrete-time signal $x(n)$, ω is the discrete value for frequency, and $w(n)$ is the window function. The resolution for the discrete-time index m is less (“slower” time) than that of index n , and depends on the window function length. The window function is generally selected to be the Gaussian or Hann function that can be written as:

$$w(n) = 0.5 \times \left(1 - \cos\left(\frac{2\pi n}{N-1}\right)\right) \quad (5.6)$$

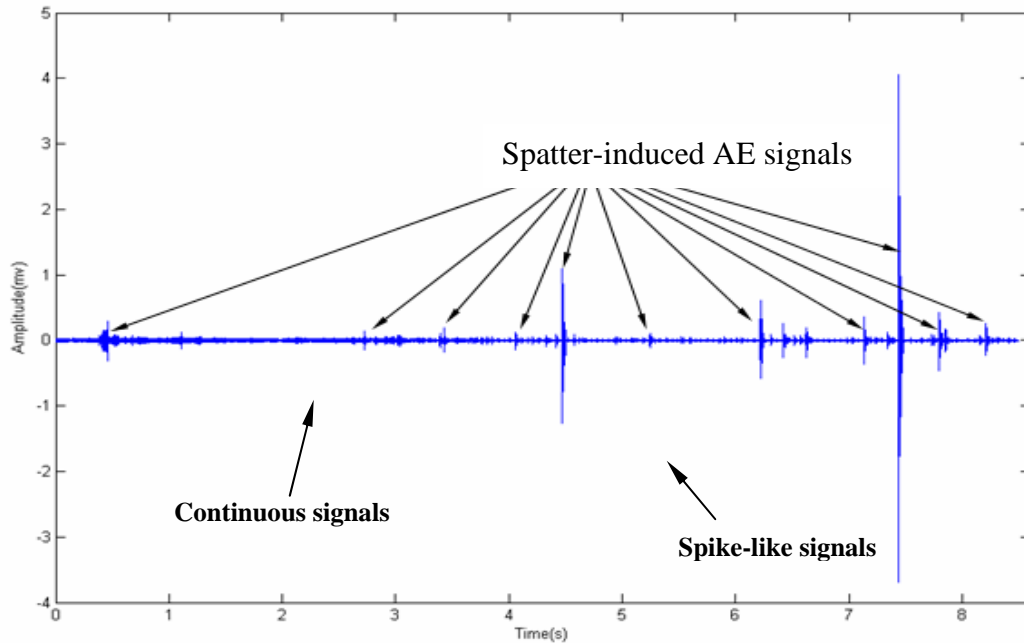
where N is the width of the discrete time window function. Typically, the value is selected as an integer to the power of 2 [204-205].

5.4.3 As-Acquired AE Signals and Welded Joints

The AE emitted from the laser welding process of the lap joint of the galvanized steel is collected on-line by the developed AE measurement system. A typical as-acquired AE signal plotted over time is shown in Figure 5.26. As seen from Figure. 5.26, the amplitude of the AE signal significantly varies in the welding process. There exist two distinct signals: (a) the continuous signal and (b) the spike-like

signal. The continuous signals are produced by the stable welding process. When the welding process is stable, the amplitudes of the AE signals are kept in a narrow range. The amplitudes of the spike-like signals vary in a wide range. When laser beam is delivered on the top metal sheet, the burst-type AE signals are rapidly generated in response to the transition of melting and solidification [206]. “Due to the considerable arrival of such burst-type AE signals with the amplitudes in a sustained level, they are treated as the continuous signal” [207]. When the spatter is produced, a spike-like AE signal with higher amplitude compared to that of the continuous AE signals appears in the collected AE signal. The spatter-induced AE signal is of a short duration; “the amplitude of which rises rapidly to a maximum value and decays very fast” [208]. Additionally, the amplitude and duration of the spatter-induced AE signal are directly related to the severity of the spatter occurrence. By comparing the collected AE signals to the obtained weld in this case, it is found that when the amplitude of the AE signals is more than 0.8mV, blowholes are present in the weld. The experimental results also showed that the welds with spatters will produce higher amplitude and a longer duration than the AE signals.

The as-welded specimen shown in Figure 5.27 confirms that there are many spatters on the top surface with some blowholes in the weld. The spatters deposited on the sheet surface and weld zone greatly degrade the weld quality. Additionally, post-weld cleaning is a time-consuming job.



(a)

Figure 5.26 AE signals acquired in the welding process

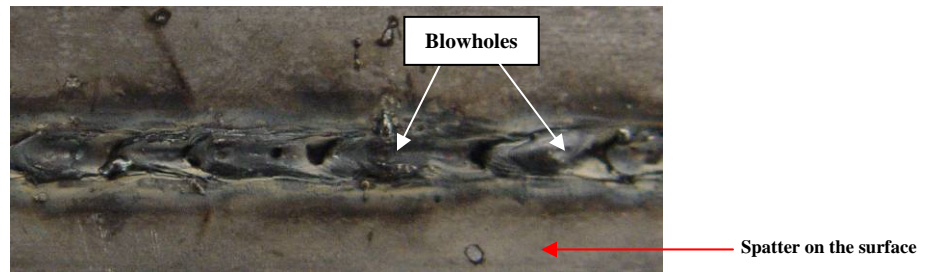


Figure 5.27 Typical as-welded lap joint obtained by laser welding

5.4.4 The Processed AE Signals Using the Short Time Fourier Transform

The AE signals emitted by the laser welding process not only contain the information from the time domain but also include frequency, energy, and power information because of the transient nature of the laser welding process. In order to investigate the features of the spatter-induced AE signals in the frequency domain, the collected signals in the time domain are further transformed into a time-

frequency power spectrum representation using the STFT. The typical results of the AE time-frequency power spectrum representation are shown in Figure 5.28, where the power spectrum density is the function of frequency and time. In general, the power spectrum amplitude is reflected in the color intensity; the darker the color, the higher the power spectrum amplitude. There are several pulses with a higher power spectrum, as shown in the Figure 5.28. A strike signal represents a discrete and burst-type AE signal that corresponds to spatter generation. As can be seen in Figure 5.28, the spatter-induced AE signal usually extends along a large frequency range. There exist two major frequency ranges: 2 kHz- 6 Hz and 6.3 kHz-7.6 kHz that generally have a higher power spectrum intensity compared to other frequency ranges. When the extent of spatter formation becomes more severe, the highest value of the frequency range is extended to 10 kHz. Additionally, the amplitudes of the power spectrum are usually very low in the frequency range (7.5 kHz-10 kHz). The sharp increase in the power spectrum intensity at these two frequencies indicates significant changes in the welding status. It is also clearly demonstrated at the bottom of STFT plot that there is a narrow frequency range (0 Hz-100 Hz) with the sustained power spectrum. The background noise is a main contributor to the frequency range. Based on the above discussion, the spatter-induced AE signals also exhibit the distinct features in the frequency domain.

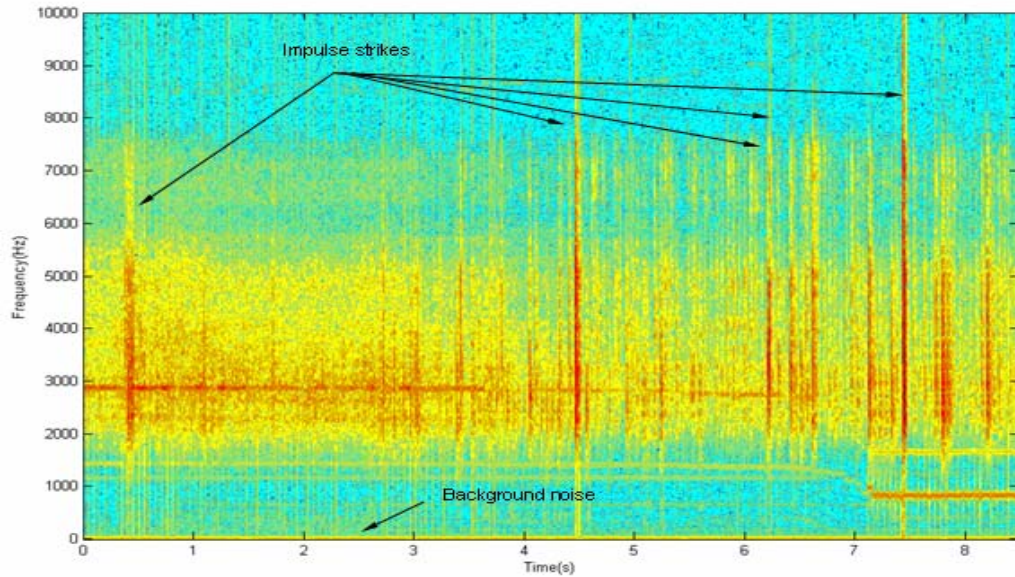


Figure 5.28 STFT Processed AE signals

5.5 Monitoring the Transition of the Welding Modes and Stability of the Welding Process by Machine Vision

5.5.1 Illumination of the Molten Pool

Because the high-speed CCD video camera is sensitive to a strong arc light and a zinc vapor plume, visualization of the molten pool can not be achieved with a conventional light source during the laser or hybrid welding process. An illumination source with high brightness is needed to acquire clear molten pool images. In this study, the band-pass green laser (Model: Coherent TracER green forensic laser system) with the center wavelength of 532 nm and a maximum output power of 6 W is selected as the illumination light source to suppress the strong arc light and zinc vapor plume. Figure 5.29 shows the experimental setup. As shown in the Figure 5.29, the green laser head is installed on one side of the laser welding head at an inclined angle of 45 degree with respect to the specimen and the high-

speed video CCD camera is installed on the other side with an incidence angle of 45 degrees with respect to the specimen in order to pick up the specular reflection of the green laser from the molten pool. The green laser head and the CCD camera travel simultaneously with the laser welding head along the welding direction.

The illumination green light is not used for the investigation of the relationship between the transition of the welding modes and the shape of the laser-induced plume directly above the specimens. However, the illumination green light will be selected as the illumination sources to suppress the strong laser beam light when studying the behavior of the keyhole and the molten pool in various welding conditions.

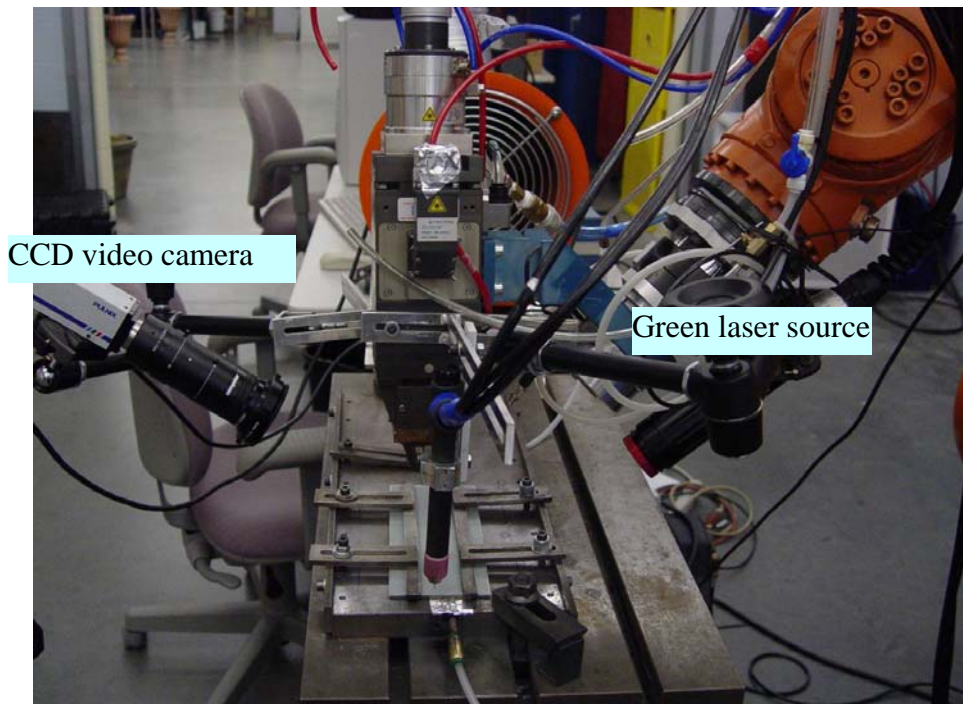


Figure 5.29 Experimental setup of illumination

5.5.2 Detection of the Transition of Welding Modes by the Shape of Laser-induced Plume

The conduction and keyhole welding modes can be easily distinguished by the shape of the plume. The video camera with a frame rate of 30 f/s, which is mounted at 45 degree with respect to the workpiece, is used to monitor the behavior of the plume directly above the specimens. The images of the molten pool and plasma plume are recorded on-line and displayed on a monitor screen.

It was found that when the welding process is under the conduction mode, the plume directly above the specimen is in the form of a diverging bright elliptical shape different from the fantail-shaped plume recorded in Holbert's study [209]. When the welding process is under the keyhole mode; however, the shape of the laser plume becomes columnar and agrees with the observations of Holbert et al. [209]. Figure 5.30 demonstrates the observed results of the CCD video camera for these two different welding modes. Furthermore, when the welding process is stable, the shape and height of the plume are kept almost constant. Figure 5.31 shows six successive images of the plasma plume when the weld processing is stable. As shown in Figure 5.31, the size and the height of the plasma plume is almost kept constant. The same phenomena occurred when the welding process is under the keyhole mode. Detailed studies of the time variation of the plume are not possible due to the slowness of the frame rate relative to the plume variation frequencies that are known to range up to about 15 kHz [210].

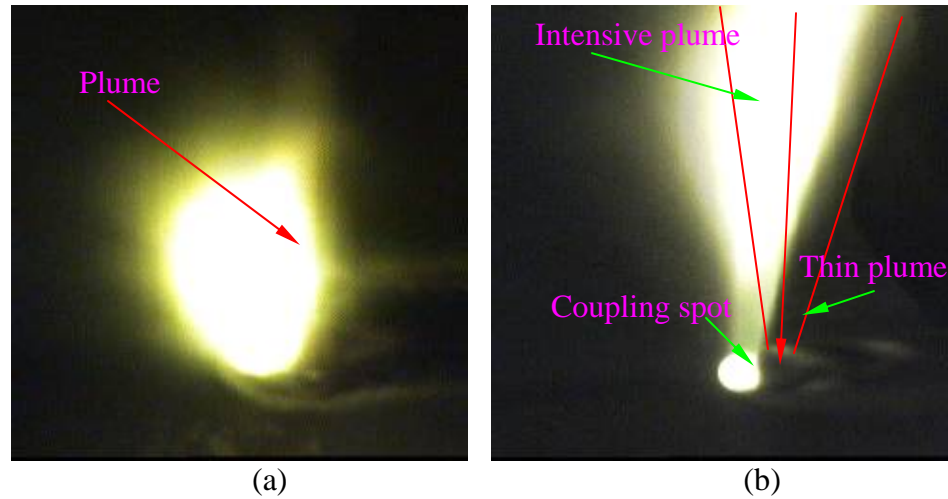


Figure 5.30 Plasma images (a) The plasma plume image corresponding to the fusion welding with respect to the laser power of 1300 W (b) The plasma plume with respect to the laser power of 1630 W.

As stated previously, the plasma plume has a significant influence on the coupling of the laser energy into the specimen. When the intensive plasma plume cloud forms straight above the workpiece, it is very difficult to form a keyhole when the laser power is very high. This can be explained by the fact that the intensive plasma plume defocuses, scatters and absorbs most of the laser beam intensity, thus preventing the laser beam energy from coupling into the material. The plasma plume can be blown out using cold shielding gas, as shown in the Figure 5.32. When the shielding gas is turned on, it forces the plasma plume to be blown away from the molten pool. At the same time the cold shielding gas can further prevent the formation of the plasma plume. As a result, the coupling rate of the laser beam energy is enhanced and helps in facilitating the formation of the keyhole. Figure 5.33 shows the effect of the shielding gas on the formation of the plasma plume. As shown in Figure 5.33 (a), when the shielding gas is turned off, the arc plume is formed directly above the specimens. When the shielding gas is

turned on, however, the arc plume is blown away from the top of the molten pool, as presented in the Figure 5.33 (c). From the cross-section views of the above welds, it is found that the deeper penetration is obtained when the shielding gas is turned on (Figure 5.33 d).

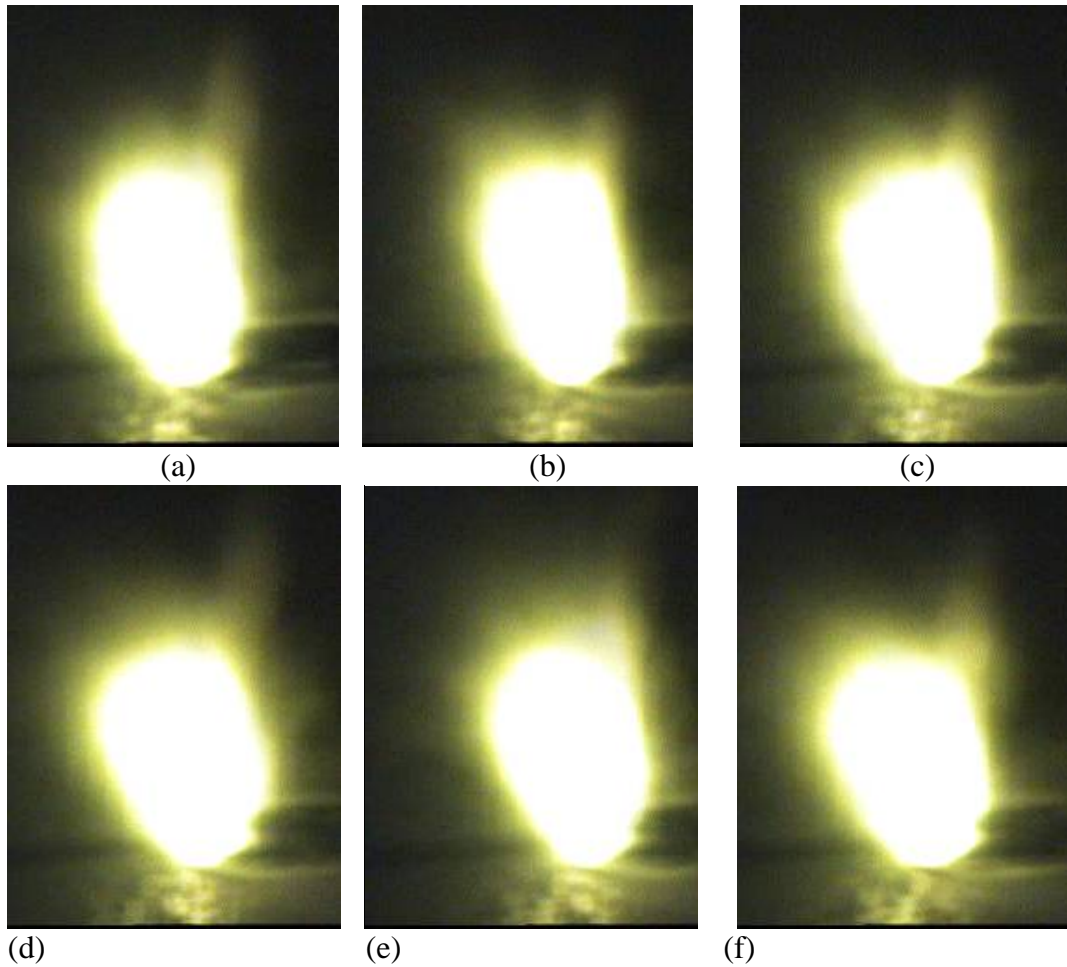


Figure 5.31 Six successive images of the plume when the weld pool is under the stable conduction mode

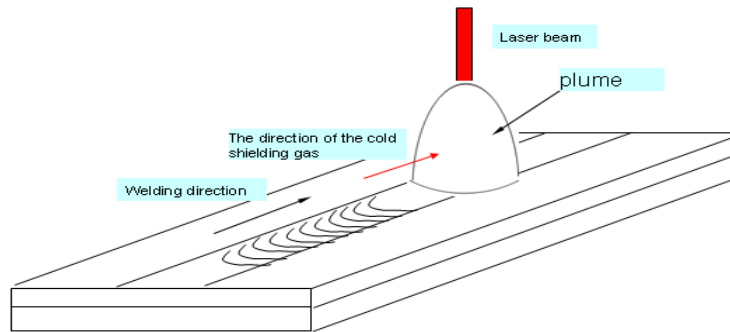
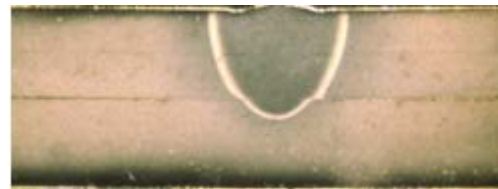


Figure 5.32 Schematic presentation of the shielding gas for blowing out the plasma plume



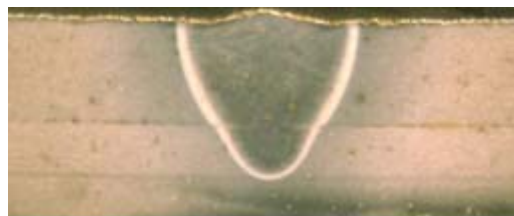
(a)



(b)



(c)



(d)

Figure 5.33 Effect of the shielding gas on the shape of the plasma plume and the weld penetration (a) the shape of the plasma plume when the shielding gas is turned off (b) the cross-section view of the weld when the shielding gas is turned off (c) the shape of plasma plume when the shielding gas is turned off (d) the cross-section view of the weld when the shielding gas is turned off (Laser power: 3000 W, welding speed: 30 mm/s, lap joint of 1.2mm-1.5mm DP 980 steel without zinc coating at the interface)

5.5.3 On-line Monitoring the Stability of the Laser/ GTAW Preheating Welding Process

As discussed in Chapter 3, the sustained opening of the keyhole is the most important factor for the successful production of a sound lap joint for galvanized DP 980 steel. On-line detection and analysis of the keyhole behavior by high-speed CCD video camera is a promising approach to investigate the dynamic behavior of the keyhole in different welding conditions. Figure 5.34 shows the schematic representation of the keyhole.

With the help of the illumination from the green laser light, the shape of the keyhole and the molten pool can be clearly observed by the CCD video camera because the green light can suppress the stronger light of the plasma and vapor plume. For this reason, on-line monitoring of the behavior of the keyhole becomes possible in a laser/GTAW preheating welding process. Figure 5.35 shows the images of the keyhole extracted from the stable welding process. Figure 5.36 shows the images of the keyhole extracted from the instable welding process. Generally speaking, when the welding process is stable, the flow of the metal in the molten pool is smooth and continuous without the swirling at the rear of the keyhole. Furthermore, the shape and size of the keyhole are changed temporally and spatially, and the keyhole always remains open in the stable welding status. However, it is observed that when the welding process is instable, the flow of the metal at the molten pool is dramatically turbulent and the keyhole fluctuates between a collapsed and an open status. In the stable welding process, the weld seam is very smooth and no spatters and blowholes are present, as shown in Figure 5.35 (a). However, a large number of spatters and blowholes are observed in the weld seam

when the welding process is instable. These weld defects are attributed to the failure to evacuate the high-pressurized zinc vapor at the interface. Examples of the appearance of the weld bead surfaces obtained from the instable welding process are shown in Figure 5.36. According to the R.Fabbro et al. study [211], the swirling melt flow in the rear of the keyhole is contributed to “the friction forces of the ejected metal vapor escaping from the keyhole.”

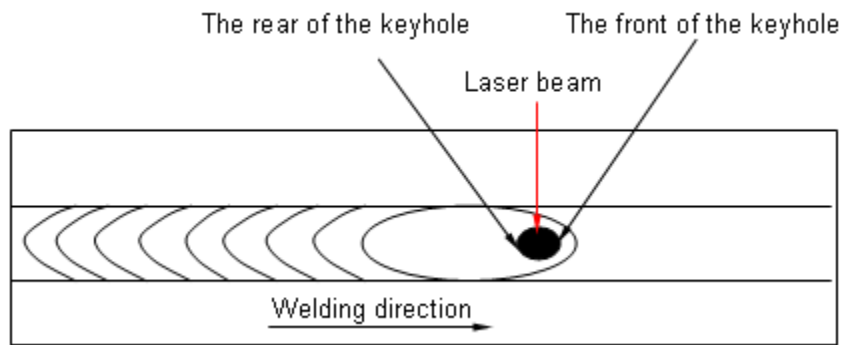
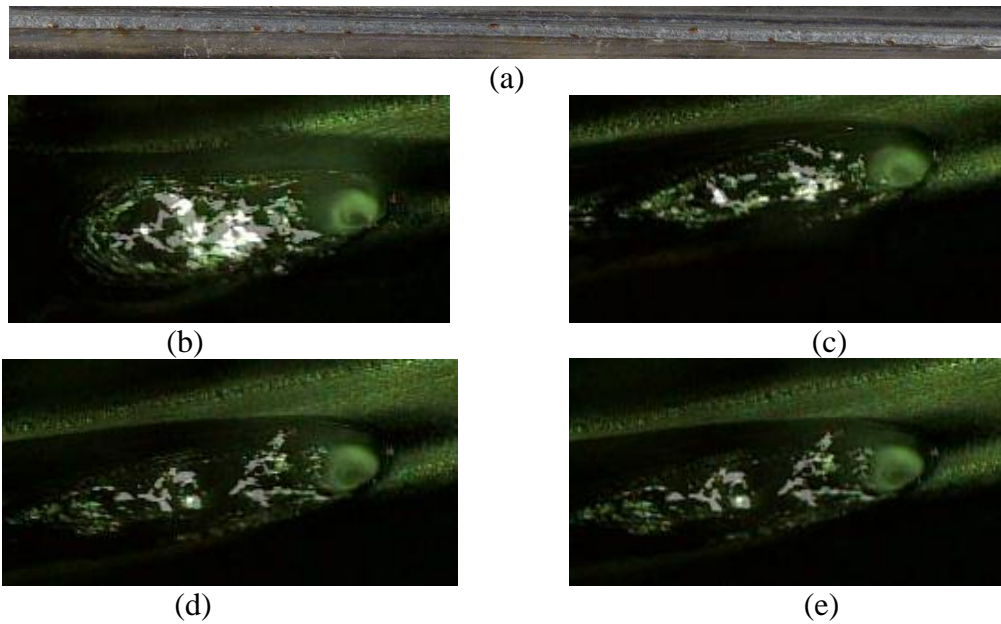


Figure 5.34 Schematic of the keyhole and the molten pool



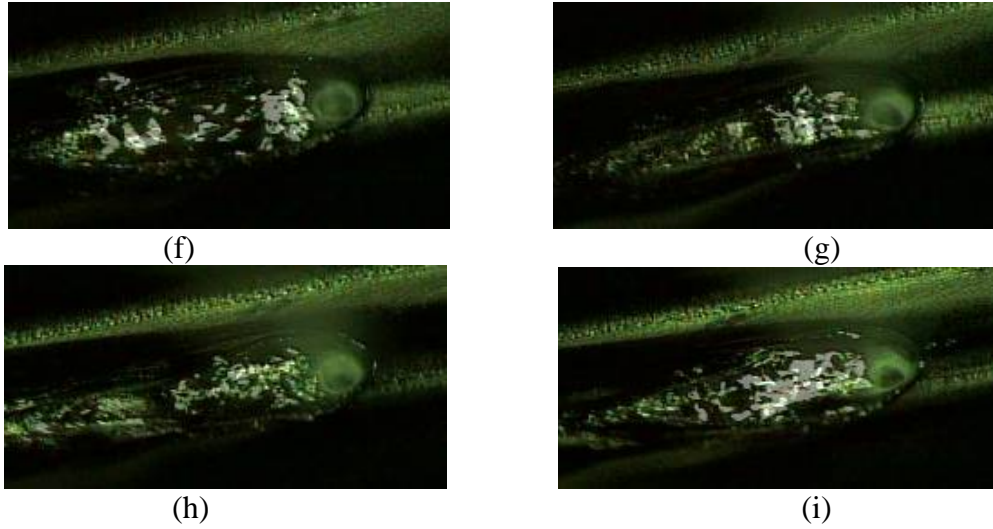
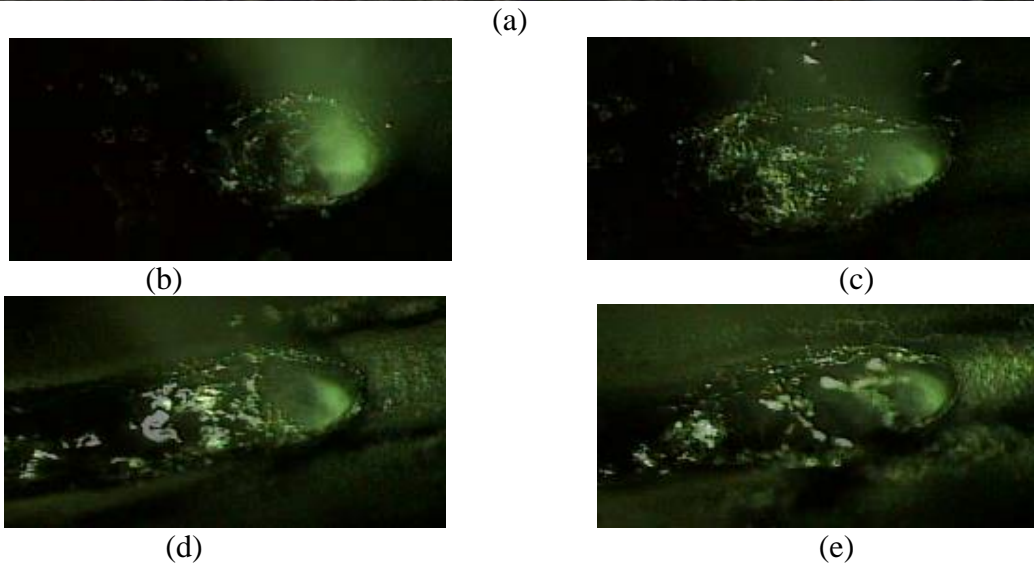


Figure 5.35 Images of the keyhole in the stable welding process (a) the top view of the weld surface in the stable welding process (b) $t = 0$ s (c) $t = 0.03$ s (d) $t = 0.07$ s (e) $t = 0.1$ s (f) $t = 0.13$ s (g) $t = 0.17$ s (h) $t = 0.2$ s (i) $t = 0.23$ s (j) $t = 0.27$ s (the welding parameters: a laser power of 3 kW, a welding speed of 30 mm/s, a preheating arc current of 200 A, a preheating welding speed of 30 mm/s and an argon gas flow rate of 30 SCFH)



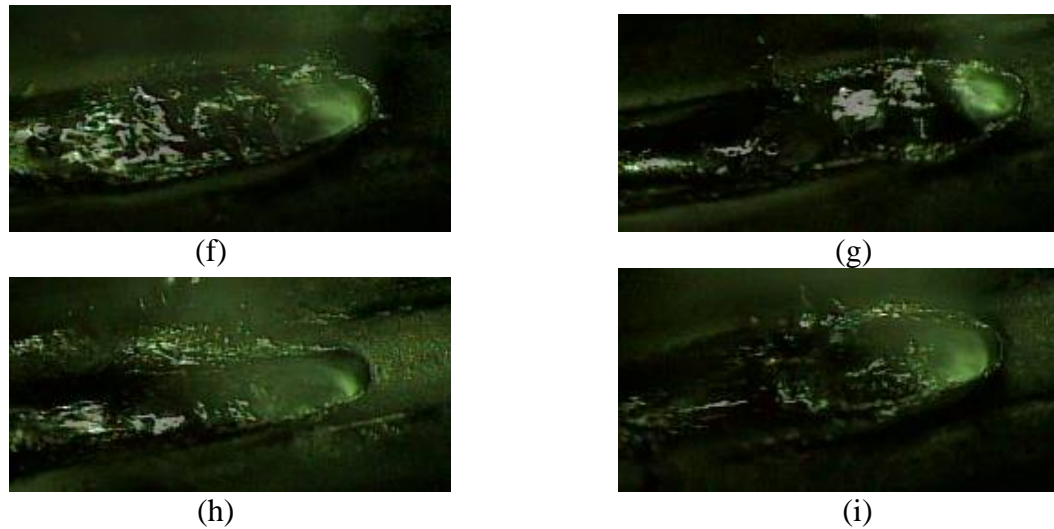


Figure 5.36 Images of the keyhole in the instable welding process (a) the top view of the weld surface in the stable welding process (b) $t = 0$ s (c) $t = 0.03$ s (d) $t = 0.07$ s (e) $t = 0.1$ s (f) $t = 0.13$ s (g) $t = 0.17$ s (h) $t = 0.2$ s (i) $t = 0.23$ s (i) $t = 0.27$ s (the welding parameters: a laser power of 3 kW, a welding speed of 30 mm/s, a preheating arc current of 120 A, a preheating welding speed of 30 mm/s and an argon gas flow rate of 30 SCFH)

5.6 Conclusion

In this study, a machine vision system based on the high-frame rate CCD camera is used to monitor the laser welding process of galvanized steels in lap joint configuration with different welding conditions. The main results are summarized as the following:

1. When using the single laser welding of galvanized steels in a gap-free lap joint configuration, the welding process is very instable, which is exhibited by the significant variation of the major axis length of the molten pool. However, in the stable welding process the major axis length of the molten pool varies in a very narrow range.

2. The number of spatters and blowholes are reduced by the use of hybrid laser-GTAW welding for joining the galvanized steels. However, due to the instable interaction of GTAW arc and laser beam there is still spatters and blowholes presented in the welds.
3. The completely defect-free lap joints are obtained by using the hybrid laser-GTAW welding with the separate molten pool in a gap-free lap joint configuration. The main reason for the successful achievement of the sound weld is that the zinc coating is burned off by the GTAW torch preheating and a thin layer of metal oxides are produced on the top surface of the first metal sheet. Under these welding conditions, the stable keyhole is maintained open and offers the channel of the evacuation of the highly-pressurized zinc vapor developed at the interface of two sheet metals.
4. The presence of the zinc coating at the top surface of the first metal sheet provides a smooth weld surface. However, the depth of weld penetration is decreased due to the defocus function of the laser-induced zinc plume compared to that obtained in the case of no zinc coating at the top surface of the first metal sheet.
5. The GTAW preheating process generates a thin layer of metal oxides at the top surface of the first metal sheet, which improve the coupling of laser beam energy into the specimens. When the GTAW preheating process is synchronously performed with the laser welding process at the specific distance for joining the galvanized steel, the depth of penetration is dramatically improved in comparison with the case of GTAW preheating for the specimens

and cooling prior to laser welding process and the case of no GTAW preheating for the specimens.

6. The undercuts are produced in the weld when the extensive gap exists at the interface of two metals. The wider gap results in more deeply concave undercuts in the weld. Additionally, the presence of the gap at the interface decreases the major length values of the molten pool.
7. When the spatter is formed, a spike-like AE signal with high amplitude will appear in the collected signals. The more severely spatters are produced, the higher the amplitude and the longer the duration of the AE signals. Generally speaking, the spatter-related AE signals have the higher power spectra compared to those associated with continuous AE signals and background noise.
8. The welding modes in the form of the keyhole mode and the conduction mode can be distinguished by the shape of the induced plume. In the keyhole welding process, a columnar-shaped plume is formed above the specimen. However, a diverging bright elliptical shape will appear above the specimen when the welding process is in the conduction mode. In order to directly obtain the molten pool, a band-pass green laser light is used to suppress the strong light of the plasma plume from the metal and the zinc vapor plume. It is found that when the keyhole is stable and stays open, the high-pressurized zinc vapor at the interface of two metal sheets can be vented out and completely defect-free welds are obtained. Nevertheless, the welding process becomes dramatically instable and lots of the spatters are produced in the welds when the keyhole is

collapsed. In addition, the flow of the metal in the molten pool becomes turbulent when the welding process is instable.

Chapter 6

NUMERICAL SIMULATION OF THE TEMPERATURE FIELD FOR HYBRID LASER-ARC WELDING OF GALVANIZED STEELS

6.1 Introduction

As shown in Chapter 3, there is a significant influence of the GTAW preheating arc current as well as the distance between laser beam and GTAW torch on the weld quality [212]. Additionally, it has been revealed that there is a direct relationship between the temperature distribution and the pressure level of the zinc vapor [213]. Until now, effects of various hybrid welding parameters on the transient temperature profiles during the hybrid welding process have not been fully explored since there is a coupling interaction of the two heat source. It is time-consuming and expensive using experimental method to determine the temperature profiles for the hybrid welding process. Sometimes it is even more difficult to get accurate results due to the interaction of the strong arc and the generated plasma during the welding process. The numerical analysis based on finite element method is the powerful tool to predict the temperature distribution for the welding process.

To simulate the conduction and keyhole welding modes, different heat source models have been used. Rosenthal [214] and Rykalin [215] developed a moving heat source to calculate the thermal history during the welding process. The accuracy of temperature distributions from the Rosenthal's model is limited by the

assumption of the infinite temperature at the heat source [216]. To overcome these limitations in the Rosenthal's model, Pavelic et al. [217] first proposed a heat source with the Gaussian normal distribution for the welding process. Not long after that, Krutz et al [218] and Friedman [219] combine the Pavelic's 'disc' model with finite element method (FEM) analysis to simulate the temperature distributions in the fusion zone and heat affected zone (HAZ). In comparison to the results obtained by the Rosenthal model, the better temperature distributions were achieved. The consequent works of Paley et al [220] and Westby [221] use a constant power density distribution in the fusion zone to simulate temperature distribution profiles with the finite difference analysis. Goldak et al [222]. proposed a three-dimensional "double ellipsoid" heat source model, which has been used to simulate the shallow and deep penetration welding process. This model is considered as the more realistic model with the flexible heat source than the other proposed heat source models since the characteristic parameters of the double ellipsoid heat source are selected on the basis of the real molten pool dimensions. Furthermore, Nguyen et al. [223] use the analytical solution to simulate the transient temperature of semi-infinite body with the 3D double ellipsoidal moving heat source. However, in the past the most of research was concentrated on the conduction welding mode.

In the recent years, various numerical models have been developed to simulate the keyhole welding process. Sudnik et al. [224] applied a semi-empirical approach to simulate the stationary penetration welding, which takes into account the laser-induced keyhole formation, the multiple reflection inside the keyhole and the plasma generation. It was found that there is a linear relationship between the depth

and length of the weld pool with the laser beam intensity. Fabbro et al. [225] built a model to study the keyhole geometry under different welding conditions where the front and rear of the keyhole wall are separately considered. It was found that the drilling velocity and the welding velocity resulted in the inclination of the front keyhole wall. Kroos et al [226] developed a model to study the stability of the keyhole, which is considered as the cylindrical shape and concentric to the laser beam. Ki et al. [227] developed a three-dimensional model to study the effects of evaporation, free surface evolution and the fluid flow and heat transfer. In addition, Dowden et al. [228] developed a model for the keyhole welding under the conditions of low welding speed. Lankalapalli et al. [229] assumed the keyhole as the conical shape and a two-dimensional heat conduction model is developed to predict the weld penetration depth. Recently, Wang et al [230] combined a rotary volumetric flux and the double ellipsoidal heat source to simulate the effect of assist gas flow on the shielding during laser deep welding. Also, Fang et al. [231] applied the double ellipsoidal heat source to model the influence of the welding sequence on the welding residual stress of a thick plate.

As discussed above, in the past most of keyhole modeling studies were focused on the laser welding only. There is no result in the open literature on studying the temperature distribution profiles for the gap-free hybrid laser-arc keyhole welding of galvanized steels by using FEM method. The main reason for this lack mainly arises from the complexity of the welding of galvanized steels in a gap-free lap joint configuration, including the uncertain physical interaction between laser beam and arc and the unknown dynamic behavior of the zinc coating at the interface of two

metal sheets. To better understand the influence of various welding parameters on the temperature distribution during the hybrid laser-GTAW process, a 3D FE model was developed to simulate the temperature distribution with the various GTAW arc current, the welding speed, and the distance between the laser beam and GTAW torch. In addition, effects of the characteristic parameters on the power density distribution in the heat source volume are studied. Based on the numerical results with the various combinations of the characteristic parameters of the double ellipsoidal heat source, a modified double ellipsoidal heat source model is proposed for the deep penetration hybrid laser-arc keyhole welding. The effect of zinc coating at the interface of two metal sheets on the temperature distribution profiles was taken into account. Experiments of hybrid laser-GTAW welding of galvanized steels in a gap-free lap joint configuration were performed with the measurements of the temperature history by the thermocouples. Optical microscopy examinations were performed to observe the dimensions and shape of fusion zone. The high speed camera was used to on-line monitor the welding process in order to obtain the shape of the molten pool, which is used for the comparison with the calculated results from the FEM model. The geometry of the molten pool and the weld penetration can be predicted by the modified double ellipsoidal heat source. The good agreement between the numerical and experimental results show the potential application of this newly modified double ellipsoidal heat source for various deep penetration keyhole welding processes such as laser keyhole welding and electron beam keyhole welding. The simulation was carried out with the ANSYS APDL program.

6.2 Material and Experimental Procedure

The used material for welding in this paper is galvanized high-strength dual phase (DP) 980 steel with the thicknesses of 1.2 mm and 1.5 mm. The chemical composition is shown in the Table 1 [232]. In this study, the melting point of DP 980 is assumed to 1400°C and its boiling point is fixed to 2600°C for the simulation.

Table 6.1 Chemical composition (%) of the DP 980 steel [232]

Steel	C	Si	Mn	Mo	Al	Cr	B
DP 980	0.135	0.05	2.1	0.35	0.45	0.15	0.007

The experiments on hybrid laser-GTAW torch preheating were performed on the coupons with the size of 120mm x 60 mm x 1.2 mm and 120 mm x 60 mm x 1.5 mm in a gap-free lap joint configuration. During the hybrid laser-arc welding process, the high-power laser beam is preceded by the GTAW welding process at the specific distance, which is used as a preheating source. Pure argon gas was selected as the shielding gas with the flow rate of 30 SCFH. Additionally, the temperature measurements were performed by the K-type thermocouples. A high-speed camera with the frame rate of 4000 f/ps was used to obtain the shape and size of the molten pool. Figure 6.1 shows the experimental setup.

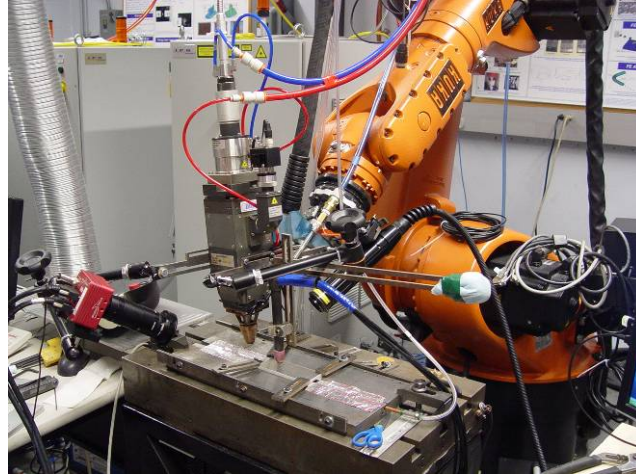


Figure 6.1 Experimental setup

6.3 Numerical Model

6.3.1 FE Model and the Build of Hybrid Heat Source Model

The full 3D FE model with the dimensions of 70 mm x 50mm x 2.740 mm for the laser-GTAW welding process is developed in ANSYS, as shown in Figure 6.2. The SOLID70 with linear 8-node brick element is selected for the thermal analysis. A relatively fine mesh is used around the weld zone and heat-affected zone due to the expected high temperature and heat flux around them. In the regions away from the fusion zone and HAZ zone, the relatively coarse mesh is applied. The total number of elements and nodes are 54,600 and 60,634, respectively. The thickness of zinc coating for one layer is assumed to be $20 \mu\text{m}$. The volume of the FEM model is 70 mm x 50 mm x 2.74mm.

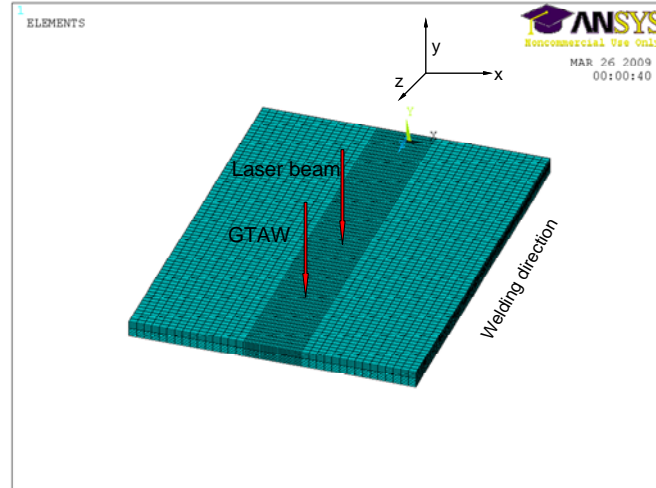


Figure 6.2 3D FE model

In comparison to the point, line and plane heat source models [215] as well as the rotary Gaussian body heat source model [214], the double ellipsoidal distributed heat source becomes more and more popular due to its flexibility of accurately modeling the shape of the molten pool and the nonlinearities such as the temperature dependences of the specific heat and thermal conductivity [233]. In this investigation, the moving double ellipsoidal distributed heat source is used to simulate the hybrid the laser-GTAW torch preheating process. Figure 6.3 shows the configuration of double ellipsoid heat source [233]. The governing equations of the double ellipsoidal distributed heat source that control the deposited heat in the welded material are given by the following equations [233]:

For the front quadrant:

$$q(x, y, z, t) = \frac{6\sqrt{3}f_f Q_L}{a_f b c \pi \sqrt{\pi}} e^{-3x^2/a^2} e^{-3y^2/b^2} e^{-3[z+v(\tau-t)]^2/c^2} \quad (6.1)$$

For the rear quadrant

$$q(x, y, z, t) = \frac{6\sqrt{3}f_r Q_L}{a_r b c \pi \sqrt{\pi}} e^{-3x^2/a^2} e^{-3y^2/b^2} e^{-3[z+v(\tau-t)]^2/c^2} \quad (6.2)$$

Where f_r and f_f are the fractions of the heat applied in the front and rear quadrants of the joint, Q_L is the energy input rate of the laser power, v is the welding speed, τ is the lag time, and t is the time. The relationship between f_f and f_r is $f_f + f_r = 2$ [233]. The GTAW preheating heat flow is in the form of Gaussian distribution. It can be defined as the following [236]:

$$q(x, z, t) = \frac{3Q_{arc}}{\pi r_b^2} \exp\left(-\frac{3}{r_b^2}[x^2 + (x - vt)^2]\right) \quad (6.3)$$

Where Q_{arc} the heat is input and r_b is the distribution radius.

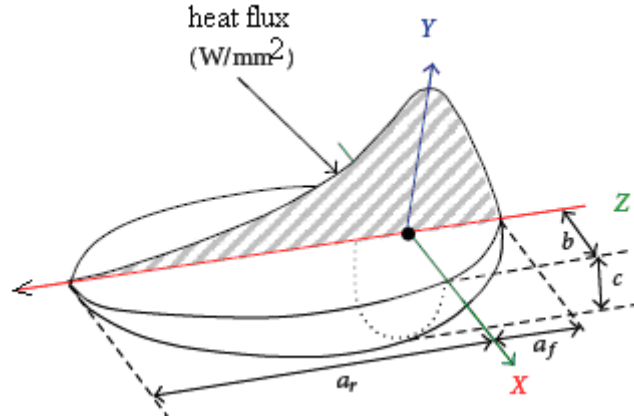


Figure 6.3 Double ellipsoidal heat source configuration [233]

6.3.2 Assumptions

To build the model, the following assumptions were made:

- Since different chemical composition can be produced with different GTAW preheating conditions, effect of the zinc coating at the top surface of metal sheets on the temperature distribution was neglected. Its effect on the temperature distribution profiles was only taken into account to enhance the absorptivity of laser beam energy into the welded materials.
- During the leading GTAW preheating process, the zinc coating at the interface of two metal sheets along the weld line is transformed into zinc oxides. So, the thermo-physics material properties for the zinc coating at the interface of two metal sheets are switched from zinc into zinc oxide and steel when the temperature is beyond the 420°C (melting point for the zinc).
- Effect of zinc coating at the bottom surface on the temperature distribution is neglected. In addition, when the laser beam shares the same molten pool with the arc during the hybrid laser-GTAW torch preheating welding process, the interaction between laser beam and arc is neglected. Since the temperature-dependent thermophysical properties of DP 980 steel is applied in the FEM model and the transformation of the zinc coating during the hybrid laser-arc welding process is also taken into account, the thermal analysis in this study is highly nonlinear. To reduce the calculation time, the thermal contact resistance between the top and bottom plate is also not included in the present model.

6.3.3 Governing equation, initial and boundary conditions

The governing equation for transient heat transfer analysis is given by (6.4):

$$\rho C_p \left(\frac{\partial T}{\partial t} - v \frac{\partial T}{\partial z} \right) = \frac{\partial}{\partial x} \left(k \frac{\partial T}{\partial x} \right) + \frac{\partial}{\partial y} \left(k \frac{\partial T}{\partial y} \right) + \frac{\partial}{\partial z} \left(k \frac{\partial T}{\partial z} \right) + Q_v \quad (6.4)$$

Where ρ is density, C_p is specific heat, T is temperature, k is thermal conductivity, Q_v is volumetric heat source, v is the travel speed and x, y, z are the coordinate system attached to the heat source, respectively. The natural boundary condition is given by the equation:

$$k_n \frac{\partial T}{\partial n} - q + h_{con} (T - T_0) + \sigma \varepsilon (T^4 - T_0^4) = 0 \quad (6.5)$$

on the regions S_A which are subject to the heat flux, convection, and radiation. k_n is the thermal conductivity normal to the S_A , h_{con} is the heat coefficient for convection, σ is the Stefan-Boltzmann constant for radiation ($5.67 \times 10^{-8} \text{ Wm}^{-2} \text{ K}^{-4}$), ε is the emissivity, and T_0 is the ambient temperature, q is the heat input normal to the regions S_A . For the weld zone, the combined heat transfer coefficient for convection and radiation is calculated to determine the total heat loss by the convection and radiation from the relationship [233]:

$$H = 24.1 \times 10^{-4} \varepsilon T^{1.61} \quad (6.6)$$

Where H is the combined heat transfer coefficient for convection and radiation and T is the temperature. A value of 0.9 was assumed for ε (theoretically speaking, emissivity is equal to the absorption which is assumed to 0.9 in the later section) since the generated metal oxides by GTAW preheating can dramatically improved the coupling efficiency of laser beam energy into the welded material by 2-3 times. At the symmetric plate of YOZ,

$$\frac{\partial T}{\partial X} = 0 \quad (6.7)$$

The initial temperature of the whole metal sheets is given by;

$$T(x, y, x, 0) = T_0 \quad (6.8)$$

Where T_0 is ambient temperature (20 °C).

6.3.4 Determination of the Thermophysical Properties of DP 980 for the Thermal Analysis

Due to its commercial proprietary of DP 980 steel, the thermophysical properties of DP 980 steel is still absent. In this study, the assumption is made that the chemical compositions is uniformly and completed mixed together in the DP 980 steel and no interactions between the individual components occur. Also, no alloy element is evaporated during the hybrid laser-GTAW preheating process. Additionally, effects of the variations of martensite and ferrite fractions on the thermophysical properties of DP 980 steel were neglected. Based on the aforementioned assumptions, the thermophysical properties of DP 980 steel can be mathematically calculated by the linear combination of the thermophysical properties of the individual components. In this study, the temperature-dependent themophysical properties of DP 980 are approximately given by the following equations:

$$K^T = f_{Fe} K_{Fe}^T + f_{Cr} K_{Cr}^T + f_{Si} K_{Si}^T + f_{Al} K_{Al}^T + f_{Mo} K_{Mo}^T + f_C K_C^T \quad (6.9)$$

$$C_p = f_{Fe} C_{PFe}^T + f_{Cr} C_{PCr}^T + f_{Si} C_{PSi}^T + f_{Al} C_{PAL}^T + f_{Mo} C_{PMo}^T + f_C K_{PC}^T \quad (6.10)$$

$$Q = \rho \bar{C}_p \Delta T = Q_{Fe} + Q_{Cr} + Q_{Si} + Q_{Al} + Q_{Mo} + Q_C \quad (6.11)$$

$$\bar{C}_p = \frac{V_{Fe}\rho_{Fe}C_{pFe} + V_{Cr}\rho_{Cr}C_{pCr} + V_{Si}\rho_{Si}C_{pSi} + V_{Al}\rho_{Al}C_{pAl} + V_{Mo}\rho_{Mo}C_{pMo} + V_C\rho_C C_{pC}}{\rho_{Fe}C_{pFe} + \rho_{Cr}C_{pCr} + \rho_{Si}C_{pSi} + \rho_{Al}C_{pAl} + \rho_{Mo}C_{pMo} + \rho_C C_{pC}} \quad (6.12)$$

Where K^T is the thermal conductivity at the temperature T, f_i is the weight percentage of the individual chemical composition (i = Fe, Cr, Si, Al, Mo, and C), K_i^T is the thermal conductivity of the individual chemical composition at the specific temperature T (i = Fe, Cr, Si, Al, Mo, and C), and C_{pi}^T is the heat capability of the individual chemical composition at the specific temperature T. The thermal conductivity and heat capacity of the individual chemical composition are taken from the reference [215]. Table 2 gives the values of thermal conductivity and heat capability at the different temperatures. The liquid phase enthalpy is given by the equation:

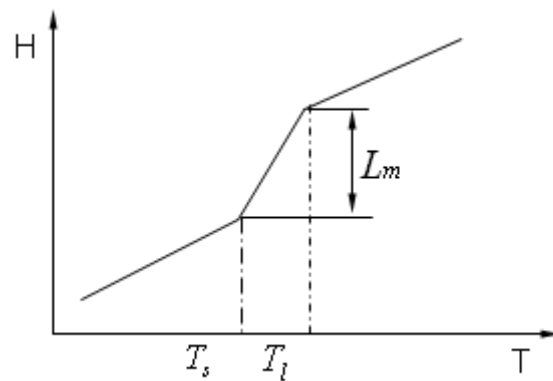
$$H_l = \int_0^{T_s} C_{pT_s} dT + L_m + \int_{T_s}^{T_l} C_{pT_l} dT \quad (6.13)$$

Where T_s and T_l is the solidus and liquidus temperatures and L_m is the heat of fusion. In this study, the solidus and liquidus temperature (T_s and T_l) are assumed to 1380 °C and 1400°C, respectively. The heat of fusion during the hybrid laser-arc preheating welding process can be considered by varying the specific heat [240]. Since the heat of fusion for iron is 2.66 KJ/Kg [241], the heat of fusion is given by the following equation:

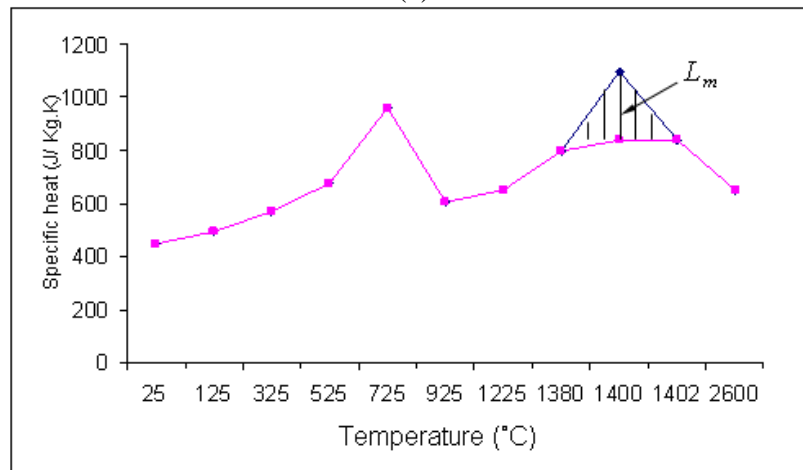
$$\sum C_p \Delta T_i = H_i \quad (6.14)$$

$$\Delta T = T_l - T_s \quad (6.15)$$

At the liquidus temperature of 1400 °C, the specific heat for the DP 980 steel is assumed to the value of 0.8368 KJ/Kg.K, which is the specific heat of the 304 stainless steel [242]. From the equations of (6.14) and (6.15), the increased specific heat (ΔC_{pl}) accounting for the latent heat is 0.266 KJ/Kg.K. Therefore, at the temperature of 1400 °C, the specific heat of DP 980 steel is set to the value of 1.1 KJ/Kg.K in order to take into account the heat of fusion. Figure 6.4 demonstrates the temperature-dependent specific heat graph.



(a)



(b)

Figure 6.4 Temperature-dependent specific heat (a) schematic representation of enthalpy (b) time-dependent specific heat

Compared to the values of the thermophysical properties of dual phase steel obtained in reference from the experiment [238], the approximate thermophysical properties calculated by the equations 8 and 9 are reliable to be used in the FEM model. The density of DP 980 steel is assumed to 7850 kg/m³.

Table 6.2 the approximate thermophysical properties of DP 980 steel

Temperature (°C)	25	125	325	525	725	925	1225
Specific heat (KJ/kg•K)	0.449	0.491	0.572	0.675	0.961	0.607	0.651
Thermal conductivity (W/m•K)	69.5	66.5	55.1	44.3	40.5	36.6	36.6

The thermophysical properties of the zinc coating at the interface of two metal sheets are used from the pure zinc (20 °C<T<420 °C) and the zinc oxide (420 °C <T< 1400 °C) to steel (T>1400 °C) since the zinc coating along the weld line is transformed into zinc oxide during the GTAW preheating by GTAW [239]. The constant values of 7100 kg/ m³ and 5675 kg/m³ are used as the densities of zinc and zinc oxide, respectively. This method is used in the present work to account for the latent heat corresponding to the melting and evaporation in fusion zone and the keyhole formation in the FEM model. In addition, the laser energy input is equal to $\eta_{laser} P_{laser}$, where P_{laser} is the input laser power and η_{laser} is the efficiency of laser. The η_{laser} was considered as 0.9 since the zinc oxides can improve the coupling efficiency of laser power into the welded material by 2-3 times [243]. The arc heat deposited into the material is taken as $\eta_{arc} UI_{arc}$, where η_{arc} is the efficiency of arc

power, U is the voltage and I_{arc} is the arc current. Here, the η_{arc} is fixed to 0.7 in this study.

6.4 Results and discussions

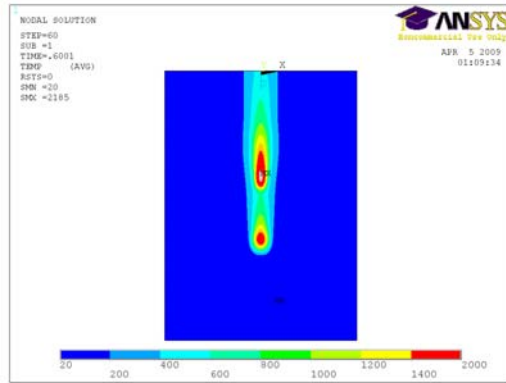
6.4.1 Selection of the Characteristic Parameters of the Heat Source

As shown in Equation (1) and (2) there are four characteristic parameters i.e.a, b, c, f, which is needed to be determined for the moving double ellipsoidal heat source. The values of a,b,c,f in the Equation (1) and (2) can be different from each other because they are independent [234]. By trials, it was found that the shape profile and magnitude of the power density distribution profiles of the heat source are non-linearly changed by the variations of the characteristic parameters of the heat source. Small changes in these characteristic parameters will result in the significant changes in the profiles and magnitude of the power density distribution. Consequently, the transient temperature distribution profiles and peak temperatures during the welding process are changed. Therefore, it is very critical to select the values of the characteristic parameters of the heat source in order to accurately predict the temperature distribution profiles for hybrid laser-arc welding of galvanized steels in a gap-free lap joint configuration.

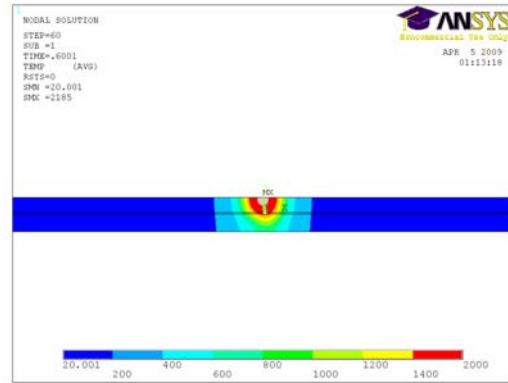
Physically, the values of characteristic parameters a_f, a_r, b , and c are equal to the sizes of the molten zone in front, behind, to the side and underneath the heat source”, respectively [234]. Therefore, in the present work the dimensions of the characteristic parameters of the heat source were related to the dimensions of the real molten pool obtained under the different welding conditions. Some of the

values were linked to the size of the solidified weld bead. For instance, the width and depth of the cross-section of the weld bead were used to determine the width and depth of the heat source. The lengths of the front and rear quadrants of the heat source are calculated based on the molten pool size recorded by the high speed camera. Based on the experimental results, a_f, a_r, b, c are selected to meet the real situation as the 1 mm, 4mm, 2mm, and 2.7 mm for the case of laser power of 3000 W, GTAW arc current of 300 A and welding speed of 3 m/s, respectively. In order to keep the continuity of the volumetric heat source at the XOY plane, $f_f, f_r, a_f,$ and a_r should be meet the relationships between them: $f_f = 2a_f / (a_f + a_r)$ and $f_r = 2a_r / (a_f + a_r)$ [235]. Therefore, for $a_f = 1$ and $a_r = 4$, here f_f and f_r are equal to 0.6 and 1.4, respectively.

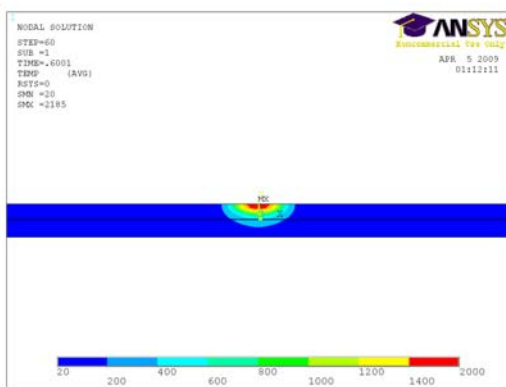
Figure 6.5 shows the temperature distribution profiles. As shown in Figure 6.5(a), the calculated shape of the molten pool in Figure 6.5 (a) obtained by the FEM model has a good agreement with the shape of the real molten pool, obtained by the CCD camera. However, as shown in Figure 6.5(b) only the very shallow of the penetration is obtained by the FEM model, which is not in accordance with the experimental achievement of full penetration in Figure 6.6 (c). Therefore, it is become very important and necessary to find a way to adapt the proposed double ellipsoidal heat source model in order to be able to model the deep penetration for the keyhole welding process. Figure 6.7 schematically shows the keyhole welding mode and conduction mode.



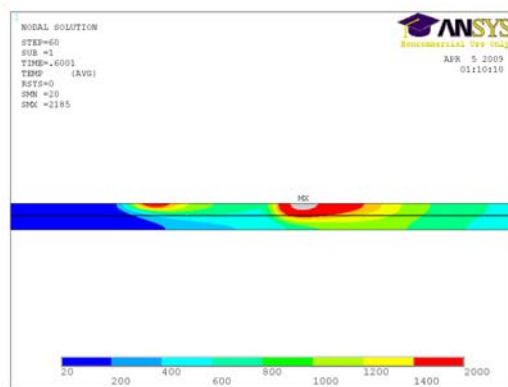
(a)



(b)



(c)



(d)

Figure 6.5 Temperature distribution profiles obtained by the numerical results (a) temperature profiles of top view in the numerical result (b) temperature profiles of cross-sectional view of the laser-welded fusion zone in the numerical result (c) temperature profiles of cross-sectional view of the arc-welded fusion zone in the numerical result (d) temperature profiles of the longitudinal view of hybrid laser-arc weld zone (Laser power: 3000 W; arc current: 300 A; welding speed: 50 mm/s; $a_f = 1, a_r = 4, b = 2, c = 2.7, f_f = 0.6, f_r = 1.4$; $t = 0.6$ s);



(a)

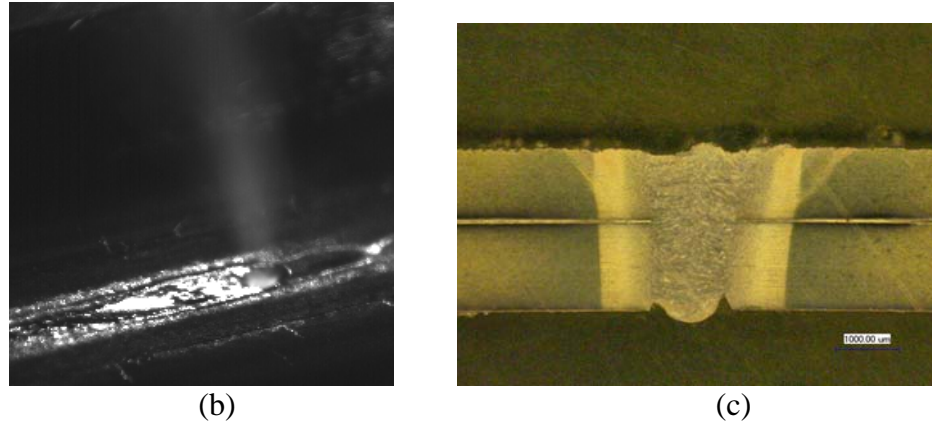


Figure 6.6 Experimental results obtained during the hybrid laser-arc welding process (a) top view of the welded lap joint (b) the real molten pool (c) the cross-sectional view of the lap joint (Laser power: 3000 w; welding speed: 3.0 m/min; GTAW preheating arc current: 300 A; distance between laser beam and GTAW torch: 15 mm)

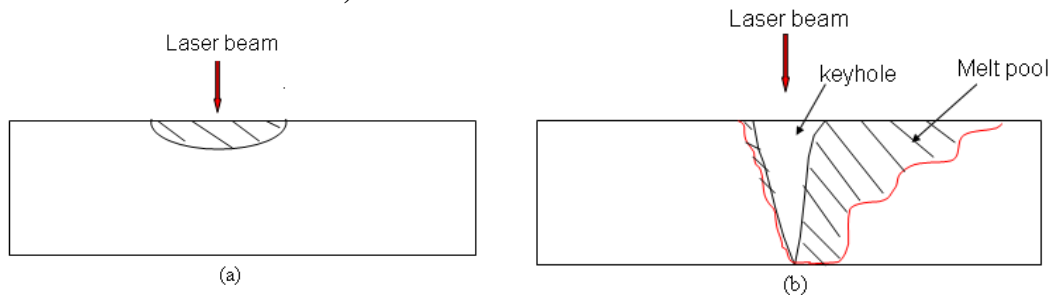


Figure 6.7 the schematic presentation of the conduction and keyhole welding modes

It is well-known that the deep penetration by laser is possible only if the power density is in excess of $10^6 W/cm^2$ [244]. Furthermore, due to the function of the multiple reflection and Fresnel absorption of laser beam inside the keyhole most of laser beam energy can be coupled into the welded material compared to the conduction welding mode. As shown in the Figure 6.8 (a), it was clearly seen that the power density is immediately decreased to a very lower level along the weld penetration direction when using the present double ellipsoidal heat source. Therefore, it is conjectured that the reason for the failure of achieving the deep weld

penetration with the present double ellipsoidal heat source is that the power density distribution is not identical to the real situation and suitable for the deep penetration keyhole welding. This speculation is reasonable since there are different absorption and heat distribution mechanisms between the keyhole welding mode and the conduction welding mode. The reason for the high accuracy of the numerical results obtained by the present double ellipsoidal heat source model for the conduction welding mode is the fact that no heat flux is applied inside the welded materials and the energy is mainly delivered into the workpiece through the thermal conductivity. In contrast, there is the heat flux directly deposited inside the keyhole wall and delivered to the welded materials through the thermal conductivity when the welding process is conducted in the keyhole welding. Therefore, the conclusion can be made that the power density is not diminished in the way described by the present double ellipsoidal heat source model.

As a volume heat source, it can be imaged that for the constant volume increasing the power density distribution inside the double ellipsoidal volume will increase the temperature of the welded materials. There are two promising ways to achieve this goal: one is to linearly increase the input power in the double ellipsoidal heat source equation; another is to change the power density distribution inside the volume. From the numerical results, it was found that linear increasing the input laser power still fails to provide the deep penetration, as shown in Figure 6.9. Moreover, the calculated molten pool sizes are larger than those dimensions of the molten pool corresponding to the real input power. Therefore, it is not in accordance with the real situation. It was conjectured that the main problem of

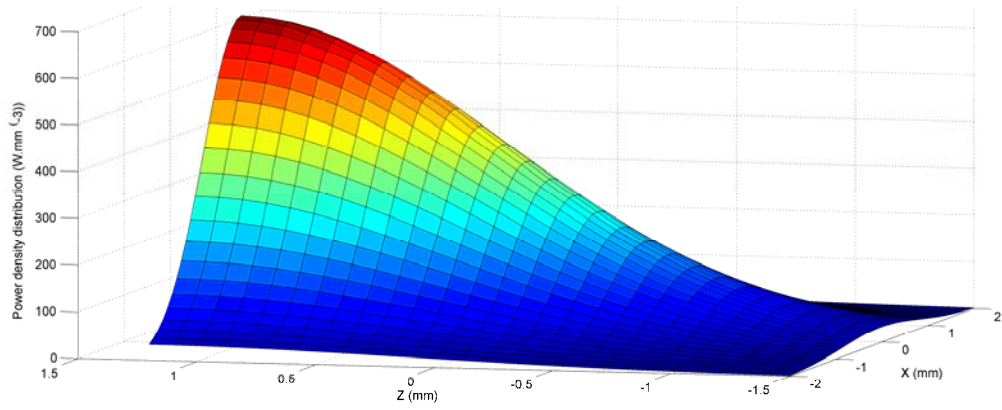
using the double ellipsoidal heat source to model the deep penetration welding process comes from the sharp decrease of the power density distribution of heat deposited inside the volume along the weld penetration direction. Recently, Fabbro et al. [245] used a calibrated integrating sphere, which is placed directly under the metal sheet, to collect the laser light with the wavelength of $1.06\mu m$ and experimentally measure the reflectivity of laser beam during laser full penetration welding of thin metal sheet at high welding speed. It was found that the reflection rate is in the range of 20-30%. Based on their results, therefore, it is reasonable for the hypothesis made above in this study.

From the above discussion, the moving double heat source works well for the welding processes with conduction mode such as GTAW, submerged arc welding. However, if this model of heat source is going to be applied on the simulation on the welding processes with the keyhole, then this model has to be modified. The proposed modification way is to change the power density distribution along the depth of weld. It is proposed to introduce the correction coefficient L , which should be less than 1. The correction coefficient L (less than 1) is introduced to adjust the term of $e^{-\frac{3y^2}{c^2}}$ to $e^{-\frac{3L*y^2}{c^2}}$ to reflect the power density distribution along the depth of the heat source volume. In practice, L is a function of the shape and depth of the keyhole and the weld depth obtained from the experiments. It can be determined by the comparison of the experimentally measured profile and calculated profile of power density distribution which is similarly used by the other researcher [246]. The idea of experimentally determining the value of L can be described as: firstly the power density at the specific point along the weld line at the bottom of

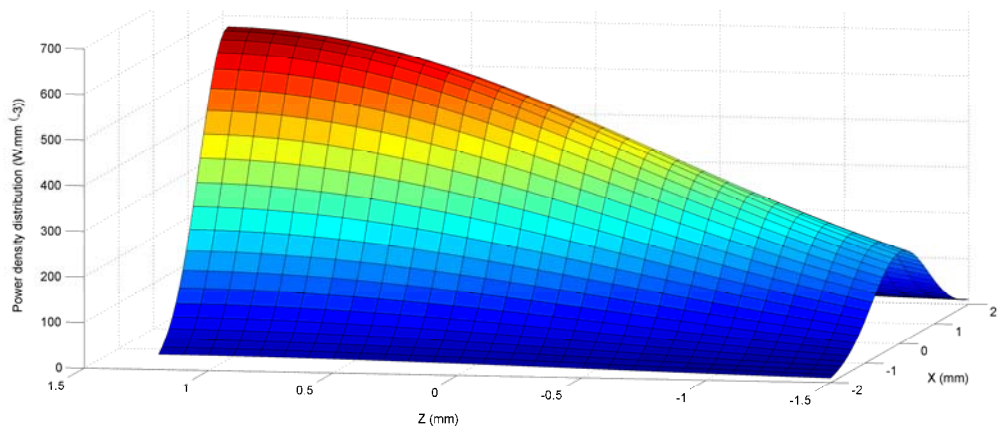
workpiece is measured by the power density profile measurement instrument; then the measured value is substituted into the power density distribution equation of the modified moving double ellipsoidal heat source to approximately obtain the value of L . Further study is needed to develop the relationship between the L and different welding conditions by the experimental measurements. The deeper the keyhole and the weld depth, the smaller L is.

Figure 6.8 shows the effect of the value of L on the power density distribution along the depth of the weld (in the XOY plane). As shown in Figure 6.8, the introduction of coefficient L into the moving double ellipsoidal heat source will dramatically increase the magnitude of the power density distribution along the weld penetration direction, especially at the bottom part of the lap joint. The increase in the power density along the depth of weld will melt more material, which makes it possible to obtain the deeper weld penetration. In addition, Figure 6.10 illustrates the effect of the coefficient L on the power density distribution at the ZOY planes with different Y values (this is along the depth of weld). The power density distribution in XOY plane is also increased by the introduction of coefficient L (less than 1) into the double ellipsoidal heat source, as shown in Figure 6.10. When the values of Y are larger than 0, the increasing rate of power density at ZOY plane is slightly increased, compared to those in Figure 6.10 (a)-(b) and Figure 6.10 (d)-(e). However, when the values of Y are less than 0, the increasing rate of power density at ZOY plane is dramatically increased, compared to that in Fig. 6.10 (c) and Fig. 6.10 (f). The reason for this phenomenon is the

negative exponential distribution characteristic of the power density of the double ellipsoidal heat source.



(a)



(b)

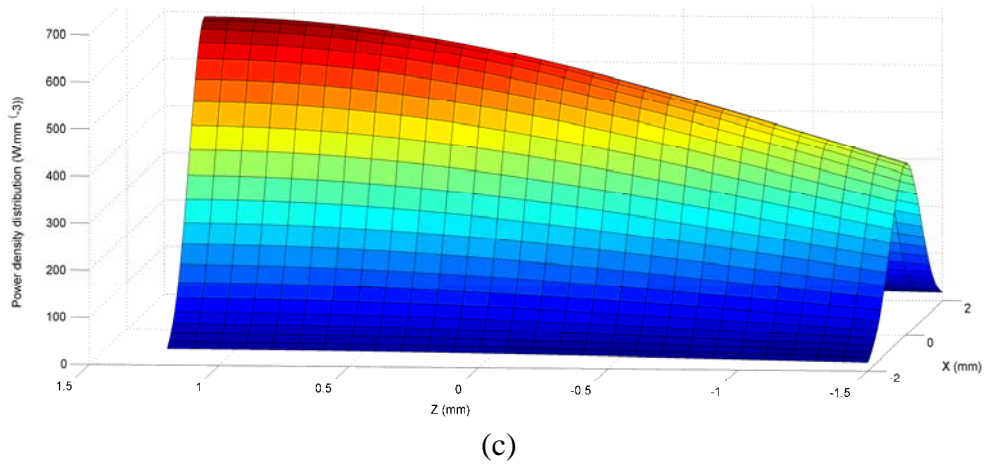
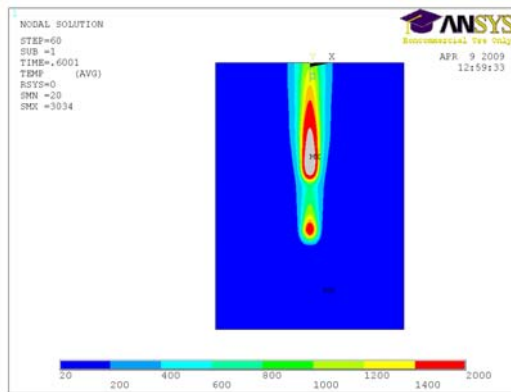
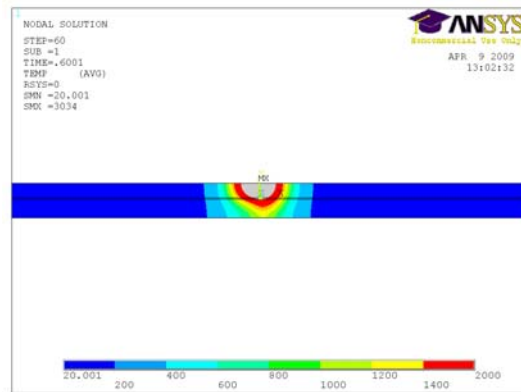


Figure 6.8 Effect of coefficient L on the power density distribution along the weld penetration direction (a) $L = 1$ (b) $L = 0.4$ (c) $L = 0.2$ (laser power: 3000 W; $a_f = 1\text{mm}$; $a_r = 4\text{mm}$; $b = 2\text{mm}$; $c = 2.7\text{mm}$; $f_f = 0.6$; $f_r = 1.4$)

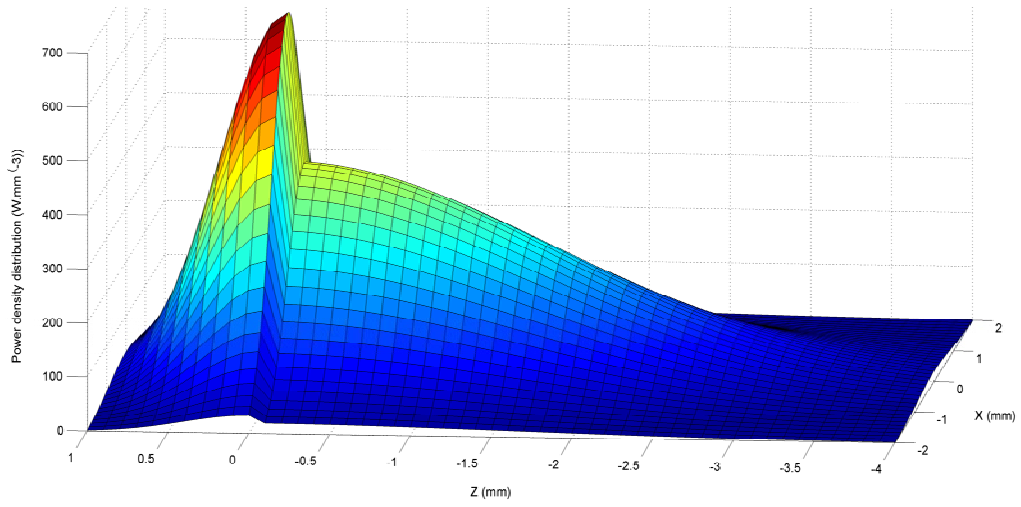


(a)

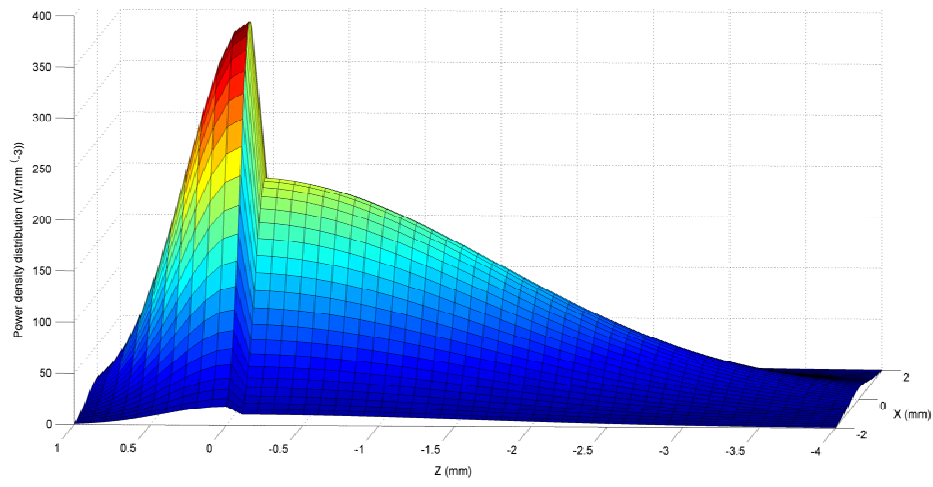


(b)

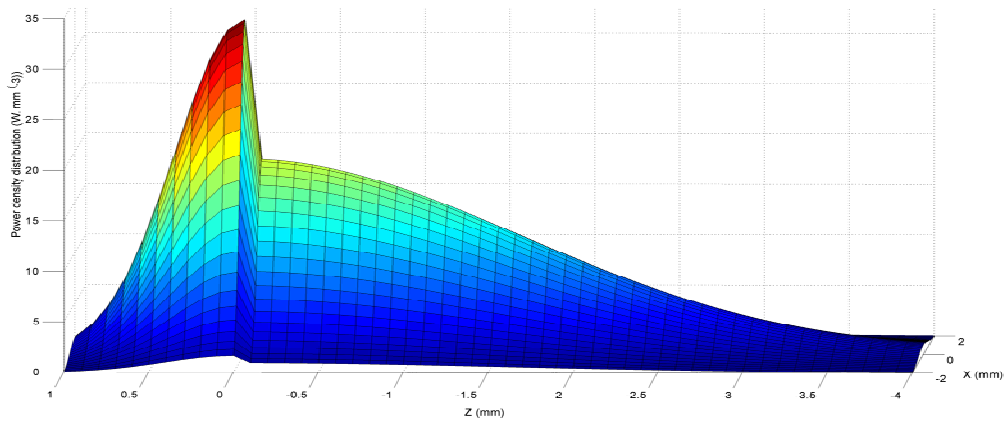
Figure 6.9 Temperature distribution profiles with the laser power of 6000 W (a) top view (b) cross-sectional view



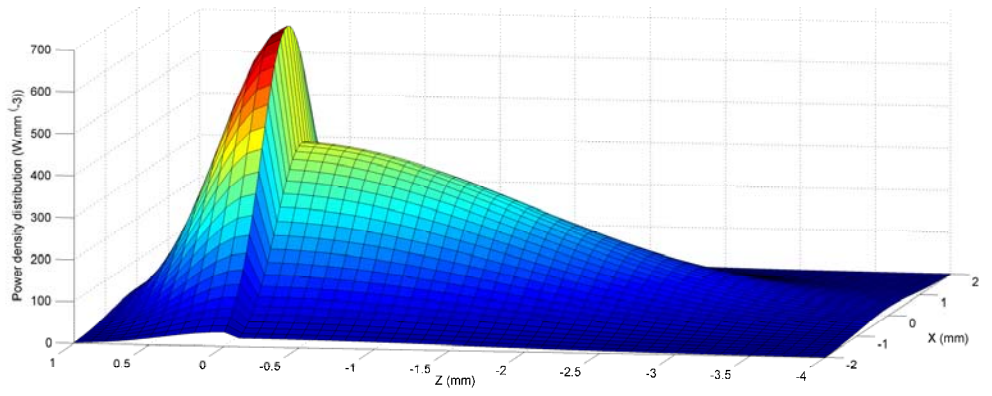
(a)



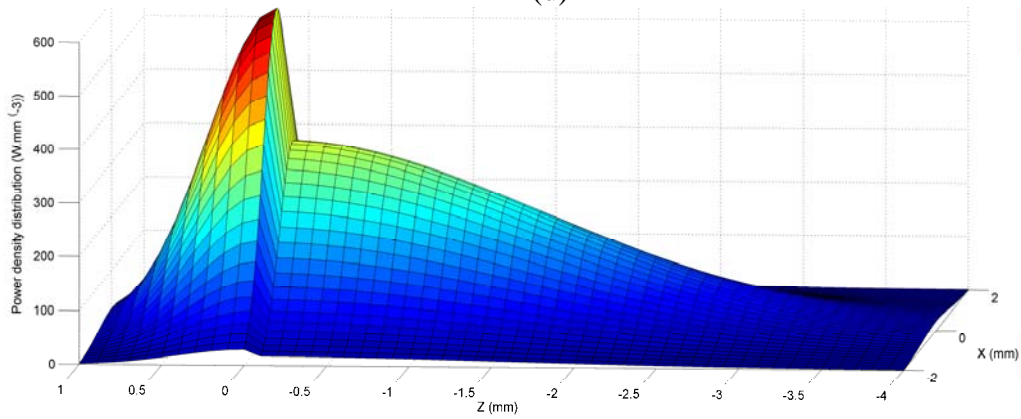
(b)



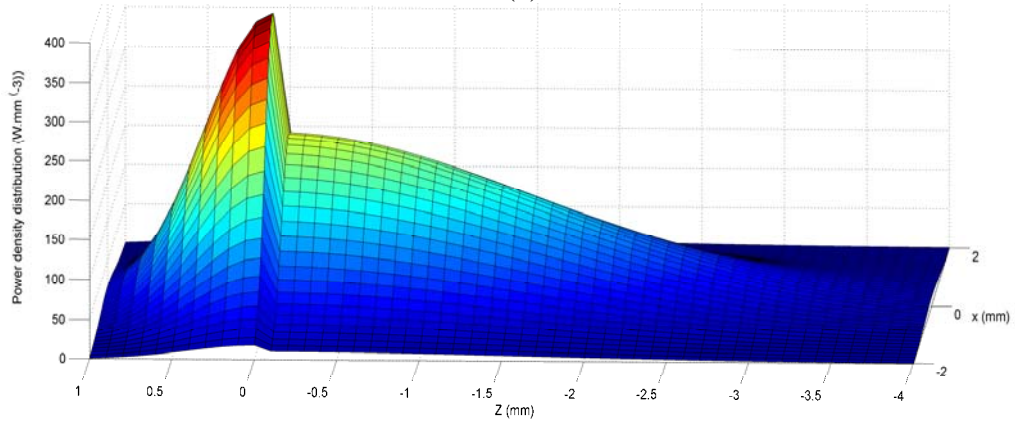
(c)



(d)



(e)



(f)

Figure 6.10 Effect of the L on the power density distribution on the ZOX plates with different Y values (a) $L = 1, Y = 1.2\text{mm}$ (b) $L = 1, Y = 0\text{mm}$; (c) $L = 1, Y = -1.5\text{mm}$ (d) $L = 0.2, Y = 1.2\text{mm}$ (e) $L = 0.2, Y = 0\text{mm}$ (f) $L = 0.2, Y = -1.5\text{mm}$ (laser power: 3000 W ; $a_f = 1\text{mm}$; $a_r = 4\text{mm}$; $b = 2\text{mm}$; $c = 2.7\text{mm}$; $f_f = 0.6$; $f_r = 1.4$)

Figure 6.11 shows the temperature distribution profiles and the shape of the fusion zone and heat affected zone obtained by the application of modified moving double ellipsoidal heat source. As shown in Figure 6.11 (a), it can be seen that a long “nail” like molten pool is presented in the numerical simulation, similar to the shape of the real molten pool obtained by the high-speed CCD camera shown in Figure 6.6(b). The “nail” like shape of the molten pool is one of the significant features of the high speed keyhole welding. The simulated full penetration weld shown in Figure 6.11 (b) is matching very well with the experimental result shown in Figure 6.6 (c). The width of the numerical simulation fusion zone is 2.8 mm, which is a little less than that of the real fusion zone that is of 3.0 mm. A slight difference between the shapes of the real fusion zone with respect to the numerical counterpart was observed. These discrepancies between the experimental and numerical results is mainly attributed to the imprecise prediction of the thermophysical parameters of the DP steel used in this study and the absence of the thermal resistance between two plates. Figure 6.12 presents the isotherm temperature distribution profiles at the time of 0.6 s. Figure 6.13 demonstrates the temperature history at the weld centerline point away from the welding beginning point of 30 mm. As shown in Figure 6.13, there are two peak temperatures. The value of temperature at peak A is produced by the leading arc. The temperature at the peak B is caused by the high energy density of the followed laser beam. Figure 6.14 shows the temperature histories of the numerical and the experimental results obtained by the thermocouples at the point of 10 mm away from the center weld line and 30 mm away from the beginning point along the welding direction on the

upper surface of the welded sheet. As shown in Figure 6.14, the numerical peak temperature is 311 °C, which has a good agreement with the measured experimental peak temperature of 339°C.

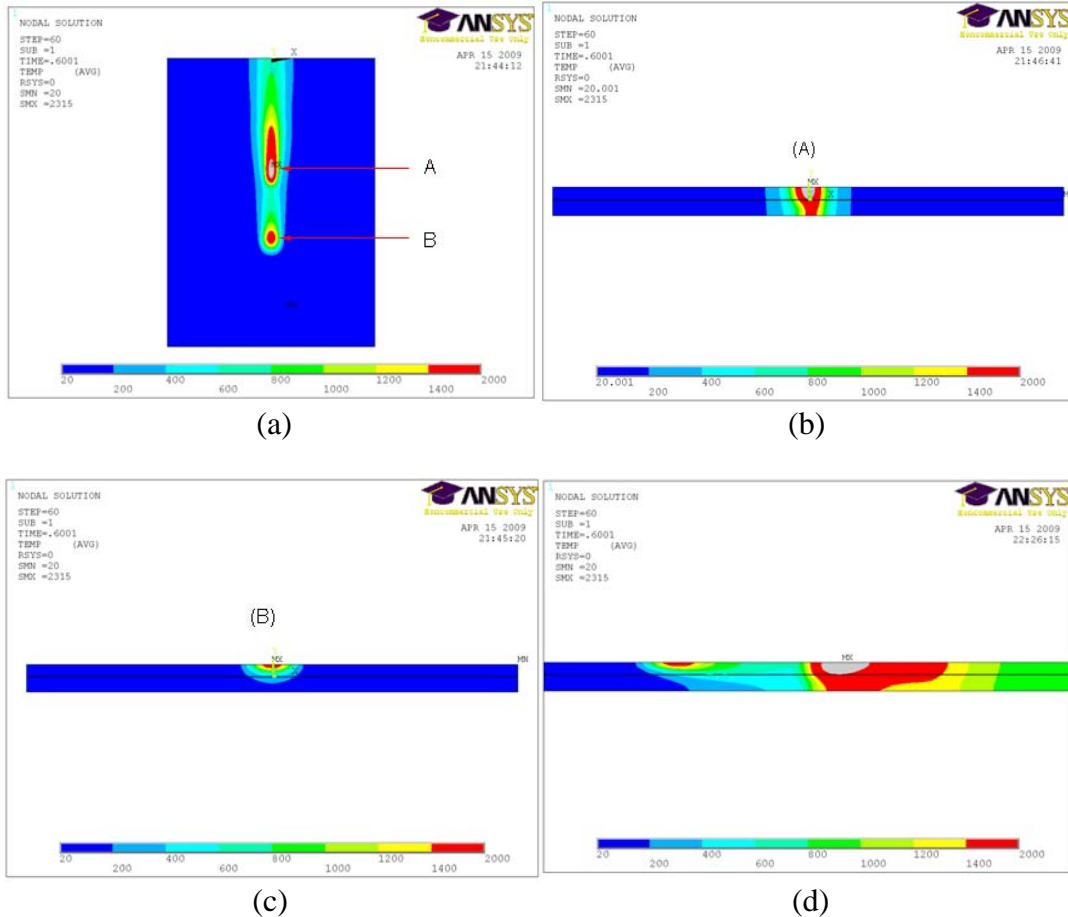


Figure 6.11 Temperature distribution profiles obtained by the numerical results (a) temperature profiles of top view in the numerical result (b) temperature profiles of cross-sectional view of the laser-welded fusion zone in the numerical result (c) temperature profiles of cross-sectional view of the arc-welded fusion zone in the numerical result (d) temperature profiles of the longitudinal view of hybrid laser-arc weld zone (Laser power: 3000 W; arc current: 300 A; welding speed: 50 mm/s; $a_f = 1, a_r = 4, b = 2, c = 2.7, f_f = 0.6, f_r = 1.4$; $t = 0.6$ s; $L = 0.2$)

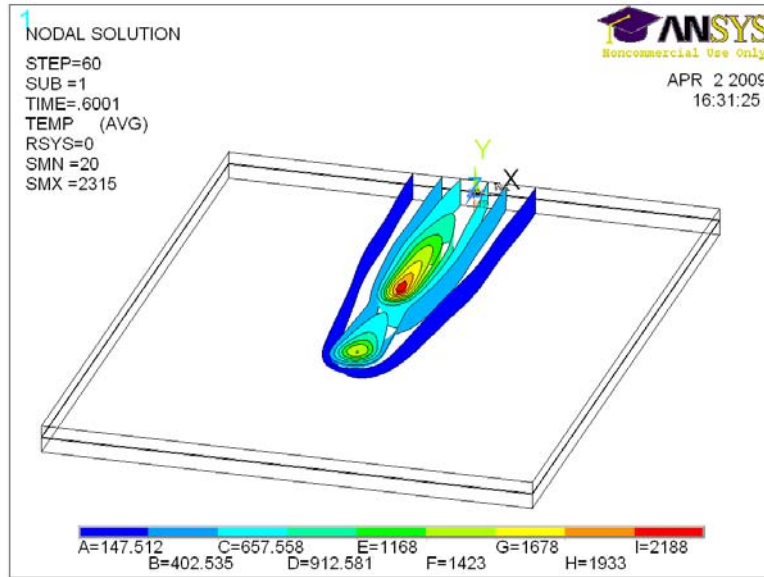


Figure 6.12 Temperature distribution profiles

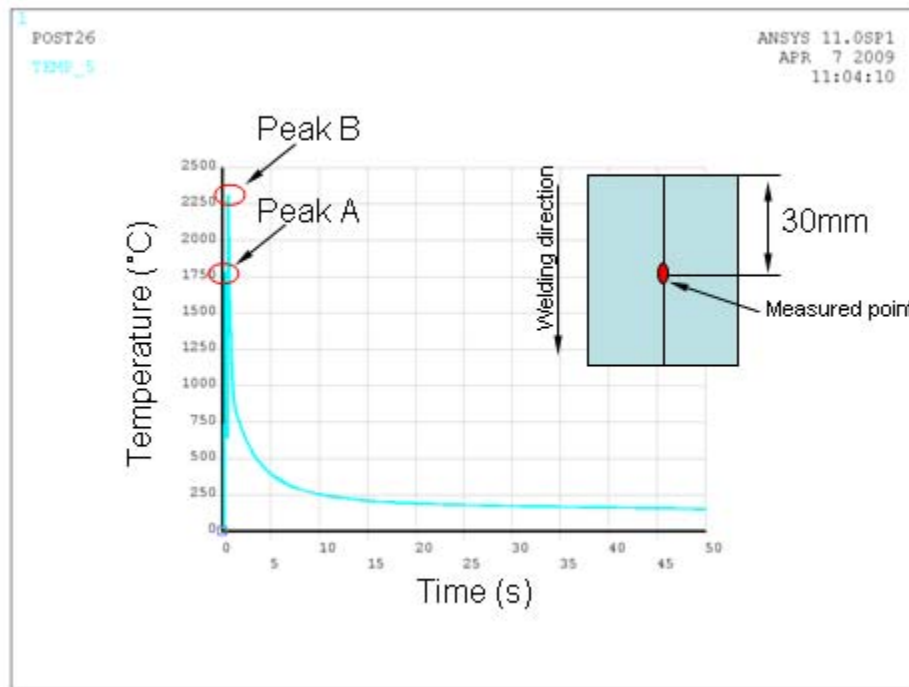


Figure 6.13 Temperature history at the center point ($z=-30$ mm, $x=0$ mm, $y=0$ mm)

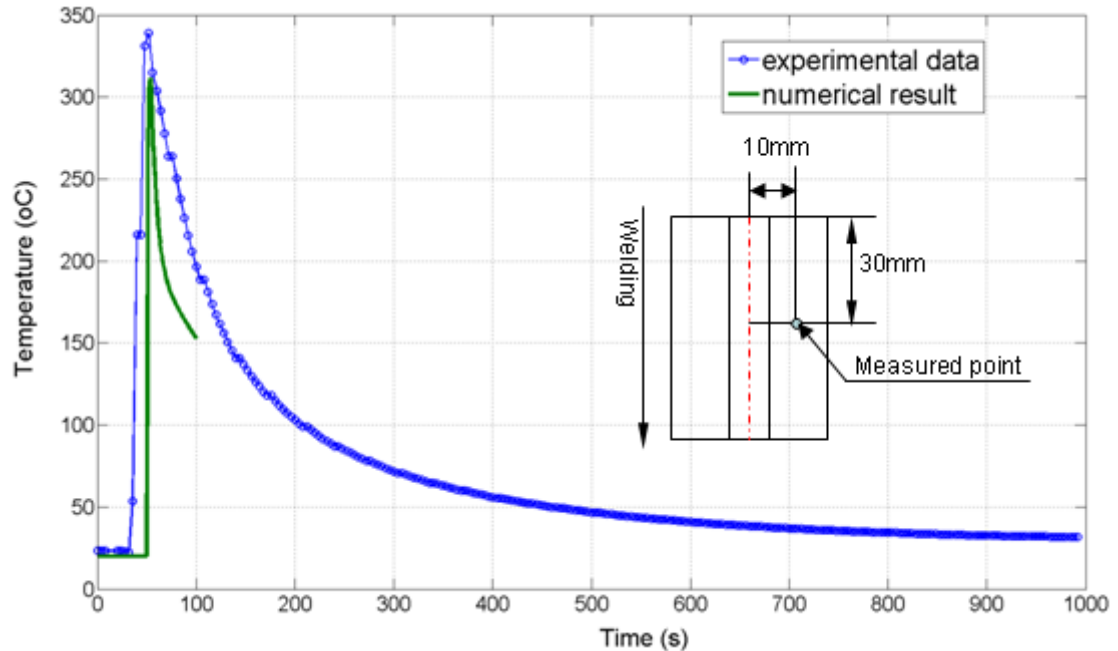


Figure 6.14 Comparison of the numerical and experimental temperature histories measured at the specific point (in numerical calculation the time is just taken by 50 s)

6.4.2 Effects of the Hybrid Laser-Arc Welding Parameters on the Temperature Distribution Profiles

From the aforementioned discussion, it is evident that the modified moving double ellipsoidal heat source can be used to predict the transient temperature field profiles for the hybrid laser-arc welding of galvanized steels in a gap-free lap joint configuration. The modified double ellipsoidal heat source was further used to investigate the influences of the distance between the laser beam and the GTAW torch as well as the arc current on the temperature distribution profiles. various welding parameters In the following analyses in this welding, the a_f, a_r, b, c, f_f were set for the fixed welding conditions of laser power:3000 W; to 1mm, 4mm, 2mm, 2.7mm, and 0.6 mm, respectively.

6.4.2.1 Effect of Distance between Laser Beam and GTAW Preheating Torch

To investigate the effect of distance between the laser beam and the GTAW torch on the temperature distribution, the distance between laser beam and GTAW torch was varied from 5 mm to 15 mm at the increment of 5mm. Figure 6.15 shows the temperature distribution profiles at the top surface of the workpiece with the different distances. Figure 6.16 depicts the peak temperatures as a function of the distance between laser beam and GTAW torch. As shown in Figure 6.16, the peak temperature is increased with the decrease in the distance between the laser beam and the GTAW torch. At the 5mm distance, the laser beam and GTAW torch begins to share the common molten pool through the heat conductivity. Furthermore, it can be seen that the molten pool is elongated and widen at the distance of 5 mm, compared to those at the distance of 10mm and 15 mm. This can be explained by the fact that when decreasing the distance more heat from the laser beam and arc was deposited into the welded material through the thermal conductivity. It should be mentioned that the shorter distance between the laser beam and GTAW torch during hybrid laser-arc welding of galvanized steels in a gap-free lap joint configuration will lead to the instable interaction between laser beam and arc, which significantly influences the coupling of laser beam energy into the welded material and leads to the instable welding process that will decrease the weld depth [212]. In the present model, the influence of the instable interaction between laser beam and arc on the temperature distribution is neglected by taking distance of 15mm.

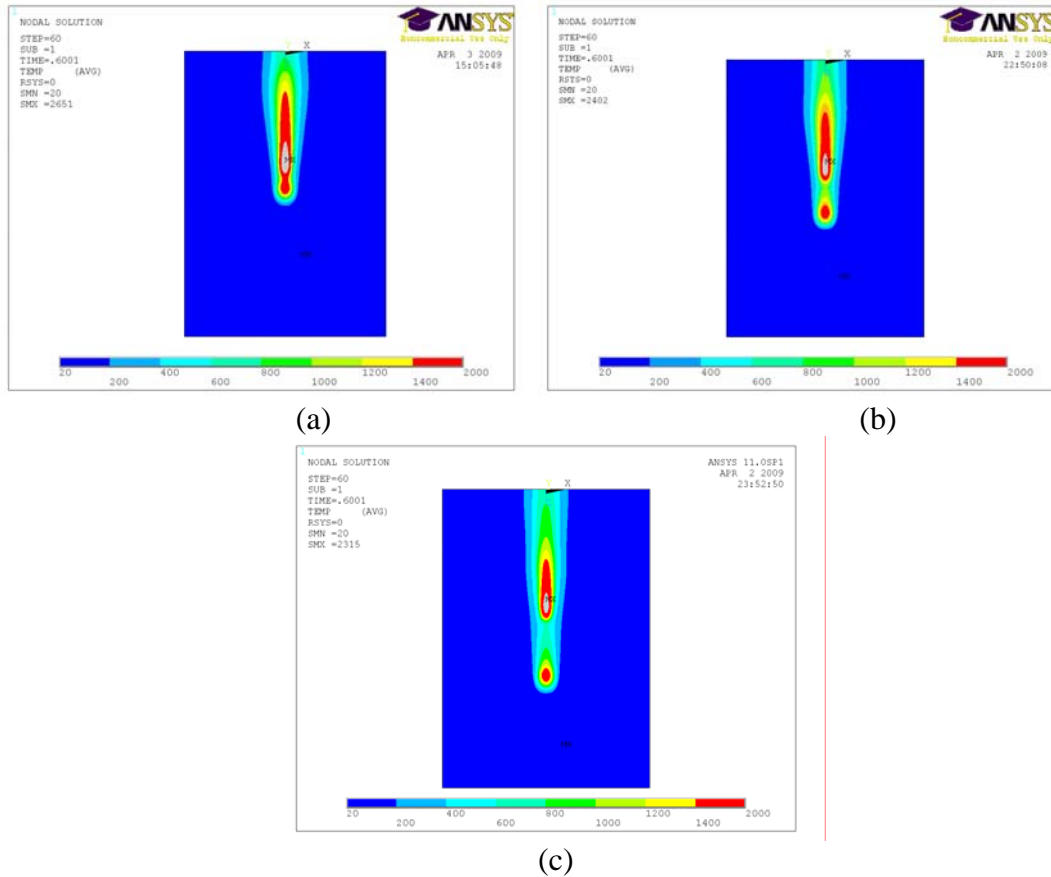


Figure 6.15 Effect of the distance between laser beam and GTAW torch preheating (1) $d = 5$ mm (b) $d = 10$ mm (c) $d = 15$ mm (Laser power: 3000 W; arc current: 300 A; welding speed: 50 mm/s; $a_f = 1$; $a_r = 4$; $b = 2$; $c = 2.7$; $f_f = 0.6$; $f_r = 1.4$; $t = 0.6$ s; $L = 0.2$)

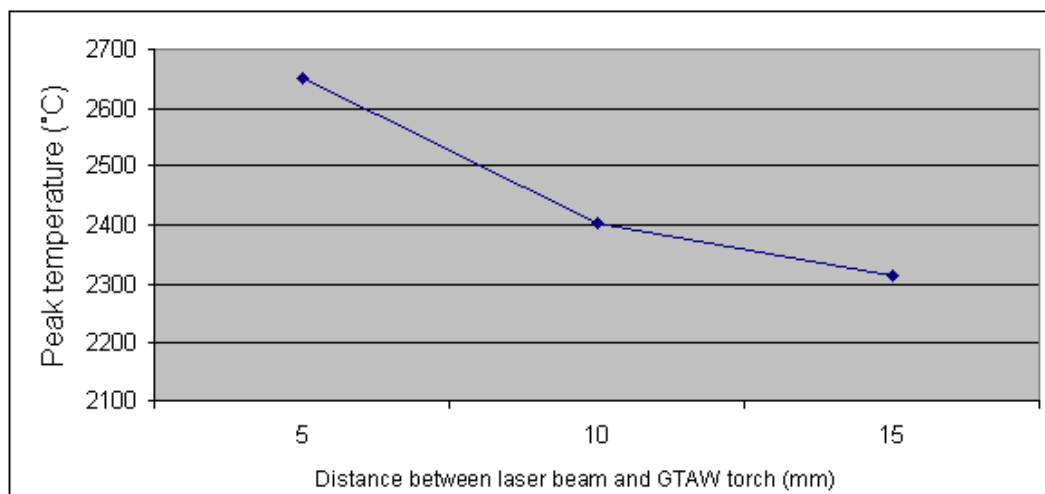
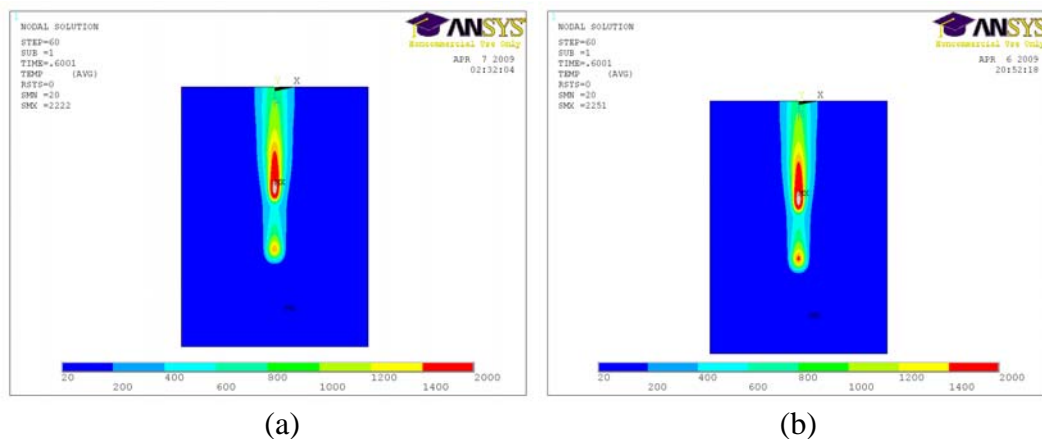
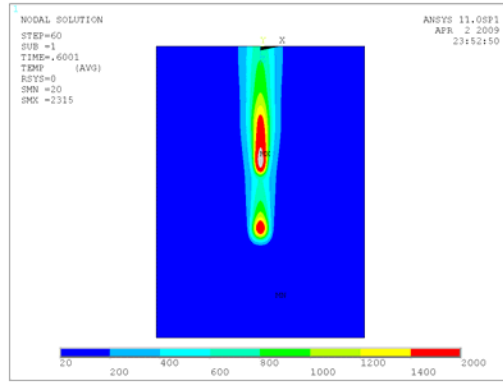


Figure 6.16 Relationship between the peak temperature and the distance between laser beam and GTAW torch on the top surface at the time of 0.6 s

6.4.2.2 Effect of GTAW Arc Current

Figure 6.17 shows the temperature distribution profiles with different GTAW arc currents. The GTAW arc current is changed from 220A, 260 A and 300A. It can be seen that the temperature distribution profiles just slight change with the increase of the arc current from 220 A to 300 A due to the high welding speed, but the peak temperature values are obviously different. Figure 6.18 shows the calculated peak temperature as a function of GTAW arc current. It can be seen that the highest peak temperature is at the GTAW arc current of 300 A. As shown in Figure 6.19, at the arc current of 220A and 260A no melting occurs and temperatures at the interface are relatively low. However, the increase in the arc current to 300 A results in the increase in the magnitude of the temperature distribution and a shallow molten pool is generated. The increased temperature and the formation of the shallow molten pool at the arc current of 300 A are obviously caused by the increased arc energy input to the welded material.





(c)

Figure 6.17 Temperature distributions with various preheating arc current (a) 220 A (b) 260 A (c) 300A; characteristic parameters of heat source: $a_f = 0.5mm$; $a_r = 2mm$; $b = 2mm$; $c = 2.7mm$; $f_f = 0.6$;and $f_r = 1.4$; $L = 0.2$)

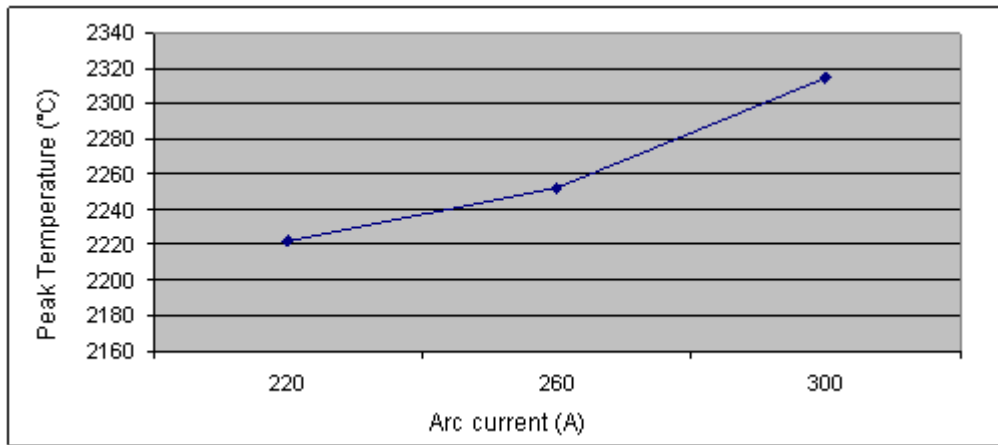
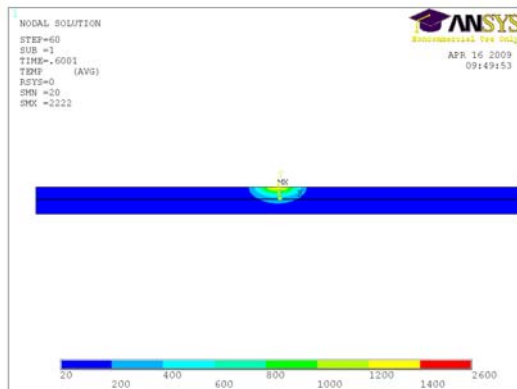
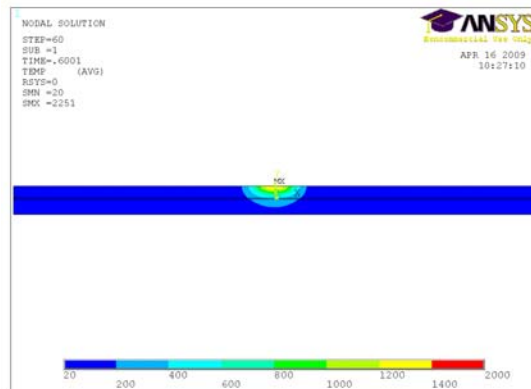


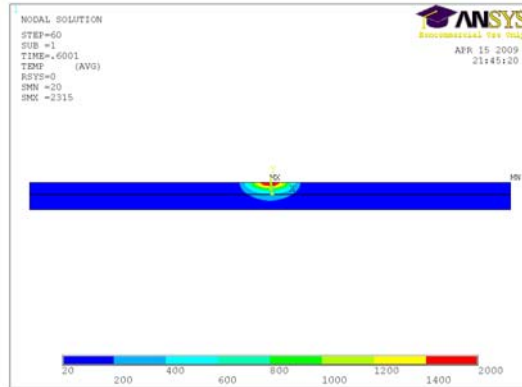
Figure 6.18 Relationship between the peak temperature and the GTAW preheating arc current on the top surface at the time of 0.6 s



(a)



(b)



(c)

Figure 6.19 The temperature distribution profiles in the cross-sectional view with the arc current of (a) 220 A (b) 260 A (c) 300A; (characteristic parameters of heat

source: $a_f = 0.5\text{mm}$; $a_r = 2\text{mm}$; $b = 2\text{mm}$; $c = 2.7\text{mm}$; $f_f = 0.6$; and $f_r = 1.4$; $L = 0.2$)

6.4.2.3 Effect of Welding Speed on the Temperature Distribution Profiles

Figure 6.20 presents the temperature distribution profiles with the welding speed of 40mm/s, 50mm/s, and 60mm/s, respectively. Figure 6.19 shows the calculated peak temperatures as a function of GTAW arc current. As shown in Figure 6.21, the peak temperature was decreased by the increase in the welding speed. The high peak temperature is obtained at the welding speed of 40 mm/s. It was also observed that the higher welding speed of 60 mm/s leads to the longer and narrower “nail” molten pool when compared to those obtained by the relatively lower welding speeds of 40mm/s and 50 mm/s. The main reason for this is that increasing the welding speed decreases the heat input of laser power into the welded materials.

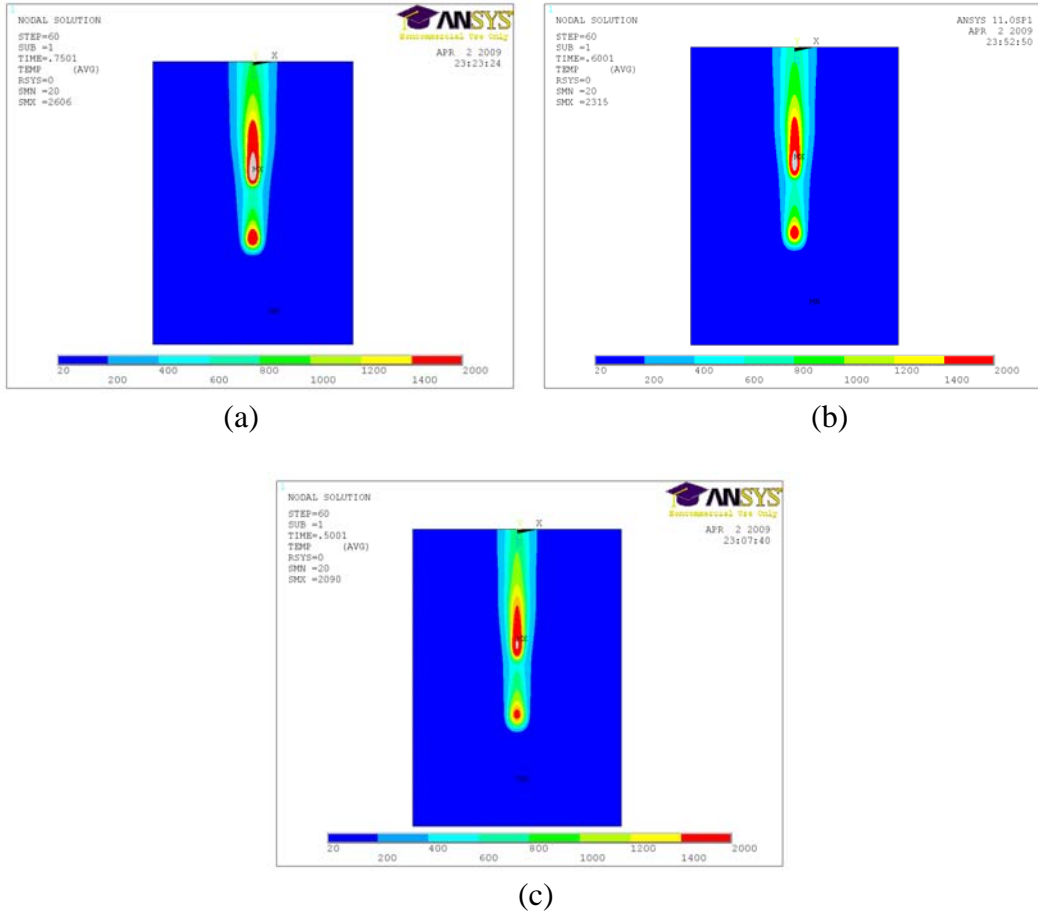


Figure 6.20 Effect of welding speed on the temperature distribution profiles (a) $v = 40$ mm/s (b) $v = 50$ mm/s (c) $v = 60$ mm/s (Laser power: 3000 W; arc current: 300 A; $d = 15$ mm; $a_f = 1$; $a_r = 4$; $b = 2$; $c = 2.7$; $f_f = 1.6$; $f_r = 0.4$; $t = 0.6$ s; $L = 0.2$)

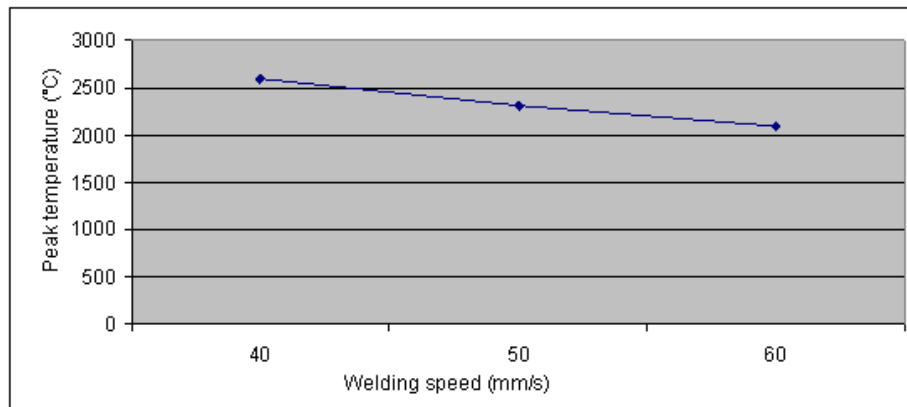


Figure 6.21 the relationship between the peak temperature and the welding speed on the top surface at the time of 0.6 s

6.5 Conclusions

The transient temperature distribution profiles during hybrid laser-arc welding process of galvanized steels in a gap-free lap joint configuration were calculated by the developed FEM model. A moving double ellipsoidal heat source was used in this present work. From the numerical results, the following conclusions can be made as follows:

1. The numerical results are significantly sensitive to the selection of the characteristic parameters of the moving double ellipsoidal heat source. Any change of these characteristic parameters results in different numerical results in the fusion zone and heat affected zone (HAZ).
2. The geometry of the molten pool can be precisely predicted by the FEM model. The calculated shape of the molten pool shows a good agreement with the experimental results. However, it is difficult to estimate the weld penetration depth by the double ellipsoidal heat source in the case of the keyhole welding process.
3. The FEM using the modified moving double ellipsoidal heat source can not only precisely predict the shape of the molten pool but also estimates the depth of the weld penetration. This proposed moving heat source has promising potential application for deep penetration keyhole welding processes such as laser keyhole welding and the electron beam keyhole welding.
4. For the deep keyhole welding process, the coefficient L (less than 1) is introduced in the moving heat source model to enhance the level of power

density distribution along the depth of the weld. The selection of L is as a function of the obtained weld depth. In addition, the fraction of heat in the front of the molten pool is preferred to be less than 1 for the deep keyhole welding process.

5. The “nail” shape of the molten pool is one of the characteristics of the deep keyhole welding process.
6. Decreasing the distance between the laser beam and GTAW torch increases the peak temperature. At the distance of 5 mm, the laser beam and GTAW torch shares the common molten pool. In addition, decreasing the GTAW torch power decreases the peak temperature. Similarly, the peak temperature is decreased with the increase in the welding speed.

Reference:

212. S.L.Yang, W.Huang, D.C.Lin, F.R.Kong, and R. Kovacevic, Hybrid laser/GTAW welding of galvanized steels in a gap-free lap joint configuration, 2009 TMS Annual Meeting and Exhibition, February 15-19, San Francisco, California, USA
213. J.F.Shackelford and W.Alexander 2000.Materials science and engineering handbook (third edition), CRC press
214. D.Rosenthal, The theory of moving sources of heat and its application to metal treatments, Trans ASME,Vol.68,1946,pp.849-865
215. R.R.Rykalin, Energy sources for welding, Welding in the world, Vol.12,No.9-10,1974,pp. 227-248
216. P.O.Myers,O.A.Uyehara and G.L.Borman, Fundamentals of heat flow in welding ,Welding Research Council Bulletin, New York No.123,1967
217. V.Pavelic, R.Tanbakuchi,O.A.Uyehara, and Myers, Experimental and computed temperature histories in gas tungsten arc welding of thin plates, Welding Journal, Vol.48,pp 295s-305s,1969
218. G.W.Krutz, and L.J.Segerlind, Finite element analysis of welded structures, Welding Journal, Vol.57, 1978, pp.211s-216s
219. E.Friedman, Thermo-mechanical analysis of the welding process using the finite element method, Journal of Pressure Vessel Technology, Trans.ASME,Vol.97,No.3,1975,pp.206-213
220. Z.Paley and P.D.Hibbert, Computation of temperatures in actual weld designs, Welding Journal, Vol.54,1975,pp.385s-392s
221. O.Westby, Temperature distribution in the workpiece by welding ,Department of Metallurgy and Metals Working, The Technical University, Trondheim Norway, 1968
222. J.Goldak, A.Chakravarti, and M.Bibby, A finite element model for welding heat sources, Metallurgical Transactions B, Vol.15B, 1984, pp. 299-305
223. N.T.Nguyen,A.Ohta,K.Matsuoka,M.Suzuki and Y.Maeda, Analytical solutions for transient temperature of semi-infinite body subjected to 3-D moving heat sources, Welding Journal,Vol.78, 1999, pp. 265-s-274-s

224. W.Sudnik, D.Radaj, and W. Erofeew, Computerized simulation of laser beam welding, modeling and verification, Journal of Physics: D Applied Physics, Vol.29, 1996, pp. 2811-2817.
225. R.Fabbro and K.Chouf, Keyhole modeling during laser welding, Journal of applied physics, Vol.87, 1999, 4075-4083
226. J.Kroos, U.Gratzke and G.Simon, Towards a self-consistent model of the keyhole in penetration laser beam welding, Journal of applied physics, Vol.26, 1993, 474-480
227. H.Ki, P.S.Mohanty, and J.Mazumder, Modeling of laser keyhole welding: Part I. mathematical modeling, numerical methodology, role of recoil pressure, multiple reflections, and free surface evolution, Metallurgical and materials Transactions A, Vol.33A, 2002, pp.1817-1830
228. J.Dowden, M.Davis, P.Kapadia, Some aspects of the fluid dynamics of laser welding, Journal of Fluid Mechanics, Vol.126, 1983, pp.123-146
229. K.N.Lankalapalli, J.F.Tu, and M.Gartner, Journal of Applied Physics, Vol.29, 1996, 1831-1841
230. H.Wang, Y.Shi, S.Gong, and A.Duan, Effect of assist gas flow on the gas shielding during laser deep penetration welding, Journal of Materials Processing Technology, Vol. 184, 2007, pp.379-385
231. S.D. Ji, H.Y.Fang, X.S Liu, and Q.G Meng, Influence of a welding sequence on the welding residual stress of a thick plate, Modelling and Simulation in Material Science and Engineering, Vol.13, 2005, pp.553-565
232. N.Screenivasan, M.Xia, S.Lawson, and Y.Zhou, Effect of laser welding on formability of DP980 steel, Journal of Engineering Material and technology, Vol.130, 2008, pp. 041004-1-9
233. J.A.Goldak and M. Akhlaghi. Computational welding mechanics, 2003, Springer press, New York, USA
234. J.Goldak, A. Chakravarti, and M.Bibby, A new finite element model for welding heat source, Journal of Metallurgical Transactions B, Vol.15B, 1984, pp.299-305
235. N.T.Nguyen, Y.W.Mai, S.Simpson, and A.Ohta, Analytical approximate solution for double ellipsoidal heat source in finite thick plate, Welding Journal, Vol.83, 2004, pp.82-s-93-s

236. S.A.A.Akbari Mousavi, and R.Miresmaeili, Experimental and numerical analyses of residual stress distributions in TIG welding process for 304L stainless steel, *Journal of Material Processing Technology*, 2008, pp.383-394
237. A.Bejan, Heat transfer, John Wiley & Sons Inc., New York, USA, 1993
238. M.Brand and D.Siegele, Numerical simulation of distortion and residual stresses of dual phase steels weldments, *Welding in the World*, Vol.51,2007, pp. 56-62
239. S.L Yang, R. Kovacevic, R. Ruokolainen and B. Carlson, GTAW-assisted laser welding of galvanized high-strength steel in a gap-free lap joint configuration, accepted for publication at *2009 TMS Annual Meeting and Exhibition*, February 15- 19, San Francisco, California, USA
240. J.Miettinen, Calculation of solidification-related thermophysical properties for steels, *Metallurgical and Materials Transactions B*, Vol. 28B, 1997, pp. 281-297
241. Y.S.Touloukian,R.W.Powell,C.Y.Ho,and P.G.Klemens, Thermo-physical Properties of high temperature Solid Materials, Macmillan, New York,1976
242. X.He,P.W.Fuerschbach and T.DebRoy, Heat transfer and fluid flow during laser spot welding of 304 stainless steel, *Journal of Physics D: Applied Physics*, Vol.36,2003,pp. 1338-1398
243. A.G.Grigoryants, Basics of Laser Material Processing, CRC press,1994, Ann Arbor, USA
244. J.Ion, Laser Processing of Engineering Materials:Principles, Procedure and industrial application,Butterworth-Heinemann;1 edition, 2005, USA
245. R.Fabbro,S.Slimani,F.Coste and F.Briand, Study of keyhole behavior for full penetration laser welding, *Journal of Physics: D Applied Physics*, 2005, pp. 1881-1887
246. M.R.Frewin and D.A Scott, Finite element model of pulsed laser welding, *Welding Journal*, Vol.78,n1,pp.15-s-22-s
247. R.Komanduri and Z.B.Hou, Thermal analysis of the arc welding process: part II effect of variation of thermophysical properties with temperature, *Metallurgical and Materials Transactions B*, Vol.32B,2001, pp.483499
248. J.A.Goldak and M. Akhlaghi. Computational welding mechanics,2003, Springer press, New York, USA

249. D.Grey, H.Long, and P.Maropoulos, Effects of welding speed, energy input and heat source distribution on temperature variations in butt joint welding, *Journal of Materials Processing Technology*, 2005, pp.393-401

Chapter 7

CONCLUSIONS AND FUTURE WORK

7.1 Conclusions

7.1 Summary and Conclusions- Feasibility Study of Welding of the Galvanized DP 980 Steel

7.1.1 The Lap Joint of Galvanized DP 980 Steel by the GTAW

The welding of galvanized dual-phase (DP) 980 steel in a gap-free configuration was conducted using the gas tungsten arc welding (GTAW) process. It was found that the (GTAW) welds are generally characterized by various kinds of weld defects such as spatters, blowholes, partial penetration, undercuts etc. Furthermore, with an increase in the arc current or traverse speed, humping was formed in the welds. Only in a very narrow range of welding parameters, can sound welds be achieved. However, a low welding speed can not meet the production rates accepted by the automotive industry.

7.1.2 The Lap Joint of Galvanized DP 980 Steel by Laser Welding

As in the GTAW welding process, the high-pressurized zinc vapor is developed at the interface of two metal sheets during the laser welding process. As a result, a large amount of spatters and blowholes are observed in the laser welding. Increasing the laser power will increase the instability of the welding process and

more spatters are produced while maintaining the other welding parameters constant. The instable induced plume above the molten pool leads to a varied coupling of the laser beam energy into the specimens, which results in an inconsistent penetration depth of the welds. In addition, the introduction of the spacer along the interface of two metal sheets in order to vent out the zinc vapor does not create a sound weld. Furthermore, the entrapped air in the molten pool may result in the formation of porosity in the welds. Usually, the generated spatters tend to severely damage the optics of the laser welding head.

7.1.3 The Lap Joint of Galvanized DP 980 Steel Using Hybrid Laser/GTAW Welding

Welding of the galvanized DP 980 steel in gap-free lap joint configuration was also investigated with the hybrid laser/GTAW welding processes. The two heat sources are used to generate the common molten pool. During the welding process, the molten pool generated by the GTAW allows the laser beam to produce a keyhole and a portion of the high-pressurized zinc vapor will vent out through the keyhole. However, the interaction between the laser beam and arc plasma is significantly instable. Thus, the coupling of laser beam into the welded material is instable, which results in the nonstable keyhole. When the keyhole is collapsed, there is no channel for the zinc vapor to be vented out from the interface of two metal sheets. As a result, the zinc vapor trapped into the molten pool will eject a large volume of liquid metal. The ejected liquid metal droplets will condense in the air and will be deposited in or around the weld zone. The spatters severely damage the electrode tip and the optics of the laser welding head. Therefore, it is required to

reshape the tip of electrode frequently, which will result in higher welding costs. The porosity is observed at the weld surface as well as internally because of the entrapment of the air into the molten pool. In addition, the collapse of the keyhole is the other primary reason for the formation of porosities in the hybrid welds. Experimental investigation shows that with the increase of the distance between the laser beam and the electrode tip will improve the weld quality. Also, the increase in the arc current can stabilize the welding process. The variation in laser power does not have a significant effect on the stability of the welding process.

7.1.4 The Lap Joint of Galvanized DP 980 Steel Using the Hybrid Laser/GTAW where GTAW is used as a Preheating Source

The hybrid laser/GTAW welding procedure where GTAW is used as a preheating source is developed to weld the galvanized DP980 steel in a gap-free lap joint configuration. The completely defect-free lap joints are achieved. The cross-sectional view of the welds reveals that no porosity is present in the welds. Due to the separation of laser beam from the arc, the welding process is free from the influence of the zinc plume. Consequently, the coupling of laser beam energy is stable and the generated keyhole is kept open.

From the analysis of the treated surface by the GTAW by X-ray Photoelectron Spectroscopy (XPS), it is found that a thin layer of metal oxides are formed at the top surface of the workpiece during the GTAW preheating process. The produced metal oxides can dramatically improve the coupling of laser beam energy into the specimen. Therefore, the keyhole is readily formed during the hybrid laser/GATW where the GTAW torch is used as the preheating source. The high-pressurized zinc

vapor developed at the interface of two metal sheets is vent out through the keyhole, thus ensuring the stability of the welding process. The visualization of the welding process by using the high speed video camera indicates that a stable welding process mainly depends on the sustainability of the keyhole. Once the keyhole collapses, the welding process tends to be instable resulting in the weld defects. In addition, the XPS analysis results show that the zinc coating at the interface is partially oxidized, which also helps to stabilize the welding process due to its high melting point (around 1975 °C for zinc oxides).

The tensile shear test results show that a weld with high strength is obtained. In addition, the micro-hardness profiles of the welds have demonstrated that the heat affected zone (HAZ) is softened. Generally speaking, the majority of welds are fractured in the HAZ during the tensile shear test.

7.1.5 The Lap Joint of Galvanized DP 980 Steel Using the Hybrid Laser- DCEP VPGTAW where VPGTAW is used as a Preheating Source

The zinc coating at the top surface of the workpiece is removed during the DCEP VPGTAW preheating process. Similar to the hybrid laser-arc welding of galvanized steels with the separate molten pool, a thin layer of metal oxides is generated, which mainly consists of iron oxides. Additionally, the zinc coating along the weld zone at the interface of two metal sheets is transferred into the zinc oxides. The generated metal oxides at the top surface of the workpiece and the roughened surface drastically increase the coupling of the laser beam energy into the welded material. Under these circumstances, the keyhole is readily produced and is kept stable, which allows the highly-pressurized zinc vapor formed along the

interface of two metal sheets to be vented out. The sound lap joints have been obtained in a gap-free configuration. More importantly, the distance between the laser beam and GTAW torch was shortened by introducing the DCEP of 20% which will decrease the level of the needed preheating arc current of VPGTAW with respect to the needed arc current in the GTAW preheating process.

7.2 Conclusions- Monitoring of Welding Process

7.2.1 Monitoring the Formation of Weld Defects by Machine Vision

By applying the image processing algorithms to process the acquired images, the noises in the images can be suppressed and the clear images of the molten pool can be obtained. The formation of spatters and blowholes can be detected by the calculation of the length of the major axis. The analysis results reveal that the presence of gap between metal sheets will reduce the length of the major axis of the molten pool. Additionally, it was found that the preheating process can increase the length of the major axis of the molten pool

7.2.2 Monitoring the Formation of Spatters by AE Technique

The acoustic emission (AE) signals are acquired in real time during the laser welding process. The Short Time Fourier Transform (STFT) signal processing technique is used to extract the features of the AE signals in the frequency domain. There are two distinct types of AE signals: continuous AE signals and spike-like signals. The continuous AE signals represent a stable welding process. However, the spike-like AE signals indicate the formation of spatters. The spatter-induced AE

signals have a higher power spectra compared to those associated with continuous AE signals and background noise. The spatter-related AE signals cover a wide frequency range domain. In this study, the frequency ranges of [2 kHz- 6 kHz] and [6.3 kHz – 7.6 kHz] are directly related to the spatter formation.

7.2.3 Monitoring the Weld Modes and Stability of the Welding Process

The welding modes can be distinguished by the shape of the laser-induced plume. When the welding process is in the keyhole mode, the shape of the laser-induced plume is usually in the shape of a column. When the welding process is shifted from the keyhole mode to the conduction mode, the laser-induced plasma has a diverging bright elliptical shape. In general, the shape and size of the plasma plume are changed temporally and spatially. Furthermore, it is found that the plasma plume above the molten pool affects the stability of the welding process. The high speed CCD camera of up to 400 fps assisted with the green laser light of 532 nm wavelength as an illumination source is used to monitor the stability of the welding process in real time. It is revealed that when the keyhole is open and stable, the high quality welds are achieved. Contrarily, a collapsed keyhole prevents the high-pressurized zinc vapor at the interface of two metal sheets to escape from the molten pool so that the welding process becomes instable and produces different weld defects. In addition, experimental results show that the plasma plume can be blown away from the molten pool by a side shielding gas jet. This technique will improve the coupling of the laser beam energy with the specimens; thus, achieving the deeper penetration.

7.3 Conclusions-Numerical Simulation of the Temperature Field for Hybrid Laser-Arc Welding of Galvanized Steels

A three-dimensional finite element model is developed to simulate the transient temperature field profiles for the hybrid laser-arc welding of galvanized steels in a gap-free lap joint configuration. Temperature-dependent thermophysical properties are applied in the model. Numerical results present the limitation of moving double ellipsoidal heat source in modeling of hybrid laser-arc deep keyhole welding process. The main reason for the failure of simulating the hybrid-arc deep keyhole welding process by applying the moving double ellipsoidal heat source distribution is attributed to the rather low power density distribution along the weld depth direction, which can not reflect the actual description of the energy distribution inside the keyhole.

To accurately model the temperature field profiles, a correction coefficient L is introduced into the moving double ellipsoidal heat source. The welding experiments are carried out and temperature is measured to verify the modeling results. The geometry of fusion zone is accurately predicted. There is an excellent agreement of the temperature field profiles between the numerical results and the experimental ones. The numerical results suggest that the modified moving double ellipsoidal heat source can be used in modeling of the other deep keyhole welding process such laser keyhole welding process and electron beam keyhole welding process. In addition, effects of different welding parameters on the temperature field profiles are also studied by using the modified moving double ellipsoidal heat source.

7.4 Future Studies

7.4.1 Monitoring the Dynamic Behavior of the Zinc Coating by the Optical Sensor

The interaction between the laser-induced plasma and arc plasma is significantly instable and changes the coupling efficiency of the laser beam into the welded material when the laser beam and arc share a common molten pool. The behavior of the plasma is represented by its electron temperature and density, which can be determined by the Boltzmann plot method and Stark broadening effect.

The optical sensor such as a spectrometer can provide spectral content from the emitted light. A spectrometer will be used for real-time recording the light signal emitted from the welding process. The plasma plume's electron temperature and density will be determined by using the measured Ar or Zn spectral lines. Based on the values of the obtained electron densities, the plasma absorption coefficient can be determined. After the plasma absorption coefficient is obtained, the coupling efficiency of the laser beam energy into specimen can be determined. In addition, the emitted light signals can be used to monitor the weld defects, the welding modes, the stability of the welding process and the weld penetration.

7.4.2 Investigate the Relationship between the Pressure Level of Zinc Vapor and Temperature by Using the Infrared Pyrometer and Microphone

Until now, there is no study performed on the relationship between the pressure level of zinc vapor and temperature in the welding process of galvanized steels. The pressure level of zinc vapor can be measured by the microphone. The temperature profiles at the top surface can be measured with the infrared pyrometer or

thermocouples. By using the heat transfer model, the temperature distribution at the interface of two metal sheets can be derived. Through the value of the measured zinc vapor pressure level and the calculated temperature values, the relationship between pressure level of zinc vapor and temperature can be approximately developed. In addition, the stability of the welding process and welding mode can be quantitatively analyzed.

REFERENCES

1. W.Bleck, Proc. Of International Conference on TRIP Aided High Strength Ferrous Alloys, 2002, Ghent, 247
2. D.J.Schaeffler, Introduction to advanced high strength steels, <http://www.thefabricator.com>
3. B. Corbett and A. Priddle, Dual phase leads revival online at: <http://www.wardsauto.com>
4. G. Rocheleau, J. Robin, C. Gordon, and R. Bhatnagar, Advanced high strength steel outer panels in the Ford Mustang, available online at: <http://www.autosteel.org>
5. International iron&steel institute committee on automotive application, Advanced high-strength steel (AHSS) application guidelines, 2006, online at: www.worldautosteel.org
6. X.D. Zhu, Z.H. Ma, and L.Wang, Current status of advanced high-strength steel for auto-making and its development in Baosteel.
7. Materials selected for ULSAB-AVC, online at: www.worldautosteel.org
8. V. Wesling et al, Investigations into the resistance spot welding of newly developed sheets made of higher-strength and super-high-strength steels, *Welding and cutting*, v 3, n 3, 2004, p 168-173
9. J.W.Martin, Concise encyclopedia of the structure of materials, Elsevier Science press, 2006
10. ThyssenKrupp Steel, Complex-phase steels CP-W[®] and CP-K[®] for the production of low-weight high-strength crash-relevant structural components and reinforcements is available at: <http://www.thyssenkrupp-steel.com>
11. ThyssenKrupp Steel, Martensitic-phase steel MS-W[®] for crash-relevant high-wear parts is available at: <http://www.thyssenkrupp-steel.com>

12. J.E. Gould et al, Development of appropriate resistance spot welding practice for transformation-hardened steels, *Welding journal*, v 81, n 1, 2002, p 1s-7s
13. K. Hofman et al, AC or DC for resistance welding dual-phase 600?, *Welding journal*, v 84, n1, 2005, p 46-48
14. X. Sun et al, Effects of fusion zone size and failure mode on peak load and energy absorption of advanced high-strength steel spot welds, *Welding journal*, v 86, n 1, 2007, p 18-s-25-s
15. V. Wesling et al, Investigations into the resistance spot welding of newly developed sheets made of higher-strength and super-high-strength steels, *Welding and cutting*, v 3, n 3, 2004, p 168-173
16. J.E. Gould et al, Development of appropriate resistance spot welding practice for transformation-hardened steels, *Welding journal*, v 81, n 1, 2002, p 1s-7s
17. J.Nadzam and K.Lee, Arc welding advances with new materials, *Welding Design and Fabrication*, Vol 74, 2001, pp 27-31
18. C.Chovet and S.Guiheux, Possibilities offered by MIG and TIG brazing of galvanized ultra high strength steels for automotive applications, *Metallurgia Italiana*, Vol 98, 2006, pp 47-54
19. X.Li,S, Lawson,Y, Zhou and F.Goodwin, *Journal of Laser Application*, Vol 19, 2007, pp 259-264
20. Q.Wu, G-Y. Chen, G.Wang, L-J.Li, J-K. Gong, CO2 laser welding of zinc coated high strength steel, *Zhongguo Jiguang/Chinese Journal of Lasers*,Vol 33, 2006, pp 1133-1138
21. R.Fabbro, F.Coste, D.Goebels, M,Kielwasser, Study of CW Nd-YAG laser welding of Zn-coated steel sheets, *Journal of physics D: Applied Physics*, Vol 39,2006,pp 401-409
22. S.Iqbal, M.M.S. Gualini, and F.Grassi, Laser welding of zinc-coated steel with tandem beams: Analysis and comparision, *Journal of Materials Processing Technology*, Vol 184, 2007, pp 12-18
23. J. Xie and P.Denney, Coated material welding with multiple energy beams, United States Patent 6608278.
24. K.Cheolhee, C.Woongyong, K.Jeonghan and R. Sehun, Relationship between the weldability and the process parameters for laser-TIG hybrid welding of galvanized steel sheets, *Materials Transactions*, Vol 49, 2008, pp 179-186

25. M.Ono, Y.Shinbo,A.Yoshitake and M. Ohmura, Laser-arc hybrid welding of thin steel sheets, Quarterly Journal of the Japan Welding Society, Vol 21, 2003, pp 515-521
26. M.I.Khan,Spot welding of advanced high strength steels, *Dissertation*, 2007
27. Z.Feng et al, Friction stir spot welding of advanced high-strength steels- a feasibility study, *SAE 2005*
28. Z.L. Feng, FY 2005 progress report for high strength weight reduction materials, 2005.
29. M. D. Tumuluru, Resistance spot welding of coated high-strength dual-phase steels, *Welding journal*, v 86, n 6, 2007, p 161 s-169-s
30. M. Marya et al, Development of requirements for resistance spot welding Dual-Phase (DP 600) steels part 1- The causes of interfacial fracture, *Welding journal*, v 84, n 11, 2005, p 172-s-182-s
31. Z.Feng et al, Friction stir spot welding of advanced high-strength steels- a feasibility study, *SAE 2005*
32. Z.L. Feng, FY 2005 progress report for high strength weight reduction materials, 2005.
33. M.P.Miles, J.W.Pew, T.W.Nelson, *JOM*, v 56, n 11, 2004, pp 73
34. A.N.Elliott,A.Joaquin,V.Rajan,D.Hartman,C.Jiang and C.Karas, Gas metal arc welding of coated advanced high strength steel (AHSS)-Developments for improved weld quality, 2007
35. B.Yan,S.H.Lalam and H.Zhu, Performance evaluation of GMAW welds for four advanced high strength steels, *SAE International*, 2005
36. D. Havrilla, Laser welding of AHSS in <http://www.autosteel.org/>
37. E.Essadiqi, F.E. Goodwin and M.Elboujdaini, Materials in the automotive industry, Canadian institute of mining, metallurgy and petroleum, pp3-381, 2001
38. N. Ahmed, New developments in advanced welding, CRC press, 2005
39. <http://images.pennnet.com>

40. C.Y. Kang, T.K. Han, B.K. Lee, and J.K. Kim, Characteristics of Nd:YAG laser welded 600MPa grade TRIP and DP steels. *Materials Science Forum*, vols. 539-543, 2007, pp.3967-3972
41. J.L. Bocos et al. Application of the diode laser to welding on tailored blanks. *Welding International*, Vol. 19 (7), 2007, pp. 539-543.
42. M.Gallagher,B.Yan,G.Nadharni,M.Polon,H.Zefferer and Leigich, Laser assembly welding of advanced high strength steels, Advanced laser applications conference, 2005, pp 49-58
43. T.K.Han,S.S.Park,K.H.Kim,C.Y.Kang,I.S.Woo and J.B.Lee, CO₂ laser welding characteristics of 800 MPa class TRIP steel, *ISIJ international*, Vol. 45,2005,pp.60-65
44. Advanced high-strength steel (AHSS) weld performance study for autobody structural components, www.a-sp.org.
45. H.Gu and R.Mueller, Hybrid welding of galvanized steel sheet, ICALEO 2001 Congress Proceedings, 20th International Congress on Applications of Lasers & Electro-Optics, Laser Materials Processing Congerence, pp.135-139
46. R.Akhter, W. M. Steen, and K. G. Watkins, Welding zinc-coated steel with a laser and the properties of the weldment, *Journal of Laser Applications*, v 3, n 2, 1991, pp.9-20.
47. Welding Zinc-Coated Steels, AWS WZC/D19.0-72, American Welding Society, 1972.
48. M.P. Graham, D.M. Hirak, H.W. Kerr, and D.C. Weckman, Nd:YAG laser welding of coated sheet steel, *Journal of Laser Applications*, v 6, n 4, 1994, pp. 212-222.
49. J.L.Sacks, H.Davis and W. Spilchen, Corrosion resistant wire products and method of making same, United States Patent , Patent No. 20070119715
50. M.P. Graham, D.M. Hirak, H.W. Kerr, D.C. Weckman, Nd:YAG laser beam welding of coated steels using a modified lap joint geometry”, *Welding Journal*, v 75, n 5, May 1996, pp. 162s-170s.
51. M.P. Graham, D.M. Hirak, H.W. Kerr, and D.C. Weckman, Laser welding of Zn-coated sheet steels, *Proceeding of SPIE: International society for Optical Engineering*, v 2703, 1996
52. J. Mazumder, A. Dasgupta, and M. Bembenek, Alloy based laser welding, US Patent 6,479,168, 2002.

53. Dasgupta, A., J. Mazumder, and M. Bembenek, Alloying based laser welding of galvanized Steel, *Proceedings of International Conference on Applications of Lasers and Electro Optics*, Laser Institute of America, Dearborn MI, October 2000.
54. Dasgupta and J. Mazumder, A novel method for lap welding of automotive sheet steel using high power CW CO₂ laser, *Proceedings of the 4th International Congress on Laser Advanced Materials Processing*, May 2006.
55. R.R.G.M. Pieters, J.G. Bakels, M.J.M Hermans, and G. den Ouden, Laser welding of zinc coated steels in an edge lap configuration, *Journal of Laser Applications*, v 18, n 3, 2006, pp. 199-204
56. X.G. Li, W.H. Scott Lawson and Y.Norman Zhou 2008. Lap welding of steel articles having a corrosion resisting metallic coating, United States Patent US 2008/0035615 A1
57. X.Li,S.Lawson and Y.Zhou 2007. Novel technique for laser lap welding of zinc coated sheet steels, *Journal of Laser Applications*, 19(4):259-264
58. Y.F. TZeng, Pulsed Nd:YAG laser seam welding of zinc-coated steel, *Welding Journal*, v 78, n 7, Jul. 1999, pp. 238s-244s.
59. Y.F. TZeng, Toward process optimization in pulsed Nd:YAG laser seam welding of zinc coated steel, *JSME International Journal. Series C: Mechanical Systems, Machine Elements and Manufacturing*, v 43, n 1, 2000, pp. 47-54.
60. Y.F. TZeng, Gap-free lap welding of zinc-coated steel using pulsed CO₂ laser, *International Journal of Advanced Manufacturing Technology*, v 29, n 3-4, June 2006, pp. 287-295
61. E.L Baardsen, Method of welding galvanized steel, United States Patent, Patent No. 3969604
62. W.Chen, P.Ackerson and P.Molian, CO₂ laser welding of galvanized steel sheets using vent holes, *Material & Design*, v 30,n 2, 2009, pp. 245-251
63. M. G. Forrest and F. Lu, Development of an advanced dual beam head for laser lap joining of zinc coated steel sheet without gap at the interface, *24th International Congress on Applications of Lasers and Electro-Optics*, ICALEO 2005, pp. 1069-1074.
64. M.G. Forrest, F. Lu, Fundamental Study of dual beam laser welding of zinc coated steel sheets without gap at the interface, *ICALEO 2003 International*

Congress on Applications of Lasers and Electro-Optics, Jacksonville, Florida, USA, Oct. 2003.

65. F. Lu and M.G. Forrest, Weldability comparison of different zinc coated high-strength steel sheets in laser lap joining configuration without gap, *ICALEO 2003 International Congress on Applications of Lasers and Electro-Optics*, Jacksonville, Florida, USA, Oct. 2003.
66. J. Xie, Dual beam laser welding, *Welding Journal*, v 81, n 10, 2002, pp. 223s-230s.
67. M.M.S. Gualini, S. Iqbal, F. Grassi, Modified dual-beam method for welding galvanized steel sheets in lap configuration, *Journal of Laser Applications*, v 18, n 3, 2006, pp. 185-191
68. M. G. Forrest, F. Lu, and W. A. Marttila, Process development for dual beam laser welding of zinc-coated steel sheets in lap joint configuration without gap control at the interface, available online at: <http://www.laserglobalservices.com>
69. Bagger and F. O. Olsen, Review of laser hybrid welding, *Journal of Laser Applications*, v 17, n 1, February, 2005, pp. 1-14.
70. H. W. Choi, D.F. Farson, D.F., and M.H. Cho, Using a hybrid laser plus GMAW process for controlling the bead humping defect, *Welding Journal*, v 85, n 8, 2006, pp. 174s-179s.
71. H. W. Choi, D.F. Farson, D.F., and M.H. Cho, Using a hybrid laser plus GMAW process for controlling the bead humping defect, *Welding Journal*, v 85, n 8, 2006, pp. 174s-179s.
72. S.M. Kelly, E.W. Reutzler, E.J. Whitney, J.F. Tressler, and R.P. Martukanitz, Examination of the process efficiency during hybrid laser-arc welding, *Materials Science and Technology*, v 3, *Materials Science and Technology 2005 - Proceedings of the Conference*, 2005, pp. 69-76.
73. T. Sugino, S. Tsukamoto, T. Nakamura, and G. Arakane, Fundamental study on welding phenomena in pulsed laser-GMA hybrid welding, *24th International Congress on Applications of Lasers and Electro-Optics, ICALEO 2005 - Congress Proceedings, 24th International Congress on Applications of Lasers and Electro-Optics*, ICALEO 2005- Congress Proceedings, 2005, pp. 108-116.
74. M.Y. Lee, W.S. Chang, Y.G. Kweon, and D.W. Lee, Laser-MIG hybrid weldability of high strength steel for car industry, *24th International Congress on Applications of Lasers and Electro-Optics, ICALEO 2005 - Congress Proceedings, 24th International Congress on Applications of Lasers and Electro-Optics*, ICALEO 2005 - Congress Proceedings, 2005, pp. 134-142.

75. M. Ono, Y. Shinbo, A. Yoshitake, and M. Ohmura, Development of laser-arc hybrid welding, *NKK Technical Review*, n 86, 2002, pp. 8-12.
76. W.M. Steen, M.Eboo, and J.Clarke, Arc augmented laser welding, *Advances in Welding Processes Proceedings, 4th International Conference*, Harrogate, U.K., 9-11 May 1978.
77. M.Kusch and S. Thurner, Application of the plasma-MIG technology for the joining of galvanized steel materials, *Welding and Cutting*,
78. C. Kim, W. Choi, J. Kim, and S. Rhee, Relationship between the weldability and the process parameters for laser-TIG hybrid welding of galvanized steel sheets.
79. G. Davis, *Materials for automobile bodies*, Butterworth Heinemann, 2004
80. B.Corbett and A. Priddle, Dual phase leads revial online at: <http://waw.wardsauto.com>
81. C.Ma,D.L.Chen,S.D.Bhole,G.Boudreau,A.Lee and E.Biro, Macrostructure and fracture characteristics of spot-welded DP 600 steel, *Materials Science and Engineering A*, Vol 485, 2008, pp 334-346
82. H.G. Yang, Y.S.Zhang,X.M.Lai and G.L.Chen, Critical specimen thickness of hot galvanized dual-phase steel spot welding, *Transactions of the China Welding Institution*, Vol 29, 2008, pp 93-96
83. X.Q.Zhang,G.L.Chen and Y.S.Zhang, Characteristics of electrode wear in resistance spot welding dual-phase steels, *Materials and Design*, Vol 29, 2008, pp 279-283
84. C.S. Orosz, B.Palotas and J. Dobranszky, Welding investigations of modern high strength dual-phase and TRIP-steel for automotive industry application, *Materials Science Forum*, Vol 537-538,2007, pp 431-438
85. M.Tumuluru,The effect of coatings on the resistance spot welding behavior of 780 MPa dual-phase steel, *Welding Journal*, Vol 86, 2007, pp 161/s-169/s
86. M.D.Tumuluru, Resistance spot welding of coated high-strength dual-phase steels, *Welding Journal*, Vol 85, 2006, pp 31-37
87. M.Marya and X.Q.Gayden, Development of requirements for resistance spot welding dual-phase (DP600) steels part 2: statistical analyses and process maps, *Welding Journal*, Vol 84, 2005, pp 197/s-204/s

88. V.Wesling and T.Rekersdrees, Investigations into the resistance spot welding of newly developed sheets made of higher-strength and super-high-strength steels, *Welding Research Abroad*, Vol 50, 2004, pp 26-31
89. C-Y, Kang, T-K Han, B-K Lee and J-K Kim, Characteristics of Nd:YAG laser welded 600MPa grade TRIP and DP steels, *Materials Science Forum*, Vol 539-543, 2007, pp 3967-3972
90. W. Van Haver, J.Verwimp, D. Crie and A. Dhooge, Hybrid laser welding of DP 600 dual phase steel: Microstructural and mechanical properties and joint preparation, *Welding in the world*, Vol 51, 2007, pp 65-74
91. T.Nillsson, MAG welding of high-strength and cold-rolled dual-phase steels, *A Welding Review*, Vol 53, 1998, pp 10-13
92. E.Soderstrom and P.Mendez, Humping mechanisms present in high speed welding, *Science and Technology of Welding and Joining*, Vol 11, 2006, pp 572-579
93. J.Xie, Plasma fluctuation and keyhole instability in laser welding, 1999 International Conference on Applications of Laser and Electro-Optics (ICALEO'99). Edited P. Christensen. San Diego, Calif.
94. J.Xie, Dual beam laser welding. *Welding Journal*, v 81(10), 2002, pp 223/S-230/S
95. J. Ion, *Laser processing of engineering materials: principles, procedure and industrial application*, Butterworth-Heinemann, 2005.
96. Matsunawa, J. Kim, N. Seto, M.Mizutani, and S. Katayama, Dynamics of keyhole and molten pool in laser welding. *Journal of Laser Application*, v10, 1998, pp. 247-254.
97. Y.Arata, H. Maruo,I. Miyamoto, and S. Takeuchi, Dynamic behavior of laser welding and cutting, *Proceedings of the 7th Intl. Conf. on Electron and Ion Beam Sci. and Tech*, 1979,pp.111-128
98. F.M. Haran et al, Optical signal oscillations in laser keyhole welding and potential application to lap welding, *Meas. Sci. Technol.*, v 8, 1997, pp. 627-633
99. T.Graf and H.Stauffer, Laser hybrid welding drives VW improvement, *Welding Journal*, Vol. 82, 2003, pp 42-48
100. C.F.Petring, Recent progress and innovative solutions for laser-arc hybrid welding, *Pceedings of the 1st Pacific International Conference on Application of lasers and Optics 2004*, Section 7-10

101. C.Bagger and F.O.Olsen, Review of laser hybrid welding, Journal of laser applications, Vol 17, 2005, pp 2-14
102. S.G.Gorny, V.A.Lopota, V.D.Redozubov and V.S.Smirnov, Peculiarities of metal heating in laser-arc welding, Avtomat.Svarka, No.1, pp 73-74
103. S.Kou, Welding metallurgy (second edition) , Wiley-interscience, 2002
104. Matsunawa, J.D. Kim, N. Seto, M. Mizutani, and S. Katayama, Dynamics of Keyhole and Molten Pool in Laser Welding, J. of Laser Applications, v 10, n 6, pp 247-254
105. Y.B Chen, Z.L.Lei, L.Q.Li and L.Wu, Experimental study on welding characteristics of CO₂ laser TIG hybrid welding process, Science and Technology of Welding & Joining, Vol. 11, 2006, pp. 403-411
106. N. Seto, S. Katayama and A. Matsunawa, High-speed simultaneous observation of plasma and keyhole behavior during high power CO₂ laser welding: Effect of shielding gas on porosity formation, Journal of Laser Applications, Vol 12, pp.245-250
107. G.Davis, Materials fro automobile bodies, Elsevier Ltd. 2003, Burlington MA
108. M.Gao, X.Y.Zeng, and Q.W.Hu, Effects of welding parameters on melting energy of CO₂ laser-GMA hybrid welding, Science and Technology of Welding and Joining, Vol.11, 2006, pp.517-522
109. J.F.Lancaster, The Physics of Welding, 2nd Edition, 1985, Pergamon Press
110. Y.B. Chen, L.Li, J.F.Fang, and X.S. Feng, Numerical analysis of energy effect in Laser-TIG hybrid welding, Journal of Material Science Technology, Vol.19,2003,pp.23-26
111. B.Hu and G.D.Ouden, Laser induced stabilization of the welding arc, Science and Technology of Welding and Joining, Vol.10, 2005, pp.76-81
112. M.Hamadou, R.Fabbro, and G.Caillibotte, Effect of gas shielding delivery mode on high power CO₂ laser welding, Proceedings of ICALEO 2003, Laser Welding and Brazing, San Francisco, California, 2004, pp.171-180
113. T.P.Hughes, Plasmas and laser light, Adam Hilger Led, 1975, Lodon, UK
119. S.L Yang, R. Kovacevic, R. Ruokolainen and B. Carlson, GTAW-assisted laser welding of galvanized high-strength steel in a gap-free lap joint configuration, accepted for publication at *2009 TMS Annual Meeting and Exhibition*, February 15- 19, San Francisco, California, USA

120. S.Kou, *Welding Metallurgy* (second edition), Wiley-Interscience, 2002
121. J.F.Shackelford and W.Alexander 2000.*Materials science and engineering handbook* (third edition), CRC press
122. C.D.Wagner, 1991.*The NIST x-ray photoelectron spectroscopy (XPS) database microform*, NIST technical note
123. D.Briggs and J.T.Grant, *Surface Analysis by Auger and X-ray Photoelectron Spectroscopy*, IM Publications, 2003
124. T.Fujii,F.M.F.de Groot, G.A.Sawatzky, F.C.Voogt, T.Hibma, and K.Okada, In situ XPS analysis of vaorius iron oxide films grown by NO₂-assisted molecular-beam epitaxy, *Physical Review B*, Vol.59, 1999,pp.3195-3202
125. P.Mills and J.L.Sullivan, A study of the core level electrons in iron and its three oxides by means of x-ray photoelectron spectroscopy, *Journal of Physics D: Applied Physics*, Vol.16, 1983, pp.723-732
126. S.L Yang, R. Kovacevic, R. Ruokolainen and B. Carlson, GTAW-assisted laser welding of galvanized high-strength steel in a gap-free lap joint configuration, accepted for publication at *2009 TMS Annual Meeting and Exhibition*, February 15- 19, San Francisco, California, USA
127. S.Kou, *Welding Metallurgy* (second edition), Wiley-Interscience, 2002
128. J.F.Shackelford and W.Alexander 2000.*Materials science and engineering handbook* (third edition), CRC press
129. C.D.Wagner, 1991.*The NIST x-ray photoelectron spectroscopy (XPS) database microform*, NIST technical note
130. D.Briggs and J.T.Grant, *Surface Analysis by Auger and X-ray Photoelectron Spectroscopy*, IM Publications, 2003
131. T.Fujii,F.M.F.de Groot, G.A.Sawatzky, F.C.Voogt, T.Hibma, and K.Okada, In situ XPS analysis of vaorius iron oxide films grown by NO₂-assisted molecular-beam epitaxy, *Physical Review B*, Vol.59, 1999,pp.3195-3202
132. P.Mills and J.L.Sullivan, A study of the core level electrons in iron and its three oxides by means of x-ray photoelectron spectroscopy, *Journal of Physics D: Applied Physics*, Vol.16, 1983, pp.723-732
133. M.Aronniemi, J.Lahtinen and P. Hautojarvi, Characterization of iron oxide thin films, *Surface and Interface Analysis*, Vol.36,2004, pp. 1004-1006
134. S.W.Garrenstroom and N.Winograd, *Journal of Chemistry Physics*, Vol.67, 1977, pp.3500

135. B.R.Strohmeier, and D.M.Hercules, *Journal of Catalysis*, Vol. 86, 1984, pp.26
136. G.A.Mesyats, *Cathode Phenomena in Vacuum Discharge: the breakdown, the Spark and the Arc*, 2000, Moscow
137. A.Fridman, L.A.Kennedy, *Plasma Physics and Engineering*, Taylor&Francis, 2004
138. M.N.Hirsh and H.J.Oskam, *Gaseous Electronics:Vol.1-Electrical Discharges*, Academic Press, 1978
139. K.Takeda, Dry cleaning of metal surfaces by a vacuum arc, *Surface and Coatings Technology*, Vol.131, 2004, pp. 234-238
140. H.Wang and R. Kovacevic, Rapid prototyping based on variable polarity gas tungsten arc welding for a 5356 aluminum alloy, *Journal of Engineering Manufacturing*, part B, Vol.215, 2001,pp.1519-1527
141. Y.M.Zhang and S.B.Zhang 1999.Observation of the keyhole during plasma arc welding, *Welding Journal*, 78(2):53/s-58s,
142. P.Q.Xu, G.X. Xu, X.H. Tang and S.Yao, A visual seam tracking system for robotic arc welding, *International Journal of Manufacturing Technology*, Vol 37, 2008, pp 70-75
143. H.Luo and X.Q. Chen, Laser visual sensing for seam tracking in robotic arc welding of titanium alloys, *International Journal of Manufacturing Technology*,Vol 26, 2005, pp 1012-1017
144. H.E.Beardsley, Y.M.Zhang and R. Kovacevic, Infrared sensing of full penetration state in gas tungsten arc welding, *International Journal of Machine Tool&Manufacturing*, Vol 34, 1994, pp 1079-1090
145. B.Zheng,H.J.Wang, Q.I.Wang and R. Kovacevic, Control for weld penetration in VPPAW of aluminum alloys using the front weld pool image signal, *Welding Journal*, Vol 79, 2000, pp 363/s-371/s
146. Y.M.Zhang, R.Kovacevic and L.Wu, Dynamic analysis and identification of gas tungsten arc welding process for weld penetration control, *Journal of Engineering for industry, Transactions of the ASME*, Vol 118, 1996, pp 123-136
147. R.K.Holbert, R.W.Richardson and D.F. Farson, Image-based penetration monitoring of CO2 laser beam welding. *Welding Journal*, 2000 April, 89-s – 96-s.
148. R. Kovacevic, Z.N.Cao and Y.M.Zhang, Role of welding parameters in determining the geometrical appearance of weld pool, *Journal of Engineering*

- Materials and Technology, Transactions of the ASME, Vol 118, 1996, pp 589-596
149. D.B.Zhao, J.Q.Yi, S.B.Chen, L.Wu and Q.Chen, Extraction of three-dimensional parameters for weld pool surface in pulsed GTAW with wire filler, *Journal of Manufacturing Science and Engineering*, Vol 125, 2003, pp 493-503
 150. Y.Z.Wang, Z.Jandric and R.Kovacevic, Real-time molten pool area extraction for control of gas tungsten arc welding, 11th International Conference on Computer Technology in Welding; Columbus, OH;USA;5-6 Dec.2001, pp 87-94
 151. Saeed.G. Y.Zhang,C.Jaynes, Weld pool surface monitoring and depth extraction using a calibrated CCD sensor. ASM Proceedings of the International Conference: Trends in Welding Research, v 2005, Trends in Welding Research - Proceedings of the 7th International Conference, 2005, p 671-676.
 152. Kovacevic,R.,Zhang, Y.M. and Ruan,S., Sensing and control of weld pool geometry for automated GTA welding, *ASME Journal of Engineering for Industry*, Vol.117,No.2, 1995,pp.210-222.
 153. J.Y.Jeng, T.F.Mau and S.M.Leu, Gap inspection and alignment using a vision technique for laser butt joint welding, *International Journal of Advanced Manufacture Technology*, Vol 16, 2006, pp 212-216
 154. Y.B.Chen, Z.L.Lei, L.Q.Li and L.Wu, Experimental study on welding characteristic of CO₂ laser TIG hybrid welding process, *Science and Technology of Welding and Joining*, Vol 11, 2006, pp 403-411
 155. Y.Natio, M.Mizutani and S. Katayama, Observation of keyhole behavior and melt flows during laser-arc hybrid welding, *ICALEO2003*, October13-16,Florida,USA, pp159-167
 156. P. McIntire, *Nondestructive testing handbook*, Second edition, Volume 5 Acoustic emission testing, American society for nondestructive testing
 157. J. Ion, *Laser processing of engineering materials: principles, procedure and industrial application*, Butterworth-Heinemann 2005
 158. D.F.Farson and A.Ali, Laser weld penetration monitoring with multiple emission signal measurements, *Journal of laser applications* 11(1999) 47-53
 159. H.P. Gu et al, Resonant acoustic emission during laser welding of metals, *J.Phys D: Appl. Phys.*, v 29, pp.550-555, 1996

160. Y.L Mao, G. Kinsman, W.W.Duley, Real-time fast fourier transform analysis of acoustic emission during CO₂ laser welding of materials, *Journal of laser applications* 5(1993) 17-22
161. Y.Lee., Monitoring and planning for open architecture manufacturing of precision machining using acoustic emission, Ph.D. dissertation, 1991
162. X.Chen, J.Tang and D.A.Dornfeld, Monitoring and analysis of ultraprecision metal cutting with acoustic emission, Mechanical Engineering Congress and Exposition, ASME, Atlanta,GA,1996,pp.387
163. H.V.Ravindra,Y.G.Srinivasa and R. Krishnamurthy, Acoustic emission for tool condition monitoring in metal cutting, *Wear*, Vol. 212, 1997, pp 78-84
164. W.Jolly, Acoustic emission exposes cracks during welding, *Welding Journey*, Vol. 48, 1969, pp 328-331
165. A.S.Sun, Multiple sensor monitoring of laser welding, 2001, Ph.D dissertation
166. S.M.C Van Bohemen, M.J.M Hermans and G.Den Ouden, Monitoring of martensite formation during welding by means of acoustic emission, *Journal of Physics D*, Vol. 34, 2001, pp 3312-3317
167. W.M.Steen and Weerasinghe, In process beam monitoring, *SPIE Laser Processing:Fundametnals, Applications and Systems Engineering*, Vol. 668, 1996, pp37-44
168. W.M.Steen and Weerasinghe, *Monitoring of laser material processes, SPIE High Power Lasers and Their Industrial Applications*, Vol.668, 1986, pp160-166
169. W.W. Duley and Y.L.Mao, The effect of surface condition on acoustic emission during welding of aluminium with CO₂ laser radiation, *Journey of Physic D: Applied Physics*, Vol. 27 pp 1379-1383
170. L.Grad, J.Grumb, I. Polajnar and J.M.Slabe, Feasibility study of acoustic signals for on-line monitoring in short circuit gas metal arc welding, *International Journal of Machine Tools and Manufacutre*, Vol. 44, pp 555-561
171. R.Akhter, W. M. Steen, and K. G. Watkins 1991. Welding zinc-coated steel with a laser and the properties of the weldment. *Journal of Laser Applications* 3(2):.9-20.
172. Welding Zinc-Coated Steels, AWS WZC/D19.0-72, American Welding Society, 1972.

173. M.P. Graham, D.M. Hirak, H.W. Kerr, and D.C. Weckman 1994. Nd:YAG laser welding of coated sheet steel. *Journal of Laser Applications* 6(4): 212-222.
174. R.R.G.M. Pieters, J.G. Bakels, M.J.M Hermans, and G. den Ouden 2006. Laser welding of zinc coated steels in an edge lap configuration, *Journal of Laser Applications* 18(3):199-204.
175. M.P. Graham, D.M. Hirak, H.W. Kerr, and D.C. Weckman 1994. Nd:YAG laser welding of coated sheet steel, *Journal of Laser Applications* 6(4): 212-222.
176. M.P. Graham, D.M. Hirak, H.W. Kerr, D.C. Weckman 1996. Nd:YAG laser beam welding of coated steels using a modified lap joint geometry. *Welding Journal* 75(5): 162s-170s.
177. E.J. Pennington 1987. Laser welding of galvanized steel, US Patent No. 4642446
178. S.W.Williams, P.L.Salter,G.Scott and S.J.Harris, New welding process for galvanized steel 1993. Proc. 26th Int. Symp. Automotive Technology and Automation:.49-56, Aachen, Germany.
179. Y.F. TZeng 1999. Pulsed Nd:YAG laser seam welding of zinc-coated steel, *Welding Journal* 78(7): 238s-244s.
180. G.H., Mueller 2004. Hybrid welding of galvanized steel sheet. European patent EP 1454701
181. M.Kusch and S. Thurner 2008. Application of the plasma-MIG technology for the joining of galvanized steel materials, *Welding and Cutting* 7(1): 54-59
182. C. Kim, W. Choi, J. Kim, and S. Rhee 2008. Relationship between the weldability and the process parameters for laser-TIG hybrid welding of galvanized steel sheets. *Materials Transactions* 49(1):179-186
183. H.Gu and R. Mueller 2001.Hybrid welding of galvanized steel sheet. 20th International Congress on Applications of lasers&Electro-optics, ICALEO:13-19
184. J. Xie 2002. Dual beam laser welding, *Welding Journal* 81(10): 223s-230s.
185. M.M.S. Gualini, S. Iqbal, F. Grassi 2006. Modified dual-beam method for welding galvanized steel sheets in lap configuration, *Journal of Laser Applications* 18(3): 185-191
186. M.G.Forrest and F.Lu 2005. Development of an advanced dual beam head for laser lap joining of zinc coated steel sheet without gap at the interface, 24th International Congress on Applications of Lasers and Electro-Optics:1069-1074

187. X.G. Li, W.H. Scott Lawson and Y.Norman Zhou 2008. Lap welding of steel articles having a corrosion resisting metallic coating, United States Patent US 2008/0035615 A1
188. J. Mazumder, A. Dasgupta, and M. Bembenek 2002. Alloy based laser welding, US Patent 6,479,168.
189. S.L Yang, R. Kovacevic, R. Ruokolainen and B. Carlson, GTAW-assisted laser welding of galvanized high-strength steel in a gap-free lap joint configuration, accepted for publication at *2009 TMS Annual Meeting and Exhibition*, February 15- 19, San Francisco, California, USA
190. H.Park and S.Rhee, Analysis of mechanism of plasma and spatter in CO2 laser welding of galvanized steel, *Optics and Laser Technology*, 31(2), 1999, pp. 119-126
191. S.L Yang and W. Huang, F.R. Kong, D.C Lin and R. Kovacevic, Monitoring of the spatter formation in laser welding of galvanized steels in lap joint configuration by the measurement of the acoustic emission, published in *the Procedure of 2008 international Manufacturing Science and Engineering Conference (MSEC 2008)*, October 7-10, 2008, Evanston, Illinois, USA
192. S.L. Yang, W. Huang, F.R. Kong, D.C. Lin and R. Kovacevic, Study on the formation of blowholes and molten pool behavior in laser welding of galvanized steels in lap joint configuration by machine vision, published in *the Proceeding of 47th Conference of Metallurgical (COM 2008)*, August 24-27, 2008, Winnipeg, Manitoba, Canada
193. C.T.Dawes, *Laser welding: a practical guide*, 1992, Woodhead publishing Ltd
194. D.M. Hu and R. Kovacevic, Sensing, modeling and control for laser-based additive manufacturing, *International Journal of Machine Tools&Manufacture*, Vol 43, 2003, pp. 51-60
195. G.M.Romer,M.Hoeksma,and J.Meijer, Industrial imaging controls laser surface treatment, *Photonics Spectra*, 31(11), 1997, pp. 104-109
196. R.C. Gonzalez and R.E.Woods, *Digital Image Processing*, 2nd ed., 2002, Prentice Hall, Upper Saddle River, NJ.
197. H.Hamaya, S. Furusako, Y.Mitasaki and T.Tanaka, Method of laser welding for overlapped zinc steel plates, Patent no. JP2002 160083, 2002
198. B.Criqui,L.Goby,P.Habert,and M. Loly, Device and associated process of so called laser welding bi-layer, Patent no FR 1249301, 2002

199. J.Xie and A.Kar 1999.Laser welding of thin sheet steel with surface oxidation, *Welding Journal*, 78(10):343/s-348/s
200. A.G.Grigorouants, Basics of laser material processing, CRC press, 1997
201. C S Wu, J Q Gao and M Zhang, Sensing weld pool geometrical appearance in gas-metal arc welding, Proc. Inst Metch. Engrs Part B: J. Engineering Manufacture, v 218, 2004,pp 813-818
202. C.E.Webb and J.D.C. Jones, Handbook of laser technology and applications, Volume 1, Philadelphia, 2004
203. Z.L Feng, Processes and mechanisms of welding residual stress and distortion, 2005,CRC
204. J.G.Proakis and D.K.Manolakis, Digital signal processing, Prentice Hall (4th edition), 2006
205. S.V.Vaseghi, Advanced signal processing and digital noise reduction, Wiley and Teubner press, England, 1996
206. Laser institute of America, J.F. Ready, and D.F. Farson, LIA handbook of laser material processing, Laser institute of America 2001
207. L.E. Kinsler, A.R.Frey,A.B.Coppens and J.V.Sanders, Fundamentals of acoustics, New York, 1999
208. L.H. Wang and R.X. Gao, Condition monitoring and control for intelligent manufacturing, Springer, 2006
209. R.K.Holbert et al, Image-based penetration monitoring of CO₂ laser beam welding, *Welding Journal*, Vol. 79, pp 89-96
210. P.E. Denney, E.A.Metzbower, Synchronized laser-video system study of high-power laser material interactions, ICALEO'91, pp. 84-93
211. R.Fabbro, M.Hamadou and F.Coste, Metallic vapor ejection effect on melt pool dynamics in deep penetration laser welding, *Journal of laser applications*, Vol.16, 2004, pp.16-19
212. S.L.Yang, W.Huang, D.C.Lin, F.R.Kong, and R. Kovacevic, Hybrid laser/GTAW welding of galvanized steels in a gap-free lap joint configuration, 2009 TMS Annual Meeting and Exhibition, February 15-19, San Francisco, California, USA
213. J.F.Shackelford and W.Alexander 2000.Materials science and engineering handbook (third edition), CRC press

214. D.Rosenthal, The theory of moving sources of heat and its application to metal treatments, Trans ASME, Vol.68,1946,pp.849-865
215. R.R.Rykalin, Energy sources for welding, Welding in the world, Vol.12,No.9-10,1974,pp. 227-248
216. P.O.Myers,O.A.Uyehara and G.L.Borman, Fundamentals of heat flow in welding ,Welding Research Council Bulletin, New York No.123,1967
217. V.Pavelic, R.Tanbakuchi,O.A.Uyehara, and Myers, Experimental and computed temperature histories in gas tungsten arc welding of thin plates, Welding Journal, Vol.48,pp 295s-305s,1969
218. G.W.Krutz, and L.J.Segerlind, Finite element analysis of welded structures, Welding Journal, Vol.57, 1978, pp.211s-216s
219. E.Friedman, Thermo-mechanical analysis of the welding process using the finite element method, Journal of Pressure Vessel Technology, Trans.ASME, Vol.97,No.3,1975,pp.206-213
220. Z.Paley and P.D.Hibbert, Computation of temperatures in actual weld designs, Welding Journal, Vol.54,1975,pp.385s-392s
221. O.Westby, Temperature distribution in the workpiece by welding ,Department of Metallurgy and Metals Working, The Technical University, Trondheim Norway, 1968
222. J.Goldak, A.Chakravarti, and M.Bibby, A finite element model for welding heat sources, Metallurgical Transactions B, Vol.15B, 1984, pp. 299-305
223. N.T.Nguyen,A.Ohta,K.Matsuoka,M.Suzuki and Y.Maeda, Analytical solutions for transient temperature of semi-infinite body subjected to 3-D moving heat sources, Welding Journal, Vol.78, 1999, pp. 265-s-274-s
224. W.Sudnik, D.Radaj, and W. Erofeew, Computerized simulation of laser beam welding, modeling and verification, Journal of Physics: D Applied Physics, Vol.29, 1996, pp. 2811-2817.
225. R.Fabbro and K.Chouf, Keyhole modeling during laser welding, Journal of applied physics, Vol.87, 1999, 4075-4083
226. J.Kroos, U.Gratzke and G.Simon, Towards a self-consistent model of the keyhole in penetration laser beam welding, Journal of applied physics, Vol.26, 1993, 474-480

227. H.Ki, P.S.Mohanty, and J.Mazumder, Modeling of laser keyhole welding: Part I. mathematical modeling, numerical methodology, role of recoil pressure, multiple reflections, and free surface evolution, *Metallurgical and materials Transactions A*, Vol.33A, 2002, pp.1817-1830
228. J.Dowden, M.Davis, P.Kapadia, Some aspects of the fluid dynamics of laser welding, *Journal of Fluid Mechanics*, Vol.126, 1983, pp.123-146
229. K.N.Lankalapalli, J.F.Tu, and M.Gartner, *Journal of Applied Physics*, Vol.29, 1996, 1831-1841
230. H.Wang, Y.Shi, S.Gong, and A.Duan, Effect of assist gas flow on the gas shielding during laser deep penetration welding, *Journal of Materials Processing Technology*, Vol. 184, 2007, pp.379-385
231. S.D. Ji, H.Y.Fang, X.S Liu, and Q.G Meng, Influence of a welding sequence on the welding residual stress of a thick plate, *Modelling and Simulation in Material Science and Engineering*, Vol.13, 2005, pp.553-565
232. N.Screenivasan, M.Xia, S.Lawson, and Y.Zhou, Effect of laser welding on formability of DP980 steel, *Journal of Engineering Material and technology*, Vol.130, 2008, pp. 041004-1-9
233. J.A.Goldak and M. Akhlaghi. *Computational welding mechanics*, 2003, Springer press, New York, USA
234. J.Goldak, A. Chakravarti, and M.Bibby, A new finite element model for welding heat source, *Journal of Metallurgical Transactions B*, Vol.15B, 1984, pp.299-305
235. N.T.Nguyen, Y.W.Mai, S.Simpson, and A.Ohta, Analytical approximate solution for double ellipsoidal heat source in finite thick plate, *Welding Journal*, Vol.83, 2004, pp.82-s-93-s
236. S.A.A.Akbari Mousavi, and R.Miresmaeili, Experimental and numerical analyses of residual stress distributions in TIG welding process for 304L stainless steel, *Journal of Material Processing Technology*, 2008, pp.383-394
237. A.Bejan, *Heat transfer*, John Wiley & Sons Inc., New York, USA, 1993
238. M.Brand and D.Siegele, Numerical simulation of distortion and residual stresses of dual phase steels weldments, *Welding in the World*, Vol.51, 2007, pp. 56-62
239. S.L Yang, R. Kovacevic, R. Ruokolainen and B. Carlson, GTAW-assisted laser welding of galvanized high-strength steel in a gap-free lap joint configuration,

accepted for publication at *2009 TMS Annual Meeting and Exhibition*, February 15- 19, San Francisco, California, USA

240. J.Miettinen, Calculation of solidification-related thermophysical properties for steels, *Metallurgical and Materials Transactions B*, Vol. 28B, 1997, pp. 281-297
241. Y.S.Touloukian,R.W.Powell,C.Y.Ho,and P.G.Klemens, *Thermo-physical Properties of high temperature Solid Materials*, Macmillan, New York,1976
242. X.He,P.W.Fuerschbach and T.DebRoy, Heat transfer and fluid flow during laser spot welding of 304 stainless steel, *Journal of Physics D: Applied Physics*, Vol.36,2003,pp. 1338-1398
243. A.G.Grigoryants, *Basics of Laser Material Processing*, CRC press,1994, Ann Arbor, USA
244. J.Ion, *Laser Processing of Engineering Materials:Principles, Procedure and industrial application*,Butterworth-Heinemann;1 edition, 2005, USA
245. R.Fabbro,S.Slimani,F.Coste and F.Briand, Study of keyhole behavior for full penetration laser welding, *Journal of Physics: D Applied Physics*, 2005, pp. 1881-1887
246. M.R.Frewin and D.A Scott, Finite element model of pulsed laser welding, *Welding Journal*, Vol.78,n1,pp.15-s-22-s
247. R.Komanduri and Z.B.Hou, Thermal analysis of the arc welding process: part II effect of variation of thermophysical properties with temperature, *Metallurgical and Materials Transactions B*, Vol.32B,2001, pp.483499
248. J.A.Goldak and M. Akhlaghi. *Computational welding mechanics*,2003, Springer press, New York, USA
249. D.Grey, H.Long, and P.Maropoulos, Effects of welding speed, energy input and heat source distribution on temperature variations in butt joint welding, *Journal of Materials Processing Technology*, 2005, pp.393-401